

# REDMOON: Radiation Environment and Dose Monitoring On-board a Nano-Rover

The Science Payload for the Lunar Zebro

Abhimanyu Shanbhag



Delft University of Technology

*"Revolution is an art that I pursue rather than a goal I expect to achieve. Nor is this a source of dismay; a lost cause can be as spiritually satisfying as a victory. "*

- Robert A. Heinlein, *The Moon Is a Harsh Mistress*

# REDMOON: Radiation Environment and Dose Monitoring On-board a Nano-Rover

## The Science Payload for the Lunar Zebro

by

**Abhimanyu Shanbhag**

to obtain the degree of Master of Science  
at the Delft University of Technology,  
to be defended publicly on Thursday November 10, 2022 at 14:00 PM.

Student number:	5244315	
Project Duration:	February 24 — November 1, 2022	
Thesis committee:	Prof. dr. E.K.A Gill	TU Delft, Chair
	Dr. A. Menicucci	TU Delft, Supervisor
	Dr. ir. C.J.M. Verhoeven	TU Delft, Examiner

An electronic version of this thesis is available at <http://repository.tudelft.nl/>.

Cover Image: NASA

# Preface

This project was made possible by the unique expertise and guidance provided by my supervisor, Dr. Alessandra Menicucci. Much of the groundwork and foundation for this thesis was created by the work of my friend and colleague, William de Meyer. William aided me with research, experiment preparation and software development concerning the Floating Gate Dosimeter (FGDOS). I'm grateful to Dr. Danzeca, Dr Brucoli and Alessandro Zimmaro from CERN for their critical feedback on my experimental results and for their extensive research and development work with the FGDOS technology. I'm thankful for the support of Wouter van Burik from HollandPTC in conducting proton beam radiation tests. Jasper Dijks provided help by means of various discussions about payload development and FGDOS testing.

In the last couple of years, I was fortunate to experience the excellence and ingenuity of the people at the Faculty of Aerospace Engineering in Delft. This graduate program has been the best learning experience of my life so far. I harbor sincere gratitude and admiration for all the professors and researchers who taught me and trained me. I was inspired by the ambitious mission and vision of the Lunar Zebro and Da Vinci Satellite Student Teams. They helped me become a better engineer by providing hands-on experience with hardware for space missions. My internship experience at ICE Cubes, SpaceApps also contributed significantly to this process. I wish to thank Debby van der Sande and the SPE secretariat for their assistance with procurement and logistics. I'm indebted to the support and service staff of TU Delft as well.

I'm grateful to Dr. Chris Verhoeven and Maneesh Verma from Lunar Zebro for leading this amazing team and for giving me a chance to contribute. Simon Stenger, Simon van Hulle and Jason James helped me tremendously during my tenure with Lunar Zebro and facilitated my work. I want to thank Floris van Mourik, Olasoji Makinwa and Sevket Uludag for helping me with various aspects of electronic design, prototyping and testing. I'm especially grateful to Floris for educating me with interesting discussions about engineering and electronics. Nic Kalis, Sil Barendregt, Aart Rozendaal and Sam Mastenbroek helped me with AIT related tasks. I'd also like to thank Yuri Klassens, Marco van Eederen and Emirhan from the LZ S/W department for their collaboration. Sid Dixit, Pietro Squillace and Riccardo Brambilla provided assistance with mechanical and thermal engineering tasks. Marnix Verkammen and other LZ team members provided a congenial and enjoyable atmosphere for research.

My time in Delft was made rich and enjoyable by the experiences I shared with my friends during the past two years. I wish them all the best for their future endeavors. Finally, I wish to thank my family and friends for their unconditional support and encouragement. Drawing from her vast experience in the industry, my mother continues to inspire me to work on space projects. I'm indebted to my sister for her advice on academic matters and for help with reviewing drafts of this thesis. Above all, I'm grateful to my grandparents for their kindness and love.

*Abhimanyu Shanbhag  
Delft, November 2022*

# Summary

The space radiation environment poses considerable challenges to crewed and uncrewed space missions. This is due to the presence of high energy ionizing radiation in space [39]. Space radiation has the ability to cause damage and degradation in space systems and it also poses numerous health risks and hazards to astronauts. Lunar missions can be vulnerable to radiation exposure and damage from both cosmic rays and solar energetic particles [105]. It is of paramount importance to study, understand and monitor the space environment such that exploration, science and commerce can be carried out in a safe, sustainable and economically feasible manner.

In-situ radiation measurements at the Moon have only been acquired on a handful of previous occasions. To date, only a small complement of instruments has directly measured the radiation environment near the Moon [32, 87, 27], and only once in history have the lunar surface radiation levels been measured [159]. Hence, a lacuna exists in direct, in-situ measurements of the radiation environment on the Moon. Anticipating the current roster of lunar spaceflight activities [128], development of a complete and consistent understanding of the lunar radiation environment and its effects is essential. Implementation of these efforts can be carried out using a two pronged approach: (a) performing actual radiation measurements using spaceborne instruments and (b) developing theoretical and empirical models of the space radiation environment. The latter can be augmented and improved by taking the data from instruments into consideration, while specification and engineering of instruments involves consideration of predictions and estimates based on theoretical models. Advances in semiconductor technology and fabrication processes have led to the development of a variety of solid state detectors for the purpose of monitoring ionizing radiation in space. The floating gate MOSFET based dosimeter - FGDOS [27] developed by Sealicon and CERN is a prime example and offers a low cost, low power and compact solution for measuring radiation on platforms with very tight constraints on resources, such as nano-satellites and miniaturized robots. This thesis aims to advance the work done by de Meyere [90] on characterisation of the FGDOS for space applications. This work also presents (i) Radiation Payload design & development, (ii) Modelling and analysis of the radiation environment in the context of the science mission of Lunar Zebro and (iii) Extended characterisation and testing of the FGDOS for its application as the core detector of the Radiation Payload.

As a part of this thesis, a miniaturized instrument was designed to enable in-situ measurements of the lunar radiation environment. The instrument is designated to function as the science payload for the first mission of the Lunar Zebro Nano-Rover. Characterization and testing of the FGDOS was advanced with an emphasis on utilization as the core detector for the payload during the Lunar Zebro mission. A prototype of the Radiation Payload was designed, produced and tested to verify and validate its design. Radiation environment simulations were performed using SPENVIS and OLTARIS to estimate the conditions during various phases of the lunar mission. A radiation transport model of the payload was prepared and simulated, as a foundation for more extensive simulations in the future.

The work described in this thesis calls for further research and development of the FGDOS technology, including experimental mapping of the complete envelope of FGDOS sensitivity w.r.t expected mission environments. The Radiation Payload prototype is to be subjected to a system level environmental test campaign with the rover to further validate the design. The use of additional noise reduction measures and thermal characterization at lunar mission conditions is also recommended, as a stepping stone to iterating and improving the payload design such that it can be made flight-worthy.

**Keywords:** Lunar Radiation Environment, Floating Gate Dosimeter (FGDOS), Radiation Monitoring, Miniaturized Space Instrumentation, Lunar Zebro Radiation Payload

# Contents

Preface	i
Summary	ii
List of Figures	vii
List of Tables	xii
List of Symbols & Acronyms	xiv
1 Introduction	1
2 Background	3
2.1 Space Radiation Environment . . . . .	3
2.1.1 Space Radiation. . . . .	3
2.1.2 Lunar Radiation Environment. . . . .	5
2.1.3 Space Radiation Environment Modelling. . . . .	7
2.1.4 Space Radiation Transport. . . . .	8
2.2 Space Radiation Measurement . . . . .	9
2.2.1 Instruments for in-situ measurement of ionizing radiation. . . . .	9
2.2.2 Miniaturized Dosimeters for Space Applications. . . . .	20
2.3 Lunar Zebro Radiation Payload . . . . .	23
2.3.1 Mission Objectives . . . . .	23
2.3.2 System Architecture . . . . .	24
2.3.3 Science Mission & Payload. . . . .	24
2.4 Research Objectives & Questions . . . . .	25
3 Radiation Payload Design & Development	27
3.1 Radiation Payload Systems Engineering . . . . .	27
3.1.1 Need & Mission Statement. . . . .	27
3.1.2 Science Mission Objectives & Definition . . . . .	27
3.1.3 Stakeholders . . . . .	29
3.1.4 System Requirements . . . . .	32
3.1.5 Functional Breakdown . . . . .	38
3.1.6 Functional Flow. . . . .	38
3.1.7 Payload Subsystem Architecture . . . . .	40
3.1.8 Interfaces . . . . .	41
3.1.9 Technical Budgets . . . . .	44
3.1.10 Risk Evaluation & Management . . . . .	46
3.1.11 Work Breakdown Structure. . . . .	47
3.2 Detailed Design & Implementation . . . . .	48
3.2.1 Design Philosophy & Considerations . . . . .	48
3.2.2 Mechanical Design . . . . .	49
3.2.3 Electronic Design. . . . .	53
3.2.4 Software Design. . . . .	56
3.2.5 Operational FFBD . . . . .	62
3.2.6 Telemetry & Telecommands . . . . .	65

3.3	Manufacturing, Assembly and Integration . . . . .	66
3.3.1	Production of breadboard models. . . . .	66
3.3.2	Development Model: MAIN Board Production. . . . .	67
3.3.3	Development Model: Daughterboard PCB Production . . . . .	68
3.3.4	Assembly into Belka 2 . . . . .	68
3.3.5	Integration . . . . .	69
4	Radiation Environment Modelling & Transport Simulations . . . . .	70
4.1	Overview of Radiation Payload Science. . . . .	70
4.2	Radiation Environment Analysis & Modelling . . . . .	71
4.2.1	Mission Segments & Models . . . . .	72
4.2.2	SPENVIS & OLTARIS Analysis . . . . .	72
4.2.3	Assumptions and limitations . . . . .	80
4.2.4	Results & Discussion . . . . .	81
4.3	Radiation Transport Simulations using Geant4 . . . . .	83
4.3.1	Simulation Methodology & Plan. . . . .	84
4.3.2	Radiation Payload MAIN Board in mono-energetic proton beam . . . . .	85
4.3.3	Payload MAIN and Daughterboard with Rover . . . . .	87
4.3.4	Payload MAIN Board with multi-spectral and multi-directional source . . . . .	88
4.3.5	Payload Boards and Rover with multi-spectral and multi-directional source . . . . .	89
4.3.6	Rover on the Moon . . . . .	89
4.3.7	Rover inside a Lunar Lava Tube . . . . .	90
4.3.8	Assumptions and limitations . . . . .	92
4.3.9	Conclusions & Recommendations . . . . .	93
5	Verification & Validation . . . . .	94
5.1	FGDOS Radiation Characterization & Performance Testing . . . . .	94
5.1.1	Test Setup . . . . .	94
5.1.2	Test Levels. . . . .	96
5.1.3	Methodology . . . . .	98
5.1.4	Observations . . . . .	98
5.1.5	Assumptions and limitations . . . . .	108
5.1.6	Results and Conclusions . . . . .	108
5.1.7	Open Questions. . . . .	110
5.2	FGDOS Temperature Characterization . . . . .	111
5.2.1	Test setup . . . . .	111
5.2.2	Test Levels. . . . .	112
5.2.3	Methodology . . . . .	112
5.2.4	Observations . . . . .	113
5.2.5	Limitations and assumptions . . . . .	115
5.2.6	Results & Conclusions . . . . .	116
5.3	FGDOS Sensor Characterization: Simultaneous Irradiation and Temperature variation . . . . .	118
5.3.1	Aim & Rationale. . . . .	118
5.3.2	Test Setup . . . . .	118
5.3.3	Test Levels. . . . .	119
5.3.4	Methodology . . . . .	121
5.3.5	Observations . . . . .	129
5.3.6	Limitations and assumptions . . . . .	137
5.3.7	Results & Conclusions . . . . .	137
5.4	Radiation Payload Prototype Functional Testing. . . . .	138
5.4.1	Inspection & Post soldering . . . . .	138
5.4.2	Electronics & S/W functional testing . . . . .	139

5.5	Radiation Payload Performance Testing . . . . .	141
5.5.1	Noise Characterisation, Power consumption & Temperature Monitor Calibration . . . . .	141
5.5.2	Daughterboard Interface Test . . . . .	144
5.6	Radiation Payload Performance Testing: Proton Beam Irradiation . . . . .	145
5.6.1	Aim & Rationale. . . . .	145
5.6.2	Test Setup . . . . .	145
5.6.3	Test Levels. . . . .	146
5.6.4	Methodology . . . . .	147
5.6.5	Observations & Inferences. . . . .	148
5.6.6	Limitations and assumptions . . . . .	157
5.6.7	Results & Conclusions . . . . .	157
5.7	Environmental Testing. . . . .	158
5.7.1	Functional Tests . . . . .	158
5.7.2	Mechanical loads: Vibration and Shock Testing . . . . .	158
5.7.3	Thermal-Vacuum Test . . . . .	159
5.7.4	Radiation Hardness Assurance . . . . .	159
6	Conclusions . . . . .	160
6.1	Radiation Payload Development . . . . .	160
6.2	Radiation Environment Modelling and Transport Simulations . . . . .	161
6.3	FGDOS Characterization & Testing . . . . .	161
6.4	Research Questions . . . . .	162
6.4.1	RQ-1 . . . . .	162
7	Recommendations for Further Work . . . . .	165
7.1	Lunar Zebro Radiation Payload . . . . .	165
7.1.1	Payload Design & Development . . . . .	165
7.1.2	Verification & Validation . . . . .	166
7.1.3	Long Term Applications . . . . .	166
7.2	Space Radiation Environment Modelling & Simulations . . . . .	167
7.2.1	Space Environment Models . . . . .	167
7.2.2	Radiation Transport Simulations . . . . .	167
7.3	FGDOS Testing & Characterization . . . . .	167
7.4	Outlook Toward the Future . . . . .	168
A	Design Documentation . . . . .	178
A.1	Electrical Schematics . . . . .	178
A.1.1	Radiation Payload MAIN V1 . . . . .	178
A.1.2	Radiation Payload Daughterboard V1. . . . .	180
A.1.3	FGD-03F Breakout Board . . . . .	182
A.2	PCB Layouts . . . . .	182
A.2.1	Payload MAIN V1 . . . . .	182
A.2.2	Payload Daughterboard V1 . . . . .	184
B	Software . . . . .	186
B.1	Radiation Payload Telemetry and Commands . . . . .	186
C	Test Results . . . . .	190
C.1	FGDOS Sensor Characterization . . . . .	190
C.1.1	Simultaneous Irradiation & Temperature Characterization . . . . .	190
C.2	Radiation Payload Functional Testing . . . . .	191
C.2.1	Noise, power, temperature. . . . .	191
C.3	Radiation Payload Performance Testing: Proton beam Irradiation . . . . .	192

---

D	Systems Engineering Supplement	193
D.1	Work Breakdown Structure . . . . .	193
D.2	Risk Management . . . . .	194
D.3	Radiation Detector Comparison . . . . .	204
D.4	Payload Financial Budget . . . . .	206
E	Simulation Results	208
E.1	Radiation Environment Modelling . . . . .	208
E.1.1	SPENVIS Methodology . . . . .	208
E.1.2	SPENVIS: Supplementary Analysis Results . . . . .	212
E.1.3	OLTARIS Methodology . . . . .	212
E.1.4	OLTARIS: Supplementary Analysis Results . . . . .	214
E.2	Radiation Transport Simulations: Supplementary Results . . . . .	215
E.2.1	Basic model setup in Geant4. . . . .	215
E.2.2	Radiation Payload MAIN Board Model . . . . .	215
E.2.3	Rover on a lunar regolith slab . . . . .	216
E.2.4	Rover in a lunar lava tube . . . . .	216
E.2.5	Source macro generated in SPENVIS . . . . .	216
F	Miscellaneous	219
F.1	Radiation Measurement & Relevant Quantities . . . . .	219

# List of Figures

2.1	Interaction of ionizing radiation with matter [59]	3
2.2	Elemental composition of cosmic rays in terms of dose, fluence and dose equivalent [105]	4
2.3	Contribution of various sources (from GCR) to the absorbed dose rate at the moon [130]	6
2.4	Dose rate comparison behind different levels of shielding in interplanetary space [87]	6
2.5	Schematic of DOSTEL detector setup [26]	10
2.6	CRaTER telescope and dosimeter	11
2.7	CRaTER mission results	12
2.8	RADOM electronic functional block diagram [32]	13
2.9	Mission results from the RADOM instrument [32]	14
2.10	Schematic view of the LND instrument [154]	15
2.11	Total, neutral particle and charged particle dose rates measured by LND during the first couple of lunar days after landing. Note: The background noise from radioactive sources has already been subtracted from the data in the plots [159]	16
2.12	DRALUX experiment block diagram [27]	17
2.13	Comparison of simulation results (without shielding) and mission data from DRALUX [27]	17
2.14	NASA LET Spectrometer instrument [55]	18
2.15	Dose rate measured at Mars surface by RAD [61]	20
2.16	FGDOS operation and physical schematic	22
2.17	FGD-03F block diagram [117]	22
2.18	Engineering Model Belka-1 [81]	23
2.19	Subsystems of the lunar rover [68]	24
2.20	Potential location of the Radiation Payload in the Lunar Zebro rover [53]	24
3.1	Indicative lunar mission plan ([67])	29
3.2	Radiation Payload Functional Breakdown	38
3.3	Radiation Payload Functional Flow Diagram	39
3.4	Radiation Payload System Architecture	40
3.5	Risk Matrix	47
3.6	Radiation Payload Work Breakdown Structure. Blocks indicated in violet involve close collaboration with the Lunar Zebro team	48
3.7	Placeholder Payload PCB position inside the rover chassis (highlighted in green)- front section view	49
3.8	CAD model of Radiation Payload MAIN Board (without DF13 connector)	50
3.9	Placeholder Payload PCB position inside the rover chassis (highlighted in green) - side section view	50
3.10	CAD model of Radiation Payload prototype boards mounted on custom fixtures	51
3.11	Placeholder Daughterboard position under SPP	51
3.12	Temperature dependence of LZ rover on internal dissipation [17]	53
3.13	Radiation Payload Electronics Block Diagram V1	54
3.14	Visualization of the Radiation Payload MAIN PCB design	56
3.15	CDHS Architecture	57
3.16	Functional Breakdown of Radiation Payload Firmware	59
3.17	Functional Breakdown of Radiation Payload Driver App	60
3.18	State transition diagram	61
3.19	Operational FFBD of Radiation Payload	62
3.20	Operational FFBD: Launch	63
3.21	Operational FFBD: Active Transit	63
3.22	Operational FFBD: Landing	64

3.23 Operational FFBD: Rover Deployment . . . . .	64
3.24 Operational FFBD: Nominal Operations . . . . .	64
3.25 Operational FFBD: Hibernation and beyond . . . . .	65
3.26 Breadboard schematics . . . . .	66
3.27 Radiation Payload Main V1 PCBs - post manufacturing . . . . .	67
3.28 Daughterboard bare PCBs . . . . .	68
3.29 Radiation Payload Assembly plan (excerpt from [136]) . . . . .	69
4.1 Science Scheme of the Radiation Payload . . . . .	70
4.2 Distribution of differential and integral flux from trapped particles in Earth orbit . . . . .	73
4.3 Integral flux from trapped radiation vs orbital time elapsed . . . . .	74
4.4 Peak differential and integral flux of solar particles from CREME-96 . . . . .	74
4.5 Total differential and integral fluence of solar particles from ESP-PSYCHIC . . . . .	75
4.6 Shielded flux from SPENVIS . . . . .	75
4.7 Proton GCR spectrum . . . . .	76
4.8 Dose depth curve obtained from SHIELDOSE-2Q . . . . .	76
4.9 Typical OLTARIS Workflow [126] . . . . .	77
4.10 GCR differential flux at boundary . . . . .	77
4.11 GCR dose v depth curve . . . . .	78
4.12 GCR dose v depth curve: contribution of various particles . . . . .	78
4.13 Lunar albedo flux . . . . .	78
4.14 Lunar albedo dose v depth curve . . . . .	79
4.15 Lunar albedo dose v depth curve: contribution of various particles . . . . .	79
4.16 SPE dose v depth curve . . . . .	80
4.17 SPE dose v depth curve . . . . .	80
4.18 Dose rates from crater microdosimeter [146] . . . . .	83
4.19 Plan for Radiation Payload Modelling with Geant4 . . . . .	84
4.20 Workflow used for Geant4 simulations (based on [82]) . . . . .	85
4.21 Radiation Payload MAIN Board simplified geometry . . . . .	86
4.22 Generation of secondaries from proton interaction with simplified Payload board . . . . .	86
4.23 Pencil beam of protons incident on Radiation Payload MAIN Board . . . . .	87
4.24 Wire-frame view of simplified LZ rover with Radiation payload MAIN and Daughter boards . . . . .	87
4.25 Simplified model of LZ rover exposed to proton beam . . . . .	88
4.26 Multi-spectral, multi-directional sources with payload MAIN Board . . . . .	88
4.27 Multi-spectral, multi-directional sources with payload MAIN Board . . . . .	89
4.28 Wire-frame view of rover on a lunar regolith slab . . . . .	90
4.29 Rover on lunar regolith slab: Exposure to point GCR spectrum with cosine angular distribution from point source . . . . .	90
4.30 Vertical entrance of a lunar lava tube . . . . .	91
4.31 LZ rover positioned inside the lava tube entrance . . . . .	91
4.32 Rover shielded from incident radiation within the lava tube . . . . .	92
5.1 FGDOS radiation characterisation test setup . . . . .	95
5.2 HPTC Beam Line Setup . . . . .	96
5.3 FGDOS characteristic over extended frequency range . . . . .	100
5.4 FGDOS recharge characteristic over extended frequency range . . . . .	100
5.5 Frequency characteristic within LDR - HISSENS Mode . . . . .	101
5.6 Variation of FGDOS sensitivity with beam energy - HISSENS mode . . . . .	101
5.7 Variation of FGDOS sensitivity with dose rate at 70 MeV . . . . .	102
5.8 Variation of FGDOS sensitivity with dose rate at 120 MeV . . . . .	102
5.9 Variation of FGDOS sensitivity with dose rate at 200 MeV . . . . .	102
5.10 Frequency characteristic in LDR - LOW SENS Mode . . . . .	103
5.11 Sensitivity variation with Beam Energy - LOW SENS Mode . . . . .	103
5.12 Sensitivity degradation with TID . . . . .	104

5.13 Increase in FGDOS power consumption with TID . . . . .	104
5.14 <i>Rapid Recovery</i> effect observed at 70 MeV . . . . .	105
5.15 <i>Rapid Recovery</i> effect observed at 120 MeV . . . . .	105
5.16 SEE in FGDOS . . . . .	106
5.17 Post SEE readout and irradiation . . . . .	107
5.18 Sensor response at very low dose rate (1 mGy/min) . . . . .	108
5.19 Temperature characterization test setup . . . . .	111
5.20 Temperature characterisation test setup - alternate views . . . . .	112
5.21 Temperature measured by the FGDOS internal monitor and the thermocouple during the heating phase . . . . .	113
5.22 Correlation between FGDOS internal temperature monitor readings and thermocouple measurements over the heating phase. Sensor 1 recorded the ambient temperature . . . . .	114
5.23 Variation of Sensor and reference frequencies with temperature . . . . .	114
5.24 FGDOS Sensor power consumption during the heating phase. Sensor 2 (in Blue) was the DUT while Sensor 1 showed high power consumption due to TID degradation from previously conducted proton beam tests . . . . .	115
5.25 Evolution of sensor frequency, reference frequency and temperature (in green) during the heating phase . . . . .	115
5.26 Relationship between sensor and reference frequency with temperature variation. A linear fit approximating this relation is shown by the green line . . . . .	117
5.27 Experiment room arrangement during testing at HPTC . . . . .	118
5.28 Setup schematic . . . . .	119
5.29 Experiment setup at HPTC . . . . .	119
5.30 - Radiation & Temperature change: Pre-test characterization setup . . . . .	121
5.31 Pre-test temperature characterization: Constant heater power . . . . .	122
5.32 Pre-test temperature characterization: Quasi-linear profile . . . . .	122
5.33 Pre-test temperature characterization: Sawtooth profile . . . . .	123
5.34 Pre-test temperature characterization: Rising sawtooth profile . . . . .	123
5.35 Pre-test temperature characterization: effect of cycling on sensor v ref freq characteristic for staircase profile . . . . .	124
5.36 Pre-test temperature characterization: effect of cycling on sensor v ref freq characteristic for sawtooth profile . . . . .	124
5.37 Pre-test temperature characterization: Cold spike . . . . .	125
5.38 Pre-test temperature characterization: Quasi-linear with oscillation . . . . .	125
5.39 Pre-test temperature characterization: Quasi-linear with oscillation . . . . .	126
5.40 Pre-test temperature characterization: Cold spike . . . . .	126
5.41 Pre-test temperature characterization: Cold spike . . . . .	126
5.42 Pre-test temperature characterization: Cold spike . . . . .	127
5.43 Pre-test temperature characterization: Sawtooth profile compensation . . . . .	128
5.44 Radiation characterisation: Extended frequency characteristic . . . . .	129
5.45 Dependence of FGDOS sensitivity on beam kinetic energy . . . . .	130
5.46 Dependence of FGDOS sensitivity on dose rate of irradiation . . . . .	130
5.47 Degradation of FGDOS sensitivity as a function of accumulated TID . . . . .	130
5.48 Evolution of average power consumption as a function of TID . . . . .	131
5.49 Passive mode baseline . . . . .	131
5.50 Comparison of external (Daughterboard) and internal (FGDOS) temperature readings . . . . .	132
5.51 Compensation for quasi-linear temperature profile at medium dose rate . . . . .	132
5.52 Compensation of the effect of sawtooth profile at very low dose rate . . . . .	133
5.53 Compensation of the effect of staircase profile on s2 frequency . . . . .	133
5.54 Summary of temperature compensation error for the HOT Board . . . . .	134
5.55 Summary of temperature compensation error for the COLD Board . . . . .	134
5.56 Simultaneous temperature change and irradiation for FGDOS in passive mode . . . . .	135
5.57 Extreme temperature variation run . . . . .	136

5.58 Post test thermal degradation run . . . . .	136
5.59 MAIN Board assembly . . . . .	139
5.60 Assembled Daughterboard PCB . . . . .	139
5.61 MCU being tested via interface with an MSP430 LaunchPad development board . . . . .	140
5.62 PCB Electrical testing . . . . .	140
5.63 Setup for noise characterisation, power consumption and temperature monitor calibration test	141
5.64 Raw sensor frequency noise distribution: effect of power supply . . . . .	142
5.65 Filtered sensor frequencies . . . . .	142
5.66 Filtered sensor frequencies with raw signal subtracted . . . . .	142
5.67 Payload prototype power consumption . . . . .	143
5.68 FGDOS temperature monitor calibration . . . . .	143
5.69 Daughterboard unit testing . . . . .	144
5.70 Daughterboard Interface test setup . . . . .	144
5.71 Radiation Payload performance testing at HPTC . . . . .	145
5.72 Close up views of payload performance test setup . . . . .	146
5.73 Close up views of payload performance test setup . . . . .	146
5.74 Payload Performance: HISENS characteristic over full frequency range . . . . .	149
5.75 Payload Performance: LOWSENS characteristic . . . . .	149
5.76 Payload Performance: Sensitivity variation with beam kinetic energy . . . . .	150
5.77 Payload Performance: Sensitivity variation with dose rate at various beam energies . . . . .	150
5.78 Payload Performance: measurement at low dose rate (0.02 Gy/min) . . . . .	151
5.79 Payload Performance: measurement at medium dose rate (0.12 Gy/min) . . . . .	151
5.80 Payload Performance: FGDOS response to very high dose rates at 244 MeV . . . . .	152
5.81 Payload Performance: Sensitivity degradation with TID . . . . .	153
5.82 Payload Performance: Change in power consumption with TID . . . . .	154
5.83 Payload Performance: <i>Rapid Recovery</i> effect . . . . .	154
5.84 Payload Performance: Post test frequency fading . . . . .	155
5.85 Payload Performance: Temperature monitoring . . . . .	155
5.86 Payload Performance: Recharge characteristic at 14.5 V recharge voltage . . . . .	156
5.87 Payload Performance: Passive mode . . . . .	156
C.1 Sensor vs. reference frequency characteristic for temperature compensation with constant heater power . . . . .	190
C.2 Anomalous behavior of s1 frequency with change in temperature . . . . .	190
C.3 Sensor vs reference frequency relationship under irradiation at constant temperature . . . . .	190
C.4 Post test thermal degradation run . . . . .	191
C.5 Time history plot of FGDOS frequencies using LDO supply . . . . .	191
C.6 Time history plot of FGDOS frequencies using lab supply . . . . .	191
C.7 Payload Performance: Nominal power consumption . . . . .	192
C.8 Payload Performance: Reference frequency and power variation in passive mode . . . . .	192
C.9 Payload Performance: Passive mode . . . . .	192
D.1 Radiation Payload Work Breakdown Structure . . . . .	193
D.2 Radiation Payload Work Breakdown Structure . . . . .	194
D.3 Risk Matrix . . . . .	204
E.1 Project setup in SPENVIS . . . . .	208
E.2 Set up of mission segments . . . . .	208
E.3 Set up of mission segment 1 . . . . .	209
E.4 Set up of mission segment 2 . . . . .	209
E.5 Set up of mission segment 3 . . . . .	210
E.6 Summary of mission segments . . . . .	210
E.7 Trapped radiation model setup . . . . .	210
E.8 Solar particle fluxes . . . . .	210

---

E.9 Solar particle fluences . . . . .	211
E.10 GCR spectra setup . . . . .	211
E.11 Set up of shielded flux from MFLUX . . . . .	211
E.12 Set up of dose depth curve using SHIELDOSE . . . . .	211
E.13 AP8 MIN: World Map . . . . .	212
E.14 AE8 MIN: World Map . . . . .	212
E.15 OLTARIS GCR analysis set up 1 . . . . .	212
E.16 OLTARIS GCR analysis set up 2 . . . . .	213
E.17 OLTARIS GCR analysis set up 3 . . . . .	213
E.18 OLTARIS SPE analysis set up 1 . . . . .	213
E.19 OLTARIS SPE analysis set up 2 . . . . .	214
E.20 OLTARIS GCR analysis results 1 . . . . .	214
E.21 OLTARIS GCR analysis results 2 . . . . .	214
E.22 OLTARIS SPE analysis results . . . . .	215
E.23 Mock simulation setup visualized in Geant4 . . . . .	215
E.24 Electron and proton incidence on simplified Radiation Payload MAIN . . . . .	215
E.25 Monte Carlo simulation of the rover on a lunar regolith slab . . . . .	216
E.26 Monte Carlo simulation of the rover inside a lunar lava tube . . . . .	216
F.1 Summary of radiation exposure quantities [5] . . . . .	220

# List of Tables

3.1	Mission Definition for the Lunar Zebro Science Mission . . . . .	28
3.2	Stakeholders in the Lunar Zebro Science Mission . . . . .	30
3.3	Stakeholder Requirements . . . . .	31
3.4	Radiation Payload System Requirements . . . . .	33
3.5	N2 Chart: Payload subsystem internal interfaces . . . . .	42
3.6	N2 Interface chart: Payload and rover subsystems . . . . .	43
3.7	Radiation Payload Mass Budget . . . . .	44
3.8	Radiation Payload Power Budget . . . . .	45
3.9	Radiation Payload data storage . . . . .	45
3.10	Radiation Payload data budget . . . . .	46
3.11	Thermal constraints for the Radiation Payload . . . . .	52
4.1	Overview of radiation environment modelling . . . . .	72
4.2	Models used in SPENVIS for various radiation source types . . . . .	72
4.3	Summary of mission doses and dose rates (behind 1.5 mm Al shielding) . . . . .	81
4.4	Dose results from historic data . . . . .	82
4.5	Dose deposition results in MAIN Board FGDOS from large field proton beam irradiation . . . . .	86
4.6	Dose deposition results in MAIN Board FGDOS from pencil beam irradiation . . . . .	87
4.7	Dose deposition results in MAIN Board FGDOS from GCR spectrum based point source with cosine distribution . . . . .	89
5.1	FGDOS Proton Beam Characterization: Test Campaign Summary . . . . .	94
5.2	FGDOS configuration details . . . . .	95
5.3	Test levels: Beam Kinetic Energy . . . . .	96
5.4	Test levels: Dose rates . . . . .	97
5.5	Test run overview: 8 March . . . . .	97
5.6	Test run overview: 24 March . . . . .	98
5.7	Test run overview: 12 April . . . . .	99
5.8	FGDOS noise and resolution estimates from various sources . . . . .	109
5.9	FGDOS Temperature Characterization Test Levels . . . . .	112
5.10	Irradiation & temperature characterization: Test run summary . . . . .	120
5.11	Pre-test temperature characterization results (s1 denotes sensor 1) . . . . .	127
5.12	Radiation Payload performance: Sensor noise characterization (s1 refers to sensor 1) . . . . .	143
5.13	Payload performance test: Beam kinetic energy levels . . . . .	147
5.14	Payload performance test: Dose rate levels . . . . .	147
5.15	Radiation Payload VI Performance Testing: Summary of test runs . . . . .	148
B.1	Radiation Payload Telecommands and Telemetry List . . . . .	187
D.1	Radiation Payload Risk Register . . . . .	195
D.1	Radiation Payload Risk Register . . . . .	196
D.1	Radiation Payload Risk Register . . . . .	197
D.1	Radiation Payload Risk Register . . . . .	198
D.1	Radiation Payload Risk Register . . . . .	199
D.1	Radiation Payload Risk Register . . . . .	200
D.1	Radiation Payload Risk Register . . . . .	201
D.1	Radiation Payload Risk Register . . . . .	202
D.1	Radiation Payload Risk Register . . . . .	203
D.2	Summary of some miniaturized radiation detectors . . . . .	205

# Listings

3.1	Firmware pseudo code . . . . .	58
3.2	Driver App pseudo code . . . . .	61
E.1	Particle source definition macro . . . . .	216

# List of Symbols & Acronyms

## Symbols

<i>Al</i>	Aluminium
<i>c</i>	Speed of light in a vacuum
<i>Cf – 252</i>	Isotope of Californium
<i>Co – 60</i>	Isotope of Cobalt
<i>D</i>	Absorbed Dose
<i>d</i>	Dose Rate
<i>E</i>	Energy
<i>eV</i>	Electronvolt
<i>f<sub>ref</sub></i>	FGDOS Reference Frequency
<i>f<sub>sens</sub></i>	FGDOS Sensor Frequency
<i>H<sub>T</sub></i>	Equivalent Dose
<i>I</i>	Current
<i>m</i>	Mass
<i>n</i>	Nucleon
<i>S</i>	FGDOS Sensitivity
<i>Si</i>	Silicon
<i>SiC</i>	Silicon Carbide
<i>V</i>	Voltage
<i>w<sub>R</sub></i>	Radiation weighting factor
<i>w<sub>T</sub></i>	Tissue weighting factor

## Acronyms & Abbreviations

<i>ADC</i>	Analog to Digital Converter
<i>AE</i>	Aerospace Engineering, TU Delft
<i>CDHS</i>	Command and Data Handling Subsystem
<i>CERN</i>	European Organization for Nuclear Research
<i>CLPS</i>	Commercial Lunar Payload Services
<i>COMMS</i>	Communications Subsystem
<i>CRaTER</i>	Cosmic Ray Telescope for the Effects of Radiation
<i>DAC</i>	Digital to Analog Converter
<i>DC</i>	Direct Current
<i>DD</i>	Displacement Damage
<i>DM</i>	Development Model
<i>DOSTEL</i>	Dosimetry Telescope
<i>ECSS</i>	European Cooperation for Space Standardization
<i>EM</i>	Engineering Model
<i>EPS</i>	Electrical Power Subsystem
<i>ESA</i>	European Space Agency
<i>FDIR</i>	Fault Detection, Isolation and Recovery
<i>FEM</i>	Finite Element Analysis
<i>FGDOS</i>	Floating Gate Dosimeter
<i>FLUKA</i>	Fluctuating Cascade
<i>FM</i>	Flight Model

---

<i>FOV</i>	Field of View
<i>GCR</i>	Galactic Cosmic Rays
<i>Geant4</i>	Geometry and Tracking4
<i>GND</i>	Electrical Ground
<i>HPTC</i>	Holland Proton Therapy Centre
<i>ISS</i>	International Space Station
<i>JPL</i>	Jet Propulsion Laboratory
<i>LDR</i>	Linear Dynamic Range
<i>LEO</i>	Low Earth Orbit
<i>LET</i>	Linear Energy Transfer
<i>LRO</i>	Lunar Reconnaissance Orbiter
<i>LZ</i>	Lunar Zebro
<i>MCU</i>	Micro-controller Unit
<i>MOM</i>	Lunar Zebro Motherboard
<i>MOSFET</i>	Metal-oxide-semiconductor Field-Effect Transistor
<i>MSL</i>	Mars Science Laboratory
<i>NASA</i>	National Aeronautics & Space Administration
<i>NIEL</i>	Non-ionizing Energy Loss
<i>OBC</i>	On-board Computer
<i>OLTARIS</i>	On-line Tool for Assessment of Radiation In Space
<i>PCB</i>	Printed Circuit Board
<i>PFM</i>	Proto-flight Model
<i>PI</i>	Principal Investigator
<i>RAD</i>	Radiation Assessment Detector
<i>RADOM</i>	Radiation Dose Monitor
<i>RHA</i>	Radiation Hardness Assurance
<i>RMS</i>	Root Mean Square
<i>S/C</i>	Spacecraft
<i>S/W</i>	Software
<i>SAA</i>	South Atlantic Anomaly
<i>SEE</i>	Single Event Effect
<i>SEL</i>	Single Event Latchup
<i>SEP</i>	Solar Energetic Particle
<i>SET</i>	Single Event Transient
<i>SEU</i>	Single Event Upset
<i>SMART</i>	Specific, Measurable, Achievable, Realistic and Traceable
<i>SoC</i>	System on a Chip
<i>SPE</i>	Solar Particle Event
<i>SPENVIS</i>	Space Environment Information System
<i>SPP</i>	Solar Panel Plate
<i>SRIM</i>	Stopping and Range of Ions in Matter
<i>SSE</i>	Space Systems Engineering
<i>STR</i>	Structural Subsystem
<i>TID</i>	Total Ionizing Dose
<i>TLI</i>	Trans-lunar Injection
<i>VAB</i>	Van Allen Radiation Belts
<i>VUCA</i>	Volatile, Unpredictable, Complex and Ambiguous

# 1 Introduction

The Moon has been at the forefront of exploration since the dawn of the era of flight, and it continues to be the destination of choice for many space programs and missions looming on the horizon. Programs such as NASA's Artemis aim to return humanity to the moon in the 21st century [128]. Synergistic commercial and academic efforts are underway worldwide, to perform robotic and crewed missions to the Moon, for science and exploration in a scalable and sustainable manner [46]. This has been made possible by the rapid growth of capabilities in the commercial spaceflight sector in the past few years [102, 12], supported by large private and public investments in research and development activities [134]. The return to the Moon is seen as a precursor to groundbreaking space exploration, research and commerce [72]. Plans to establish research outposts and settlements on the Moon and Mars have been set in motion. It is envisioned that these activities will bring forth our civilization's expansion beyond Earth and further out into the solar system, making humanity a multi-planet species and an advanced spacefaring civilization [92].

After a long hiatus of five decades following the conclusion of the Apollo program [28], there has been a powerful resurgence in human spaceflight activities targeted toward the Moon, bolstered by a vibrant and active commercial space ecosystem. Under the Commercial Lunar Payload Services (CLPS) program [25], commercial entities are developing orbiters, landers and lunar roving vehicles to deliver payloads to the lunar orbit and surface for scientific research, technology development, education, outreach and artistic purposes [112, 29]. Among these entities lies a student team at TU Delft, namely Lunar Zebro. The aim of Lunar Zebro is to demonstrate the feasibility of its innovative nano-rover concept on the Moon, as a stepping stone to loftier goals of operating swarms of nano-rovers on extra-terrestrial bodies in the future [81]. The Lunar Zebro is a shoe-box sized hexapod robot with C-shaped legs, being built by TU Delft students with the aim of being the world's smallest and lightest student built rover to explore the Lunar South Pole.

Numerous technological, scientific, social, economic and political challenges need to be overcome in order to achieve these ambitious goals. A majority of the technological hurdles that exist are created by the harsh and unforgiving nature of the space environment. This includes conditions such as the vacuum of space, extreme thermal environments, varying gravity fields, the *tyranny of the rocket equation*<sup>1</sup>, and the existence of extreme, high energy radiation in space [104]. These factors have led to various anomalies, errors and failures in space systems to date [60]. To realize the overarching goals of rapid exploration, scientific research and industrial/commercial activities in space, it is of the utmost importance to understand and prepare for the harsh conditions in space such that exploration, science and commerce can be carried out in a safe, sustainable and economically feasible manner. Space radiation has the ability to cause damage and degeneration in space systems and poses numerous health risks and hazards to astronauts [39]. Lunar missions are exposed to a plethora of the aforementioned hazards, ionizing radiation environments being one of the toughest to predict and mitigate.

Accurate characterization and understanding of the space radiation environment is needed since radiation can severely hamper space missions and have undesirable and often unpredictable impacts on space systems [105]. Effective and pragmatic risk mitigation and management strategies are also required to make the *next giant leap* in spaceflight a reality in the foreseeable future. The first step toward solving these problems calls for extensive in-situ measurement, observation and investigation of radiation environments for various conditions and mission scenarios. Such efforts are carried out by spaceborne radiation measurement instruments. The data collected by these instruments leads to improvements in analytical and theoretical models of the space environment and its effects on space systems. It naturally follows that for lunar missions and exploration, more in-situ measurement data of the lunar radiation environment is needed. While the convention so far has been to use sophisticated, complex and expensive instruments for this purpose, such measurements can also be performed in the near future by developing a miniaturized instrument that

---

<sup>1</sup>the tyranny of the rocket equation refers to the unfavorable exponential relation which dictates the amount of mass that can be launched to space w.r.t a given mass of propellant

can be flown on the innovative nano-rover platform that is the Lunar Zebro [124]. A flight opportunity is available on-board this rover to carry out scientific research and observations in space and on the Moon [52]. The research work carried out in this thesis is intended to be manifested as the science payload, in context of the science mission, for Lunar Zebro's first voyage to the Moon.

Recent advances in semiconductor technology and the increased usage of COTS components have led to the development of a variety of solid state detectors for the purpose of monitoring ionizing radiation in space. The floating gate MOSFET based dosimeter (FGDOS) [51] is a prime example and offers a low cost, low power and compact solution for measuring radiation in systems with very tight constraints on resources such as nano-satellites and miniaturized robots [7]. Moreover, this sensor has already been demonstrated to operate in space, on-board a lunar flyby mission [27].

Based on previous FGDOS research and the flight opportunity available with Lunar Zebro, a literature study was conducted to further explore the possibilities of monitoring the lunar radiation environment using a low cost, miniaturized payload [122]. From this literature study, it was concluded that the design and development of a miniaturized payload (utilizing the FGDOS), for the science mission of Lunar Zebro would be an interesting avenue for research [122]. This serves as the main focus of this MSc thesis, in conjunction with investigation and characterisation of the FGDOS detector, as well as simulation of the mission radiation environment.

Having introduced the general domain of this thesis and the topic of research, a review of relevant literature is presented in chapter 2. The last few sections of this chapter serve to set up the background of the current research and development efforts. Chapter 3 details the front end systems engineering and detailed design of the Radiation Payload of Lunar Zebro, followed by a description of the manufacturing, assembly and integration activities that were carried out. Chapter 4 presents space radiation environment modelling and analysis that was performed in order to predict the expected radiation environment that the Radiation Payload will experience during flight on-board the Lunar Zebro rover. The results from this lead into radiation transport simulations which were performed to investigate and predict the interaction of various species of ionizing radiation with the FGDOS sensor, including the effects of shielding, secondary particles and the influence of lunar landscape features. Chapter 5 describes the verification and validation activities performed during this research project, including FGDOS characterization, payload functional testing and performance testing. Chapter 6 presents the main conclusions of the thesis, along with answers to the research questions which were posed in the beginning. Lastly, chapter 7 outlines recommendations for further research, experimentation and engineering work. Supplementary information such as design data, charts, schematics, tables, test results and links to software scripts can be found in Appendix A to Appendix F.

# 2 Background

This chapter is divided into 4 sections. The space radiation environment is introduced in section 2.1, where subsection 2.1.3 focuses on various models and tools used to study and predict space radiation and to simulate its effects on space systems and biological organisms. Instruments which have been used for in-situ observations of ionizing radiation for lunar missions, including their observations and results have been explored in section 2.2. A brief summary of Lunar Zebro, including its mission and rover system, is given in section 2.3. This section includes an introduction to the the Radiation Payload concept. Finally, section 2.4 describes the research questions and objectives which were formulated in order to structure this thesis [122].

## 2.1. Space Radiation Environment

Radiation is commonly defined as energy that travels through space. Radiation can be divided into ionizing and non-ionizing, based on the amount of energy possessed by it. Ionizing radiation possesses enough energy to cause ionization of electrons from atoms and molecules. Radiation can also be classified into charged particles such as protons and electrons, and neutral particles such as neutrons. Different radiation particles undergo interactions with matter in various ways, as shown in Figure 2.1.

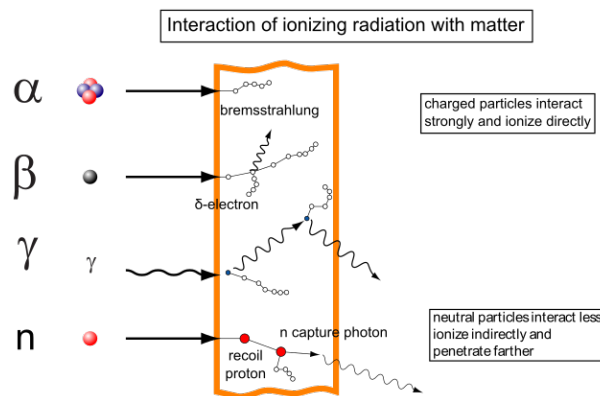


Figure 2.1: Interaction of ionizing radiation with matter [59]

### 2.1.1. Space Radiation

Radiation in space arises from within the solar system i.e. from the sun, or from extra-solar celestial bodies and astrophysical phenomena in the galaxy. In its characteristics and effects, the space radiation environment is substantially different from what is experienced on Earth [39]. The spectrum of radiation in space consists of a mixed field of electrons, protons, gamma rays, high mass and charge ions with energies ranging from a few MeV/nucleon to as high as TeV/nucleon levels. The flux and intensity of radiation also varies based on the environment of observation and the source of radiation <sup>1</sup>. A brief primer on radiation related quantities is provided in Appendix F. Based on the source of origin, space radiation can be divided in three categories as described in the rest of this section:

#### Solar Wind & SPEs

In addition to electromagnetic radiation (EM), the sun is also a source of particle radiation, mainly protons and electrons. This is called the solar wind, a continuous stream of ionized plasma originating from the

<sup>1</sup>When alluding to "space radiation", it is usually the high energy constituents of electromagnetic radiation and particle radiation which are being referenced. Beyond an energy of generally 10 eV, radiation becomes ionizing as it possesses the ability to ionize atomic and molecular species. While the thermal, optical and other lower energy components are also radiation types in theory, these species are less relevant in space radiation discussions due to their comparatively lower tendency to cause adverse effects on space systems

sun. It interacts with the magnetic fields of planetary bodies and with radiation from other sources. The solar wind consists of particles of comparatively lower energies and hence can be easily combated by use of low thickness shielding [39]. Besides solar wind, the sun also acts as the source for highly energetic radiation species (mostly protons and heavy ions) called Solar Energetic Particles (SEPs). SEPs are accelerated outward into the solar system during violent and sporadic phenomena called Solar Particle Events (SPEs). SPEs can take the form of solar flares or Coronal Mass Ejections (CMEs). During an SPE, the energy and flux of SEPs can build up exponentially and reach peak values of about 500 MeV/nucleon and  $100 \text{ cm}^{-2} \text{ s}^{-1} \text{ sr}^{-1}$  within several minutes to hours [32].

SPEs have a higher chance of occurring during solar maxima but no clear pattern has been established yet. A rough estimation is that at least one major SPE is observed every year for about nine years out of the eleven year solar cycle [39]. On average, about 100 SPE events have been observed to occur during the course of a solar cycle. While SPEs are relatively rare and short lived in nature, they can be highly consequential when it comes to exposing crew and spacecrafts to danger. Outside the geomagnetic field, SPEs can cause the delivery of possibly lethal doses to unprotected astronauts [39].

### Galactic Cosmic Rays (GCRs)

GCRs originate from high energy events and astronomical phenomena occurring outside the solar system. Neutron stars, pulsars, active galactic nuclei (AGNs), supernovae and hypernovae explosions are among the likely sources. Due to their interactions with complex interstellar magnetic fields, the precise direction of origin of GCRs is unknown and in general, they are thought to be coming in at all directions from outside the solar system [105]. GCRs are mainly composed of baryons (98%) with a minority of electrons (about 2%). The baryonic component consists of about 85% protons, 14% alpha particles and the remainder being high energy and charge ions and nuclei, known as HZE particles [105]. Figure 2.2 shows the composition of cosmic radiation in terms of the abundance of constituent elements and their relative contribution to the fluence and dose. HZE particles can penetrate deeply and have a big bearing on radiation damage and dose since they have a high linear energy transfer (LET), mass and charge. The deposited energy in an irradiated volume is proportional to the square of charge. Hence, HZE ions possess the ability to transfer a high amount of energy into matter. This is reflected in Figure 2.2. While the fluence of more massive particles is relatively low, the doses and dose equivalents are comparable to that of more abundant, low charge and mass elements.

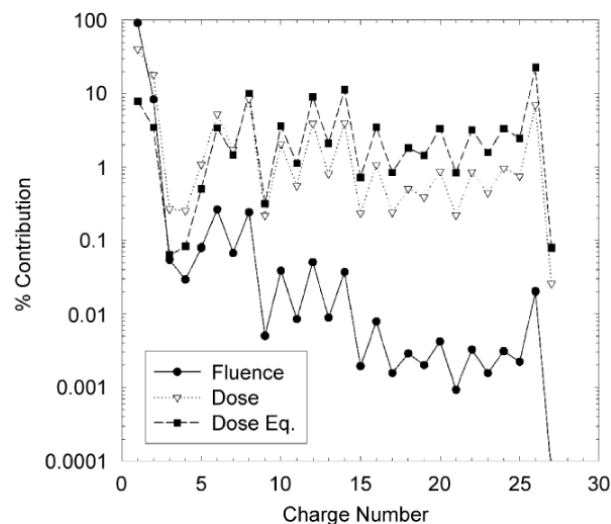


**Figure 2.2:** Elemental composition of cosmic rays in terms of dose, fluence and dose equivalent [105]

The activity of the sun dictates the outflux of solar wind and modulates the cosmic radiation flux in the solar system and in its vicinity<sup>2</sup>. The flux and spectra of cosmic rays up to energy levels of 1 GeV/nucleon are de-

<sup>2</sup>Solar activity depends on the 11 year solar cycle and can be loosely predicted on the basis of the observed number of Sunspots. This can be quantified using the Wolf Number ([https://en.wikipedia.org/wiki/Wolf\\_number](https://en.wikipedia.org/wiki/Wolf_number)), which varies periodically during the course of the 11-year long solar cycle

pendent on the solar cycle [32]. GCR flux is anti-correlated with solar activity and therefore, maximum GCR is observed during periods of minimum solar activity. During periods of heightened solar activity i.e. solar maxima, the GCR contribution is markedly lower. This can be seen as a factor of 3 to 4 decrease in GCR flux during periods of increased solar activity [105]. Compared to SEPs, GCRs prove to be a relatively constant part of the radiation environment and their contribution to radiation exposure in a specific location within the solar system depends on the aforementioned modulation by solar activity. GCRs make up about 80% of the effective dose to astronauts in spacecrafts such as the International Space Station (ISS) [39], which is a testament to their high penetration capabilities and bearing on living tissue.

The anomalous component of space radiation consists of neutral particles from the interstellar dust, which get singly ionized upon entry into the heliosphere after interaction with the solar wind [39]. Due to the lower charge content as compared to cosmic rays, particles belonging to the anomalous component can penetrate deeper into the Earth's magnetosphere. An interesting effect of GCRs over long spans of time is the alteration of exposed planetary surfaces and landscapes. *Space weathering* is the process of change of planetary atmospheres and surfaces due to exposure to space environment factors such as solar ultraviolet (UV) radiation, GCRs, solar wind, plasma and other particles that impinge on a given celestial body. Interaction of the soil with GCRs can cause modifications which go as deep as several meters. Incident radiation can lead to the formation of complex chemicals and oxidants for life [116]<sup>3</sup>.

### **Trapped Particles: Van Allen Radiation Belts**

Earth's magnetic field traps and deflects charged particles that enter its region of influence. The Van Allen Radiation Belts (VABs) are two toroidal regions within the geomagnetic field where these charged particles are trapped in Earth orbit. The inner belt is composed of high energy protons (levels up to about 100 MeV) and electrons (up to 10 MeV). It starts at an altitude of about one-tenth of Earth radius and extends up to four Earth radii approximately. The outer VAB is made up of mostly electrons of energy levels up to 10 MeV and it exists in an altitude bracket of approximately 4 to 10 Earth radii [32]. The outer belt is mainly populated by trapped solar particles and electrons [104].

In Low Earth Orbit (LEO), a significant increase in radiation exposure is observed over the South Atlantic Anomaly (SAA), where the inner Van Allen Belt (proton belt) reaches down to altitudes as low as 200 km over the coastal Brazilian region [105]. The SAA exists due to the relative tilt of the Earth's magnetic dipole axis w.r.t its axis of rotation. Spacecrafts in LEO passing through the SAA experience a temporary but marked increase in radiation exposure compared to the rest of their orbit [104]. Although the transit through the SAA might constitute a minor fraction of the orbital period, it is the primary source of radiation exposure at low orbital inclinations [105].

### **2.1.2. Lunar Radiation Environment**

The lunar radiation environment is significantly different from what is experienced on the Earth. The Moon does not possess a magnetosphere which can deflect or trap charged particles coming in from external sources. The Moon has no discernible atmosphere, thereby incident radiation is not attenuated or shielded against in any form as it reaches the surface, unlike the conditions on Earth. Primary radiation interacts and gets reflected by the lunar regolith, resulting in the production of secondary radiation and albedo [116]. While the Earth surface also experiences secondary radiation, the cause and composition is different from that on the Moon.

---

<sup>3</sup>In the case of Mars, where protection against radiation from the atmosphere is minimal, the Martian soil and rocks have been bombarded by highly energetic particles from the sun and from galactic sources for most of the Red Planet's history. This has resulted in the chemistry and composition of Martian regolith being altered over time [61]. At the same time, radiation can also destroy signs of chemical biology and signatures on the surface of planetary bodies, necessitating scientific robots and rovers to probe the subsurface to find such signatures, if present

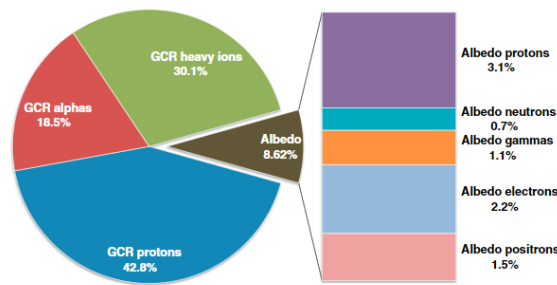


Figure 2.3: Contribution of various sources (from GCR) to the absorbed dose rate at the moon [130]

Bodies in the vicinity of the Moon are exposed to radiation from GCRs and from SPEs and the solar wind that propagates outward from the sun along heliospheric magnetic field lines. SPEs are sporadic in nature and difficult to predict whereas GCR levels are comparatively steady. While SPEs possess a very high intensity, the energy of the radiation is lower than GCRs, which makes it easier to shield against SPEs. During SPE events, high energy electrons (~ 0.5 to 1 MeV) and protons (~ 20 to 80 MeV) can arrive at the Moon within a few hours, with the exception of some very high energy protons that can arrive within half an hour [32]. For objects in lunar orbit, the body of the Moon itself provides shielding against a part of the incoming GCR flux as it blocks out part of the sky from the viewpoint of the orbiting body. This was observed as far back as the late 1960s in the pioneering work of Lin [78]. The blocking depends on the view factor of the Moon w.r.t the orbiting body, meaning that the shielding is higher for objects orbiting closer to the Moon. For objects on the surface, almost half the incoming GCR is blocked by the Moon.

It has been estimated that the lunar landscape and surface also contribute a minor but non-negligible amount to the absorbed dose due to the production of secondary radiation from incoming cosmic rays [130]. Thus, this contribution made by the albedo should also be taken into consideration during the radiation environment specification and risk assessment. Figure 2.3 shows the contribution of various sources to the absorbed dose and dose rate near the Moon due to GCR, as estimated by [130]. It can be seen that the albedo accounts for a non-negligible amount of the dose and hence it cannot be completely neglected for high accuracy radiation exposure estimates. Closer to the Moon and at the lunar surface, the contribution of albedo and secondaries to the radiation exposure is expected to rise. The contribution of the albedo to the total dose rates at the surface has been estimated to be as high as 20% [154].

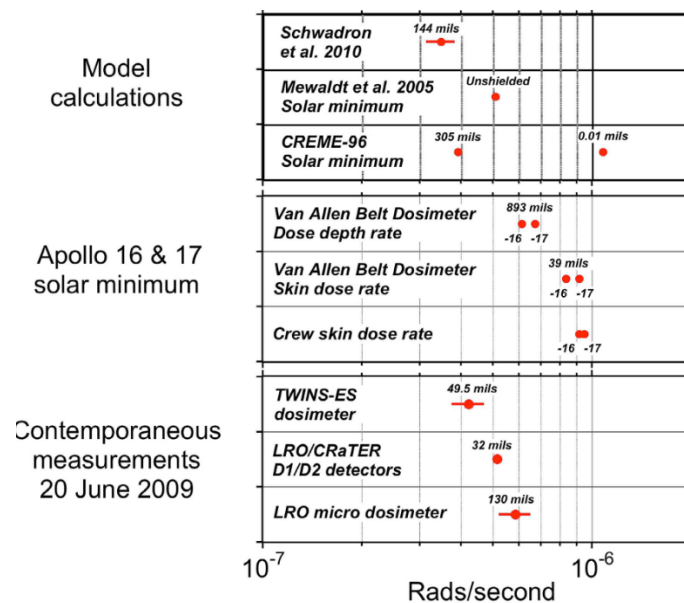


Figure 2.4: Dose rate comparison behind different levels of shielding in interplanetary space [87]

A spacecraft on a moon mission can be exposed to space radiation from multiple sources [150]. Within

the geomagnetic field, spacecrafts in LEO are protected from SPEs. However, this protection is no longer available once the spacecraft leaves LEO and transitions outward from the magnetosphere of Earth. The dose rates, while a spacecraft passes through the VABs, can be quite high [27]. Depending on the trans-lunar trajectory chosen, the radiation exposure while crossing the radiation belts of the Earth can add a sizeable contribution to the cumulative radiation exposure during the mission.

In cis-lunar space, the dose rates are quite low [32] and similar to values observed in interplanetary space, for example during transit to Mars [158]. Figure 2.4 shows the typical dose rates in cis-lunar space (measured during solar minimum conditions such that the contribution of GCRs was high). During EVAs on the lunar surface or in lunar orbit, intense SPE events could potentially deliver lethal doses to astronauts [39]. During shuttle missions, the main exposure to astronauts was observed to be caused by radiation belt transit and protons encountered therein. However, in Apollo missions, it was GCRs that contributed most of the exposure. Flux and particle tracks of high energy and charge ions with  $LET > 100 \text{ keV}/\mu\text{m}$  inside the Apollo spacecrafts were measured [24].

### 2.1.3. Space Radiation Environment Modelling

Galactic Cosmic ray environments are described by various mathematical and semi-empirical models such as Badhwar-O'Neill (BON), Nymmik, CREME96, CREME86, ISO-15390. These models mainly differ in how the local interstellar spectrum function is formulated and the choice of solar activity parameter that is used in the model [39]. The Badhwar-O'Neill (BON) series of GCR models make use of mathematical equations to provide GCR fluxes and intensities outside the Earth's magnetosphere. It has a modulation parameter  $\Phi$ , to capture the effects of solar and heliospheric transport. The value of the modulation parameter is chosen so as to best fit real world observations made by space weather observatories. Several editions of the BON model are available such as BON2010, BON2014, BON2020 etc [127]. In contrast, Nymmik's model uses a semi-empirical approach in which the GCR intensity variation based on solar cycle changes are correlated to Wolf sunspot numbers [98]. It has uncertainty levels below 15% [39]. The ISO model is similar to Nymmik's model except the fact that the GCR flux drops for decreasing energies below 10 MeV/nucleon [48].

Ionizing radiation emitted by the Sun is covered by models such as JPL-91, ESP, SOLPRO and SAPPHIRE [48]. Statistical predictions of SPE events can be obtained from models such as JPL, ESP and King. The ESP model is mathematically more sound than the King and JPL models since these models lack complete datasets and the ESP model uses an approach based on maximum entropy theory to come up with SPE fluence distributions [39]. The SAPPHIRE model covers "all SEP environment timescales across all relevant species in a consistent probabilistic manner" [48].

NASA's AP8/AE8 proton and electron belt models are used frequently in space engineering applications to derive information about trapped particle radiation in the VABs. These models are based on data collected from numerous satellites in the previous century and cover the complete radiation belt region with wide electron and proton energy ranges [39]. These models were improved upon by the introduction of the AE9/AP9/SPM (energetic electrons, energetic protons, and Standard Plasma Model) model set that incorporates data from over 40 different spacecraft on-board measurement collections<sup>4</sup>.

#### SPENVIS & Other Tools

The Space Environment Information System (SPENVIS) is a comprehensive framework for accessing and using various models of the space environment and its effects on space vehicles and systems [62]. It is a modular and extensible tool which can be accessed by users via a web browser. SPENVIS includes models and effects arising from the radiation belts, SEPs, cosmic rays, plasmas, micro-particles and gases [48]. It enables rapid analyses of space environment related issues and effects, even for users with relatively little familiarity with the platform. Data from relevant ECSS standards and actual flight data from various missions can also be accessed in SPENVIS. SPENVIS allows users to generate points along a spacecraft trajectory or on a coordinate grid, which can then be used for calculations such as [48]:

- Geomagnetic coordinates
- Ion LET and flux spectra and single event upset rates trapped proton flux anisotropy
- Trapped proton and electron fluxes and solar proton fluences

<sup>4</sup><https://www.vdl.afrl.af.mil/programs/ae9ap9/>

- Atmospheric and ionospheric densities and temperatures
- Radiation doses (ionising and non-ionising) for simple geometries
- Damage equivalent fluences for Si, GaAs and multi-junction solar cells
- Sectoring analysis for dose calculations in more complex geometries
- Geant4 Monte Carlo analysis for doses and pulse height rates in planar and spherical shields

Similar to SPENVIS, OMERE is a freely available framework that contains several space environment models [103]. "OMERE computes the space environment in terms of particle fluxes and radiation effects on electronic devices in terms of dose, displacement damage, single event effects and solar cell degradation"<sup>5</sup>. NASA's On-Line Tool for the Assessment of Radiation in Space (OLTARIS) is an integrated tool set intended to help scientists and engineers study the effects of space radiation on shielding materials, electronics, and biological systems<sup>6</sup>. It makes use of NASA's HZETRN radiation transport tool.

#### 2.1.4. Space Radiation Transport

Space radiation transport simulations have been applied to three main areas of investigation [6]:

- Simulation of the interaction of radiation with spacecrafts, space instruments and inhabitants of crewed vehicles (such as living organisms and tissues)
- Simulation of radiation spectra, surface and subsurface radiation levels for planetary bodies and other celestial objects
- Simulation of radiation effects and hardening in microelectronic devices

Various software based tools that can be used to perform radiation transport simulations have been developed in the domains of space science and engineering, high energy physics, medical physics, nuclear radiation and reactor design etc. These include tools such as, Geant4, PHITS, MCNP, FASTRAD, FLUKA and NOVICE [69]. Radiation transport modelling codes chiefly make use of two methods; (a) computing a solution of the Boltzmann transport equation or (b) using Monte Carlo techniques to sample from interaction processes of primary or secondary radiation as they pass through target materials and geometries [39]. The Boltzmann approach is deterministic in nature and is based on getting approximate solutions of integro-differential equations that are based on conservation laws. Complex spacecraft structures and shapes can be incorporated into the codes using ray tracing techniques. Monte Carlo codes use the absorption cross-section to determine the occurrence of nuclear interactions in the process of developing Monte Carlo histories. This use of the cross-section parameter works out prudently since accurate experimental and theoretical data for absorption cross-sections are readily available for various combinations of impinging projectile particles and absorbing materials [39]. Compared to deterministic approaches, Monte Carlo based codes can be applied to highly complex geometries representing collections of spacecraft parts or components and sub-assemblies of space instruments [30]. The contents, orientation and configuration of spacecrafts can influence the generation of secondary particles which are produced by scatter events. Hence, Monte Carlo method based codes can be used to model these effects and provide useful estimates of quantities such as dose rates, fluences, energy deposition and dose equivalents. While Monte Carlo codes offer more flexibility than deterministic codes, they usually require much higher computational resources.

Space radiation transport models can be validated and assessments about the uncertainties can be made using the following approaches [39]:

- Comparison amongst different transport codes and benchmarking for similar environmental conditions and scenarios
- Comparison with actual measurements made by spaceborne instruments
- Comparison with data collected in ground based radiation test facilities and research centres. These are usually done with an assortment of targets for different beam configurations such that the characteristics of space radiation can be emulated in an approximate manner

Currently used Monte Carlo method based tools and transport codes, as well as deterministic codes can provide good descriptions of the interaction of cosmic rays with matter [39]. However, more accurate and efficient methods are needed that can perform these computations in a frugal manner. Codes that can

<sup>5</sup><https://www.trad.fr/en/space/omere-software/>

<sup>6</sup><https://oltaris.nasa.gov/>

compute double differential nuclear cross-sections can provide results that are closer to physical reality. Models that can describe the deposition of energy in living organisms for purposes of risk assessment also need further improvements. This is the area where major uncertainties lie with respect to estimation of radiation effects in space. The predictions made by models can differ from actual measurements made by instruments due to factors such as variation in experimental conditions, nuances and limitations of the sensing and detector technology, different solar activity and heliospheric conditions than modelled, localized contributions by sources such as albedo, and secondary radiation from materials in the vicinity of the instruments i.e. spacecraft structures, instrument housings, detector bodies etc.

#### **Geant4**

Geant4 is a Monte Carlo method based toolkit for radiation transport simulations. It was developed by engineers and scientists from the high energy particle physics domain and has been adapted increasingly over the years for use in space radiation research [3]. Geant4 has found applications in high energy particle physics, medical physics, space and instrumentation fields, among others. In the space domain, it has been used for applications such as shielding analysis, instrument and detector response studies, analysis of radiation effects on electronics and biology, shielding optimization, and scientific studies involving interaction of radiation with instruments or spacecraft components [111]. Geant4 enables the simulation of trajectories of particles of various types through user defined 3D geometries with various material properties. The physics of hadronic processes included in Geant4 is relevant to applications in the realm of space. Elastic and inelastic hadronic processes as well as production of secondaries is highly important in radiation transport simulations for spacecrafts and instruments. Particles from pre-defined or user-defined sources with a variety of energy, vertex position and angular distributions can be used as the radiation source(s) [111].

## **2.2. Space Radiation Measurement**

Ionizing radiation can be measured and quantified by the use of instruments which incorporate radiation detectors. Most detectors are made up of two main parts - a material or substance that is responsive to incident ionizing radiation, and an external device that can take this response and convert it into physical signals that can be measured and recorded <sup>7</sup>. Detectors of ionizing radiation can be categorized based on the type of radiation being detected or the purpose of the detector. Based on the purpose of the detector, the classification can be made as:

- Dosimeters: These detectors measure ionizing radiation exposure in terms of the dose i.e energy absorbed in the detector volume
- Spectrometers: These detectors measure the spectrum of incident ionizing radiation which can later be used to derive the energy of particles
- Counters: Counters detect the number of hits or interactions of ionizing radiation particles with the detector. They are used to measure radioactivity in counts per unit time.

### **2.2.1. Instruments for in-situ measurement of ionizing radiation**

Accurate modelling and simulation of the space radiation environment on ground requires real-world measurements. Extensive measurements of quantities such as the absorbed dose, LET spectra, fluence and composition and distribution of particles is needed for various radiation environments. A wide array of instruments and techniques have been developed and deployed for the purpose of measuring and characterising radiation in space. These instruments have been deployed in Earth orbit, in interplanetary space and on other extra-terrestrial locations such as the Moon and Mars. These devices have been aimed at measuring radiation for scientific purposes, as well as monitoring space weather or to keep track of radiation received by astronauts i.e. personal dosimetry.

A brief overview of the most relevant space radiation measurement instruments of recent times is provided hereon, sorted by the type of environment being measured, from LEO to the Moon and finally Mars. Of relevance here are instruments that measure the radiation environment in space in terms of ionizing radiation and its exposure <sup>8</sup>.

<sup>7</sup><https://www.nuclear-power.com/nuclear-engineering/radiation-detection/>

<sup>8</sup>Telescopes or observatories that carry out optical, UV, infrared, radio or other such low energy radiation observations as well as X-Ray or Gamma-Ray observatories, neutrino detectors lie outside the scope of this literature review

An overview of the radiation measurement instruments that have been deployed at the ISS and in LEO is provided in [26] and [10]. Besides the ISS, many radiation detectors and instruments have been used to characterize and map the radiation field in Earth Orbit, on-board various satellites [105, 56, 33]. The radiation field in the upper atmosphere has also been studied by the use of high altitude balloon flights [107]. Spacecraft with orbits that intersect with the VABs have been deployed to study the intense radiation environment in the proton and electron belts [63]. As early as 1968, Geiger Muller tubes on board the Explorer 35 spacecraft were used to make measurements of energetic particles and plasma of the Moon [78]. In recent times, a handful of instruments have been deployed to measure the lunar radiation environment. The RADOM instrument on-board Chandrayaan-1 measured the radiation environment for a Moon orbiter mission [32]. Around the same time, the CRaTER instrument on-board NASA's Lunar Reconnaissance Orbiter spacecraft performed measurements of cosmic rays in lunar orbit [80]. In 2019, the LND instrument measured ionizing radiation on the lunar surface, as a part of the Chang'e 4 mission [159].

In the remainder of this section, the instruments and missions that are most relevant for this thesis are described in more detail. These include DOSTEL, CRaTER, RADOM, LND, L4M as well as some upcoming instruments like LETS, M42 and RAD-PC.

### DOSTEL - ISS

The DOSTEL (Dosimetry Telescope) instrument on board the ISS was used in two major experiments called DOSIS & DOSIS3D [14].

The DOSTEL instrument is essentially a solid state Si detector telescope that consists of a stack of Si detector disks (as shown in Figure 2.5). Depending on the direction of incidence, radiation species can pass through one or more detectors and be registered by these (if they possess energies that lie above the detection threshold of a given Si disk). Count rates and doses are measured in each detector and coincidences between detectors can be used to determine the LET of incident radiation. Strong coincidence and anti-coincidence detection logic allow for discrimination between particle types, energies and spectra during post processing of the instrument data.

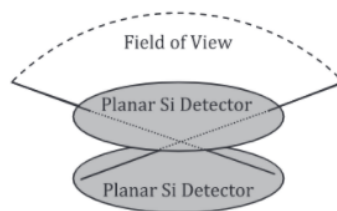


**Figure 2.5:** Schematic of DOSTEL detector setup [26]

Analog and digital circuitry connected to the detector allows for analysis of pulses produced in the Si detectors and for amplifying, measuring, recording and communicating the measurements to the Columbus module rack via an additional data processing unit. Components of the detector readout electronics include a pulse amplifier, integrating capacitors, microcontroller, timer, ADC, flash memory and RAM. The power consumption of each DOSTEL was observed at about 3W [14]. The integration time of measurements was set based on estimates of particles count rates such that statistically significant data sets could be obtained. In the DOSIS experiments, two DOSTEL telescopes were aligned with separate ISS axes to capture the temporal variations of the radiation field and its directionality. Passive detectors spread throughout the space station measured the spatial distribution in parallel.

The measured absorbed doses went as high as  $286 \mu\text{Gy}/\text{day}$  in May 2016. To give a comparison, high end measurements of about  $1400 \mu\text{Gy}/\text{hr}$  were measured outside the ISS by the R3D3 instrument around the same time period [14]. Variations in the measured doses rates were observed and studies w.r.t change in the ISS altitude, passage over the South Atlantic Anomaly (SAA), change in ISS configuration due to Space Shuttle docking and variations in solar activity, were conducted.

Comparisons of DOSTEL results with data from other radiation measurement instruments inside the station

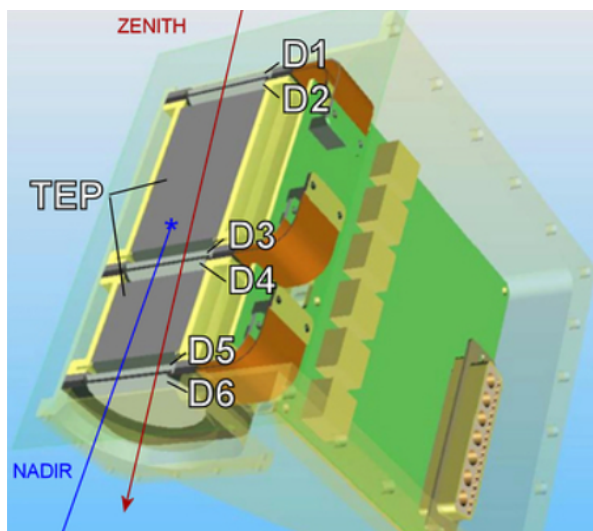
showed good agreement. It was observed that the doses reported by one of the DOSTELs was always about 20% lower than the other [14]<sup>9</sup>. A notable limitation of Si detector based telescopes like DOSTEL is that the LET is derived by assuming that the distance travelled by incident particles is equivalent to the mean chord length between consecutive detector disks [26]. In reality, this assumption is more accurate for particles that lie within a very narrow bracket within the field of view (FOV) of the telescope.

### CRaTER - LRO

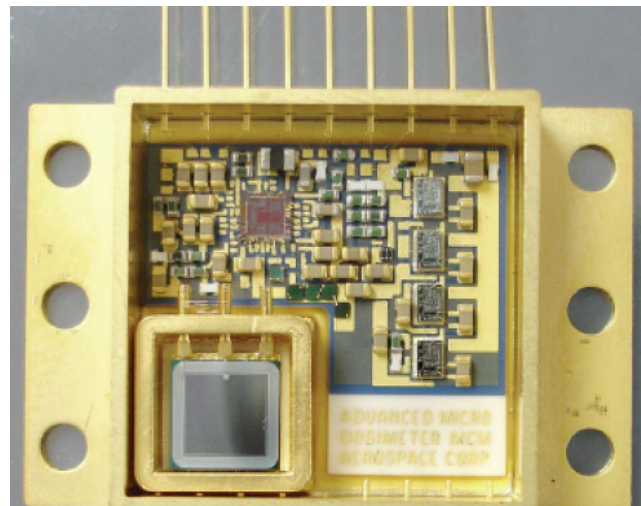
One of the main scientific goals of NASA's Lunar Reconnaissance Orbiter (LRO) was to perform measurements of ionizing radiation in the lunar environment [143]. To achieve this goal, the Cosmic Ray Telescope for the Effects of Radiation (CRaTER), was manifested on-board the LRO spacecraft in 2009. The goal of CRaTER is to measure the lunar radiation environment, with the purpose of identifying the absorbed radiation dose to prepare for future manned and unmanned missions to the Moon [80]. The data collected by CRaTER was successfully used to characterize radiation in the lunar orbit and on transit from the Earth to the Moon. The instrument is similar in makeup to DOSTEL [14]. CRaTER also houses a small, high resolution micro-dosimeter which was used as an independent way to make radiation measurements [79]. The micro-dosimeter can be seen without its cover lid in Figure 2.6b. While originally developed by the Aerospace Corporation, this micro-dosimeter technology was later adapted by Teledyne for its UDOS-001<sup>10</sup> and UDOS-007<sup>11</sup> micro-dosimeters which have been used in several space missions [79, 107].

### Instrument Setup & Operation

The CRaTER telescope consists of a stack of 3 pairs of thick and thin solid state Si detectors arranged in a line, along with disks of tissue equivalent plastic (TEP) sandwiched in between. The stack is assembled into a telescope shaped Al housing. In each Si detector pair, the thick detectors can detect low energy particles, down to single particle species. The thin detectors have a higher energy threshold so that only high energy and charge particles can be detected in these. Most protons and alpha particles are not picked up by the thin detectors and the thick detectors can get saturated with relative ease, on encounter with a moderately high charge ion [80]. With the readings acquired from the detectors, a detailed characterization and calibration database is used on the back end to determine LET spectra [87].



(a) Cut-away view of the CRaTER telescope, showing the detector stack [153]



(b) The micro-dosimeter on the CRaTER instrument [87]

**Figure 2.6:** CRaTER telescope and dosimeter

<sup>9</sup>The reason for this was the different direction of the second telescope as well as a higher effective local shielding from the ISS. It is also interesting to note that in the DOSIS experiments, the GCR measurements were only performed over the northern hemisphere in the orbit of the ISS. This was done to avoid pollution due to measurements made in the SAA. Effectively, GCR data from the Northern hemisphere was doubled to estimate the dose and dose rates over the entire ISS orbit

<sup>10</sup>[https://www.datasheetarchive.com/whats\\_new/7a08bbe0a08a4f486f2921ef18d7e707.html](https://www.datasheetarchive.com/whats_new/7a08bbe0a08a4f486f2921ef18d7e707.html)

<sup>11</sup>[https://www.datasheetarchive.com/whats\\_new/88783532be11dd2453aaededef3f95f4.html](https://www.datasheetarchive.com/whats_new/88783532be11dd2453aaededef3f95f4.html)

The micro-dosimeter has a resolution of about  $13 \mu rad$ <sup>12</sup>, which enables high precision measurements of the dose in the lunar environment and a range of about 40 krads. The Total Ionizing Dose (TID) accuracy of the device was tested to be  $\pm 20\%$  [87]. The micro-dosimeter consists of a silicon detector in which charge is deposited by incident radiation, and a CMOS based ASIC that performs most of the signal processing. From the detector, the ASIC amplifies current pulses and integrates them. When the magnitude of the integrated pulses reaches a dose quantum, the counters increment and an output is produced by the DACs. The output consists of Analog DC voltages that are proportional to the TID. There are 3 different step sizes for the DACs which correspond to dose quanta of 13.6  $\mu Rad$ , 3.6  $mRad$  and 0.88  $Rad$  respectively. Processing of the telemetered data on ground is performed to track the rolling over of counters, TID and dose rate, along with tracking of power outages, failures or periods of inactivity [87].

### Observations & Results

The LRO CRaTER telescope and micro-dosimeter performed measurements during a period of very low solar activity, corresponding to the lowest solar minimum in recent history [14]. The highest GCR dose rate measured by CRaTER was about 11.7  $cGy/yr$  [116]. The average dose rate measured by the micro-dosimeter in lunar orbit varied from about 14 - 21  $\mu Gy/h$ , with a reduction observed with decreasing altitude of the orbit (as expected due to the shadowing provided by the Moon) [87]. The dose rate measured while LRO was at a lunar orbit of 50 km altitude was seen to be about 30% less than the dose rates observed during Earth to Moon transit [87]. Figure 2.7a shows the measured dose rate and corresponding altitude of the LRO spacecraft w.r.t time. A decreasing trend can be seen in this plot. More results from CRaTER and the LRO mission can be found at the CRaTER data products repository<sup>13</sup>.

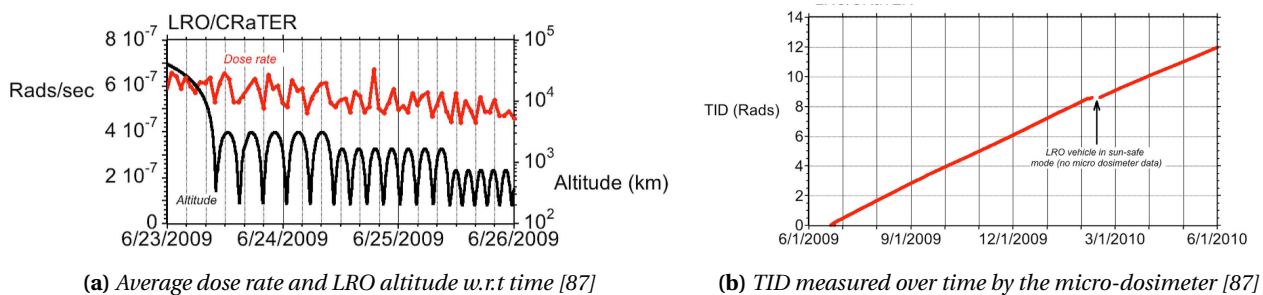


**Figure 2.7:** CRaTER mission results

Figure 2.7b shows the total ionizing dose measurements made by the micro-dosimeter over nearly a year long period from June 2009 to May 2010. It was observed that gradual TID changes occurred on time scales of several hours. Comparison between the data from the CRaTER telescope and the micro-dosimeter revealed an uncertainty of about 15% in the measurements. The dose rates were similar but the micro-dosimeter measured slightly higher dose rates at about 18.9  $cGy/yr$  compared to the telescope at 16.5  $cGy/yr$  from June 2009 to May 2010 [116]. One reason for this may be the slight variation in shielding that is experienced by the detectors of the two instruments.

A drawback of the CRaTER instrument is that it cannot be used to detect neutrons since it lacks a scintillator. An important observation made during simulations and data analysis in [80] was that due to the arrangement of its detector stack, the CRaTER instrument's sensitivity to GCRs is direction dependent. When this dependency is coupled with changes in the pointing direction of the instrument, it can result in under-detection of some radiation species. This leads to the operational consideration that for instruments that display directional dependency in sensitivity to radiation, rigorous tracking and bookkeeping of the instrument/spacecraft attitude during measurement periods is necessary.

<sup>12</sup>This equates to a resolution of 0.13  $\mu Gy$

<sup>13</sup>[https://prediccs.sr.unh.edu//craterweb/products.php?numplots=1&durationtype=span&ProductG111=doserates&SepGcrAllType111=all&InvCombG111=doserates\\_micro](https://prediccs.sr.unh.edu//craterweb/products.php?numplots=1&durationtype=span&ProductG111=doserates&SepGcrAllType111=all&InvCombG111=doserates_micro)

## RADOM

The Radiation Dose Monitor (RADOM) instrument on India's Chandrayaan 1 mission measured the Earth and Moon radiation environment, starting in late 2008 [32]. RADOM was a small dosimeter-spectrometer that measured the radiation environment during the Chandrayaan mission, in Earth orbit, during the transit to the Moon as well as in the lunar orbit phase at different altitudes. The instrument primarily measured the total absorbed dose, particle flux and spectra of energy deposited by particles.

### Instrument Setup & Operation

With an envelope of 100 X 40 X 20 mm and a mass of 100 grams, RADOM is a compact instrument that has a nominal power consumption of about 350 mW. It consists of a Si detector, the O/P for which is amplified using a charge sensitive pre-amplifier. The principle of detection is that incident radiation generates voltage pulses in the detector which are proportional to the deposited energy. Subsequently, an ADC converts the signal into digital form and feeds it to the slave MCU, in tandem with the action of an electronic discriminator. Deposited dose and particle flux are calculated using the multi-channel O/P of the slave MCU and ADC. A Master MCU controls the slave and manages power and telemetry interfaces with the rest of the spacecraft [32]. Figure 2.8 shows the electronic architecture of RADOM [32]. In terms of its setup and construction, RADOM is inspired by Liulin 4 type dosimeters and R3D instruments [33].

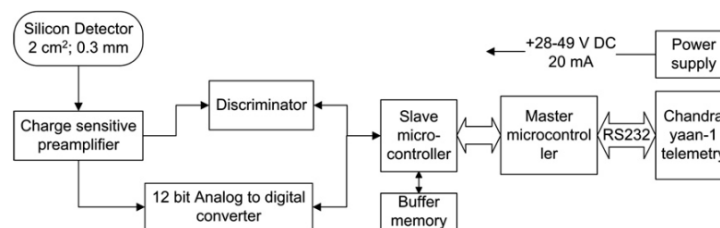


Figure 2.8: RADOM electronic functional block diagram [32]

### Observations & Results

Similar to the observations made by CRaTER, RADOM made measurements during a period of historically low solar activity circa 2009 [108], which resulted in a favorable opportunity to measure GCR since it made up the dominant component of the lunar and interplanetary radiation environment.

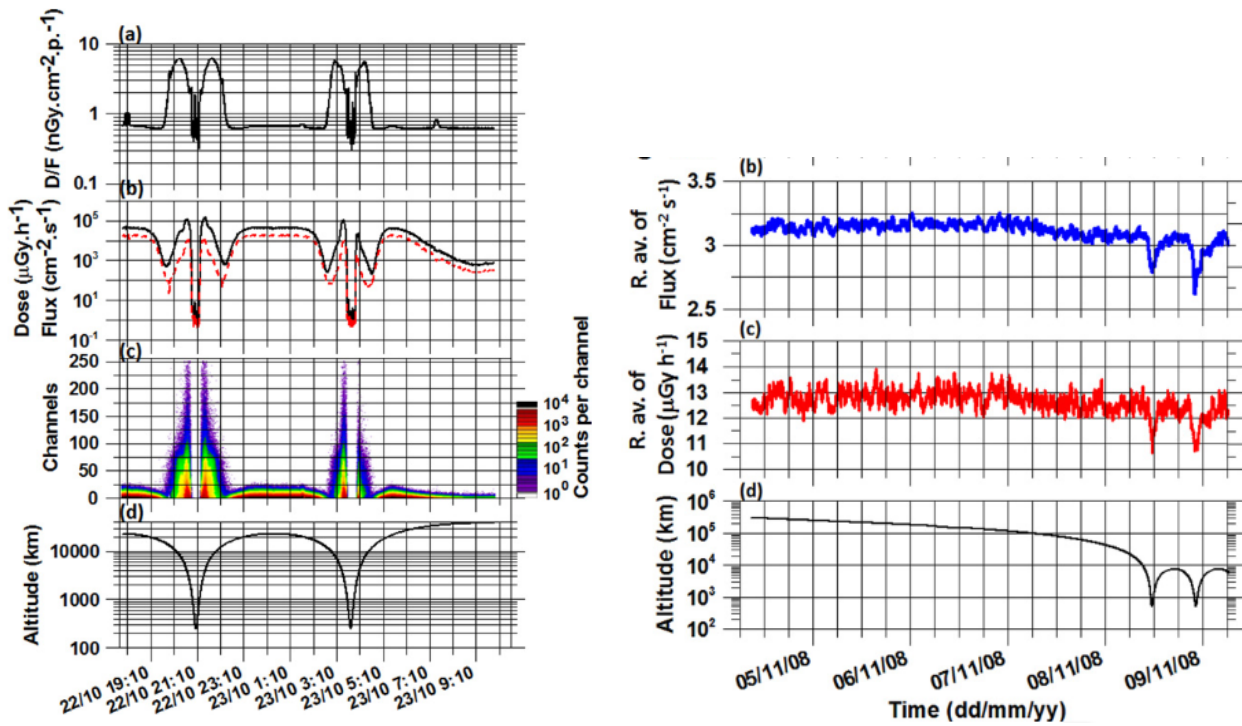
Measurements in LEO were made with a time resolution of 10s. The dose rate, flux, counts per energy channel recorded w.r.t the altitude can be seen in Figure 2.9a. Moving from left to right, high dose and flux are observed in the outer VAB and subsequently in the inner VAB. An intermediate dip is seen at the spacecraft passes through the 'slot region' between the VABs. Post passage through the inner VAB, a big drop is seen as the spacecraft enters LEO altitudes. Here, the dose rates were seen to be in line with observations made on the ISS [32]. Thereafter, this cycle repeats as the spacecraft orbits the Earth multiple times before several apogee raising maneuvers and the trans lunar injection burn take place. The type of particles were inferred from a derived quantity called the specific dose per particle. This is calculated by dividing the dose rate by the flux. The specific dose and energy values recorded in the spectrometer were used to make predictions about the incident radiation particle types.

RADOM data was compared to AP-8/MIN and CRRESS models, set up with minimal solar activity and particle energies which correspond to the detection threshold of RADOM. It was found that these models predicted flux values which were one or two orders of magnitude above RADOM data for radiation near Earth apogee. The authors chalked these differences up to several factors, such as:

- Inherent uncertainties in the model data
- RADOM electronics set up resulted in a spectrometer dead time of about  $20 \mu\text{s}$ <sup>14</sup>.

The slot region experienced by RADOM was found to be wider than the predictions made by the models. According to the investigators, this could have been caused by the abnormally low solar & geomagnetic

<sup>14</sup>This factor is relevant because of the high fluxes in the VABs



(a) Measurements of specific dose, dose rate, flux and detector counts per channel w.r.t Earth orbit altitude [32]

(b) Observations by RADOM during lunar transit and capture, adapted from [32]

**Figure 2.9:** Mission results from the RADOM instrument [32]

activity during the Chandrayaan mission, which would not be captured by the theoretical models [32].

During transit, the total dose accrued was calculated as approximately **1.3 Gy**. Average particle flux was found to be about  $3.14\text{ cm}^{-2}\text{ s}^{-1}$  and the dose rates were on average **12.76  $\mu\text{Gy}/\text{h}$**  [32]. The running average of dose rate and flux w.r.t altitude from the Moon can be seen in Figure 2.9b. Closer to the Moon, the dose rate and flux reduced because of the obstruction to incoming radiation presented by the Moon's disk. It can be seen in Figure 2.9b that the shielding effect reduces as the spacecraft ventures higher away from the Moon. Over time, an increasing trend of the average GCR flux and dose rates was observed, which was verified by Neutron monitor readings on Earth [32].

As with other micro-dosimeters, RADOM's detector had a low effectiveness toward neutrons, which are notoriously hard to detect in compact systems [10]. The shielding on the back side of the RADOM instrument was not known exactly, leading to uncertainty in the radiation species that can originate from about half of the total viewing angle of the instrument. Complex interactions of incoming radiation with the body of the spacecraft made the measurement of radiation on this side even more uncertain and difficult. A systematic discrepancy was observed when comparing RADOM data to theoretical models. The authors speculated this to be caused by a less than  $2\pi$  FOV on the front side of the detector when the instrument was actually integrated into the Chandrayaan spacecraft [32]. The investigators also speculated that the measurements made by RADOM were lower than some theoretical models due to the dead time of the spectrometer electronics, which caused a portion of the incident particles to be missed in every cycle of data acquisition.

#### LND - Chang'E 4

The Lunar Lander Neutron & Dosimetry experiment (LND) was the first instrument to perform active and time-resolved measurements on the lunar surface [159]. The instrument was operated on-board the Chinese Chang'E 4 mission which culminated with a lander descending into the Aitken basin, located in the von Karman crater at the south pole of the Moon [154]. The LND instrument was operated during solar minimum, although not as deep as the one observed in the beginning of Solar Cycle-24 by CRaTER [87]. Consequently, the measurements made by LND reflect mainly the contribution of GCRs to the lunar radiation environment and can be approximated as the upper limits of GCR dose that would generally be expected at the lunar surface.

### Instrument setup & Operation

The LND instrument is essentially a Si particle telescope and consists of 10 dual-segment Si detectors stacked in a column. The segmented detectors are geometrically arranged such that particles of various energies and LET spectra distribution can be observed. The addition of conversion foils allows the measurement of neutral particles in conjunction. This enables the direct detection of the neutral component of secondary radiation at the lunar surface. A drawback of Si solid state detector (SSD) telescopes is that the count rates measured by the telescope depend on its orientation if the radiation field is non-isotropic in nature [154].

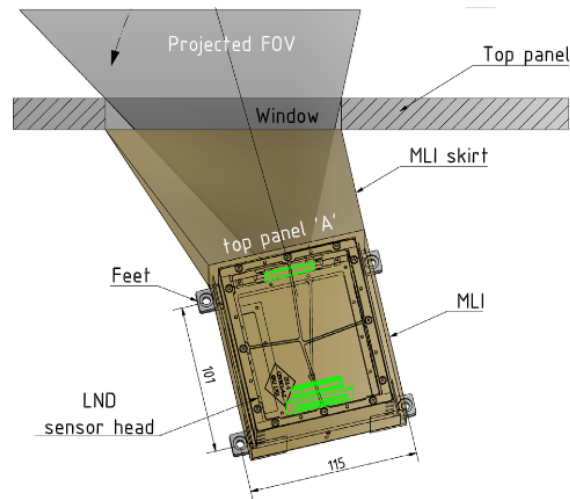


**Figure 2.10:** Schematic view of the LND instrument [154]

LND collected the following types of data at various resolutions, and measurement cadences of 1 minute, 10 minutes or 1 hour:

- Dose rate in Si from charged and neutral particles, resolved in time
- LET spectra
- Charged particle spectra
- Thermal neutron count rates
- Energy deposition spectra of neutral particles

Total and neutral particle dose rates were measured separately by LND. Subtraction of the latter from the former yields the charged particle dose rates [159]. LND was also designed to measure fast particle and thermal neutrons which are created as secondary radiation from the interaction of high energy radiation particles with the lunar surface.

### Observations & Results

On average at the lunar surface, the absorbed dose rate was measured by LND to be about  $13.2 \pm 1 \mu\text{Gy}/h$  and the dose rate of neutral particles was observed to be about  $3.1 \pm 0.5 \mu\text{Gy}/h$  [159]. The total absorbed dose rates are comparable to the measurements made by RADOM [32] and CRaTER [87] micro-dosimeters. However, the neutral particle dose rates were found to be remarkably high. This could have been due to secondary particles created on interaction of primary GCRs with the structure of the Chang'E 4 lander and the body of the instrument [159]. The dose rates and flux for charged particles remained relatively constant over the measurement period <sup>15</sup>.

For further validation, the measurements made by LND were compared with those acquired by other spacecrafts. Notably, the LRO spacecraft with its CRaTER instrument passed over the LND landing site in Feb 2019. The comparison of dose rates during this period from both instruments was found to be in good agreement at about  $10 \mu\text{Gy}/h$  [159].

<sup>15</sup>Toward the end of each lunar day, Ammonia, the working fluid flowing in heat exchanger pipes in the lander, created additional shielding during the lunar night and affected the detection of neutral particles

The presence of radioactive heating and power sources on the Chang'e 4 lander (Radioactive Heater Units - RHUs and Radioisotope Thermoelectric Generators - RTGs) necessitated an extensive effort to calibrate the LND instrument and to identify and remove sources of background noise, as discussed in [64]. Since these noise characterisation efforts were carried out before launch, the evolution of the noise sources over time and in the actual mission environment could not be determined. Furthermore, the exact shielding provided to the LND instrument by the Chang'e 4 lander was not known and had to be approximated based on best estimates of spacecraft structural materials and construction [159]. The door of the payload compartment in which LND was housed was opened during lunar days and shut during the nights to provide thermal control. This also resulted in variable shielding for the radiation measurements. The initial measurements were further polluted by the presence of the Yutu-2 rover, which contained an RTG that emitted radiation recorded by LND until it was deployed from the Chang'E 4 lander [159].

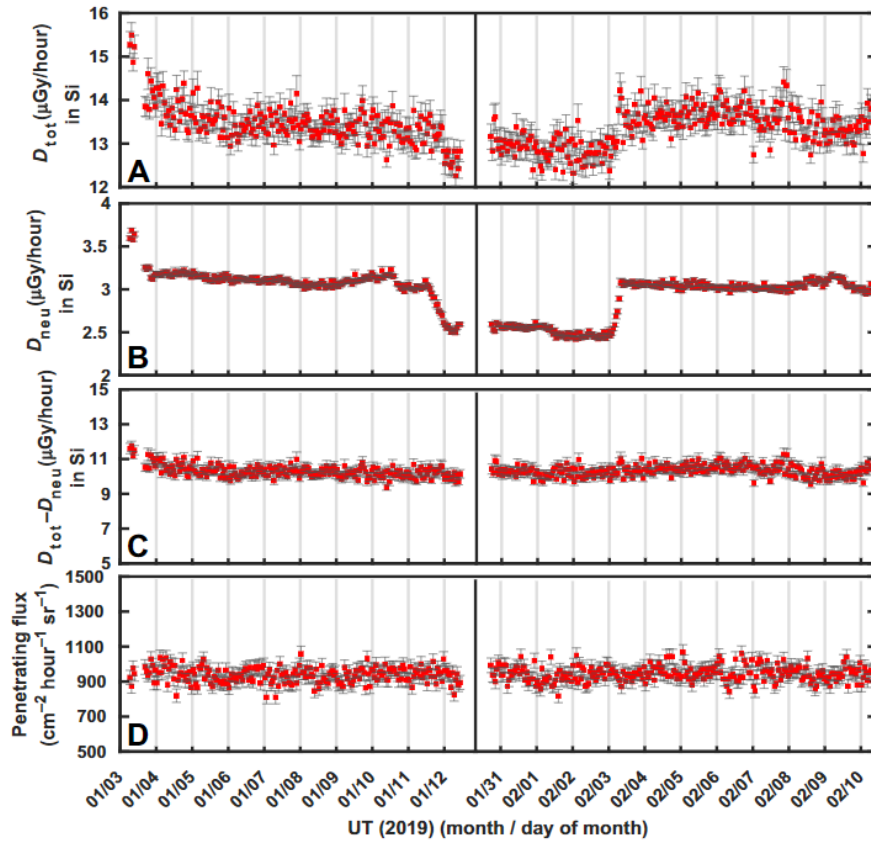


**Figure 2.11:** Total, neutral particle and charged particle dose rates measured by LND during the first couple of lunar days after landing. Note: The background noise from radioactive sources has already been subtracted from the data in the plots [159]

#### 4M - Lunar flyby

An early prototype of the FGDOS radiation sensor mentioned in subsection 2.2.2 was located on-board the Chinese Chang'e 5-T1 lunar flyby demonstrator. The FGDOS was incorporated as a part of the payload for the Lunar 4M (Manfred Memorial Moon Mission) [91] and served as the first real world demonstration of the capabilities of the FGDOS sensor in a deep space setting [27]. The hardness of the sensor w.r.t the space radiation environment was also investigated.

##### Instrument Setup & Operation

The experiment consisted of a PCB module with two FGDOS sensors interfaced with a microcontroller that controlled the sensors and some peripheral electronics chips, while also handling CD&H and communication with the On-board Computer (OBC) of 4M. The PCB was located inside aluminum housing that provided 5mm of Al shielding, which the authors claim prevented saturation of the sensors during VAB passage. Figure 2.12 shows the electronic block diagram of the payload. It is interesting to note that the portion of the housing over the FGDOS sensors was machined down to 500 microns.

One of the FGDOS sensors was set to high sensitivity whereas the other one was configured for low sensitivity. This way, the sensitivity characteristics and dependencies of the sensor had a control measure built in to the experiment. It was found during operations that the experiment board had a power consumption of about 82.5 mW and drew about 15mA of current from the 5V supply line [27]. Hence, the experiment was able to perform interesting measurements and scientific data collection on a shoestring power budget. Additionally, the 'passive mode' of the sensor could be used to perform TID measurements with virtually no power consumption. The following data fields were collected during the mission:

- FGDOS Sensor frequency
- FGDOS Reference frequency
- Sensor Chip temperature
- Number of recharges executed
- Identifier flag of the active sensor

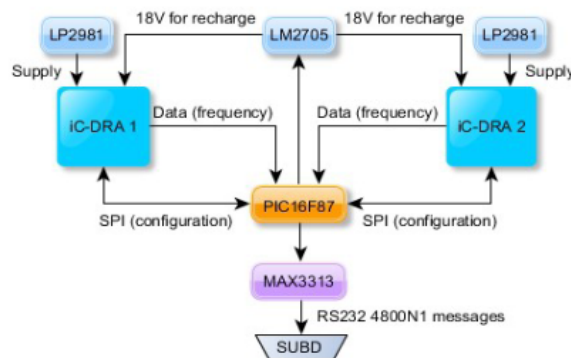


Figure 2.12: DRALUX experiment block diagram [27]

### Observations & Results

The data collected by the FGDOS sensors during the 4M mission was compared to simulations that were performed using the OMERE<sup>16</sup>. The simulations predicted that most of the TID would be accumulated during the passage of the spacecraft through the VABs [63]. The effect of the shielding provided by the Al housing was compensated for, using a weighted spherical shield model. As shown by the plots in Figure 2.13a, the sensors recorded a cumulative TID of about 23-24 rad each while the simulations predicted a higher TID of around 29.3 rad  $\pm$  5.8 rad, but the actual measurements were within the margin of error [27].

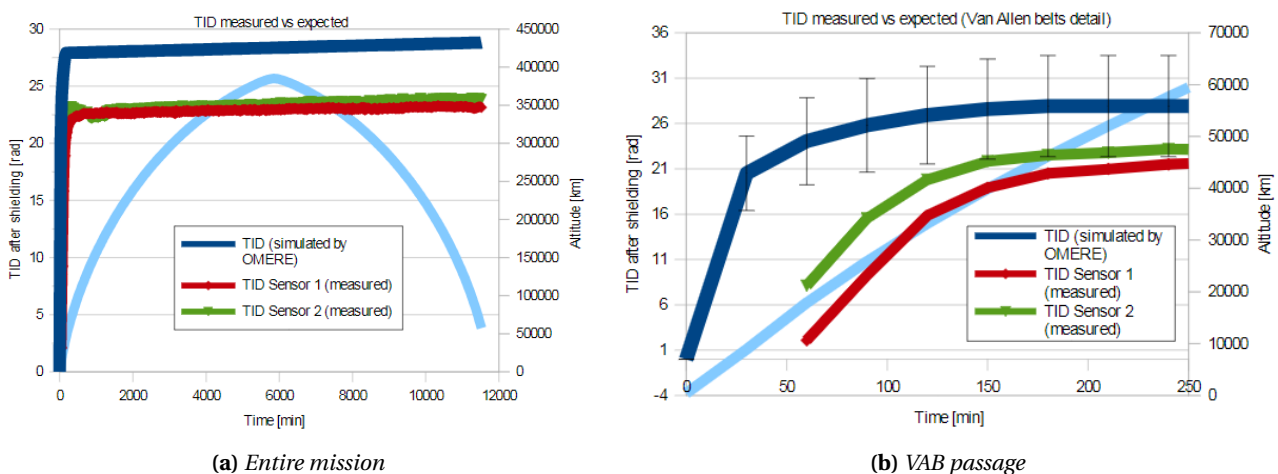


Figure 2.13: Comparison of simulation results (without shielding) and mission data from DRALUX [27]

The temperature of the sensors was seen to have a considerable effect on measurements and two differ-

<sup>16</sup><https://www.trad.fr/en/space/omere-software/>

ent compensation methods were applied to reduce this: (a) based on a look up table generated during characterization and (b) based on the measured temperature on the chip. Overall, there was considerable agreement between the experiment data and simulated results from OMERE [27]. During VAB passage, the simulations showed a higher expected TID as seen in Figure 2.13b. Since pre mission sensor characterization was only done against gamma rays and not against other radiation sources, the absolute measurements of the sensors could be error prone, leading to the necessity to rely on relative measurements and trends instead. The discrepancy between estimations from the simulations and the sensor measurements can be attributed to inaccuracies in the shielding model, lack of a complete sensor characterization effort and uncertainties in the environmental models used in the OMERE tool.

The investigation and developments that were carried out in this mission can potentially be built upon and improved in the following ways [27, 4, 34]:

- Sensors could be characterized pre-flight for both active and passive measurement modes
- The dependence of the sensitivity on dose rate can be explored further, especially in high dose rate periods such as the VAB transit
- Various particle cocktails could be used on the ground to better observe the behavior of the sensors in mixed radiation fields and in conditions that are more representative of the space radiation environment
- For radiation field characterization, methods that can be used to discriminate between particle species and their energies would be interesting to explore

### NASA's Lunar Energy Transfer Spectrometer (LETS)

A couple of Linear Energy Transfer (LET) Spectrometers developed by NASA are scheduled to fly on board upcoming commercial lunar lander flights being conducted by Masten Space Systems<sup>17</sup> and Astrobotic<sup>18</sup> in 2022-23. The LETS instruments are built around the TimePix sensor that has already been in use on the ISS [133]. The TimePix detector is a 'photon camera' that can capture the tracks of incident particles. The sensor consists of a Si detector with a pixelated ASIC for energy readout and interfacing [45]. Before landing on the Moon, similar versions of the LETS instrument are scheduled to fly in the HERA and BIRD experiments on Orion Exploration missions in the near future [118]. Figure 2.14 shows an exploded view of the LETS instrument design.

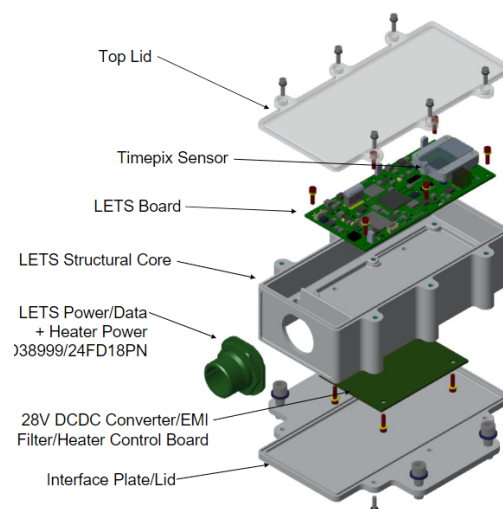


**Figure 2.14:** NASA LET Spectrometer instrument [55]

The TimePix and MediPix based instruments can provide high performance radiation measurement capabilities with data products such as track structure images, linear energy transfer, absorbed dose over a wide energy range and dose rate. However, these instruments possess a relatively large form factor (16 X

<sup>17</sup><https://masten.aero/blog/masten-mission-1-instruments-lunar-south-pole/>

<sup>18</sup><https://www.astrobotic.com/lunar-delivery/manifest/>

10 X 5 cm and mass of the order of 750 grams for LETS). Combined with the high power consumption of 2 Watts [45], these instruments are arguably suitable only for platforms such as landers or larger spacecraft. For miniaturized platforms such as micro-rovers and nanosatellites, the TimePix based instruments do not necessarily comply with design constraints and thus, these are more suitable for use in crewed capsules, orbiters, landers or smaller space probes.

### **DLR's M-42 Instrument**

The German Aerospace Lab DLR, is also scheduled to fly its M-42 radiation dose measuring instrument <sup>19</sup> to the lunar surface on-board the Peregrine lander as a part of Astrobotic's Peregrine mission 1 [13]. The M-42 instrument will perform radiation measurements at its Lacus Mortis landing site. This instrument is based on a planar Si PIN photodiode. The instrument has a whole suite of sensors in addition to the radiation detector and its readout electronics. These include accelerometers, temperature and pressure sensors [13]. Similar to the aforementioned LETS, the size, mass and power consumption characteristics of the instrument make it unsuitable for highly miniaturized and compact platforms.

### **RadPC**

The RadPC-Lunar mission is dedicated to demonstrating a new computer with relatively high performance that can recover from ionizing radiation induced errors and faults [83]. RadPC was developed at Montana State University and is scheduled to fly on-board a commercial lunar lander in 2022-23. The RadPC payload will carry a dosimeter experiment to perform characterization of the radiation field at the lunar surface and will attempt to correlate dose measurements with data about upsets and faults in the on-board computer as it performs a predetermined computational task. The dosimeter part of the payload is housed on a separate PCB from the on-board computer and it consists of three Teledyne UDOS001-C micro-dosimeter that interface with a microcontroller [79]. The dosimeters will perform measurements during transit, orbit and on the lunar surface and send telemetry to the RadPC experiment via RS422 [83].

### **Mars - MSL Rad**

NASA's Mars Radiation Environment Experiment (MARIE) <sup>20</sup>, on the Mars Odyssey probe performed measurements aimed at characterizing the radiation environment in Mars orbit and during interplanetary transit from Earth to Mars. MARIE performed flux and dose measurements and the observations returned average dose rates of about 240  $\mu$  Gy/day in Mars orbit [105].

An instrument similar in makeup to the DOSTEL instruments was flown on-board the Curiosity rover as a part of the Mars Science Laboratory (MSL) mission in 2011 and landed on the surface of Mars in 2012 [58]. The aim of the MSL Radiation Assessment Detector (RAD) instrument was to perform in-situ measurements of the ionizing radiation environment on the Martian surface [61]. The instrument can detect neutral and charged particles by making use of a silicon detector telescope, a calorimeter and a plastic scintillator.

Radiation from GCRs and SEPs was measured for different phases of the mission, namely surface operations and interplanetary transit from Earth to Mars. The average GCR dose rate at the surface was measured to be  $0.21 \pm 0.04$  mGy/day while during cruise it was measured to be more than twice that rate at  $0.48 \pm 0.08$  mGy/day [158]. The difference in the measured dose rate is due to the shielding provided to the instrument by the spacecraft being lower than that provided by the Martian atmosphere, generation of secondary radiation due to interaction of primary GCRs with the regolith and atmosphere, partial shadowing of the lower hemisphere of Mars by the planet itself and variations in the modulation of GCRs by solar activity [61].

The measured dose rates are shown in Figure 2.15. The RAD instrument also observed an SPE associated with a solar flare that occurred in April 2013. This can be seen as a sharp spike in Figure 2.15. The observations from RAD thus provide additional points of data for testing theoretical models of solar energetic particle propagation [61]. Diurnal variations in the dose rate were caused by a combination of factors such as the changes in Mars atmospheric pressure, seasonal variations and variability in the heliospheric structure along with the rotation of Mars [61]. The dose rate on the surface, was found to be anti-correlated with Mars surface atmospheric pressure. Higher pressure can lead to a small increase in the amount of shielding

<sup>19</sup>[https://www.dlr.de/content/en/articles/news/2021/02/20210422\\_m-42-will-measure-radiation-on-the-moon.html](https://www.dlr.de/content/en/articles/news/2021/02/20210422_m-42-will-measure-radiation-on-the-moon.html)

<sup>20</sup><https://mars.nasa.gov/odyssey/mission/instruments/marie/>

that the atmosphere provides to the surface locally.

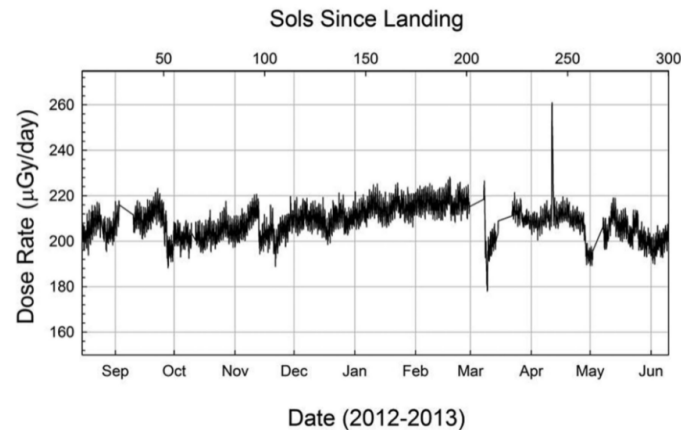


**Figure 2.15:** Dose rate measured at Mars surface by RAD [61]

Similar to Chang'e 4, the MSL had radioactive energy sources on-board which emitted radiation that acted as a source of noise for the RAD instrument. Efforts were made to characterize these sources *a priori* [158]. While these calibration and compensation efforts provide a more accurate picture of the actual radiation environment; secondary radiation due to the structure of the spacecraft, the ensconced rover and the housing of the instrument can add further uncertainty to measurements of the 'natural' space radiation environment during transit. To attempt to account for this, simplified models of the mass of the spacecraft (and its shielding) were set up and techniques such as sectoring analysis, ray tracing and radiation transport simulations were applied [158].

### 2.2.2. Miniaturized Dosimeters for Space Applications

As demonstrated by CRaTER, a relatively tiny and simple dosimeter can perform real-time measurements of the ionizing radiation environment in space, providing quantitative information about physical phenomena with low consumption of valuable spacecraft resources [87]. The requirements and constraints for detectors in space are often more demanding than that for terrestrial applications because of factors such as size, weight, power consumption and telemetry budget, which come at a premium in space applications. Moreover, detectors in space need to provide more information than their terrestrial counterparts due to the complexity and consequential nature of the space radiation environment. To completely characterize the environment, time resolved data about dose and dose rate in typically low flux environments are needed, in addition to the measurement of other properties such as LET and ionization density of particles [26]. Dosimeters can be classified as being active or passive in nature. While most passive dosimeters do not supply real-time measurements, there are some portable readout passive dosimeters that can provide periodic measurements of the dose and dose rate. Caffrey et al [26] provide an extensive comparison of active and passive detectors for dosimetry in space. Active detectors such as Si telescopes, Gas filled detectors, Neutron Bonner ball detectors and Si semiconductor detectors provide high quality, real time measurements but they have some limitations regarding LET and equivalent dose measurements. The power demands and sizes are also higher.

MOSFET based detectors (such as RADFETs) have been used abundantly in space applications because of their versatility to function as both active and passive detectors [73, 63]. The working principle is that incident ionizing radiation causes a shift in the threshold voltage of the MOSFET, which can be correlated directly with the dose. This shift is caused due to formation of electron-hole pairs in the oxide layer beneath the transistor gate when ionizing radiation passes through. While MOSFETs offer desirable capabilities, they cannot be used to measure LET distributions independently for radiation other than electrons and protons in a mixed radiation field, and neutrons can only be measured indirectly. In general, the measurement of neutrons aboard spacecrafts is a challenging task for compact dosimetry instruments [10].

Furthermore, there is a high demand for miniaturized radiation monitoring and measurement capabilities for very small platforms such as nano-satellites. The use of miniaturized spacecraft such as CubeSats

has grown exponentially over the past few decades due to their versatility, low development cost and ease of launch. Unlike large satellites, these platforms can be deployed frequently and carry out missions with higher risk profiles. They can also be utilized in a distributed and decentralized manner in the form of constellations, networks or swarms of tiny spacecrafts. A similar philosophy can be applied to planetary exploration by making use of many compact robots/vehicles. Due to these characteristics and capabilities of small spacecrafts, radiation detectors on-board these devices can have previously unexplored applications when it comes to rapid mapping and characterisation of radiation fields, space weather monitoring or studying the effect of radiation exposure on electronic systems. At the same time, the detectors need to comply with the relatively harsher constraints on resources such as volume, mass, power, compute etc. Naturally, the use of semi-conductor based solid state detectors fits such use cases well. In the next section, one such sensor with promising features is described in further detail. A complete summary of active detectors and dosimeters that have been used in space can be found in [94].

### **Floating Gate Dosimeter - FGDOS**

A novel Floating Gate MOSFET based dosimeter has been developed for use in space applications, particle accelerators and medical irradiation facilities [34]. The use of MOSFET based dosimeters which leverage floating gate (FG) MOSFETs to perform measurements in space was proposed back in 1998 by Scheick et al [115]. This followed from the observation that non volatile memory chips built from floating gate MOSFET cells were sensitive to radiation. FG MOSFET based dosimeters can be made in very small sizes, with integrated electronics for readout and low required voltage supply. The manufacturing of such chips can be achieved with a conventional CMOS process [4]. Moreover, because of the detection principle, such dosimeters can even make measurements without external bias voltage for limited time periods/doses.

The principle of detection of these dosimeters is that there are two ways in which incident radiation diminishes the charge on the floating gate [4]:

1. Charge is generated in the surrounding oxides and combines with the charge on the floating gate
2. Absorption of radiation causes emission of charge carriers that possess enough energy to break through the potential barrier in the MOSFET

The floating gate dosimeter developed by Sealcon (formerly iC-Malaga), called FGDOS, has some salient features such as temperature compensation, recharging capability and sensitivity configuration [4]. The sensor produces an output frequency signal that depends on the received TID [51]. In practice, the FGDOS chip consists of two sensors which can be read alternately. Each sensor consists of a Floating Gate (FG) MOSFET and a standard one (which is not affected by radiation and acts as the control for temperature dependency). The differential frequency that is obtained by the readout electronics, based on the voltage of the FG MOSFET and the standard one are correlated to the TID by a characteristic sensitivity in kHz/Gy. The sensitivity is based on the area of the floating gate and can be selected in software by choosing from two different MOSFETs in the chip that have different floating gate areas, and thus a different sensitivity too. Figure 2.16b shows the schematic makeup of the FG MOSFET.

In operation, the sensor is initialized by charging the FG to a pre-set value that corresponds with a target frequency. Incident radiation depletes this charge and hence the frequency starts to descend, until it reaches a threshold value, whereupon the FG must be recharged. The target and threshold are selected such that the sensor remains in the range where its behavior w.r.t the TID is approximately linear. Figure 2.16a depicts this operation cycle.

Initial characterization of FGDOS prototypes was carried out to determine whether the chip is suitable for use in space based applications and is described in [4]. Various chip samples were subjected to a Co-60 source and showed a promising linear relationship between the frequency and total ionizing dose (TID) up to 10 krad. The sensitivity was found to be consistent between different samples, but a dependence of the sensitivity on the dose rate was observed. Higher sensitivity was observed at higher dose rates and a degradation in the sensitivity was seen at lower dose rates. An interplay between the effects of dose rate and TID on the sensitivity exists and the sensitivity was found to degrade at high TID [4].

As mentioned by Benton et al [10] and Caffrey et al [26], there is a need for small, low power active detectors

with a portable readout. The FGDOS is one of the sensors that fills this gap in radiation measurement and space dosimetry instrument needs. In the realm of spaceflight where weight, power consumption and computation come at a premium, such a low cost and low footprint sensor can offer exciting scientific as well as radiation monitoring capabilities, especially when it comes to operations on board very small and compact platforms such as nano/pico-satellites, chip satellites, mini-robots and rovers etc. As described earlier, the sensor has already been used in space on a Lunar Flyby mission, to measure the dose and dose rate in the vicinity of the Moon and during transit to the Moon [27].

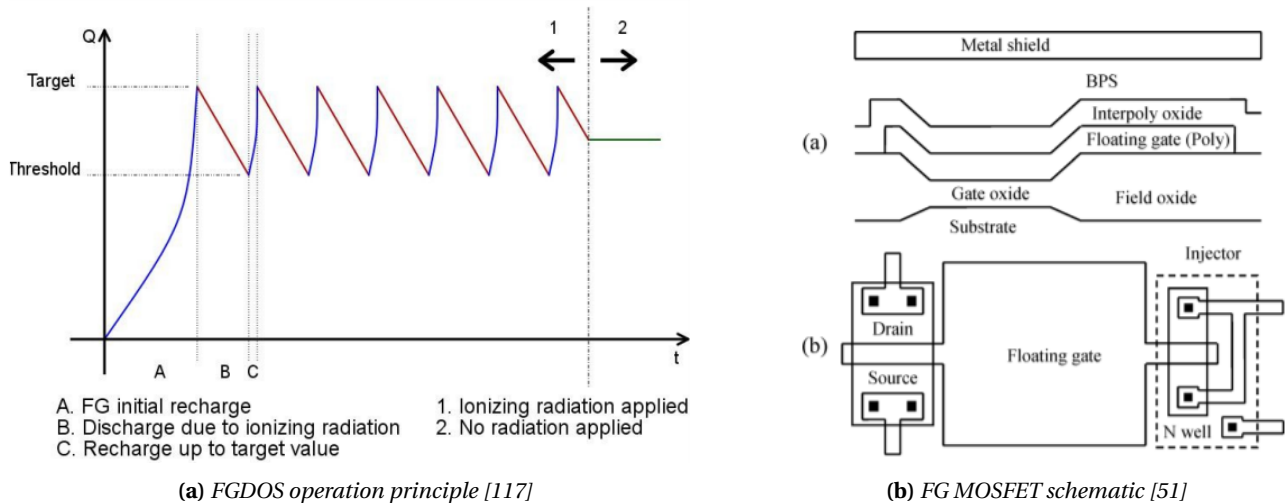


**Figure 2.16:** FGDOS operation and physical schematic

Compared to the conventional RADFETs used for ESA missions, the FGDOS sensor has a much better resolution of about 2 mGy and an extremely low power consumption of about 20-30 mW at 5V bias. It also has a higher sensitivity. The limitations are that the FGDOS sensors developed so far need a 5V supply and they possess a limited dose range which is smaller than that of RADFETs [109].

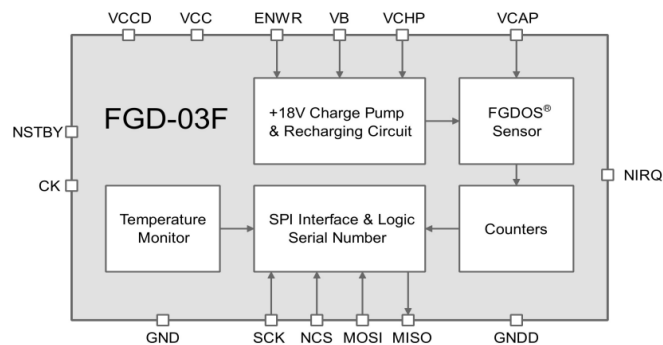


**Figure 2.17:** FGD-03F block diagram [117]

The limitation of this detector technology is that it cannot measure LET or neutrons directly. While neutron measurements can be inferred from secondary effects during post measurement analysis, only a very coarse estimate can be made by measuring absorbed dose and using an averaged mean path length to derive the LET of incident radiation. Since dose and dose rate are cumulative measures of the energy deposited by incident radiation, these cannot be used directly for complete characterization of the radiation field since the energy spectra, particle composition, flux etc. cannot be derived directly from cumulative measurements alone. This limitation applies to dosimeters in general, unless complemented by another detector technology or instrument such as an LET spectrometer or scintillator.

The FGDOS sensor and its utilization has been under research at the Space Systems Engineering (SSE) section of TU Delft. As such, some preliminary calibration of the FGD-03F sensor chip [117] was carried out and

the sensor was integrated into a FlatSat setup at ESA ESTEC [90]. Figure 2.17 shows the functional diagram of the FGD-03F sensor module that can be used for space applications. Based on current developments, this sensor could be incorporated into radiation measurement and monitoring instruments, as a part of miniaturized platforms, in the manner described in section 2.3.

An abbreviated comparison of a select number of miniaturized radiation detection technologies is provided in [122], with the resultant comparison table provided in section D.3. [70] presents a comprehensive review of ionizing radiation sensor types based on semi-conductor technology. The FGDOS offers a desirable balance between radiation measurement capabilities and size, power and mass characteristics. The FGDOS sensor can be operated on a low bias voltage and power consumption and it can even measure the TID under zero bias in passive mode. The sensor has extremely low size and is much cheaper compared to the Teledyne and Timepix detectors. In terms of performance, the sensor has much better resolution than RADFETs but lower than that of the Teledyne micro-dosimeter. The Timepix can measure LET directly and be used to identify individual incident particles. The FGDOS sensor comes with built in read out and processing circuitry and can be interfaces easily with an MCU. Hence, the readout complexity is much lower than the other detectors. Moreover, each FGDOS module comes with built-in redundancy and temperature monitoring.

## 2.3. Lunar Zebro Radiation Payload

Lunar Zebro is a lunar nano-rover being developed by a team of students at the TU Delft [124]. The project was launched in 2017 as a space themed offshoot of the Zebro project under the aegis of the TU Delft Robotics Institute [81].

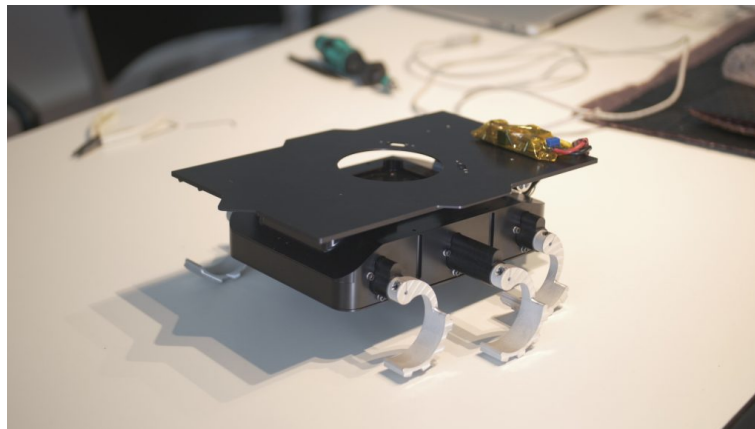


**Figure 2.18:** *Engineering Model Belka-1 [81]*

### 2.3.1. Mission Objectives

The goal of the first Lunar Zebro mission is to fly a single Lunar Zebro rover to the moon and to demonstrate its capabilities for one lunar day (14 Earth days) [68]. Hence, the first mission is aimed at conducting scientific observations (described later) and technology demonstration to prove the Lunar Zebro in its operational environment and to enable future missions where multiple rovers can be deployed to apply swarm based exploration and operations.

#### Swarming and future exploration

The long term goal of the Lunar Zebro project is to cause a paradigm shift in robotic space exploration by introducing a low cost, high robustness and low footprint approach. This is in contrast to the traditional "Mini Cooper" sized lab-on-wheels rovers and exploration probes that usually take decades to develop and result in 'astronomical' mission costs. As a part of this vision, the Lunar Zebro team plans to build on the first lunar mission by launching multiple rovers that can work collaboratively and make use of the collective intelligence of swarm robots to make rapid planetary exploration possible [137]. Collaborative human-machine exploration is another possibility, wherein astronauts make use of Zebro swarms to enhance their abilities while simultaneously protecting themselves from unknown hazards. Such capabilities have been demonstrated on Earth by means of numerous analog missions [81].

### 2.3.2. System Architecture

The Lunar Zebro is designed to be a highly miniaturized and modular lunar rover. In accordance with the trends and philosophy of NewSpace, Lunar Zebro makes use of COTS components, in-house developed modules, strategic industry collaborations and an iterative design and test approach to achieve an ambitious mission with an innovative system built at low cost. The Lunar Zebro mission consists of a Space Segment and a Ground Segment. The Space Segment consists of the Lunar Zebro rover that will be transported to the lunar surface.

Figure 2.19 shows the subsystems of the Lunar Zebro rover at a glance. A detailed description of these subsystems can be found in [68].

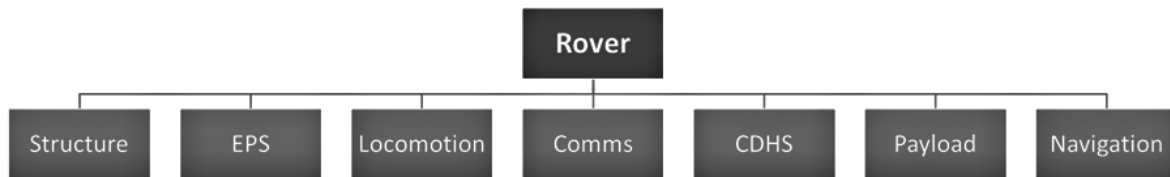


Figure 2.19: Subsystems of the lunar rover [68]

### 2.3.3. Science Mission & Payload

Given its innovative design and capabilities, the Lunar Zebro is well equipped for conducting scientific investigations on the Moon and beyond. The scientific goal of the Lunar Zebro is to measure radiation in the lunar environment [68]. Some early stage conceptual work was performed in this regard previously [52]. This served as the starting point for the present work, wherein the detailed design, implementation and, verification and validation of the LZ scientific payload is presented.

The instrument referred to as the *Radiation Payload* of Lunar Zebro, would be used to perform in-situ measurements of ionizing radiation on the lunar surface, with the added advantage of being housed on a mobile platform instead of a stationary lander. Hence, a displaced set of measurements that can augment previously performed observations on the lunar surface [159] can be provided by the proposed Lunar Zebro Payload. Since the landing window of the Lunar Zebro is estimated to be during the mid-2020s, it would also provide measurements during a different phase of the solar cycle, as opposed to previous instruments like RADOM [32] and LND [154] which were active during the solar minimum phase.

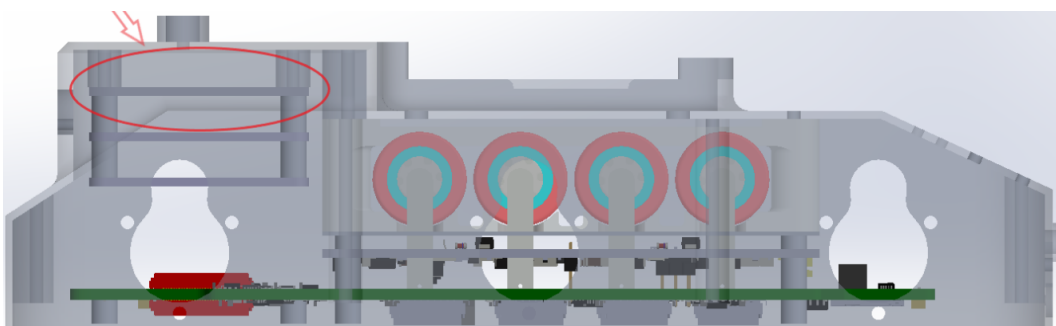


Figure 2.20: Potential location of the Radiation Payload in the Lunar Zebro rover [53]

Due to complex scattering effects and generation of secondary radiation, it may be beneficial to have the radiation sensing spatially distributed over the rover, rather than having a single point of measurement. Hence, multiple radiation sensors may add to the value of the measurements and the overall scientific investigation.

Observation of the solar energetic particles and any SPE events during the operational phase of the mission

could be used for additional data points to test and validate models of the heliosphere and how solar wind and SEPs propagate through it [61]. Similarly, observations of the protons and heavy ions in GCRs could yield additional data points for model validation and lead to the formulation of better guidelines and rules of thumb for engineering miniaturized embedded systems for lunar and space applications.

The Lunar Zebro rover with the Radiation Payload on it can be thought of as a novel laboratory for measuring radiation on the Moon and for observing its effects on subsystems which are made up of mostly COTS electronic devices. It could represent a flagship effort that probes the edges of current knowledge and enables the use of decentralized expeditions consisting of multiple miniaturized robots in the future, for the exploration of planetary surfaces. The Radiation Payload could also have long term applications when it comes to the vision of the Lunar Zebro Project. Large swarms of autonomous robots, while robust as a whole, could be individually susceptible to the adverse effects of the space environment. A prime concern could be the degeneration and damage of on-board electronics of the rovers due to the effects of space radiation. Both cumulative effects in the long term (such as TID) and sporadic, random radiation effects in the short term (such as SEEs) could lead to consequences which affect the performance of individual rovers as well as the swarm(s). Hence, it becomes apparent that a better understanding of the radiation environment over appreciably long spans of time is required to guarantee effective operations of such rover swarms. More importantly, it would advance human lunar exploration owing to the considerable challenges and hazards posed to biological organisms by the radiation environment, especially for sustaining long-term missions. Such advancements in understanding of the space environment and its effects and implications for space systems (the Lunar Zebro rover in particular) would take us closer to unprecedented exploration of the Moon via this technology.

## 2.4. Research Objectives & Questions

Space radiation has been identified as one of the main hurdles in the path to bigger and bolder spaceflight endeavors [39]. Space systems can be exposed to high energy radiation from a combination of sources. The complicated nature of space radiation makes it difficult to predict its impact and to protect against it. Monitoring and characterization of radiation from different sources is extremely important to understand the radiation environment and to make accurate predictions and risk assessments for future spacecrafts, space systems and astronauts [105]. Radiation environments for a given mission can vary based on the mission profile and spacecraft configuration. As a consequence, it becomes essential to measure the radiation conditions for each mission [14]. Lunar and interplanetary missions entail exposure to radiation from the sun in the form of SEPs, from trapped particles in the Van Allen Belts (during transit from Earth to Moon orbit) and from the ever present cosmic rays [158]. The incident radiation intensity, particle types, dose rates and energy levels change continuously over different phases of a lunar mission as the spacecraft makes its way from LEO to the lunar surface via cis-lunar space.

Direct measurements of the space radiation environment result in lower uncertainty about its characteristics and probable effects on space systems, as opposed to purely theoretical modelling and computational studies. Despite the notion that it is more expensive to build, test and fly space instruments, it is an essential practice for various missions since it enables the development of accurate theoretical models and tools used for simulations and predictions of the space environment for future missions. Direct, in-situ measurements also enable the reduction of uncertainties caused by gaps in knowledge and explicit or implicit assumptions that the models are built on. Hence, real world data from instruments is essential for the purpose of validation of models as well as definition of their scope so that their applications may be extended in the future.

A plethora of instruments have been employed to measure ionizing radiation in space. Most of these instruments have operated on-board satellites in Earth orbit and on the ISS [14]. The amount of data that exist for the radiation fields in interplanetary space [158] and on other planetary bodies is comparatively low. To date, ionizing radiation levels have been measured on the Lunar and Martian surface only once [159], [61]. The radiation environment for lunar missions assumes extreme importance as multiple robotic and crewed missions are planned in the near future [128]. This fact highlights the need for more in-situ measurements. With the rise of miniaturization in space technology and space vehicles, radiation measurements could possibly be carried out on nano-satellites or nano-rover platforms in an effective manner that involves relatively

low resources and development time. The use of these platforms necessitates compact radiation detectors that can provide active measurements while operating on meagre resources and tight technical budgets. The FGDOS [51], developed for space and particle physics applications may be suitable in this context as it has already been demonstrated on a lunar flyby mission [27].

The Lunar Zebro mission [81] presents an unparalleled opportunity to perform in-situ radiation measurements on the Moon and during transit to the Moon. Never before has radiation data been collected by a mobile platform on the Moon. It is envisaged that a compact, low cost instrument with relatively low power consumption could be created to achieve this objective [52]. Beyond the first Lunar Zebro mission, the proposed instrument could have far reaching applications in radiation monitoring for scientific as well as operational needs.

On the basis of the need to characterize the lunar radiation environment and the possibility of utilizing the FGDOS sensor in conjunction with the the Lunar Zebro rover, the main research question can be posed as:

**How can the lunar radiation environment be characterized using a miniaturized, low cost instrument that can be operated on board a lunar nano-rover platform such as the Lunar Zebro ?**

This main question is decomposed into the following sub-questions such that the research work can be broken down into a tangible set of research activities:

1. *What should the characteristics and architecture of the instrument be?*
  - *How can the FGDOS sensor be incorporated into the instrument?*
  - *How should the instrument be incorporated into the nano-rover?*

The first sub-question deals with the conceptualization, systems engineering, design and implementation of the proposed radiation instrument. Furthermore, the incorporation of the instrument into the nano-rover is a point of interest.

2. *Can the instrument, integrated on the nano-rover platform, enable radiation measurement in the influence or vicinity of lunar landscape features such as lava tubes, craters and the lunar regolith ?*

The lunar landscape is rich with features which are interesting to explore due to their potential utilization for shelter, protection or resources. High energy radiation incident on the moon can be changed and modulated upon interaction with these landscape features. The detection of these altered radiation species may lead to interesting findings about the moon as well as its radiation environment.

3. *How can it be used to measure the radiation environment during various phases of the mission ?*
  - *How should the instrument be configured and operated?*

It may be possible for the instrument to operate and acquire scientific data during various phases on the Lunar Zebro mission. As such, how the instrument can be utilized and controlled, and what value it can provide scientifically becomes a relevant aspect for this research.

4. *How can such an instrument be used to characterize the effectiveness of shielding of the nano-rover platform?*

Assuming that the instrument can be integrated into the rover, the radiation it will detect will likely be modulated due to the shielding provided by the rover's structure and subsystems. Thus estimating the effects of this shielding would appear to be an important part of analyzing the instrument's response.

# 3 Radiation Payload Design & Development

This chapter describes the design and development of the Lunar Zebro Radiation Payload with the application of systems engineering. The V Model of systems engineering was followed throughout the course of this research project. The activities involved in the Front End Systems Engineering of the Radiation Payload are described in the first section. This is followed by the detailed design and implementation of the Radiation Payload Subsystem. Finally, the Manufacturing, Assembly and Integration activities are described at the end of the chapter. While the process is laid out sequentially in this report, in reality, concurrent engineering practices were used to ensure coherent development on multiple fronts.

## 3.1. Radiation Payload Systems Engineering

The discipline of systems engineering enables the development and execution of complex space systems and realization of space missions. In order to ensure that projects are realized within constraints of time, performance, and cost, a systematic approach needs to be followed. This is especially true in light of the volatile, unpredictable, complex and ambiguous (VUCA) nature of technological endeavors in the modern world [40]. The literature study described in the previous chapter led to the selection of payload design and development as one of the major objectives of this thesis project. Naturally, the realization of this goal can be achieved through the application of space systems engineering in a rigorous way. The following sections expound on this process.

### 3.1.1. Need & Mission Statement

First and foremost, it is important to identify the problem that is to be solved and the need that is to be fulfilled by the system<sup>1</sup>. This is done by means of drafting a 'Need Statement'. The 'Need Statement' for the Radiation Payload is formulated as follows:

*Space systems need to be protected against ionizing radiation in space in order to enable commercial, technological, scientific and exploration spaceflight activities on the Moon in a safe, sustainable and effective manner. Radiation monitoring instruments are usually large, bulky and consume high amounts of resources such as power and data. They also require long development times.*

*The space radiation environment for lunar missions needs to be thoroughly understood and characterized in an economical manner.*

The Mission statement stated below supplies how the 'need' will be met with the help of the Radiation Payload and Science Mission objectives of the Lunar Zebro:

*The Radiation Payload of Lunar Zebro will enable unprecedented measurement and characterization of the lunar radiation environment with minimal impact on size, weight, power, cost and development time, by taking advantage of miniaturization and COTS technology.*

### 3.1.2. Science Mission Objectives & Definition

The Science Mission of Lunar Zebro will involve the measurement of ionizing radiation on the Moon, using the Radiation Payload. The *Mission Objectives* for the Science Mission are presented as follows:

1. To measure exposure to ionizing radiation on the lunar surface
2. To enable characterization of the radiation environment for lunar missions at various locations from Earth orbit to the lunar surface
3. To characterize effectiveness of shielding provided by the structure of the Lunar Zebro rover to its internal subsystems and components

While the mission profile and selection of launch provider for Lunar Zebro has not been finalized yet, a

---

<sup>1</sup>Hereafter, the Radiation Payload is referred to as a sub-system of the Lunar Zebro rover

baseline mission definition was developed. This was based on some general assumptions and the best estimates of the mission plan available at the time of writing. The details which were assumed for each phase of the mission are tabulated in Table 3.1. The table provides a brief description of each phase, in addition to the relevance of the phase for the Science Mission and consequently the Radiation Payload. The transition event between phases and the duration of each phase is also mentioned.

Phase	Description	Details	Payload Relevance	Transition to next phase
Pre-Launch	Final integration of rover into launch vehicle	Launch duration: <1 day	Payload and rover most likely powered off	Launch, Orbit injection and raising at L+4 days [67]
Earth Orbit	Low Earth Orbit operations (LEOP), checkout of all lander payloads	Orbit characteristics: Duration: ~4 days with 20 rads/-day of exposure [8]	Orbital radiation environment, Payload checkout and commissioning, passage through VAB	Trans-lunar injection: L+8 days >320 km altitude [67]
Cis-lunar Transit	TLI burn, passage through the VABs and transit to the Moon	Orbit char: 5-6 days up to 2 months [67] with 1 rad /day exposure [8]	Interplanetary radiation environment; GCR observation	Lunar Orbit injection : L+14 days 6000 km apolune
Lunar Orbit	Lunar orbit operations of lander payloads, checkouts, landing burn	6000 km X 100 km to 100 X 100 km ~6 days L+14 days Up to 2 months [67]	Lunar orbit radiation environment	Descent & Landing: L+20 days
Lunar Surface	Landing on lunar soil, deployment of Lunar Zebro rover, rover surface operations for about 1 lunar day, rover hibernation before lunar night	12-14 Earth days + lunar night Total TID: 10 krad with 2mm Al shielding [67]	Surface radiation levels and influence of lunar landscape, lava tubes, albedo etc.	End of mission

**Table 3.1:** Mission Definition for the Lunar Zebro Science Mission

The entire mission can be decomposed into the following phases:

1. **Pre-Launch:** The mission will begin with a pre-launch phase which consists of the final integration of the rover into the lunar lander and launch vehicle. After said integration, the rover (including the Radiation Payload) will be subjected to a routine of functional tests and checkouts to ensure proper functioning of the rover and its subsystems as well as successful electrical and data interfacing with the lander, by means of an umbilical connection from the lander to the rover [68].
2. **Earth Orbit:** Following the launch, it is expected that the lander (including the integrated rover), will spend some time in Earth orbit whereby checkouts of all lander payloads<sup>2</sup> will be performed. During this phase, it is estimated that the Radiation Payload can be commissioned and its Scientific Mission can begin with measurements of the radiation environment in LEO. This phase will terminate with the execution of a trans-lunar injection burn.
3. **Cis-lunar Transit:** In transit to the Moon, it is expected that the rover will still receive power from the lander through the aforementioned umbilical connection. Hence, the Radiation Payload can continue operating during the transit phase. In this period, the most interesting measurements are expected during the passage of the spacecraft through the Van Allen Belts (VABs). As discussed in chapter 4, a significant portion of the radiation exposure will be incurred during the passage through the inner and outer VAB, followed by a relatively quiescent period of sampling the interplanetary radiation environment. This phase will end with the injection of the spacecraft into an elliptical lunar

<sup>2</sup>The term payload in this instance refers to the Lunar Zebro rover and other spacecrafts manifested on the lander

orbit.

4. **Lunar Orbit:** Lunar orbit injection will be followed by multiple burns intended to lower and circularize the orbit. At this stage, some lander payloads which are focused on orbital operations will start to function. The Lunar Zebro rover will again be subjected to checkouts to ensure the health of the system before landing and subsequent deployment. The Radiation Payload can continue operating as it did during the transit phase, although it is expected that the dose rate would go down as the lander gets closer and closer to the Moon, due to the obstruction posed to GCRs by the Moon itself.
5. **Lunar Surface Operations:** Once the lander has safely settled on the lunar surface, checkouts and functional tests will be performed again, before the rover is deployed on the lunar surface and becomes an independent spacecraft. It is expected that this phase will begin in conjunction with the onset of the lunar day. This marks the start of the most important part of the Science Mission, which is the measurement of ionizing radiation on the lunar surface. As the rover traverses the landing site and its vicinity, the Radiation Payload will operate nominally and acquire data for downlink to the the Ground Segment. The payload will continue to make time resolved dose measurements as the rover performs various mission objectives and technology demonstration related tasks.

The assumed mission definition was based off of the payload user guides from ispace [67] and Astrobotic [8], two of the leading commercial lunar lander companies at the time of writing. Accordingly, a representative mission plan from the perspective of the launch provider is depicted in Figure 3.1.

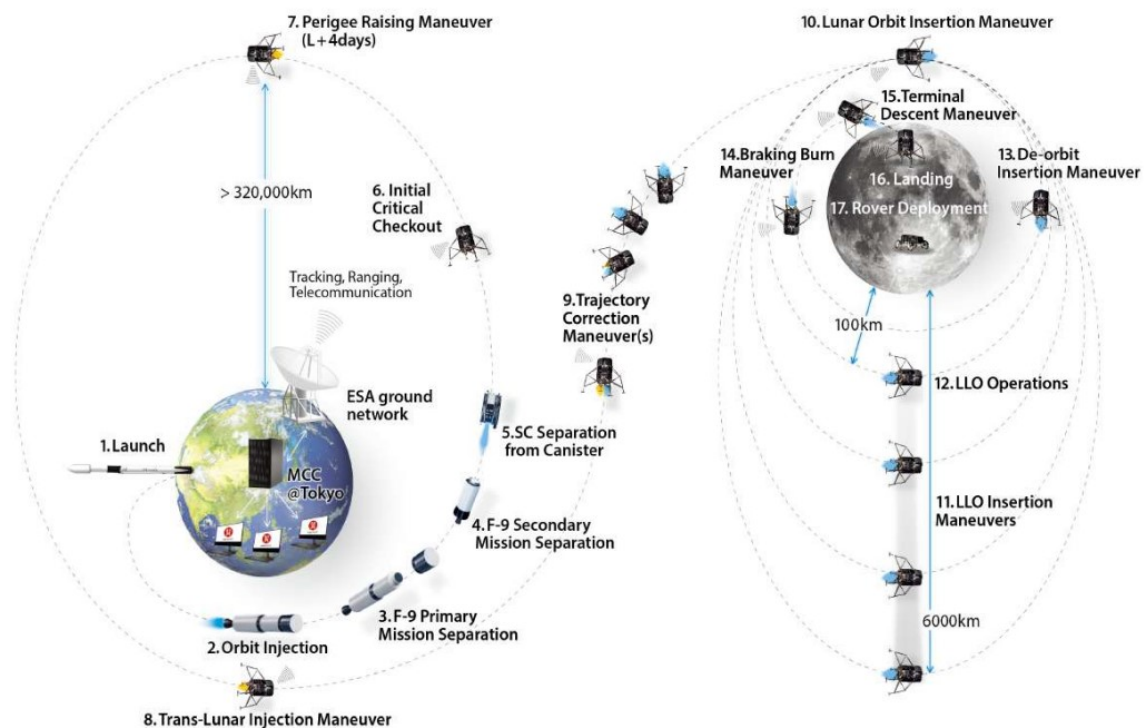


Figure 3.1: Indicative lunar mission plan ([67])

### 3.1.3. Stakeholders

Before going deeper into the design process, it is important to recognize and establish the stakeholders for the Science Mission and the Radiation Payload. A list of stakeholders was compiled, which is presented in Table 3.2. The stakeholders were also classified into *active*, *passive* or *customer* categories, based on the nature of their involvement in the Radiation Payload and Science Mission.

<b>Stakeholder</b>	<b>Group:</b> Active/ Passive/ Customer	<b>Rationale/ Motivation</b>
Principal Investigator (PI)	A	The primary investigator for the science mission and of research activities for space radiation monitoring with the FG-DOS will be actively involved in payload development, testing & operations
Lunar Zebro	A / C	Developer of the nano-rover platform. Close collaborator on payload design, development, testing and operations
Space Engineering, TU Delft	A	Researchers from this department (especially the Space Systems Engineering section) will actively contribute to the development and interact with the payload once it is operational. It also supports the Lunar Zebro project
TU Delft Space Institute	A	The institute supports and facilitates the Lunar Zebro project and its activities
TU Delft	A	Will shoulder the development of the payload at the university's faculties by providing necessary staff and resources. As a state university it will facilitate the research and make the results available for the general public. It is also responsible for the students and researchers associated with the project
TU Delft students	A	Will learn about new technologies, gain valuable expertise and know-how in a vast range of engineering disciplines by virtue of their involvement in payload design & development
Launch Provider & Vehicles	A	Will actively determine the environmental conditions which need to be sustained by the payload. Will also influence the mission definition, ConOps and other operational and design considerations
Ground Station	A	Actively involved in enabling communication and control of the rover and payload via telecommands and telemetry.
Testing and research facilities	P	Their facilities and equipment will influence the verification and validation of the payload at various levels of integration
Space scientists and engineers	P	Space scientists, engineers, researchers, PhD students and subject matter experts around the world will be highly interested in the data gathered by the mission as well as results from analysis of the measured radiation
International space agencies, research institutes and the commercial space industry	P	These agencies will make use of the mission's findings and data to create better space radiation models, to make predictions and to supplement their services. Data from the mission may be used in the design of future space systems

**Table 3.2:** Stakeholders in the Lunar Zebro Science Mission

Stakeholders requirements were identified in order to inform and guide the setup and design of the Radiation Payload subsystem and its architecture. The stakeholder requirements are presented in Table 3.3. It is assumed that these stakeholder requirements will influence and guide decisions which are made for the Radiation Payload subsystem in the future, from design to testing as well as during the operational and post-mission phases.

**Table 3.3: Stakeholder Requirements**

<b>Label</b>	<b>Content</b>	<b>Capability/Char</b>	<b>Priority: Essential / Condition- al/ Optional</b>
RADPAY-SH-1.1	The payload shall have a development cost within the financial resources of SSE and Lunar Zebro	Char	E
RADPAY-SH-1.2	The payload shall be composed of COTS parts	Char	E
RADPAY-SH-1.3	The payload shall be easy to manufacture and assemble	Char	C
RADPAY-SH-1.4	The payload shall have a development timeline which fits within the timeline of the Lunar Zebro project	Char	C
RADPAY-SH-1.5	The payload shall have low power consumption lower than 1 W	Char	E
RADPAY-SH-1.6	The payload shall have size lower than 50 x 50 x 50 mm	Char	E
RADPAY-SH-1.7	The payload shall have mass lower than 100 g	Char	E
RADPAY-SH-1.8	The payload shall use a solid state detector chip to measure radiation	Char	O
RADPAY-SH-1.9	The payload shall be radiation tolerant	Char	E
RADPAY-SH-1.10	The operating temperature range of the payload shall be adequate for interplanetary missions	Cap	O
RADPAY-SH-1.11	The payload shall be able to operate in vacuum	Char	E
RADPAY-SH-1.12	The payload shall be able to operate on the Moon	Char	E
RADPAY-SH-1.13	The payload shall be able to survive the mission radiation environment	Char	E
RADPAY-SH-1.14	The payload shall be able to withstand launch loads and vibrations	Char	E
RADPAY-SH-1.15	The payload shall operate on the Lunar Zebro nano-rover	Cap	E
RADPAY-SH-1.16	The payload shall be easy to integrate into the Lunar Zebro	Char	E
RADPAY-SH-1.17	The payload shall be able to measure radiation dose rates on the moon	Cap	E
RADPAY-SH-1.18	The payload shall be able to measure radiation dose rates during various phases of a typical lunar mission	Cap	C
RADPAY-SH-1.19	The payload shall have a minimum radiation dose measurement range of 100 Gy	Cap	C
RADPAY-SH-1.20	Raw radiation sensor data shall be down-linked from the payload	Char	C
RADPAY-SH-1.21	The payload shall provide educational value to TU Delft students	Char	C

**Table 3.3 continued from previous page**

Label	Content	Capability/Char	Priority: Essential / Condition- al/ Optional
RADPAY-SH-1.22	Payload data shall enable refinement and improvement of space radiation environment models	Cap	C

### 3.1.4. System Requirements

Upon careful study of the mission definition of Lunar Zebro, the stakeholders, the mission objectives and the previous work that was done on the payload subsystem [53], a set of technical system requirements was drafted. These were intended to guide the definition and design of the Payload Subsystem. These requirements are shown in the Verification Control Matrix shown in Table 3.4, along with the proposed method of verification, requirement rationale and ID label of each requirement. The label is structured according to the convention: **RADPAY - [REQ TYPE] - [ITERATION].[REQ NUMBER]**. The requirements presented in Table 3.4 represents the first version of consistent and coherent requirements for the Radiation Payload subsystem. These can be iterated and edited in the future as the project progresses, keeping in mind appropriate requirements control practices [150]. The requirement status provided in Table 3.4 is based on the latest developments at the time of writing<sup>3</sup>.

The system requirements are divided into 6 main categories:

- Functional
- Design
- Performance
- Interface
- Reliability, Availability, Maintainability & Safety (RAMS)
- Operational

According to the ECSS standards [41, 42], the method of verification for each requirement was also determined. The verification method is chosen from among the following:

- Review of Design
- Analysis
- Inspection
- Test

<sup>3</sup>An asterisk next to the status signifies that the requirement is only partially verified and further work is required for complete verification

**Table 3.4:** Radiation Payload System Requirements

REQ type	Label	Requirement	Rationale	Verification Method (A/T/R/I)	Status (Verified/Unverified)	Comments
Functional	RADPAY-FUNC-1.1	The payload shall be able to measure ionizing radiation on the lunar surface	Science objective	R,A	V	
	RADPAY-FUNC-1.2	The payload shall be capable of making time resolved radiation measurements	capability	R	V	
	RADPAY-FUNC-1.3	The payload shall be capable of making passive radiation measurements when unpowered	capability	R	V	
	RADPAY-FUNC-1.4	The payload shall have a minimum operational life of [140] days	operational life	R	U	14 (mission duration) + transit time + margin [67] = 4 months + 12 days
Design	RADPAY-DES-1.1	The payload shall have a mass of less than [50] g	mass constraint	I	V	From Phase B doc [53]
	RADPAY-DES-1.2	The payload shall occupy no more than [50 x 50 x 9 mm] of space inside the rover	geometric constraint	R,I	V	Footprint is 42 x 42 mm spacer height is 9 mm
	RADPAY-DES-1.3	The payload shall occupy no more than [42 x 42 x 10 mm] of space outside the rover	geometric constraint	R,I	V	
	RADPAY-DES-1.4	The payload shall have a power consumption less than [300] mW	power constraint	T	V	
	RADPAY-DES-1.5	The payload shall be composed of COTS components	development philosophy	R,I	V	
	RADPAY-DES-1.6	The payload shall have a single common electrical ground	electrical design integrity	R	V	
Performance	RADPAY-PERF-1.1	The payload shall be able to measure TID up to [120] Gy	Range	A	V	Based on mission environment analysis
	RADPAY-PERF-1.2	The payload shall have a sensitivity of [5] - [70] kHz/Gy	Sensitivity	T	V	

Table 3.4 continued from previous page

REQ type	Label	Requirement	Rationale	Verification Method (A/T/R/I)	Status (Verified/Unverified)	Comments
	RADPAY-PERF-1.3	The payload shall have a dose resolution of [0.5] mGy		A,T	U	Based on mission environment analysis and historical data
	RADPAY-PERF-1.3	The payload shall have a minimum dose measurement accuracy of [20%]	Accuracy	A	U	Contemporary instruments have 15-30 % accuracy [87, 159, 32]
	RADPAY-PERF-1.4	The payload detector shall have a passive TID measurement mode	To enable measurements without power supply	I	V	To be triggered during power shortage or safe mode
	RADPAY-PERF-1.5	The payload shall be able to acquire measurements within windows ranging from [TBD-TBD] s in duration	Measurement window	I		
	RADPAY-PERF-1.6	The payload shall have an on-board data storage of [2] Mb	temporary data storage	R,A	V	1.2 Mb based on sampling rate of once per minute and max storage interval of 1 day
	RADPAY-PERF-1.7	The payload shall have multiple dose measurement sensitivity options	adjustment to varying dose rates	R	V	
	RADPAY-PERF-1.8	The payload shall have an adjustable sampling rate	adjustment to varying dose rates and link budgets	R	V	
	RADPAY-PERF-1.9	The payload's radiation sensor(s) shall be characterized before flight	detector calibration	T	U	

Table 3.4 continued from previous page

REQ type	Label	Requirement	Rationale	Verification Method (A/T/R/I)	Status (Verified/Unverified)	Comments
Interface	RADPAY-INT-1.1	The payload shall be able to communicate with the rover OBC using an RS-485 interface based data bus	rover data interface specification	R,T	V*	
	RADPAY-INT-1.2	The payload shall be able to communicate with the rover's PPU over its data bus	contingency function	R,T	V*	
	RADPAY-INT-1.3	The payload shall be able to operate on a supply voltage of 5V	supply voltage from rover	R	V	
	RADPAY-INT-1.4	The payload shall interface with the rover Motherboard using a single cable harness	cabling reduction	R	V	
	RADPAY-INT-1.5	The payload connector(s) shall be fool-proof		R,I	V	
	RADPAY-INT-1.6	The payload shall be able to be switched ON/OFF by the Motherboard		R, T	U	
	RADPAY-INT-1.7	The payload system shall be supported by a driver application running on the OBC	rover OBC S/W architecture	R	V*	
	RADPAY-INT-1.8	The payload power consumption shall be measurable		R,T	V	I-V monitor on MOM
	RADPAY-INT-1.9	The payload shall be able to send its telemetry to the rover OBC		R,T	U	
	RADPAY-INT-1.10	The payload shall have a maximum data transfer rate of [1] Mb/s over the data bus		R	V	max Motherboard transceiver data rate
RAMS	RADPAY-RAMS-1.1	The payload shall be able to withstand TID up to [200] Gy in operation		A,T	V*	Based on SPENVIS analysis; typical recommendation is 10 krad behind 2mm shielding [67]
	RADPAY-RAMS-1.2	The payload shall not include pressure vessels or pyrotechnics		R,I	V	

Table 3.4 continued from previous page

REQ type	Label	Requirement	Rationale	Verification Method (A/T/R/I)	Status (Verified/Unverified)	Comments
	RADPAY-RAMS-1.3	The payload shall be able to survive the launch loads experienced by the rover	structural loads	A, T	U	Refer to Global requirement on rover
	RADPAY-RAMS-1.4	The payload shall be able to operate in a vacuum	operational environment	A, T	V*	
	RADPAY-RAMS-1.5	The payload shall release CVCM less than [TBD]		T	U	based on global rover requirement
	RADPAY-RAMS-1.6	The payload shall have an operational temperature range of [TBD] to [TBD]		A, T	U	global rover requirement and thermal analysis TBD
	RADPAY-RAMS-1.7	The payload shall have a storage temperature range of [TBD] to [TBD]		A,T	U	to be based on launch provider recommendations
	RADPAY-RAMS-1.8	The payload shall be protected against latch-ups	radiation tolerance & protection	R,T	V*	Latchup protection on rover Motherboard
	RADPAY-RAMS-1.9	The payload firmware shall be fault tolerant		R,T	U	
	RADPAY-RAMS-1.10	The payload shall be resistant to SEUs		R,T	U	
	RADPAY-RAMS-1.11	The payload shall have redundancy in radiation measurement		R, T	V	
	RADPAY-RAMS-1.12	The payload shall be protected against direct exposure from lunar dust	Lunar dust is electrostatically charged and can cause electrical issues	R, T	U	

Table 3.4 continued from previous page

REQ type	Label	Requirement	Rationale	Verification Method (A/T/R/I)	Status (Verified/Unverified)	Comments
Operational	RADPAY-OP-1.1	The payload telemetry shall include data about measured radiation and temperature		R,I	V*	
	RADPAY-OP-1.2	Radiation sensor data shall undergo minimal processing before being downlinked	necessity of raw data	R	U	
	RADPAY-OP-1.3	Payload data shall be periodically backed up onboard the rover's data storage		R	U	
	RADPAY-OP-1.4	The payload shall be able to conduct measurements independent of the rover's location in space		R	V	

### 3.1.5. Functional Breakdown

The formation of high level system requirements and objectives leads to the definition of the functionality that the Radiation Payload subsystem needs to possess. Hence, the functions that need to be performed by the payload were identified explicitly such that the objective of the payload can be broken down into smaller, more manageable functions that can be translated to engineering problems / work packages and solved in a systematic manner. This is captured in the form of a high level functional breakdown (FBD), as seen in Figure 3.2.

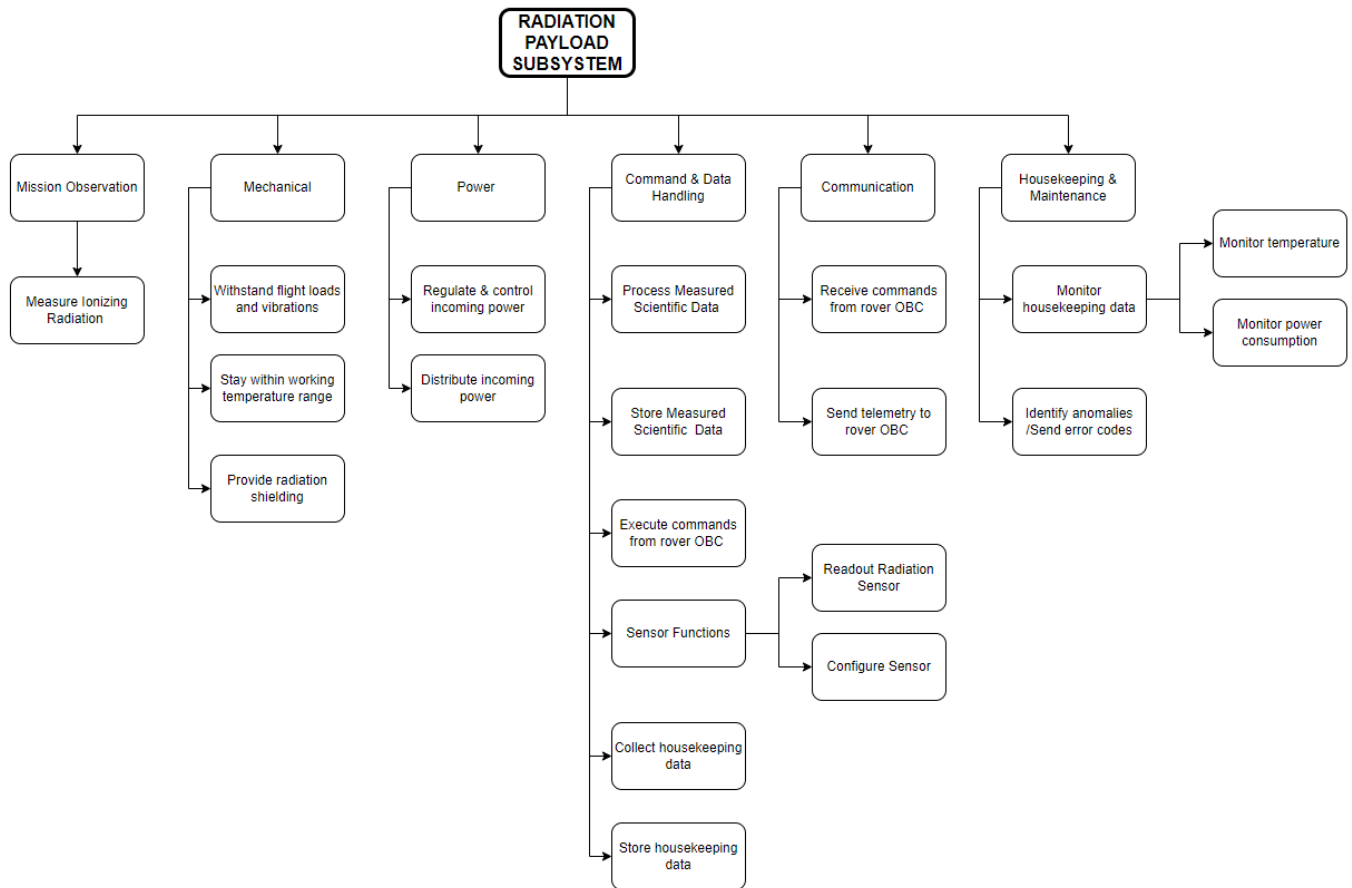


Figure 3.2: Radiation Payload Functional Breakdown

The FBD has six main branches into which the functions are divided <sup>4</sup>:

- **A:** Mission Observation / Science
- **B:** Mechanical
- **C:** Electrical
- **D:** Command & Data Handling
- **E:** Communication
- **F:** Housekeeping & Maintenance

While the functions are intended to be mutually exclusive individually and exhaustive collectively, this is an ideal notion and some deviations from this can be observed in the FBD.

### 3.1.6. Functional Flow

A functional flow diagram (FFD), which is shown in Figure 3.3, was created to visualize the operation of various functions of the payload and to see the flow of physical quantities through the payload subsystem and across its interfaces with the rover and finally to the ground segment.

<sup>4</sup>the functions are numbered according to the branch and the order in which they appear in the FBD from top to bottom. Eg: 'Readout Radiation Sensor' will be identified as Function D.4.1

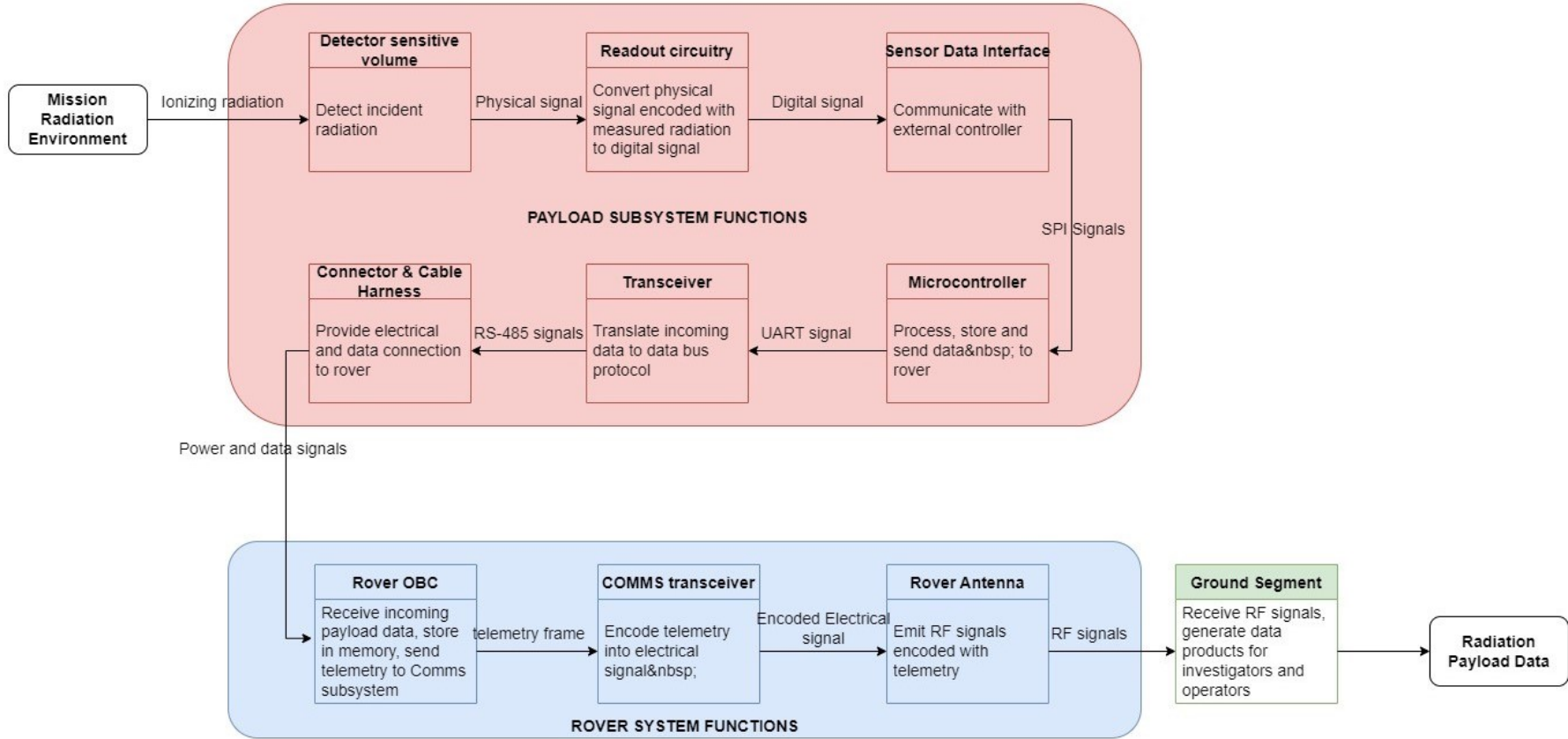
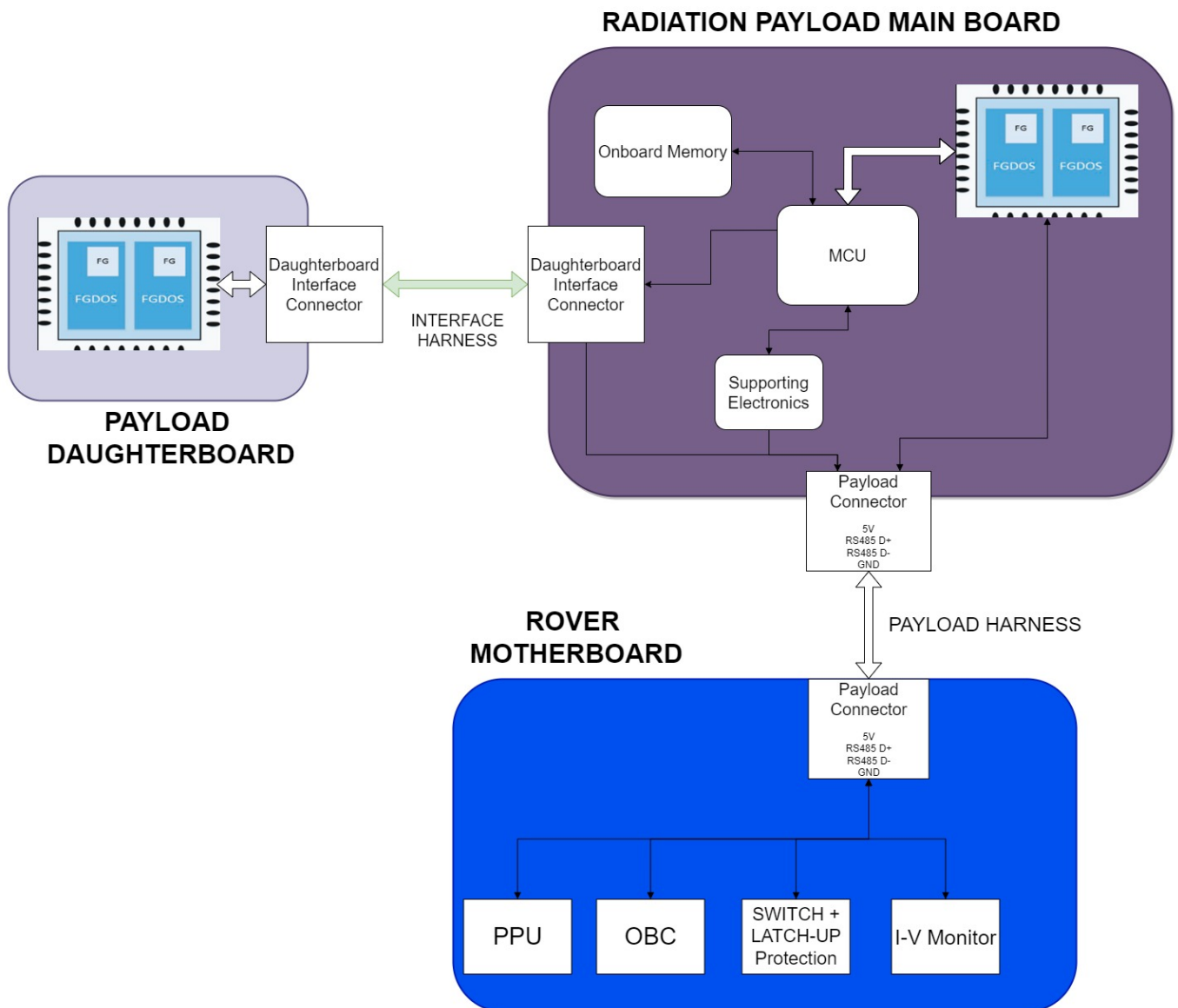


Figure 3.3: Radiation Payload Functional Flow Diagram

From top left to bottom right, the diagram shows how incident ionizing radiation is detected, measured, encoded, recorded and communicated by the constituents of the payload subsystem and the rover. On passing through the ground segment, the final product of importance is the payload data received by the scientific investigators and the operations team. It also shows the functional boundary (red box) and interface of the subsystem with the rover (blue) and the ground segment (green).

### 3.1.7. Payload Subsystem Architecture

A high level system architecture for the Radiation Payload was developed, taking the existing system architecture of the Lunar Zebro rover into consideration. This architecture is visually represented in the form of a block diagram in Figure 3.4.



**Figure 3.4:** Radiation Payload System Architecture

In the literature study conducted in preparation for this thesis (chapter 2), it was concluded that the Floating gate MOSFET based radiation sensor developed by Sealcon (formerly ic-Malaga) - FGDOS, can be realistically implemented within the constraints of a nano-rover platform, while offering a desirable combination of characteristics when compared with similar miniaturized radiation detectors [122]. Hence, the FGDOS System on a Chip (SoC) [117] was chosen as the core detector of the Radiation Payload and the rest of the system architecture was built up around it, whilst keeping the constraints and interfaces with the nano-rover in consideration.

It was previously proposed that another identical radiation sensing module could be flown outside the rover chassis in order to extend the scientific return of the Radiation Payload [53]. In the current system architecture, this idea was developed further and materialized into what is called the '*Radiation Payload Daughterboard*'. This is envisioned as an auxiliary circuit board to be mounted outside the chassis of the rover, such that it experiences comparatively lower radiation shielding compared to the main unit of the Radiation Payload which will be housed within the rover. This main unit is referred to as the - '*Radiation Payload MAIN*'. Hence, the Radiation Payload would be physically distributed into two parts - a Main Board housed within the rover, mounted in a stack of PCBs, as well as a Daughterboard that would be mounted external to the chassis, providing an extra set of measurements that reflect (mostly) unshielded exposure to ionizing radiation.

### 3.1.8. Interfaces

The Radiation Payload has interfaces within the subsystem between various functions/components as well as external interfaces with the rover. It was important to define these interfaces early in the design process in order to simplify implementation, integration and testing down the line.

The interfaces within the boundaries of the payload subsystem are shown in the form of an N2 chart in Table 3.5. The interfaces of the payload subsystem with the rover are captured by N2 chart in Table 3.6. This is meant to contextualize the interfaces of the Radiation Payload w.r.t the other subsystems in the rover and not as an exhaustive summary of all interfaces of the rover system. Hence, only payload relevant interfaces have been captured in Table 3.6. This chart represents the interfaces within the space segment of the Lunar Zebro mission. Inputs to a given unit are arranged in the vertical direction and its outputs are arranged in the horizontal direction.

Within the payload subsystem, the microcontroller unit (MCU) controls the radiation detector and receives data from it over SPI signals that are translated between 3V and 5V by the use of level shifters. The payload data can be stored in the onboard memory and/or transmitted to the rover's Command and Data Handling Subsystem (CDHS) through an RS485 transceiver and via the payload to motherboard connector physically. This connector also supplies a regulated 5V supply, which is converted to 3V by a voltage regulator according to the demands of some constituent elements of the payload. An external watchdog can reset the MCU if it fails to send a regular "heartbeat signal" to the watchdog, in case of a fault or an error.

From a holistic viewpoint, the Radiation Payload has interfaces with various rover subsystems such as the CDHS, Electrical Power Subsystem (EPS), Communications Subsystem (COMMS), Power Processing Unit (PPU) and Structural Subsystem (STR). The structure of the rover will transmit heat and mechanical loads to the payload boards. The electrical power subsystem provides the payload with a regulated 5V supply as well as a GND return path and the power consumption is measured by the PPU. The payload data will be sent to the CDHS of the rover, whereby it will be included in the telemetry packet of the rover and downlinked to the ground segment via the COMMS subsystem. In a symmetric manner, commands received from the ground will be received by COMMS and relayed to the payload via the CDHS. Additionally, estimates of the approximate location of the rover on the Moon, provided by the rover navigation subsystem, can be used during payload data analysis to add a spatial component to radiation dose data. This is not a strict interface as such.

**Table 3.5:** N2 Chart: Payload subsystem internal interfaces

<b>Radiation Sensor</b>	5V SPI signals – sensor data & config						
5V SPI signals – readout requests and sensor registers	<b>Level Shifter</b>	3V SPI signals - readout requests and sensor registers					
	3V SPI signals - sensor data & config	<b>MCU</b>	Payload Data	Payload Telemetry and data - UART	Heartbeat pulse		
		Payload Data for transfer to Rover CDHS	<b>Memory</b>				
		Commands and data from Rover - UART		<b>Transceiver</b>			Payload Telemetry and data - RS485
		Reset Signal			<b>Watchdog</b>		
	Regulated 3V supply – for reference	Regulated 3V supply	Regulated 3V supply	Regulated 3V supply		<b>Voltage Regulator</b>	
5V supply from Rover	5V supply from Rover – for reference			Commands and data from Rover - RS485	5V supply from Rover	5V supply from Rover	<b>Supply Connector</b>

**Table 3.6:** N2 Interface chart: Payload and rover subsystems

<b>Locomotion</b>							
	<b>Navigation</b>		Rover location on the Moon				
		<b>Structure</b>	Structural & Thermal loads, shielding				
			<b>Radiation Payload</b>	Payload data			
			Payload commands	<b>CDHS</b>			Payload telemetry
			Power monitoring & cycling	Payload power consumption data	<b>PPU</b>		
			Regulated 5V supply			<b>EPS</b>	
				Payload telecommands from operator			<b>COMMS</b>

### 3.1.9. Technical Budgets

As a part of the Payload development efforts, it was important to establish and track the technical budgets. While various iterations of the payload need to be within constraints specified by system requirements at the time of completion, it is also useful to track the trends seen in various budget related quantities and resources during the development process itself. This would help steer the design process such that over-consumption of resources or violation of constraints could be predicted in advance and be prevented thereafter. In addition to the constraints, a sufficient margin of about 20% was applied for the power, mass and data budget to allow for uncertainties in estimation and to allow sufficient room for changes in the future. The non-technical i.e. the financial budget and expenditure on the Radiation Payload was also tracked and can be found in Appendix D.

After completion of the first version (V1) of the Radiation Payload design and upon preliminary functional testing, it was found that the design satisfied the aforementioned constraints and that the technical budgets could be closed.

#### Mass Budget

The constraint on the total mass of the Radiation Payload was specified to be 50 g [53].

#	Component	Qty	Nominal mass (in g)	Worst Case Mass (in g)	Comments
1	Main PCB	1	10	10	With components soldered on
2	Payload MAIN Cable harness	1	2	5	Including connectors
3	Daughterboard PCB	1	5	10	With components soldered on
4	Daughterboard Interface Cable Harness	1	5	10	Estimated
	Total			35	
	Margin (20%)			7	Margin for miscellaneous components such as fasteners, seals, spacers, connectors
	<b>TOTAL</b>			<b>42g</b>	margin included

**Table 3.7:** Radiation Payload Mass Budget

As evidenced by Table 3.7, the version 1 design of the Radiation Payload lies within the specified mass constraints, with ample margin included.

#### Power Budget

The limit for the total power consumption of the Payload was set at 300 mW by the Lunar Zebro team [68]. Table 3.8 shows the current power budget for V1 of the Radiation Payload.

#	Component	Qty	Supply Voltage	Current consumption	Nominal power per unit (mW)	Total nominal power	Max. Power (worst case)	Total worst case power (mW)	Comments
1	MCU: MSP430	1	3V	2mA @ 16MHz			6	6	Depends on clock speed High sensitivity mode consumption per sensor [117]
2	FGDOS sensor module : FGD-03F	1	5V	4mA	20 mW	40	30	60	
3	RS485 transceiver: MAX3078EESA+T	1	3V	1.5mA	4.5	9			4Mb FRAM
4	On board memory : CY15B104QN-50SXI	1	3V	2.6mA	7.8	7.8			
5	Level shifter: MAX3001EEUP+	2	5V/3V	50 uA	0.25	0.5			
6	Low dropout regulator: LP2981-30DBVR	1	5V	600 uA quiescent current	3	3			
8	External Watchdog TPS3813I50DBVT	1	5V	9 uA	0.045	0.045			Only the FGDOS will have a noticeable power consumption
9	Daughterboard FGDOS module	1	5V			40			
	Margin (20%)					21.27			
	<b>TOTAL</b>					<b>127.62 mW</b>			

**Table 3.8:** Radiation Payload Power Budget

Hence, based on the current estimates, the Radiation Payload will comfortably operate within the power constraints posed by the rover.

### Data Budget

The Lunar Zebro rover uses RS485 half-duplex connections for the data bus which can transfer data at speeds up to 1 Mbps. The rover's data bus has 5 different branches which connect each subsystem to the OBC or the PPU, or both. The data rate limitation is imposed by the RS485 (to UART) transceivers used on the rover side, to translate the inverting and non-inverting signals to UART.

Table 3.9 shows the amount of data generated in comparison with the amount of memory storage available for use by the Radiation Payload.

Memory location	Memory Type	Available Memory	Comments
Payload MCU	FRAM	64 KB	Unified Memory = Program + Data + Storage Error Correction Coding (ECC)
Payload MCU	SRAM	2 KB	Miscellaneous storage
Payload Onboard memory	FRAM	4Mb	Temporary storage of payload data
Rover	SD Cards	TBC	Amount of space allocated to Payload TBD
Rover	FRAM	TBC	Amount of space allocated to Payload TBD
Rover	OBC storage	TBC	Amount of space allocated to Payload TBD

**Table 3.9:** Radiation Payload data storage

Table 3.10 delineates the amount of data generated by the payload based on the size of payload telemetry and sampling rate, with respect to the available bandwidth on the data bus of the rover. The amount of data is based on the telemetry list presented in Table B.1 A higher margin is used in this case to allow for the overhead in various message protocols, which may be used for communication between the rover's subsystems. The sampling rate has been assumed to be very high in order to get a conservative estimate of the required data rate.

Description	Data Type	Nominal Sampling Rate	Word size (bits)	Required data rate (bps)	Comments
FGDOS Data	Radiation + sensor data	1/60 Hz	576	9.6	18 bytes of data per FG DOS sensor; sampling rate TBD
Payload general data	Payload status and health	Idem	56	0.93	Includes Housekeeping data
Payload onboard memory dump	Temporarily stored collection of full telemetry	TBD	TBD	TBD	
	Total Margin (~20%)		632	~11	
	<b>TOTAL</b>		<b>128</b> <b>760</b>	<b>2</b> <b>13</b>	

**Table 3.10:** Radiation Payload data budget

It should be noted that the data budget presented here does not take the overhead in the message protocol for communication on the rover's data bus into account.

### Financial Budget

A preliminary financial budget was drafted for the design and development of the Radiation Payload and can be found under Appendix D.

### 3.1.10. Risk Evaluation & Management

A qualitative risk assessment was performed to ensure that the Radiation Payload is developed to the desired performance and functionality while staying within schedule, cost and technical constraints. Numerous risks were identified and then categorized into the following types:

1. Technical Risk - type A
2. Schedule Risk - type B
3. Cost Risk - type C
4. Safety Risk - type D

These risks are listed in Table D.1. For each identified risk, potential causes and potential consequences were identified in conjunction. The estimated probability of occurrence of each risk and its severity is determined to make a simple estimate of the criticality of the risk according to Equation 3.1. The probability and severity were judged qualitatively based on the guidelines provided in [76].

$$\text{Risk Magnitude} = \text{Probability of Occurrence} \times \text{Severity} \quad (3.1)$$

According to the calculated magnitude, each risk is tabulated into the Risk Matrix shown in Figure D.3. This allows for visual interpretation of the magnitude of each risk along the dimensions of probability of occurrence (along vertical axis) and severity (along horizontal axis).

	NEGLIGIBLE	MINOR	MODERATE	SIGNIFICANT	SEVERE
VERY LIKELY			C-1	A-13, B-1	
LIKELY			A-4, A-5, A-6, B-5		
POSSIBLE			A-2, A-8	A-1, A-10, A-15	A-17, A-18, B-6, C-2
UNLIKELY		A-9, A-14, D-1, D-2	A-3, A-11, A-12	A-16, A-20, B-2, B-3, C-3	A-7, A-19, B-4
VERY UNLIKELY					

Figure 3.5: Risk Matrix

For each catalogued risk, a mitigation measure is identified and briefly described in Table D.1. The risk mitigation measures can be grouped into one or more of the strategies listed below [76].

1. Risk Removal
2. Risk Reduction
3. Risk Acceptance
4. Risk Transfer

Of the risks listed in the risk register and matrix, the highest priority risks, that require further monitoring and special consideration, are listed below:

1. **A13**: The Daughterboard goes out of operating temperature range of the FGDOS and other electronics
2. **B1**: Electronic components are unavailable during production
3. **A17**: Poor connections on PCBs
4. **A18**: Payload connector gets detached from the PCB in flight
5. **B6**: The payload Development Model (DM) is not produced in time to be assembled into Belka 2 i.e. the second Engineering Model of LZ

Since risk management is a continuous and recurring process over the life cycle of a space mission, the risks identified and evaluated in this section should be reevaluated and monitored in the future as the project progresses, until launch, and also through the actual mission. As such, more risks which are relevant to operations may be identified and added to the current risk register in Table D.1. The Mission risk and implementation risks have not been separated at present. However these may be segregated in the future if it is determined that risk management activities are made easier by such bifurcation.

### 3.1.11. Work Breakdown Structure

A Work Breakdown Structure (WBS) was prepared to organize the systems engineering process as well as the design, research and development activities covered in this thesis. The WBS is shown in Figure 3.6.

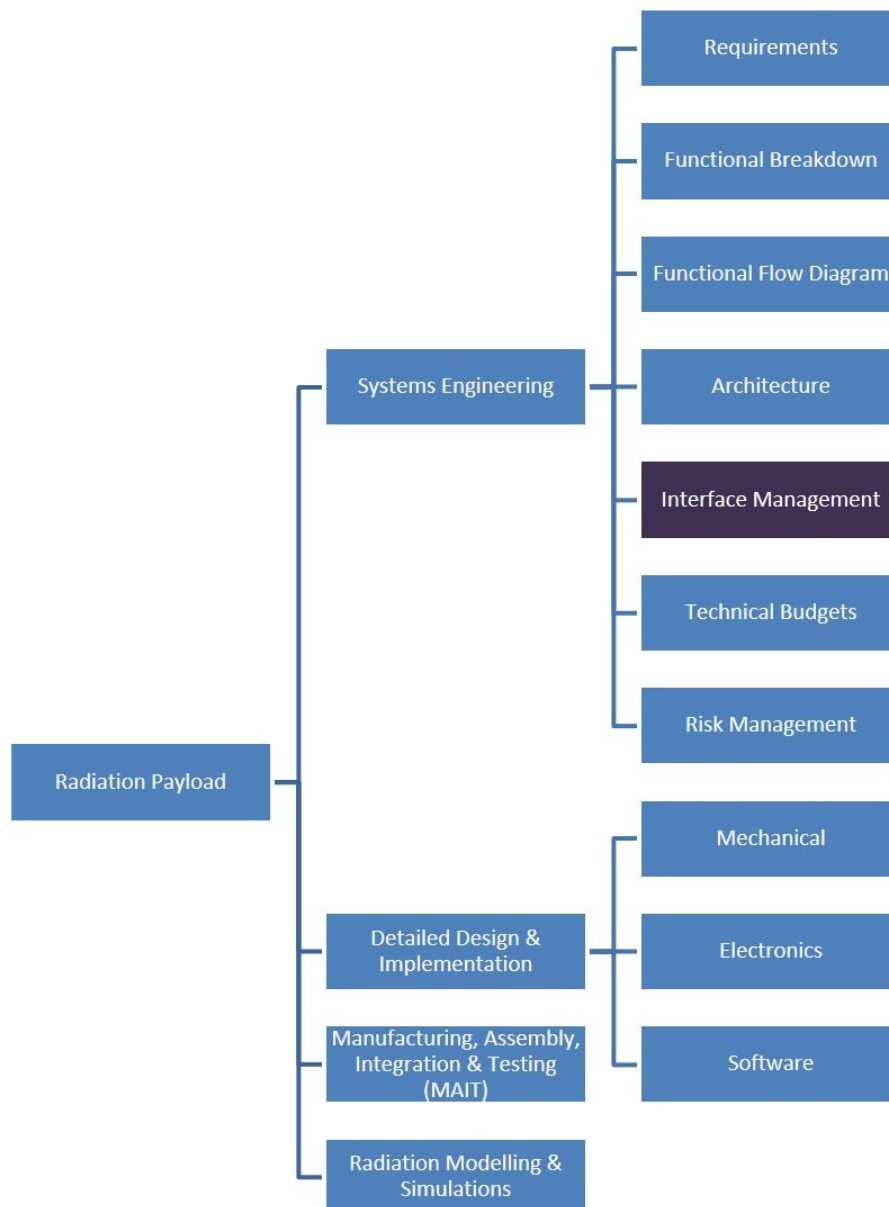


**Figure 3.6:** Radiation Payload Work Breakdown Structure. Blocks indicated in violet involve close collaboration with the Lunar Zebro team

The work packages concerning the detailed design and implementation are further decomposed as shown in Figure D.1. The work packages involving MAIT activities are broken down as shown in Figure D.2. The breakdown for modelling and simulations has been presented in chapter 4.

## 3.2. Detailed Design & Implementation

Having stepped through the early decomposition phase of the V-Model, the detailed design and implementation of the Radiation Payload, along facets of mechanical, electronics and software engineering are covered in this section.

### 3.2.1. Design Philosophy & Considerations

Before stepping into the detailed design and implementation of the Radiation Payload, it is important to understand the design philosophy and various considerations which guided this process. These principles are based on the general design principles of Lunar Zebro, on some NewSpace trends [50] and common best practices which are seen in the development of miniaturized, low cost space systems such as CubeSats [145, 131]. As such, the following principles were followed:

1. The number of system requirements should be minimized and the requirements themselves should

be refined to make them specific, measurable, achievable, realistic and traceable (SMART)<sup>5</sup>.

2. The Radiation Payload is to be composed almost entirely of COTS components. This principle was cemented in the form of a system requirement (RADPAY-DES-1.5) and is in accordance with the design of other subsystems on the LZ rover [68].
3. The payload design should be focused on the functioning of the FGDOS detector, since it is directly involved in making scientific observations.
4. The payload should be as independent and self-sufficient as possible in terms of its operations. It should only rely on other rover subsystems for provision of power and sending payload data to the ground segment while the rover is operating nominally. This would ensure that the Payload can keep functioning as long as it receives power from the rover. In case problems occur with the rover's OBC or PPU, radiation data can still be collected whilst the Ground segment engineers or rover software troubleshoot these issues and payload operations will only be disrupted minimally.
5. The design of the payload should enable maximum utilization for scientific observations and hence the design should prioritize scientific return.
6. The number of parts and components required for the payload should be minimized. The number of cable harnesses, specialized mounting fixtures and fittings should also be minimized. The parts used should be interchangeable and foolproof, if possible.
7. Within bounds of usefulness, the Payload should share as many component types as possible with other subsystems on the rover. This would ensure interchangeability of components in the event of supply chain issues and shortages. Moreover, it would also ensure an abundance of functional and radiation testing data for the shared components for purposes of radiation effects assessment and hardness assurance. Lastly, the use of components on the payload which are used elsewhere on the rover would simplify the design process and minimize the amount of effort required to include the concerned components into the payload subsystem. Expertise and knowledge of the concerned components would also be available in the LZ team, reinforcing this goal.

### 3.2.2. Mechanical Design

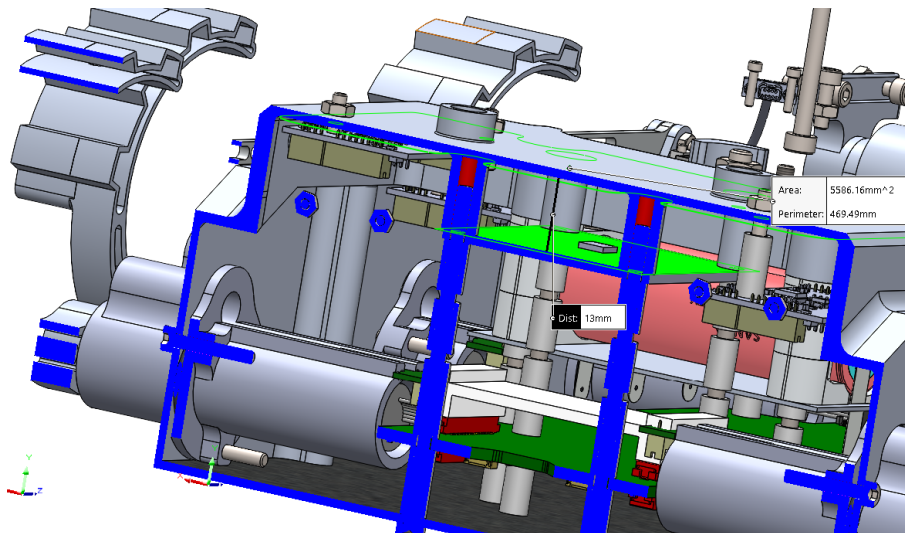


**Figure 3.7:** Placeholder Payload PCB position inside the rover chassis (highlighted in green)- front section view

Based on the system architecture, previous work and constraints posed by the rover platform, it became apparent that the most suitable morphology and physical setup for the Radiation Payload is in the form of one or more Printed Circuit Boards (PCBs). It was previously decided that the Radiation Payload would consist of one PCB housed within the rover and stacked near the front of the rover, as shown in the front section view of the rover's CAD model in Figure 3.7. The stacking is dependent on the mechanical interface provided by the rover. To ease assembly, the interface was set up such that the stack would consist of multiple PCBs with four M3 bolts going through the corners of each board in a square pattern. These bolts

<sup>5</sup>[https://en.wikipedia.org/wiki/SMART\\_criteria#cite\\_note-Doran-1981-1](https://en.wikipedia.org/wiki/SMART_criteria#cite_note-Doran-1981-1)

are secured at the other end by virtue of being threaded into four columns in the rover chassis that contain internal M3 threads. The position of the Radiation Payload PCB is the top most in this stack, while the other PCBs belong to the COMMS subsystem. These PCBs are not displayed in Figure 3.7.

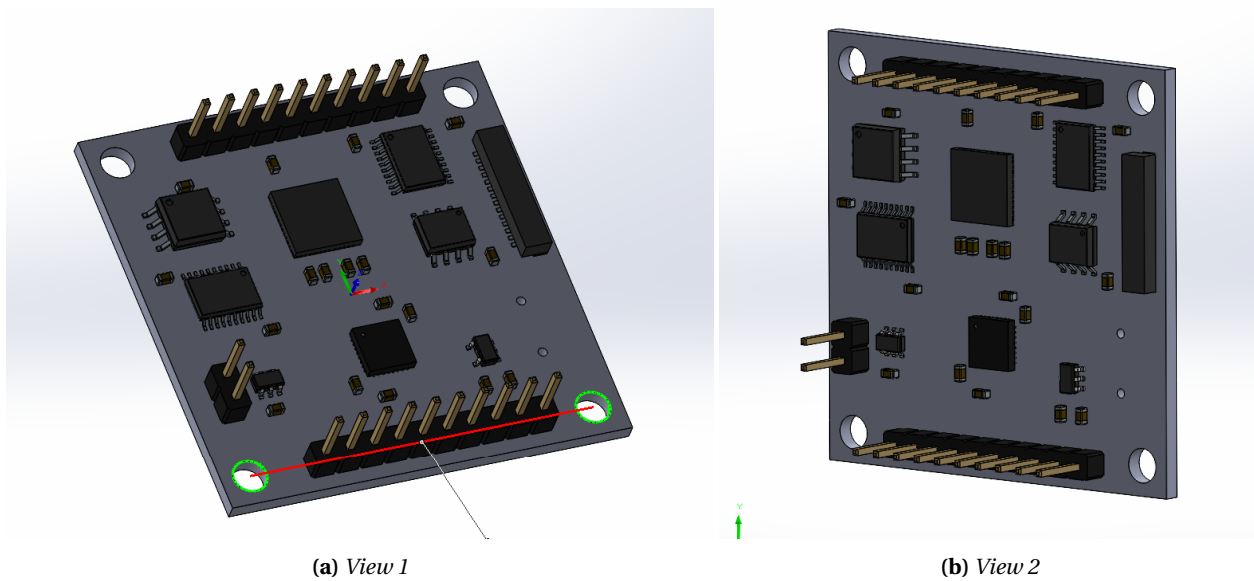


**Figure 3.8:** CAD model of Radiation Payload MAIN Board (without DF13 connector)

It was decided not to have a dedicated casing or housing for the Radiation Payload, due to two main factors:

- A housing would occupy extra space in the PCB stack, thus violating the geometrical constraints posed by the rover. Even in the event that an extremely compact housing could be produced, it would shrink the clearance between the Radiation Payload and the other rover subsystems to an imprudently low amount. As seen in Figure 3.9, the interior of the rover is already compact and crowded with other subsystems. This would complicate geometrical design iterations and modifications in the future.

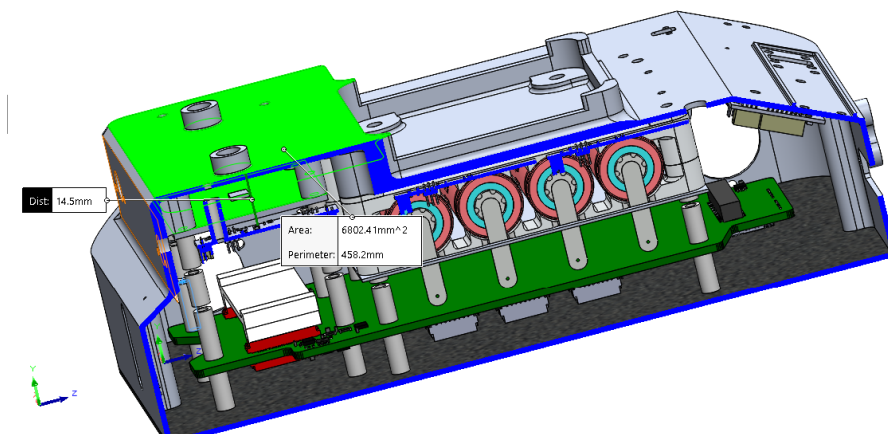


**Figure 3.9:** Placeholder Payload PCB position inside the rover chassis (highlighted in green) - side section view

- A housing would add more radiation shielding, thereby attenuating the incoming ionizing radiation particles and leading to the generation of secondary particles. In flight configuration, this would add to the shielding that would already be provided by the chassis of the rover and its other subsystems. Therefore, to simplify detection of radiation and modelling of the payload response (see section 4.3), it is advisable to omit any additional barriers or shields surrounding the Radiation Payload.

In addition to this MAIN Payload PCB which is housed within the chassis of the rover, the Daughterboard PCB would be mounted outside the chassis, underneath the deployable Solar Panel Plate (SPP) of the rover. A visualization of the CAD model of the Daughterboard can be seen in Figure 3.10b, mounted to a custom

fixture. The Daughterboard needs to be protected from exposure to lunar dust, which can cause electrostatic discharge or other issues on for electronics [148]. In the absence of an enclosure, it is desirable to achieve this protection with the use of conformal coating and/or potting on the Daughterboard. These measures can also be applied for the chassis housed Main Board, but it is expected that the rover chassis will protect all internal components against lunar dust particles. All orifices in the body of the rover have been designed with sealing and imperviousness to lunar dust in mind [68].

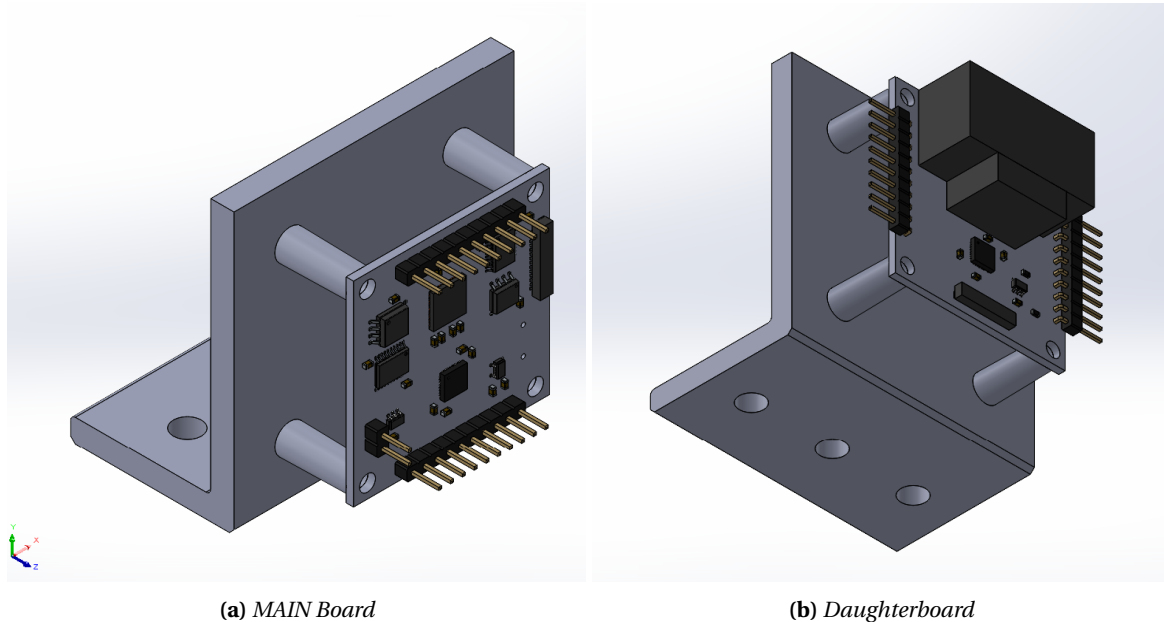


**Figure 3.10:** CAD model of Radiation Payload prototype boards mounted on custom fixtures

The Daughterboard PCB is to be bolted to the SPP using 2-4 metric fasteners. While this interface has not been implemented in the Belka-2 model of Lunar Zebro, it will be incorporated into the next iteration of the rover. The nature of this interface mainly depends on the expected thermal conditions on the Daughterboard. For instance, if the Daughterboard is expected to get extremely hot or cold in comparison to the SPP, a mechanical interface with appreciable thermal conductivity might help restore the temperature of the board to desirable values. These thermal considerations will be discussed further in Figure 3.2.2.

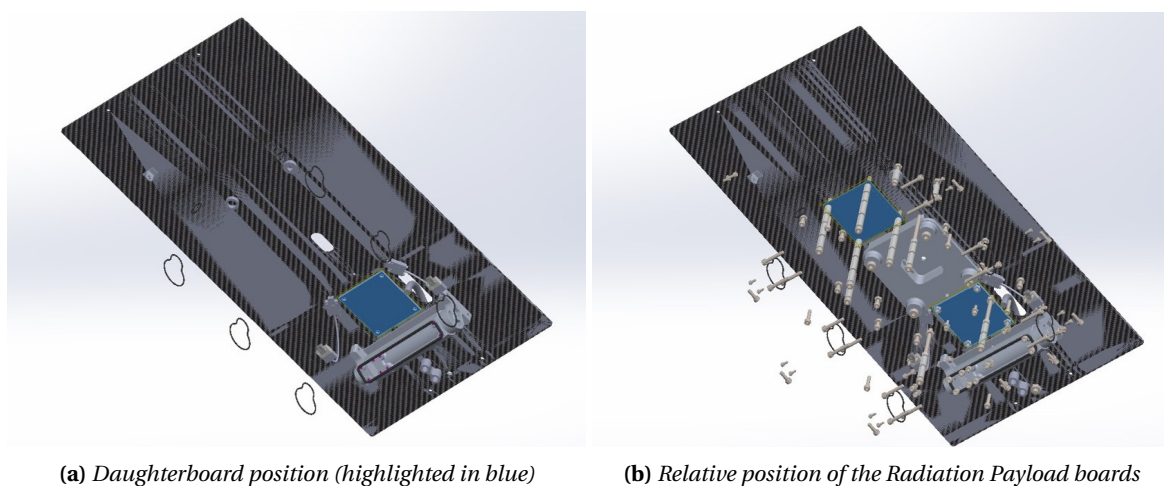


**Figure 3.11:** Placeholder Daughterboard position under SPP

### Thermal Considerations

Given the nature of the Lunar Zebro mission, one of the challenges that the rover and its subsystems face is the extreme thermal environment. This factor is strongest at the lunar surface itself, where temperatures can drop as low as 95 K in the lunar night and rise as high as 400 K in the Sun [152].

The Radiation Payload will be housed within the rover, which in turn will be housed within the lander during the mission phases - Earth orbit, Transit, Lunar orbit and Landing. The thermal environment for these phases can be derived from information provided by the "Payload User Guide" of a representative lander/launch provider to the Moon. Astrobotic's payload user guide specifies the most extreme range of expected temperatures to be about  $-120\text{ }^{\circ}\text{C}$  to  $100\text{ }^{\circ}\text{C}$  in lunar orbit and  $-30\text{ }^{\circ}\text{C}$  to  $80\text{ }^{\circ}\text{C}$  on the lunar surface [8]. Similarly, the payload temperature ranges for CubeRover, a miniaturized rover platform are stated to be  $-20\text{ }^{\circ}\text{C}$  to  $60\text{ }^{\circ}\text{C}$  [7]. It must be noted that these values are not necessarily the temperatures that the Radiation Payload would reach, given the complicated web of thermal interfaces and links existing within a compact spacecraft such as the LZ rover.

The creation and execution of a detailed thermal model of the rover lies outside the scope of this thesis, but a preliminary analysis of the current design and configuration was performed to identify potential thermal risks. Detailed thermal modelling of the rover is being performed by the LZ team and will be used to draw inferences about thermal conditions, and susceptibility of the Radiation Payload to these conditions [17]. The lunar surface operations phase is the most interesting from a thermal perspective, since the rover will be housed within the lander before deployment. This phase can be split into two parts, lunar day and lunar night. Since the rover is currently not expected to survive lunar night, it is assumed that the mission will most likely be concluded once the rover goes into hibernation at the onset of lunar night.

The payload Main Board and Daughterboard will experience different thermal conditions since the Daughterboard is to be mounted outside the chassis of the rover, implying that it will be exposed to space directly. However, since the mounting location is chosen to be underneath the deployable solar panel, direct exposure to the Sun will be avoided, serving as a moderating influence on the local thermal environment for this board. To uncover the exact thermal environment that will be experienced by the Radiation Payload during the lunar mission, it was decided to have the Payload subsystem operate and actively send telemetry during thermal vacuum tests of the Belka 2 rover (see subsection 5.7.3). Additionally, the temperatures measured by the payload's FGDOS chips will be tallied against the temperatures measured by external temperature probes placed on and in the vicinity of the Radiation Payload MAIN and Daughterboard modules.

Thermal constraints on the Payload's operations are primarily imposed by the operating temperature ranges of the various electronic chips used on the PCBs. From the perspective of the science mission objectives, the most important of these chips is the FGDOS itself, followed by the MCU. A simplified single node analysis for an FGDOS chip exposed to vacuum in LEO has been provided in [90].

#	Component	Operating temperature range (deg C)	Max allowable temperature range (deg C)	Source
1	PCB - FR4	NA	-50 – 150	Glass transition temperature for IS400
2	FGDOS	-40 – 85	-40 – 150	FGD-03F Datasheet [117]
3	MCU	-40 – 85	-40 – 125	MSP430FR5969 Datasheet [141]

**Table 3.11:** Thermal constraints for the Radiation Payload

From Table 3.11, it is clear that the microcontroller is the limiting factor that determines the allowable temperature range which the payload can survive. Given that the operating temperature range is lower, it may be prudent to turn off the payload or to use effective thermal control methods at (rover) system level to sustain peak heating periods.

At first glance, it may appear that more pronounced thermal extremes would be experienced by the FGDOS mounted on the Daughterboard PCB, albeit this needs to be verified by reliable thermal test data as mentioned previously. Preliminary thermal multi-node analysis by the LZ team has shown that the internal payload board i.e. the MAIN Board may attain higher temperature values than the Daughterboard due to power dissipation of the rover's subsystems inside its tightly packed hull. It was revealed that the relative temperature of the internal and external payload boards would be influenced by the incidence angle of solar flux as well as the strength of conductive coupling between the rover's C-shaped legs with the lunar surface. Since the rover's solar panel is deployable, this would imply a change in Daughterboard temperature based

on the deployment angle of the panel. As expected, increased power dissipation of rover electronics is expected to cause elevated temperatures on both payload boards, as shown in Figure 3.12.

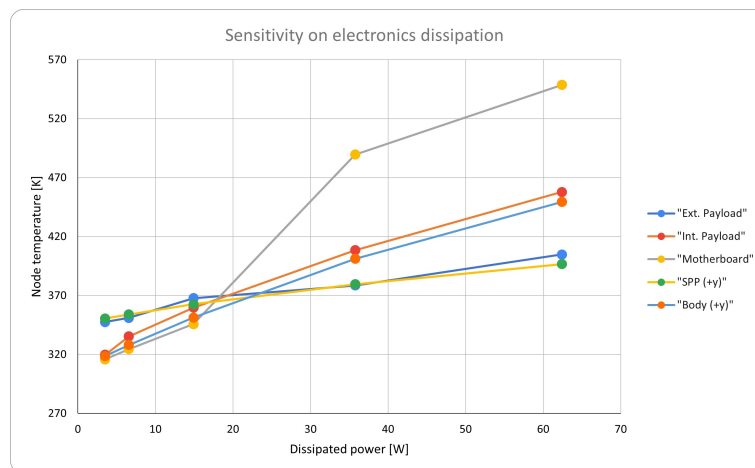


**Figure 3.12:** Temperature dependence of LZ rover on internal dissipation [17]

It should be noted that the temperature values expressed in this plot are only indicative in nature, given the myriad of assumptions that the model rests on. For instance, radiative coupling between various modules inside the rover was neglected. It is envisioned that a detailed geometric thermal model of the rover (using commercial tools) will be constructed to overcome these limitations. In summary, it is considered vital that an assembled model of the LZ rover (such as a structural thermal model (STM)) is tested under representative thermal conditions to derive the expected thermal environment(s) for various subsystems, including the Radiation Payload. This is discussed further in subsection 5.7.3.

### 3.2.3. Electronic Design

The system architecture and functional breakdown of the Radiation Payload were analyzed to identify which functions need to be performed by payload electronics. Thereafter, the type of electronic components which can perform these functions were identified. An electronic block diagram was realized to convey the interfacing and relationships among these components, as shown in Figure 3.13. The block diagram also shows how these components come together to form most of the functional hardware of the Radiation Payload.

From right to left in Figure 3.13, the main inputs from the rover to the Payload subsystem are the power bus and data bus connections. The power is supplied over a regulated 5V line. This is included in a 4 wire connection which is completed by the non-inverting and inverting inputs of the half-duplex RS-485 bus, which acts as one of the branches of the rover's data bus<sup>6</sup>. The power bus and data bus connections are physically supplied over a single cable harness from the rover to the Payload subsystem. This represents the electrical interface between the rover and the Payload.

Within the payload subsystem, 3V regulated voltage is supplied to the relevant components by the LDO which converts the 5V supply to a regulated 3V output. The 5V supply received from the rover is provided directly to the components which require a 5V VCC connection. A microcontroller and the FGDOS lie at the core of the system, with the microcontroller acting as the main control and processing hub for payload operations and communication. Since the FGDOS operates on a 5V logic level while most other payload electronic components work on a 3V/3.3V level, logic level shifters are included to facilitate bi-directional conversion of 5V logic signals to 3V. To enable data transfer between the payload subsystem's microcontroller and the data bus from the rover, an RS485 transceiver is included on the payload. A non-volatile memory module is included to serve as temporary storage for payload data and an external watchdog provides additional means to recover the payload from faults and failures. Lastly, a power and data interface connection is provided for the external 'Daughterboard' to be connected and read out from the MAIN board.

<sup>6</sup>The rover's RS-485 based data bus has five branches which enable communication between the subsystems, the OBC and the PPU. A more detailed description can be found in [68]

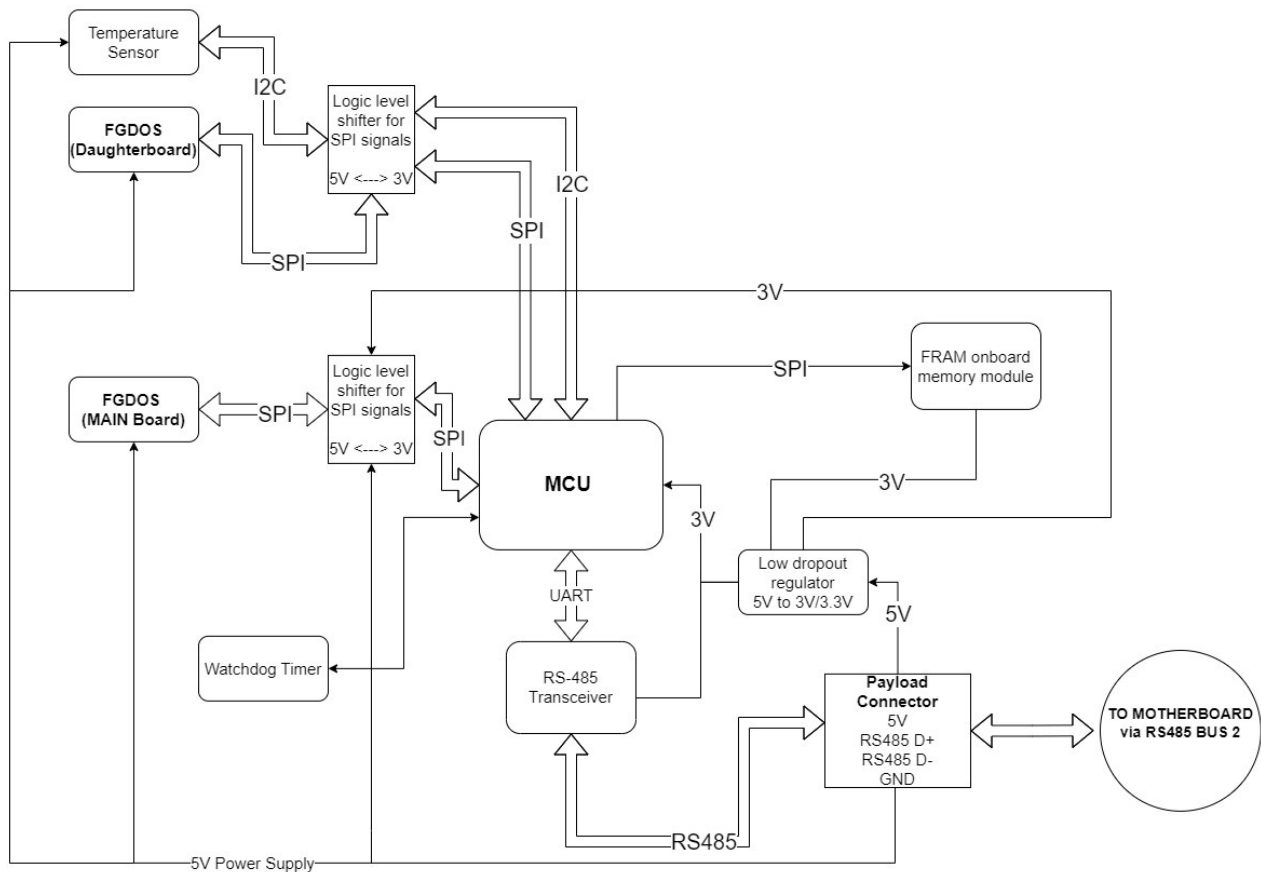


Figure 3.13: Radiation Payload Electronics Block Diagram V1

Additional choices and considerations which went into the electronic design are delineated as follows:

1. The FG DOS SoC was positioned squarely in the middle of the Radiation Payload PCB with respect to the plane of symmetry of the rover. This was done so that the amount of direction specific shielding received by the sensor (due to the chassis of the rover) would be approximately similar in the left and right halves as seen from the plane of symmetry of the rover, thereby implying that exposure to secondary radiation particles generated from the chassis may not be skewed too heavily in one direction or another. This would also simplify radiation transport simulations and shielding analysis for the sensor as well as the Radiation Payload. It is to be noted that this reasoning would be true over a statistically significant number of secondary particle impacts. The choice was made qualitatively and not verified by transport simulations or sector shielding analysis of the detailed CAD assembly of the rover
2. Components working on a 3V / 3.3V supply were preferred to 5V components to avoid excessive use of level shifting circuitry
3. A low-dropout regulator (LDO) or Buck converter was not used on the 5V input since this would likely drop the received power bus voltage down to 4.2-4.3V on the 5V inputs to various components on the Payload PCB. Such a low voltage would be undesirable for the operation of the FG DOS sensor as well as the level shifter
4. The RS-485 transceiver's RE and DE pins [86] were pulled down to GND so that the payload can always be *actively listening* over the RS-485 half duplex bus for instructions or commands from the OBC or the PPU in operation. This also allows the connection of external GSE to the payload boards' debug connectors without inadvertent pollution of the rover's data bus signals, which are shared by multiple subsystems
5. A 120 Ohm termination resistor was included across the incoming RS485 data lines to reduce noise and reflections on the data bus of the rover [86]
6. A star point grounding scheme was implemented to reduce ground offsets and noise in the Payload

circuitry. As a result, the Payload has a single GND connection to the rover (provided through the Payload MAIN cable harness) and the mounting holes are not connected to GND

7. The Payload Daughterboard connector was included in V1 of the PCB to cordon off an approximate amount of space on the edge of the board for such a connector and to minimize the amount of effort required for design of future iterations of the PCB i.e. V2, V3 etc.
8. A second level shifter was included to provide signals at appropriate 5V levels for the FGDOS sensor and any other components on the Daughterboard. This level shifter also adds redundancy to the electrical architecture. In case the first level shifter fails and data cannot be read out from the internal FGDOS sensor, the external one will still continue to give readings.
9. Decoupling capacitors of capacitance levels recommended by the respective datasheets of components were provided to reduce supply noise
10. The mounting points of all connectors were grounded and connectors with appreciably sized leads and alignment pins were preferred

Although the electronic architecture i.e. the block diagram and component selections were made based on the natural flow down from the higher level architecture, the electronic and hardware designs of other similar radiation monitoring devices and instruments was taken into account as references, and to provide partial verification. The most important ones being the LAM radiation monitoring payload [27], CERN's TIDMon system [129] and the micro dosimeter on CRaTER [87].

Once the type of components to be used in the circuit had been identified, specific parts to fulfill these roles were selected based on criteria such as:

- Supply voltage level
- Integrated circuit (IC) package type
- Mounting / soldering method
- Operating temperature range
- Automotive qualification grade
- Availability in stock<sup>7</sup>
- Availability of radiation testing data
- Flight heritage/previous use in space missions
- Cost

1. MCU: The MSP430FR5969 microcontroller from Texas Instruments [141] was selected, mainly due to its flight heritage onboard previous space missions [2], [15] and because it contains FRAM based memory which is resistant to radiation [113]. The MSP430 also offers versatility and a sizeable amount of resources to support developers
2. FGDOS Radiation Monitor: As described previously in the literature study, the FGDOS sensor [4] was chosen as the core detector of the Radiation Payload. The FGD-03F sensor is used specifically, which comes in a QFN32 package and has an SPI interface and requires a 5V supply [117]
3. Onboard Memory: To provide redundant backup storage for payload data, onboard the payload itself, a CY15B104QN-50SXI FRAM non-volatile memory module [31] was selected. Hence, this module can store payload data in the event that the data interface between the rover and payload is non-operational or the data storage of the rover is temporarily indisposed
4. Level Shifter: As described previously, level shifting circuitry is required on the Radiation Payload to enable interfacing the FGDOS sensor, which works on a 5V level, with the MCU, which operates on a 3V/3.3V voltage level. A MAX3001EEUP+ 8-channel bi-directional level shifting IC was selected for this purpose [85]
5. Voltage Regulator: The LP2981 low dropout regulator [138] provides a regulated 3V supply to relevant payload components, including the microcontroller. It also provides protection against electrical shorts and over-temperature on the 3V line
6. Daughterboard: The Radiation Payload Daughterboard mainly consists of an FGDOS FGD-03F chip. Aside from this and a connector which allows interfacing with the MAIN board, a TMP100 temper-

<sup>7</sup>Owing to the global chip shortage caused by the covid pandemic, many chips were out of stock or had extremely long lead times which did not comply with the production and testing schedule. Hence, alternate components had to be used in some cases to move forward with the design and production of the Radiation Payload Prototypes

ature sensor [142] is included to allow monitoring of the temperature of the Daughterboard, given the fact that being outside the rover's main chassis would expose the Daughterboard to significant temperature extremes

The full PCB layout and electrical schematic of V1 of the Radiation Payload Main Board can be found under Appendix A. Figure 3.14 shows a visualization of the Main PCB V1.

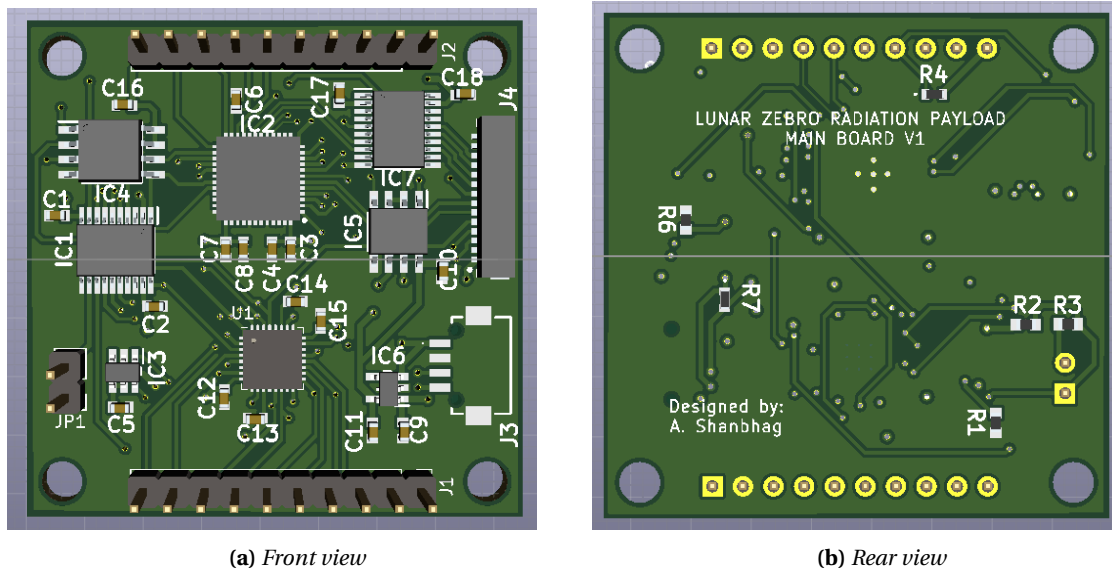


**Figure 3.14:** Visualization of the Radiation Payload MAIN PCB design

### 3.2.4. Software Design

The first phase of Radiation Payload design is brought to a close by the design of embedded software. Built upon the electronic design and system architecture, the role of the S/W is to control and operate the payload subsystem such that it performs the functions listed in the FBD (Figure 3.2). This includes enabling it to work smoothly with the avionics of the rest of the Lunar Zebro rover.

The role of the software can be informally summarized as follows:

- To command and control the electronic components that form the payload subsystem
- To control the flow of information to and from the payload subsystem
- To coordinate the operations of the payload subsystem with the rover and the mission timeline at large
- To detect, diagnose and recover the payload subsystem from faults and anomalies
- To communicate with other subsystems and the rover
- To acquire, store, process and communicate scientific data concerning the space radiation environment

### CDHS Architecture

The command and data handling architecture of the Radiation Payload Subsystem, has been structured as shown in Figure 3.15. This CDHS architecture is designed to be integrated into the overarching CDHS architecture of the rover. The embedded S/W of the Radiation Payload is split into two parts, (a) an MCU-based firmware which would run on the payload subsystem hardware only and (b) a driver S/W which will run on the OBC of the rover such that it controls and coordinates all interactions of the Payload subsystem with the rover.

The rover consists of an onboard computer (OBC) running a real-time operating system called TRON [68]. The driver S/W (also referred to as the 'Payload App') would run on the OBC under TRON. A microcontroller based system called the power processing unit (PPU) is also present in the rover. Its function is to monitor the power consumption and distribution from the EPS to various subsystems. However, under special

circumstances, the PPU is designated to function as a backup processing and control hub for the OBC, in the event that the OBC stops functioning temporarily. This is a contingency measure which would allow the rover system to continue operating with reduced functionality until the OBC can be recovered. Accordingly, a contingency function or routine relevant to the payload subsystem is intended to be set up such that a reduced amount of data can be received from the payload by the rover and transmitted for downlink. This is meant to prevent the failure of all science mission objectives mentioned in subsection 3.1.2 in the event that the rover OBC fails. Onboard data storage on the rover is composed of a pair of SD cards and an FRAM memory module, in addition to internal storage on the OBC. It is intended that a portion of this onboard storage will be allocated for the storage of Radiation Payload data. As mentioned previously, a non-volatile memory module is included in the payload hardware itself to allow data to be stored until it can be transmitted to the OBC/PPU over the data bus of the rover.

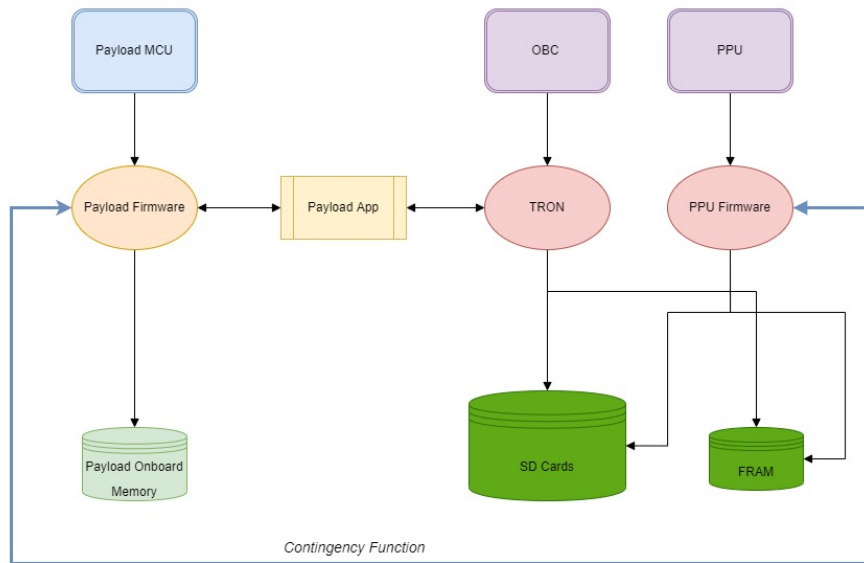


**Figure 3.15:** CDHS Architecture

Following the functional breakdown, the electronic architecture and the physical architecture, a functional breakdown tree for the Radiation Payload Software was created. This tree was bifurcated into two main branches, the first one dedicated to the payload Firmware (Figure 3.16) and the second one for the Driver App (Figure 3.17).

### Payload Firmware

The MCU serves as the brain and central nervous system of the Radiation Payload, in terms of controlling the functioning of the payload and transfer of data from one location to another. As such, the MCU firmware serves most of the aforementioned functions. The MCU firmware was written in C/C++ for the MSP430FR5969 microcontroller, using the Energia platform<sup>8</sup>. Figure 3.16 details the functional breakdown for this firmware. The functions were divided into four main branches, as shown below, and are numbered according to the branch, sub-branch and order of occurrence.

- **A** - Radiation sensing
- **B** - Data storage & processing
- **C** - Telemetry and commands
- **D** - Housekeeping and maintenance

For instance, the function "Change sensitivity" would be designated Firmware Function A.4.2. The firmware implemented in Radiation Payload V1 covers a subset of the functions shown in Figure 3.16. This was done with the objective of achieving a functional payload prototype in time for the environmental test campaign of Belka 2. However, the structure and modularity of the firmware lend itself to make it easy to add more features and sophistication in the future. The first version of this firmware was implemented using Energia,

<sup>8</sup><https://energia.nu/>

tested on the breadboard model and later flashed to the Payload MAIN PCB and tested. This firmware was iterated upon and V1.1<sup>9</sup> was tested and later utilized for the performance tests of Radiation Payload V1 under proton beam irradiation (section 5.6). V1.1 is based on a library written for reading out the FGDOS using an MSP430, and is structured into a header file, a source file and a script for initializing the payload and communicating payload telemetry over a serial port. Listing E.1 shows an abbreviated pseudo code for this firmware.

```
1 Initialize MCU:
2   Load Libraries;
3   Configure GPIO pins;
4   Initialize variables;
5   Initialize flags;
6
7   Initialize Clock module;
8   Configure watchdog;
9
10  Configure DataBus transceiver;
11  Initialize payload internal SPI comms;
12  Initialize payload internal Serial comms;
13
14  Configure onboard memory storage;
15
16
17 Initialize FGDOS:
18   Initialize SPI registers;
19   Set FGDOS sensitivity mode;
20   Set FGDOS recharging mode;
21   Set FGDOS measurement window;
22   Set FGDOS recharging mode;
23   Set FGDOS recharging source to internal charge pump;
24   Disconnect recharging system;
25   Set recharge target and threshold;
26   Set recharge voltage;
27   Enable recharging system;
28   Wait;
29   Read all FGDOS registers;
30
31
32 Loop:
33   Set WCK signal;
34   Wait;
35   Read Sensor 1 data;
36   Store Sensor 1 data;
37   Read Sensor 2 values;
38   Store Sensor 2 data
39   Wait;
40   Reset WCK signal;
41   Receive command;
42   Interpret command;
43   Enable DataBus output;
44   Send response over DataBus;
45   Disable DataBus output;
```

**Listing 3.1:** Firmware pseudo code

<sup>9</sup>[https://github.com/Abhi-2049/REDMOON/tree/main/TESTING%20CODE/Payload-MAIN-ENV\\_TEST-V1.1](https://github.com/Abhi-2049/REDMOON/tree/main/TESTING%20CODE/Payload-MAIN-ENV_TEST-V1.1)

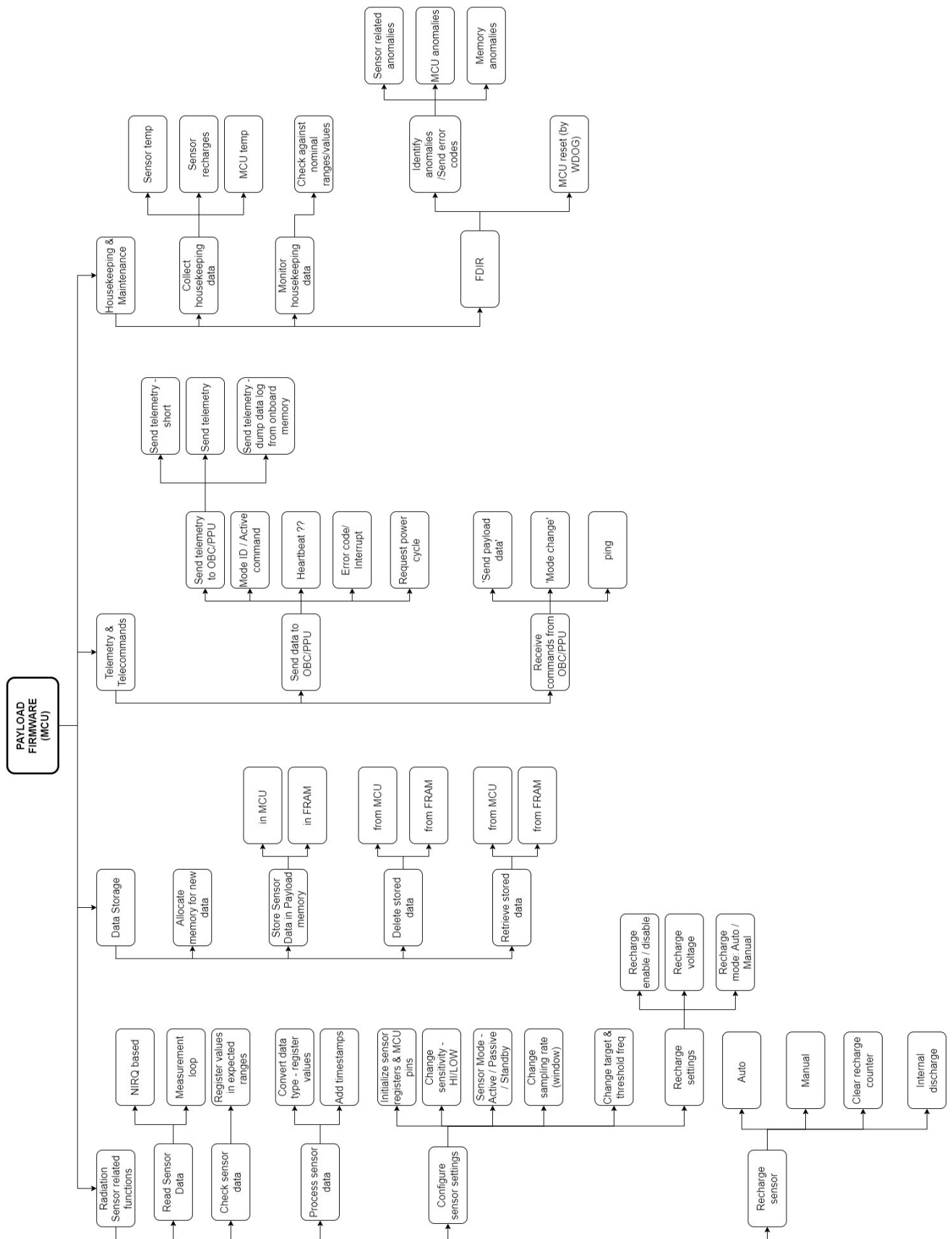
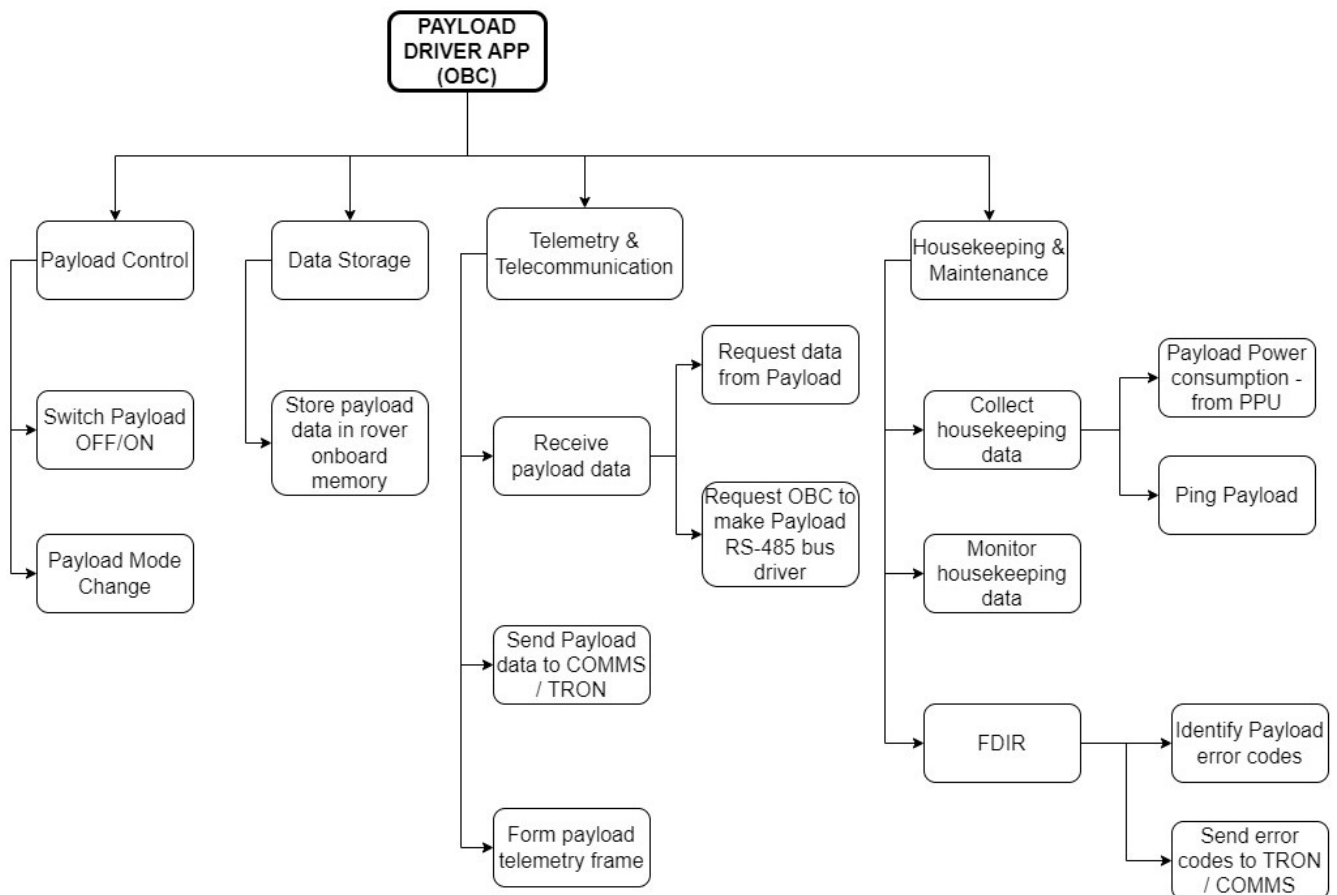


Figure 3.16: Functional Breakdown of Radiation Payload Firmware

### Driver Software

As seen in the CDHS architecture, a piece of driver software running on the rover's OBC is needed to send commands to the Radiation Payload, to receive telemetry from it and to coordinate payload operations with the rest of the rover. This driver software is referred to as the 'Payload App' by the Lunar Zebro Software department. Although the Radiation Payload Subsystem has been designed to operate and conduct scientific measurements independent of the rover's CDHS subsystem, it still needs to rely on the OBC to provide a link to the ground segment via the COMMS subsystem, in order to facilitate the execution of commands from the ground segment and to send payload data to ground. Within the architecture described here, the Payload App is mainly responsible for changing the operational mode of the Radiation Payload, to check the functioning of the Payload and, most importantly, to request and receive data from the Payload. Similar to the firmware, the driver functions are grouped into four main categories, as shown in Figure 3.17. The naming convention for the driver functions is similar to the one used for the firmware functions:

- **A** - Payload control
- **B** - Data storage
- **C** - Telemetry Commands
- **D** - Housekeeping and Maintenance



**Figure 3.17:** Functional Breakdown of Radiation Payload Driver App

Listing 3.2 shows an abbreviated pseudo code for the driver app. The driver app is under development in collaboration with the Lunar Zebro S/W Department. It is implemented in C/C++ and is designated to run on the linux based OBC. "OS" refers to the real time operating system which would be running on the OBC in its operational configuration.

```

1 Loop:
2   Recieve action from Rover OS:
3   Interpret action;
4   Choose relevant command;
5   Send command to Radiation Payload over Data Bus;
6   Recieve response over Data Bus;
7   Send recieved data to OS;

```

**Listing 3.2:** Driver App pseudo code

### Modes of Operations

The Modes of Operations of the Radiation Payload describe how this subsystem of the rover will function and operate, given various external and internal conditions such as the mission phase and the state of the rover. For the Payload S/W to be used during the Moon Mission, it is intended to be a state machine with each state corresponding to a specific operational mode. The state transitions are envisioned to be triggered by changes in pre-programmed parameters, or by external input from the rover or Ground Segment. Figure 3.18 shows the state transition diagram.

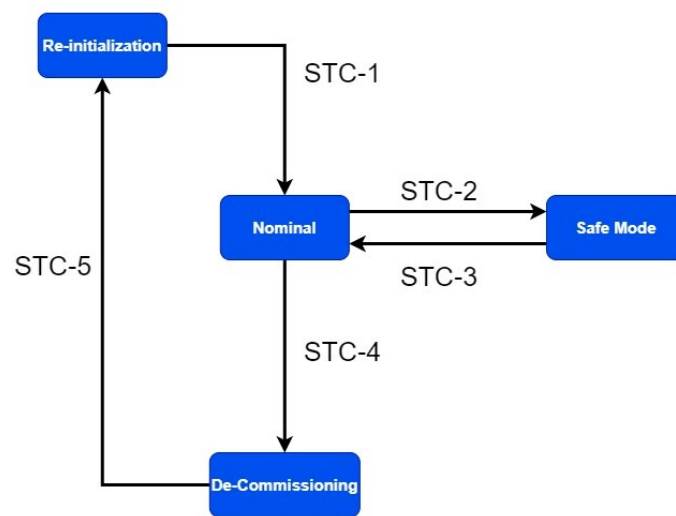


**Figure 3.18:** State transition diagram

The STCs refer to state transition conditions, which are conditional statements that check whether certain parameters have reached a pre-determined value.

As a consequence of the S/W functional breakdown presented in preceding sections, the following Modes were defined for the Radiation Payload:

1. **(Re-)initialization Mode:** The re-initialization mode deals with the start-up and initialization of the Radiation Payload subsystem. This state is entered whenever the Payload is power cycled, reprogrammed or rebooted from safe mode / hibernation. The re-initialization mode consists of initialization of the MCU, configuration of the FGDOS chips and set up of various signals, registers and variables that would become useful as the payload subsystem transitions into the nominal mode
2. **Nominal Mode:** The payload is intended to be in the nominal mode for the majority of the mission. this mode covers most of the typical payload functions such as radiation measurement, communication with the rover, data storage and transmission, housekeeping etc.
3. **Safe Mode:** In the event of a an error or a failure in the payload subsystem, the safe mode transition is triggered. This transition will most likely be based on certain diagnostic parameters going out of nominal bounds, as detected by the housekeeping and FDIR functions of the payload subsystem. The transition into safe mode may also be triggered externally by the rover, via the driver App. This would occur in case an error or failure has been detected by the rover or an unexpected anomaly related to the payload subsystem has been detected. It would also be applicable in case the rover itself has switched into its Safe Mode

4. **Decommissioning Mode:** The decommissioning mode is intended to be the final operational mode of the payload before the rover completes its nominal mission on the lunar surface and goes into hibernation for the lunar night. This mode is chiefly concerned with wrapping up the science mission and payload nominal operations. This involves offloading the payload's onboard memory storage, offloading all payload data to the rover for downlink and configuring the FG DOS sensor to perform passive, unpowered measurements. This would be followed by the payload being turned OFF. In the event that the rover makes it past the lunar night and is able to successfully reboot, the payload would 'come back to life' by entering the re-initialization mode

Each mode has a certain set of *Routines* associated with it which are meant to be carried out while the payload is in a particular operational mode. These routines are collections of tasks which can be logically grouped together and concern a certain aspect of the payload's functionality. Each task can generally be executed by a single function or subroutine in the firmware. When it comes to operations, it is also important to note that the payload firmware and electronics have been designed such that the payload can get initialized, start functioning and making measurements as soon as it receives power over the 5V power bus. The payload does not need to await the rover to be fully operational before it can start functioning. Complete description of the routines and sub-routines is considered outside the scope of this document.

### 3.2.5. Operational FFBD

The Operational Functional Flow Block Diagram (FFBD), describes how the Radiation Payload would operate in flight during the Lunar Zebro mission. Figure 3.19 shows the main mission activities in sequence and the inter-dependence between these activities. A more granular description of each mission phase is shown in the charts from Figure 3.20 to Figure 3.25. The FFBD was constructed and derived from the mission definition and functional flow presented earlier. It is important to note that the Operational FFBD of the payload subsystem was crafted to be consistent with the FFBD of the Lunar Zebro rover system [68].

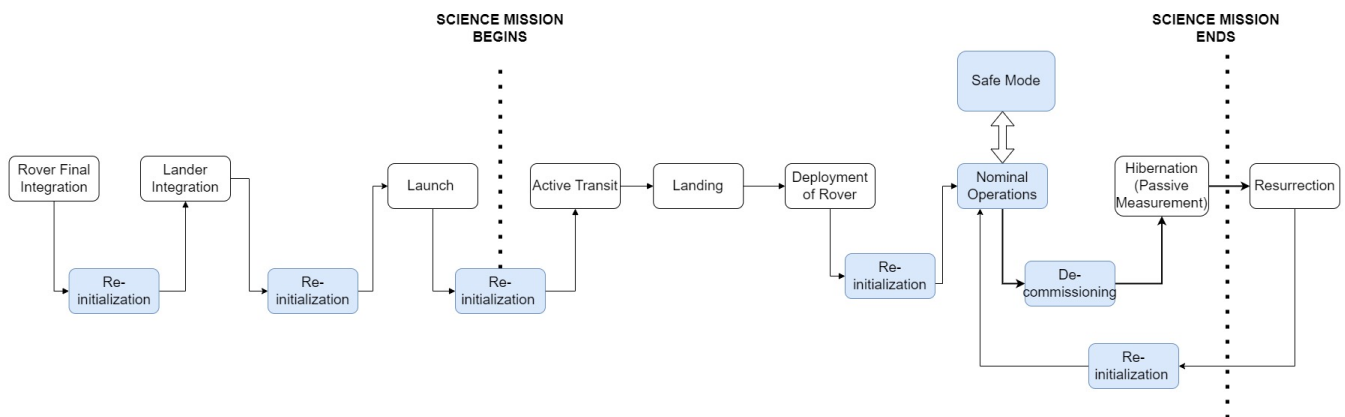


**Figure 3.19:** Operational FFBD of Radiation Payload

The blue boxes indicate operational modes of the Radiation Payload while the white boxes indicate mission phases. As such, the blue boxes have been included to inform the reader about the state of the payload as the mission progresses. The yellow boxes indicate phases which are significant from a scientific POV, but do not necessarily indicate a shift in the operational mode of the Radiation Payload or the rover. As shown in Figure 3.19, the operational FFBD begins prior to launch, with the final integration and assembly of the FM of the Radiation Payload in the Lunar Zebro rover, followed by the integration of the rover into the lunar lander<sup>10</sup>. The launch of the spacecraft into LEO and LEO operations constitute the next phase. The first two phases involve re-initialization of the payload which is intended for performing diagnostic checks and to ensure proper payload functioning. This phase terminates with the start of the 'Active Transit', wherein the Radiation Payload would make observations as the spacecraft passes from LEO to cis-lunar space, with

<sup>10</sup>Since the choice of the lander has not been finalized yet, a concrete estimate of the timeline of these pre-launch activities could not be made in the Operational FFBD

an intermediate passage through the VABs which carries high scientific value. Lunar orbit operations bring up the end of the active transit phase, which is followed by landing on the Moon. The rover would be subsequently deployed from the lander, which would bring about the execution of another re-initialization and set of checkouts of the rover and all of its subsystems, including the payload. Hereafter, the main part of the science mission begins, i.e. measurements of ionizing radiation on the lunar surface as a part of the nominal operations of the rover. If the mission proceeds as planned, the nominal operations phase would continue until the onset of lunar night, whereby the rover would slip into hibernation. Concurrently, the Radiation Payload would go through de-commissioning and all payload data would be downloaded to the ground segment. By the next lunar dawn, if the rover is able to be recovered or partially revived, the payload would be re-initialized and placed into nominal operations again. This would imply an extension of the science mission beyond its original scope. However, if the rover cannot be recovered (its EPS is non-functional), the science mission would be effectively concluded at this point.

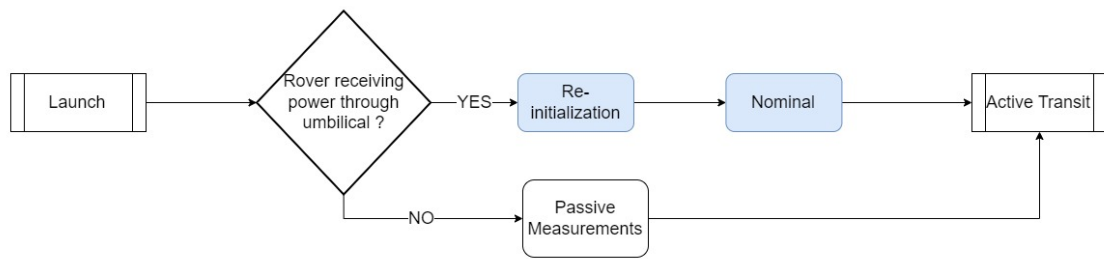


**Figure 3.20:** Operational FFBD: Launch

The launch of the spacecraft into LEO and LEO operations constitute the first phase after lander integration, as shown in Figure 3.20. Once the LEO phase of the lander commences, if the umbilical from the lander to the integrated rover is activated, the Radiation Payload can be switched on and re-initialized. Once the initialization is complete, the payload can start operating nominally to make dose measurements in LEO. Presumably, the acquired data would be downlinked to the ground segment via the lander. In case the rover is not receiving any power, it can still make measurements in passive mode, assuming that it was properly configured and successful pre-launch checkouts were performed on the Radiation Payload.

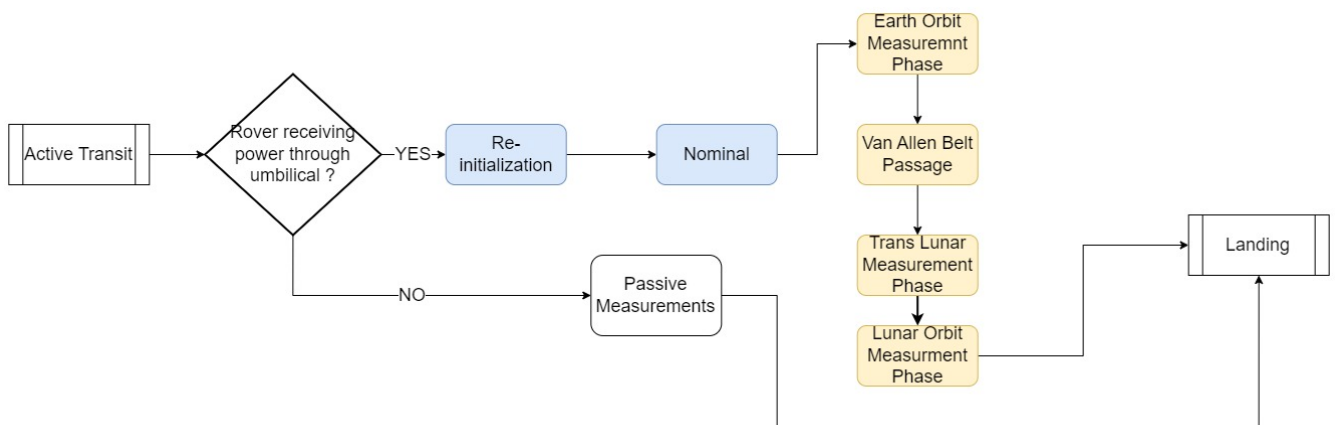


**Figure 3.21:** Operational FFBD: Active Transit

Once the lander spacecraft has been subjected to a TLI burn, the 'Active Transit' phase would begin. In the unlikely scenario that the umbilical is without power, the payload would make passive measurements until power becomes available. On the other hand, if the umbilical is active, the Radiation Payload would again enter nominal mode by way of re-initialization. This is necessary since the passage through the VABs is expected to bring the most temporally concentrated dose exposure for rover. Once the spacecraft has crossed the VABs, the payload will continue to make measurements of the interplanetary radiation environ-

ment. Here, the sampling rate might be reduced, owing to the low fluxes and dose rates expected during this period. This would also continue once the spacecraft is injected into lunar orbit.

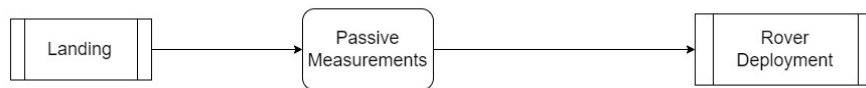


**Figure 3.22:** Operational FFBD: Landing

After lunar orbit operations are concluded, the onset of the landing phase would presumably coincide with the rover being switched OFF. As such, the payload would make passive measurements until the lander is safely parked on the moon, as depicted in Figure 3.22.

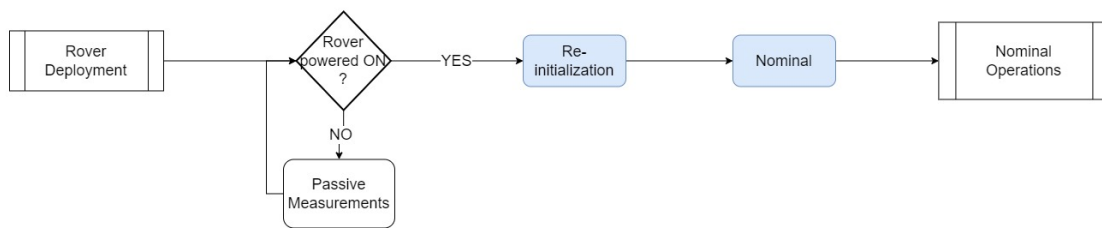


**Figure 3.23:** Operational FFBD: Rover Deployment

Before the rover is deployed from the lander, it can be foreseen that the rover would be switched ON again to perform a full checkout and functional test. As a part of this, the Radiation payload would also be functionally checked. Thereafter, the non-critical subsystems of the rover would probably be switched OFF for the deployment. Once the rover is separate from the lander and is resting safely on the lunar surface, the non-critical subsystems would be turned ON again. Predictably, the Radiation Payload would be re-initialized henceforth and would be put to nominal operations to make time resolved dose measurements on the lunar surface, which constitutes the most important part of the Lunar Zebro science mission. Figure 3.23 shows the operational flow for the *Rover Deployment* phase.

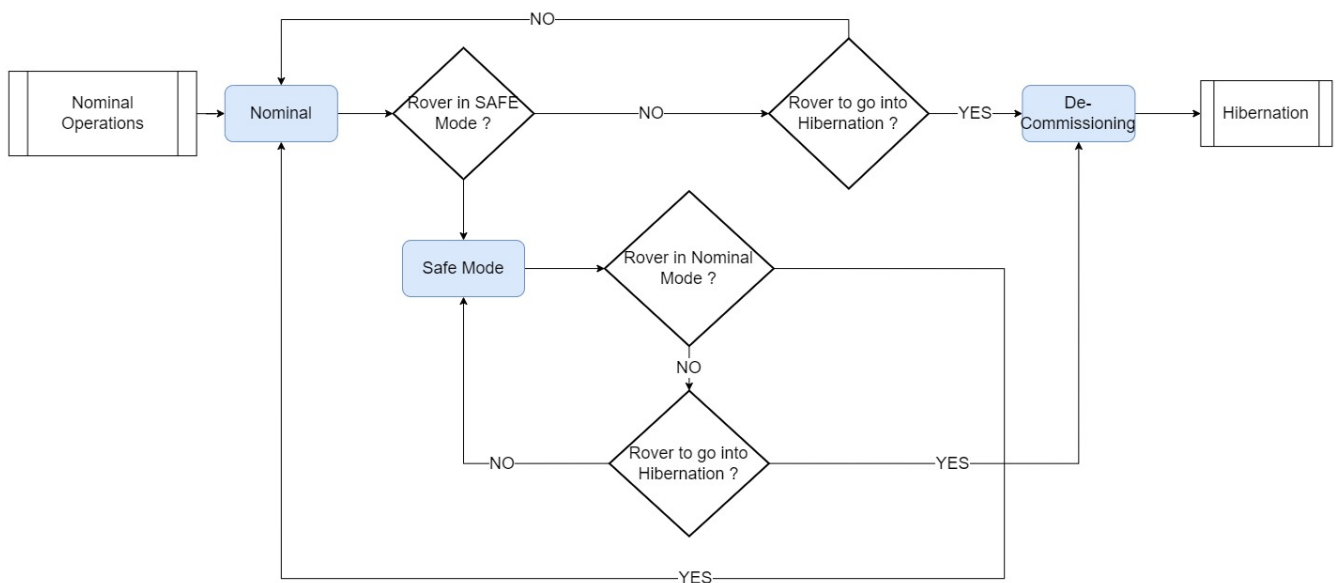


**Figure 3.24:** Operational FFBD: Nominal Operations

The 'Nominal Operations' mission phase will continue until the end of the lunar day, if the rover and Radiation payload function nominally and no problems are encountered. Thereafter, once the rover starts to

enter hibernation, the Radiation Payload would be switched to its *De-Commissioning* mode. During nominal operations, if a problem is encountered and the rover goes into safe mode, the payload would also enter its own safe mode, until the rover goes back into its nominal mode, as shown by Figure 3.24.

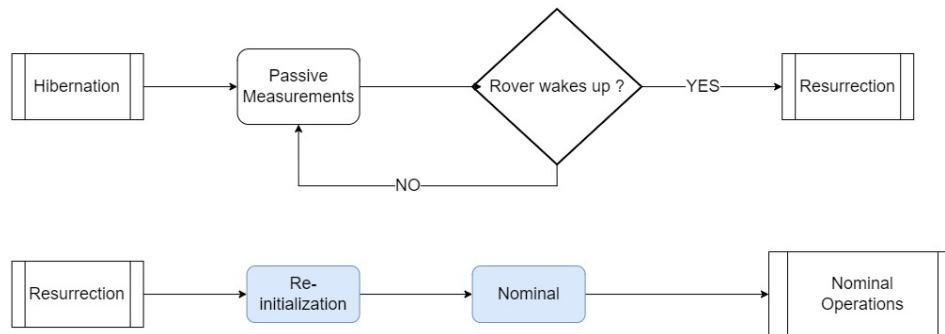


**Figure 3.25:** Operational FFBD: Hibernation and beyond

The *De-Commissioning* mode would involve conclusion of radiation measurements and the end of the science mission. Accordingly, all payload data would be downlinked to the ground segment, both from the rover as well as the onboard memory storage for the rover. Contrary to current estimates, if the rover does manage to survive the lunar night and reboot at the outset of the next lunar day, the science mission would be extended, as shown in Figure 3.25.

### 3.2.6. Telemetry & Telecommands

As a subsystem of the Lunar Zebro rover, the Radiation Payload needs to have a defined set of information that it can send to the rover to be downlinked to the Ground Segment. This data makes up the telemetry of the Radiation Payload, from the perspective of the rover. The data present in this payload telemetry would be repackaged into the rover's overall telemetry packet by the OBC before being sent to the COMMS subsystem and being downlinked to the ground segment.

In addition to the telemetry sent by the Payload, there needs to be a predefined set of commands which can be sent to the Payload by the rover in order to request data from the payload, to change its operational settings, to diagnose problems etc. These telecommands can be initiated by the rover's onboard software itself, or explicitly by the operators in the ground segment team.

In collaboration with the Lunar Zebro Software department, a set of commands that would be accepted by the Radiation Payload was drafted [36]. Correspondingly, the telemetry that would be returned by the payload subsystem in response to each command was also defined. These commands and the relevant telemetry, along with their descriptions can be perused in Table B.1. It can be seen that some commands are relevant to the Radiation Payload but do not lead to actions that are carried out by the payload subsystem itself. This includes the command to power cycle the Radiation Payload in the event that a reset is required due to a deadlock in the software or due to single event effects (SEEs). Similarly, the commands to measure the voltage, current consumption and power consumption of the payload subsystem are carried out by the PPU. But the telemetry returned as a consequence of these commands is relevant to the Radiation Payload. The telemetry and commands list was drafted such that it would be implemented in two stages:

- Some commands are meant to be executed repeatedly during the environmental test campaign to gather data during functional tests of the Radiation Payload
- A set of commands is denoted "mission only". This implies that these commands would be executed at the time of the lunar mission and are not relevant to the upcoming environmental test campaign (described in section 5.7)

The full list of telemetry and commands can be found under section B.1. This includes a description of each command, the data returned in response to it and the data type, size, and command ID. The structure of the message packets for each subsystem on the Lunar Zebro rover was standardized and decided by the Software Team and is a derivative of the BLE standard. A detailed description of this protocol can be found

in [36], since it is considered outside the scope of this report.

### 3.3. Manufacturing, Assembly and Integration

The previous sections showed how the conceptual design, detailed design and front end systems engineering of the Radiation Payload were carried out. Proceeding further along the V-model, we arrive at manufacturing, assembly and integration (MAI) activities, which entail synthesis of the design, conclusion of its implementation in the physical world and preparation for verification and validation activities (described in chapter 5). Within the scope of this project, the MAI activities consisted of the creation of breadboard models of the Radiation Payload, followed by the production of the Development Model (DM), otherwise known as Radiation Payload V1. This is planned to be followed by assembly of the DM into the Lunar Zebro Belka 2 and integration of the Radiation Payload subsystem, as a part of the larger rover system <sup>11</sup>.

#### 3.3.1. Production of breadboard models

To start the implementation of the hardware design, a couple of Breadboard models of the Radiation Payload were produced. These were based off of the electronic system design presented in Figure 3.13. The purpose of the breadboard models was to test and validate the electronic system design before moving on to the more involved process of electronic PCB design. Simplified schematic diagrams of the breadboard models can be found in Figure 3.26.



Figure 3.26: Breadboard schematics

#### Variant A

Variant A was set up with the objective of learning how to interface with the FGDOS chip (mounted on a breakout board) and how to read out the following FGDOS data from it in a repetitive fashion:

1. Sensor frequency
2. Reference frequency
3. Recharge count
4. Sensor temperature

Another objective was to learn how to initialize and configure the FGDOS sensor, and its operational characteristics in various modes. Hence the development activities with Breadboard-A also contributed to the preparation of the test setups described in chapter 5. Indeed, this variant is similar to the setup that was used during proton beam radiation testing of the FGDOS sensor [90]. Variant-A of the Radiation Payload Breadboard consists of:

<sup>11</sup>Within the current model philosophy of Lunar Zebro, the second version of its Engineering Model, named "Belka 2", is under development. With regards to the Radiation Payload, two breadboard models were produced, followed by a Development Model which is referred to as "Radiation Payload V1"

- FGD-03F sensor breakout
- Arduino Uno R3 Microcontroller Board
- 5V Supply

With this minimal setup, some simple Arduino based S/W scripts were written to read out FGDOS data and to display it on a serial terminal. These scripts can be found in Appendix B.

### Variant B

Variant B was set up with the objective of testing and validating the electronic system design of the Radiation Payload V1. The code developed for the Arduino based Breadboard-A was ported to the MSP430 for Breadboard-B and thereafter enhanced. Components in this breadboard variant were breakout boards containing chips that performed specific functions such as voltage regulation, logic level shifting etc. These components were tested individually with an Arduino to verify their functionality, before integrating them into Breadboard-B. The code used for these tests can also be found in Appendix B.

Variant-B of the Radiation Payload Breadboard consists of:

- FGD-03F sensor breakout
- MSP430-EXPFR5969 LaunchPad
- 5V Supply
- 3.3V LDO
- TXB0108 Level Shifter Breakout
- RS485 Transceiver Breakout
- FRAM Breakout
- Watchdog Breakout

This variant can also be used to test and debug any new firmware that is written for the MSP430 based MCU, before deploying it to the MCU on the DM or EM of the Radiation Payload. This way, unintended damage to the payload EM/DM electronics due to errors in the embedded S/W can be prevented.

### 3.3.2. Development Model: MAIN Board Production

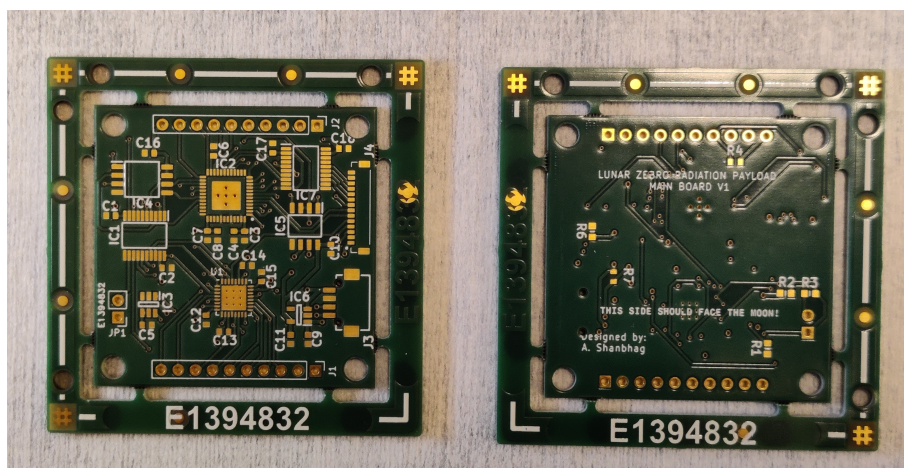


Figure 3.27: Radiation Payload Main V1 PCBs - post manufacturing

Upon successful verification of the electronic system architecture and completion of the electronic design and component selection, the Development Model (DM) PCB was designed and ordered. Two identical copies of the bare PCB for Radiation Payload MAIN V1 were produced by Eurocircuits BV<sup>12</sup>. Figure 3.27 shows the bare PCBs mounted on a panel, upon arrival from the manufacturer. The PCBs were inspected visually for manufacturing defects. This was followed by an electrical check to verify the integrity of traces, vias, solder pads, jumpers and plated through holes. Two identical copies were produced to prevent schedule delays due to inadvertent damage or destruction of either payload board as a result of development and

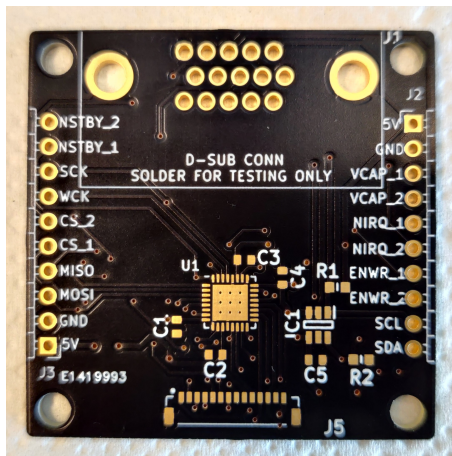
<sup>12</sup><https://www.eurocircuits.com/pcb-and-assembly/>

testing activities<sup>13</sup>.

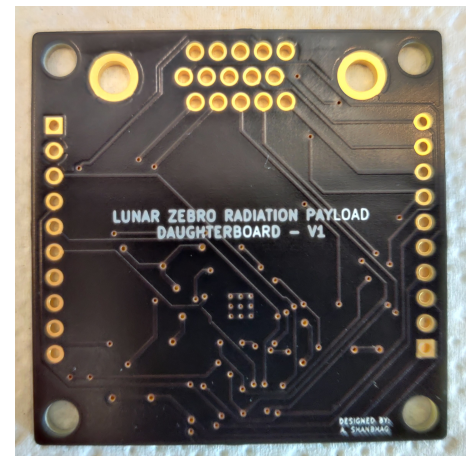
To identify and weed out any errors in the soldering process, the Dummy PCB was soldered and tested first. This ensured that problems during the assembly and testing of the Payload DM could be prevented. A subset of electronic components required for testing the basic functionality of the Radiation Payload MAIN Board were soldered on to the Dummy PCB<sup>14</sup>.

### 3.3.3. Development Model: Daughterboard PCB Production

The Daughterboard V1 was designed in order to functionally test it in an integrated form with the Payload Main Board as well as to test the thermal survivability of the Daughterboard by testing it in thermal vacuum environmental tests along with the rover (see subsection 5.7.3). This would act as a proof-of-concept for the current design of the Daughterboard and the idea of incorporating it into the rover in a minimally sheltered manner.



(a) Front view



(b) Rear view

Figure 3.28: Daughterboard bare PCBs

The 14 pin DF52 connector was designated with a similar pinout as the connector provided on the Payload Main Board V1. This is intended to enable the Daughterboard to be connected with the Main Board for standalone functional testing of the Radiation Payload in its full form. Pin headers were also provided on the sides of the Daughterboard to enable debugging and configuration of the FGDOS sensor. Additionally, a D-sub 15 pin connector was included on the Daughterboard PCB, to allow it to be compatible with the expected feed-through of the TVAC chamber. Two views of the produced Daughterboard PCB can be seen in Figure 3.28.

The electrical schematic for the Daughterboard PCB can be found in Appendix A

### 3.3.4. Assembly into Belka 2

As previously mentioned, within the physical arrangement of the Lunar Zebro Belka-2, the Radiation Payload MAIN Board is one of several PCB modules that are stacked in the front of the rover. Within this stack, the Radiation Payload PCB is the uppermost member. In other words, the Radiation Payload PCB will be the furthest away from the lunar surface while the rover is in operation. As such, the Radiation Payload Main Board is one of the last modules to be assembled on to the avionics stack before it is to be sandwiched between the rover's chassis and the bottom plate. This process is depicted in the assembly plan excerpt shown in Figure 3.29. The gray board in the foreground represents the Radiation Payload MAIN Board.

<sup>13</sup>As such, one of the boards was informally dubbed as the "Dummy PCB", since it would be subjected to the soldering and assembly process first, such that any errors in the process/design could be identified and eliminated

<sup>14</sup>Only the most essential components were soldered first, due to the chip shortage

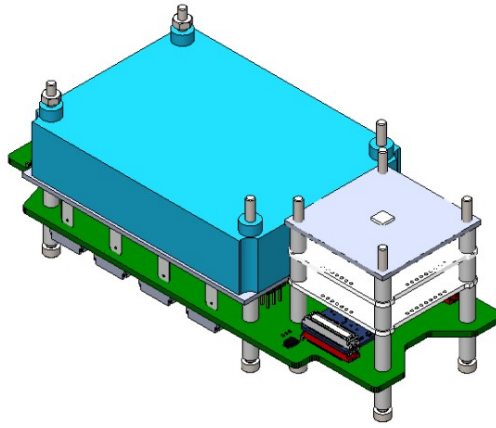


**Figure 3.29:** *Radiation Payload Assembly plan (excerpt from [136])*

### 3.3.5. Integration

Before full-fledged assembly and integration with the rover, the Payload DM was tested on its own as described in section 5.4 to section 5.5. This is to be followed by an interface test with an emulator for the rover's OBC. Once the interface test with the emulator is completed successfully, the Payload DM can be connected to a tabletop model of the rover's avionics for an integrated test. Subsequently, the Payload DM will be plugged into the rover's Motherboard during assembly of the rover in a clean room <sup>15</sup>.

<sup>15</sup>Due to external delays faced by the LZ team, the integration and assembly activities could not be finished within the timeline of this project

# 4 Radiation Environment Modelling & Transport Simulations

This chapter details the modelling and simulation efforts aimed at scoping the expected mission radiation environments and the influence of primary sources from these environments on the Radiation Payload.

## 4.1. Overview of Radiation Payload Science

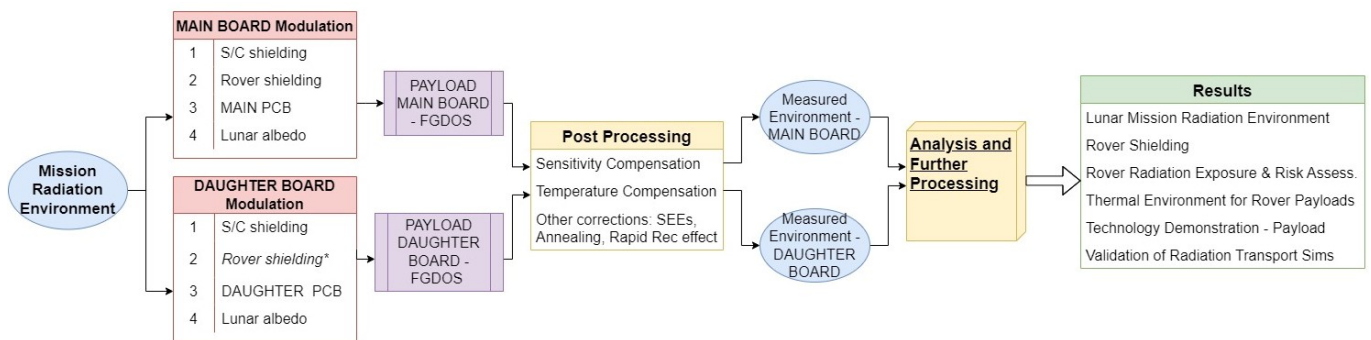


**Figure 4.1:** Science Scheme of the Radiation Payload

Figure 4.1 gives a schematic presentation of the science of the Radiation Payload within the context of the Lunar Zebro mission. It is intended to be a holistic representation of the various inputs, modulations, processes and results that would be a part of the scientific investigation. In essence, Figure 4.1 can be seen as a flow diagram of how the radiation environments encountered during the mission would be converted into mission observations and later processed to obtain scientific results. Figure 4.1 does not depict how the individual blocks and processes change with time as one mission phase is concluded and another commences. Rather, it is intended to give a generalized view of how the aforementioned incident radiation would be typically modulated, influenced and processed during the mission, without venturing too deep into the specifics of a certain mission phase or radiation environment. The utility of this schematic is to help payload engineers and scientific investigators to understand how the physical quantities that would be measured by the Radiation Payload are influenced by various external and internal factors. This would enable the creation of accurate models that can be used to simulate as well as process payload data.

Proceeding from left to right, the *Mission Radiation Environment* represents the solitary input to the system. This input refers, in an inclusive sense, to ionizing radiation that is incident on the Radiation Payload. However, in this case, since the Radiation Payload is a part of the rover, which may temporarily be a part of the lander or another spacecraft (depending on the mission phase), the *Mission Radiation Environment* actually refers to space radiation which comes in contact with the compound spacecraft that contains the Lunar Zebro rover with the Radiation Payload. The first set of red blocks represent modulations that are made to the input due to various factors such as:

- Shielding of incident radiation by the spacecraft.
- Shielding of primary and secondary radiation by the chassis and other subsystems of the Lunar Zebro rover.
- Shielding and scattering of the incoming radiation by the Payload PCBs (before the radiation reaches the detector).
- Modulation and scattering of incident radiation by the Moon, in the form of Lunar albedo or shielding.

These modulations have been treated separately for the internal and external Radiation Payload electronics boards, since the modulations at a given time would be different for the detectors placed on these boards.

Hence, from an engineering perspective it is beneficial to model these modulations separately. Naturally, these blocks have the effect of producing primary and secondary radiation particles which are now modulated in certain ways and impinge on the FGDOS detectors mounted on the payload boards. Now, the two adjacent blocks represent sensor response models of the FGDOS modules placed on the payload MAIN Board and Daughterboard respectively. Despite having identical chips, these models have been segregated since each FGDOS module is known to exhibit some variability and unique characteristics, as discussed in chapter 5 and [23]. The sensor responses produce digital signals which would be a part of the payload telemetry. This telemetry would be downlinked and the sensor data will be processed on the ground, as indicated by the yellow *Post Processing* block. The post processing would include:

- Computation of time evolution of TID, dose rates and cumulative TIDs measured by each FGDOS sensor.
- Compensation in the dose measurement to account for sensitivity degradation due to TID [22, 19].
- Compensation in sensor signals to account for variation due to temperature change [23, 22].
- Corrections for errors or anomalies arising due to SEEs [51], annealing in the floating gate MOSFET [18, 34], *Rapid Recovery* effect (see chapter 5) or any faults detected in the operation of the Radiation Payload.

It is to be noted that this is not an exhaustive list. As research and testing on the FGDOS progresses, further measures to improve the accuracy of processed data may come to the fore. The outcome of the post processing block would be an estimate of the radiation environment, as measured by the MAIN and Daughterboard sensors respectively. These estimates can then be further analyzed and interpreted by using models of the previously mentioned modulation blocks. To clarify, the models in question can be used to de-modulate the measured environments, thereby leading to the main set of processed science results that are depicted in the final green box on the right of Figure 4.1. These results would consist of:

- Characteristics of radiation environment measured over the mission duration, corresponding to various mission phases and space radiation environments including LEO, VAB, cis-lunar, lunar orbit and lunar surface. This would be expressed in the form of various metrics such as dose, dose rate and TID.
- Estimates of radiation exposure for the rover and its subsystems, which can be used for radiation risk assessments and for the specification of radiation tolerance requirements and design margins in future design iterations of the rover, or other similar miniaturized systems. The effectiveness of shielding provided by the rover's Aluminum structure can also be judged from this.
- Experimentally derived representative thermal environments for payloads and subsystems in the rover.

In addition to these results, some technologically significant results could also be derived. For instance, the measured environments could be used for radiation transport model validation at various stages and complexity levels.

In summation, the mission would involve the flow of physical quantities and digital information from left to right in Figure 4.1, until the *Measured Environments* are obtained. Using the scientific scheme discussed here and engineering models corresponding to the blocks in the science schematic, the measured environments can be propagated through analysis and further processing, to obtain estimates of the actual *Mission Radiation Environment*. This is the simplest condensed account of the science of the Lunar Zebro Radiation Payload. If the science mission is successful, the results would constitute a full-fledged technology demonstration of the Radiation Payload as well as the ability of the Lunar Zebro to host science payloads.

## 4.2. Radiation Environment Analysis & Modelling

ESA's SPENVIS tool (describe briefly in chapter 2) was used to derive the expected radiation environments which the Radiation Payload (and the Lunar Zebro rover) will be exposed to during the mission. The environment on the lunar surface was estimated using NASA's OLTARIS tool [110].

To verify that SPENVIS was being used correctly and that the generated results could be considered valid, some sample models were set up and executed in SPENVIS based on instructions and tutorials provided on the SPENVIS website [48]. The radiation environment modelling and effects evaluation presented in [89]

were reproduced using the parameters described in that study, for the purpose of further validation of the analysis methodology.

#### 4.2.1. Mission Segments & Models

Based on the functionality provided by SPENVIS and the assumed mission definition presented in chapter 3, an overview of the parameters and radiation environment models that were used for the analysis in SPENVIS and OLTARIS can be found in Table 4.1. In SPENVIS, the mission was set up as a 3-segment trajectory starting in LEO and ending in near Earth interplanetary space (which is also representative of the Lunar radiation environment) <sup>1</sup>. Starting in January 2024, the total mission duration was chosen to be 125 days, accounting for the longest possible amount of time each phase of the lunar mission could take. This results in a conservative/worst case estimation of the radiation doses and exposure that would be accrued throughout the mission. The analysis parameters and models were selected taking the recommendations made by ECSS standards into consideration [43, 44].

Phase	Details	Radiation environment analysis settings
Pre-Launch	Launch Duration: <1 day	NA
Earth Orbit	LEO orbit for ~4 days [67]; Exposure: 20 rads/day [8]	<i>SPENVIS Segment1</i> : Circular Earth Orbit; Altitude: 300 km; Inclination: 30 deg ; Duration: 4 days
Transit	cis-lunar orbit from ~5 days - 2 months [67]; 1 rad /day of exposure [8]	<i>SPENVIS Segment2</i> : Elliptical Earth Orbit with VAB passage; Perigee altitude: 300 km, Apogee: 378029 km (Earth-Moon distance) for 1 day
Lunar orbit	6000 km to 100 X 100 km for ~6 days - 2 months [67]	<i>SPENVIS Segment3</i> : Near Earth Interplanetary orbit at 1 AU (Includes cis-lunar transit); Duration: 60 days
Lunar Surface	12-14 Earth days (1 lunar day)	Lunar surface environment in OLTARIS [110] Duration: 14 Earth days

**Table 4.1:** Overview of radiation environment modelling

#### 4.2.2. SPENVIS & OLTARIS Analysis

The selection of models and environment types was based on the work presented in [89], recommendations made by the ECSS standards and the SPENVIS/OLTARIS user forums [48]. Table 4.2 presents the radiation environment models which were chosen to correspond to various radiation sources that are relevant to one or more mission segments.

Radiation source / particle type	Model used in SPENVIS
Solar particles	CREME-96 [144], ESP-PSYCHIC [156]
GCRs	ISO-15390 [97]
Trapped particles	AP-8/AE-8 & AP-9/AE-9 (IRENE models) [99]

**Table 4.2:** Models used in SPENVIS for various radiation source types

On the basis of the design of the Lunar Zebro rover's chassis, the amount of shielding was assumed equivalent to 1.5 mm of Al <sup>2</sup>. An additional 2mm of Al shielding was attributed to the lunar lander spacecraft according to the recommendation made in [67]. To simplify the analysis and calculations, the shielding was assumed to be spherical and uniformly distributed in nature.

#### Low Earth Orbit, Transit & VAB crossing

In LEO, the model was set up with a circular orbit at 300 km altitude and an inclination of 30 deg, to approximate the parking orbit and checkout phase of the mission. The orbit inclination was chosen based on the

<sup>1</sup><https://www.spennis.oma.be/forum/viewtopic.php?f=1&t=441>

<sup>2</sup>the chassis is effectively a 5-sided Al box with 1.5 mm thick walls. The bottom is made of a ceramic matrix composite (CMC) plate

orbital inclination of the the Apollo spacecrafts before trans-lunar injection <sup>3</sup>. The segment duration was chosen to be 4 days, time during which the spacecraft would be exposed to GCRs (derived from the the ISO-15390 model) and SEPs (calculated using the ESP-PSYCHIC model). During each orbit, a disproportionate contribution to the radiation exposure is provided by the SAA due to a non-zero orbital inclination. This can be seen in Figure E.13 and Figure E.14.

Segment 2 was set up to partially approximate the transit phase of the lunar mission i.e. the interval corresponding to the trajectory segment starting with the TLI burn until the passage through the outer VAB. This was done by choosing a highly elliptical Earth orbit with perigee at the same altitude as the previous circular orbit and apogee at the Moon. The inclination of the orbit was kept the same as before. It was determined that a segment duration of 2 days was sufficient to include the traversal through both VABs as well as Earth's Magnetopause [125].

Figure 4.2a and Figure 4.2b respectively show the integral/differential flux of trapped protons and trapped electrons that the spacecraft would likely experience.

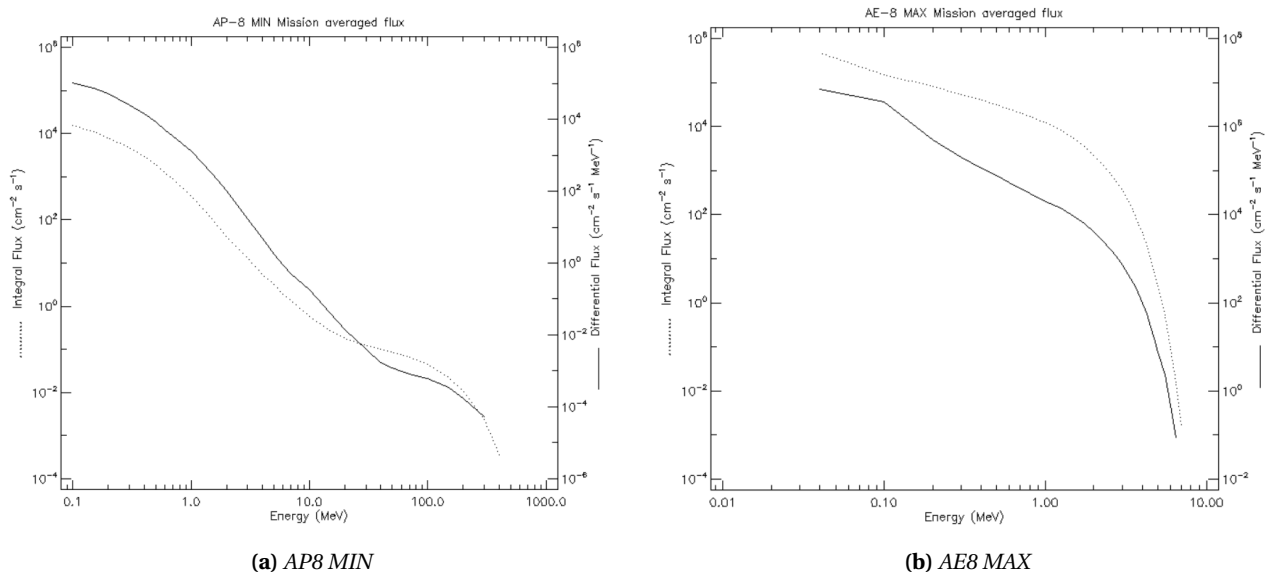


**Figure 4.2:** Distribution of differential and integral flux from trapped particles in Earth orbit

Figure 4.2 shows that incident trapped electrons have much lower kinetic energies at a given flux than trapped protons. This explains the utilization of proton beam sources for radiation testing of space hardware in general, aside from the overwhelming abundance of protons in the space radiation environment. The proton integral flux drops below  $0.01 \text{ cm}^{-2} \text{ s}^{-1}$  at 200 MeV and above. This corresponds to a flux of  $2.5 \text{ E}^{-3} \text{ s}^{-1}$  at 200 MeV over the  $5 \text{ mm} \times 5 \text{ mm}$  cross-section of the FG DOS chip. The electron integral flux drops below  $1 \text{ E}^4 \text{ cm}^{-2} \text{ s}^{-1}$  at 1 MeV and above.

The biggest peaks in the trapped radiation vs time plots (Figure 4.3) correspond to the passage of the spacecraft through the VABs. It was observed that peak for proton belt passage was sharper than electron flux peak. However, the electron flux is consistently higher in magnitude. Also, the electrons have generally lower energies than the protons. This indicates that while passing through the outer belt, electrons are the dominant source of radiation exposure. As soon as the spacecraft cruises clear of the outer VAB, the flux begins to drop steeply, going down to extremely low values that correspond to the interplanetary radiation environment.

<sup>3</sup>[https://web.archive.org/web/20041118103812/https://history.nasa.gov/SP-4029/Apollo\\_18-24\\_Translunar\\_Injection.htm](https://web.archive.org/web/20041118103812/https://history.nasa.gov/SP-4029/Apollo_18-24_Translunar_Injection.htm)

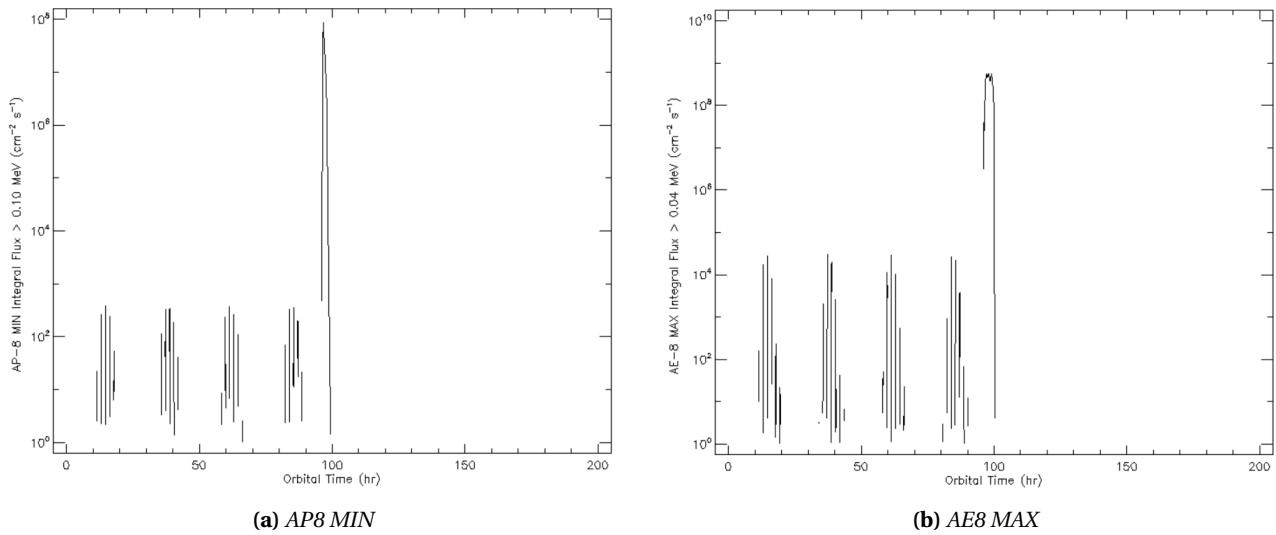


**Figure 4.3:** Integral flux from trapped radiation vs orbital time elapsed

The peak flux and total fluence of solar protons and ions was obtained using the CREME-96 and ESP-PSYCHIC models respectively as prescribed by the ECSS standards [43]. The results are shown in Figure 4.4. The peak 5 minute fluxes and total fluences with a confidence level of 97.725% were derived for a quiet magnetosphere in SPENVIS. As expected, solar proton flux is much higher than the flux of solar ions, but solar ions can cause more damage per interaction owing to the higher charge, momentum and stopping power. Similar observations can be made for the total solar particle fluences derived from ESP-PSYCHIC, shown in Figure 4.5.

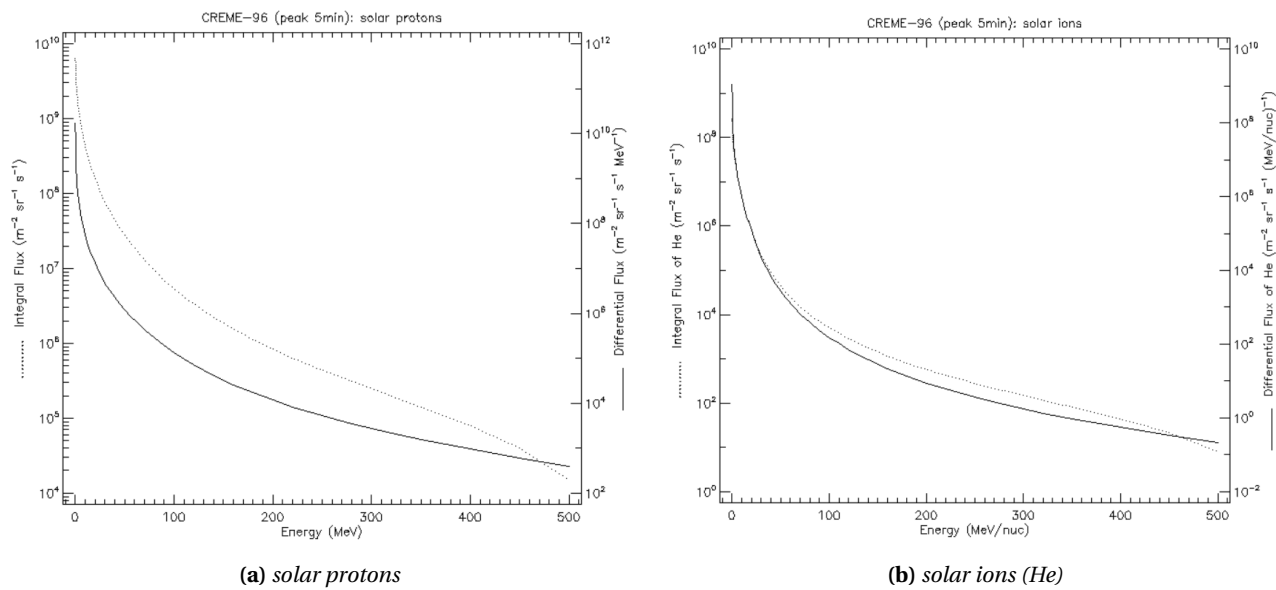


**Figure 4.4:** Peak differential and integral flux of solar particles from CREME-96

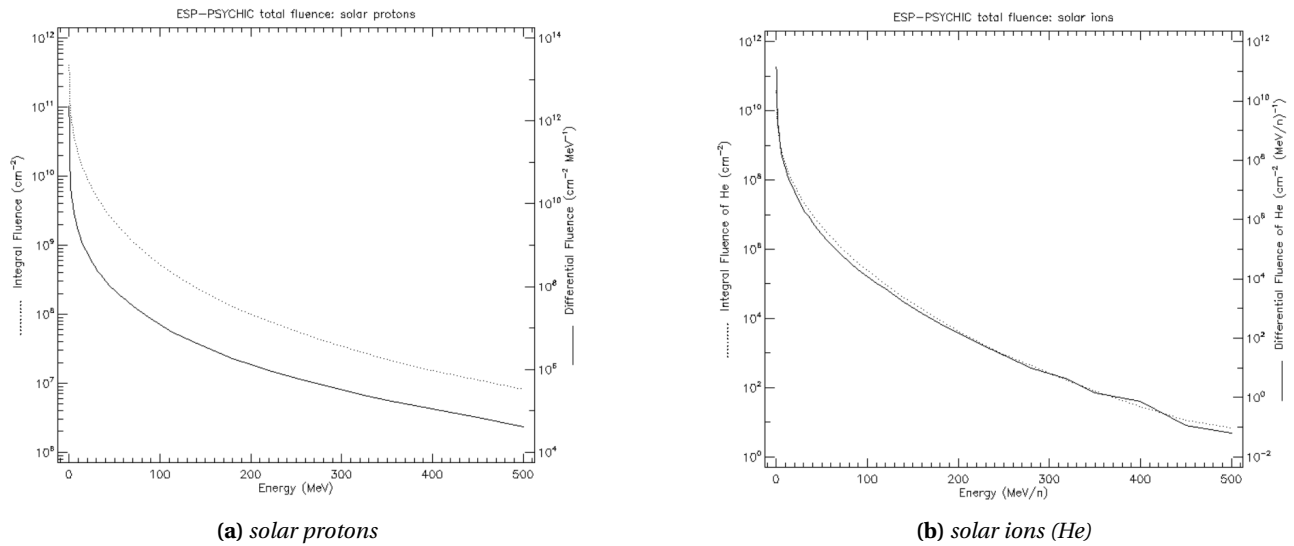


**Figure 4.5:** Total differential and integral fluence of solar particles from ESP-PSYCHIC

The orbit averaged flux behind shielding for protons, electrons and neutrons was derived from the MFLUX tool in the SPENVIS model. This information can be seen in the plots in Figure 4.6.

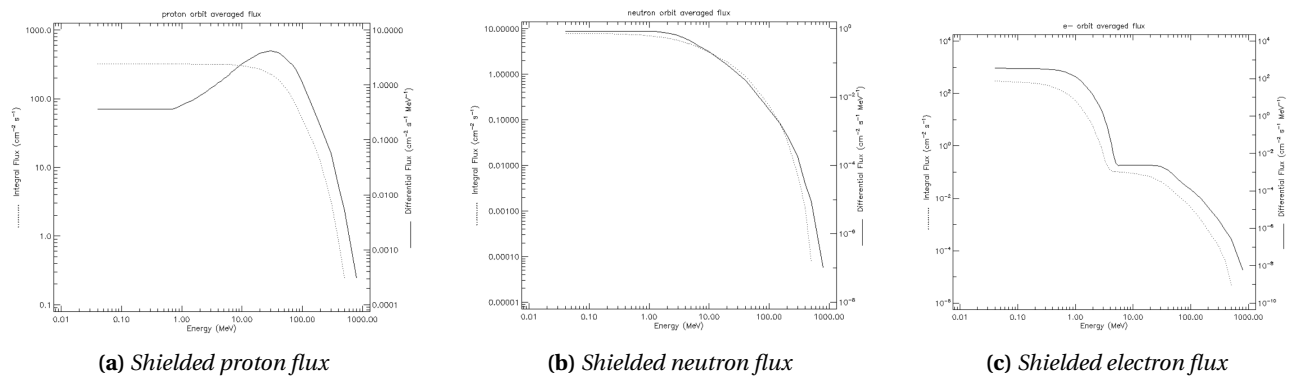


**Figure 4.6:** Shielded flux from SPENVIS

The contributions of trapped protons, trapped electrons as well as solar protons was included to calculate the shielded flux. A shielding depth of  $1.0 \text{ g/cm}^2$  ( $\sim 3.75 \text{ mm}$ ) was used to approximate the combined shielding provided by the lander spacecraft and the rover chassis. Thus, this provides an estimate of the radiation environment that would be present inside the spacecraft. The proton flux peaks at about 40 MeV. The neutron flux is seen to be relatively constant at low energies up to  $\sim 2 \text{ MeV}$ , thereafter it begins to decline. There are two energy ranges in which the electron flux remains relatively constant, up to  $\sim 0.5 \text{ MeV}$  and from about  $5 \text{ MeV} - 50 \text{ MeV}$ .

### Transit & Lunar Orbit

Segment 3 was set up to approximate the transit from the Earth to the Moon (outside the VABs) as well as the orbit of the lunar lander spacecraft around the Moon. Thus, the duration for this segment was set at 119 days. In SPENVIS, the *Near Earth Interplanetary* orbit at 1 AU was chosen for this purpose. This accounted for exposure from GCRs as well as SEPs in free space. It should be noted that during the lunar orbit phase, exposure would go down as the spacecraft approaches the Moon and transitions into successively lower orbits around it. This reduction in exposure due to shielding by the Moon's disk is not taken into account in SPENVIS.

The GCR spectrum of H ions (protons) was obtained from SPENVIS using the ISO-15390 model with a 2-sigma deviation. Again, a quiet magnetosphere condition was chosen in order to get a better appreciation of the GCR flux as a result of moderate to low shielding from the Earth's magnetic field.

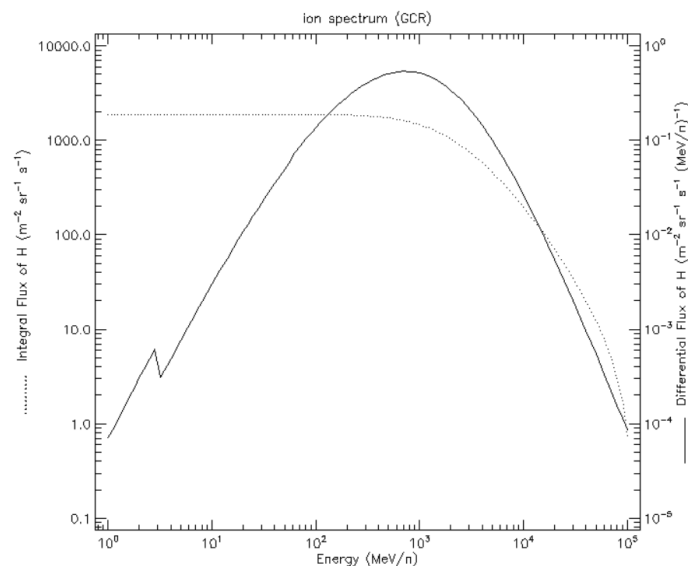


**Figure 4.7:** Proton GCR spectrum

It can be noticed that the peak proton flux corresponds to an energy of 1E3 MeV/n. Considering a solid angle of  $4\pi$  steradian, the integral flux over the cross-section of the FGDOS chip would be about  $0.1 \text{ s}^{-1}$ . Hence, this shows that the GCR flux that would interact with the FGDOS detectors would be extremely low.

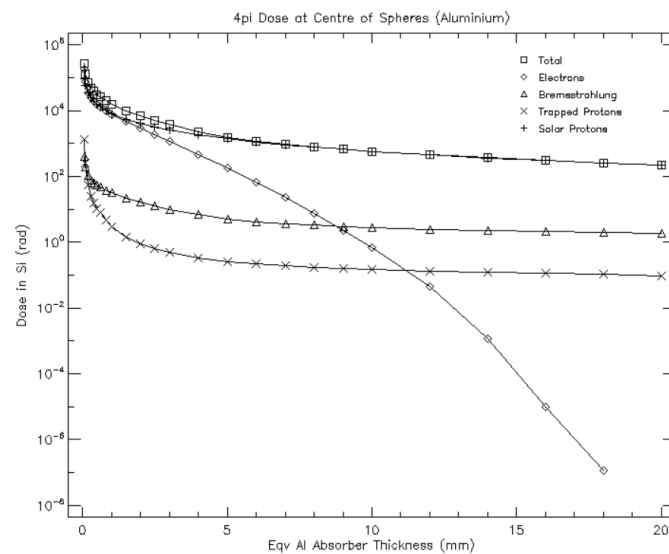


**Figure 4.8:** Dose depth curve obtained from SHIELDDOSE-2Q

About 99.8 Gy of dose is delivered behind a shielding depth of 1.5 mm Al for the entire mission. This constitutes only the shielding provided to the Radiation Payload by the rover. Considering an additional 2 mm of Al shielding from the lunar lander [67], the dose falls to about 30 Gy for the mission. It can be seen from the dose vs. depth curve in Figure 4.8 that at the relevant shielding thickness, most of the dose comes from solar protons and electrons, followed by bremsstrahlung emissions in the aluminium shielding. Trapped protons have a much lower contribution to the dose. As the shielding depth increases, the dose due to electrons is seen to drop steeply, due to the low average kinetic energies which cause electrons to deposit most of their dose at low shielding depths.

### Lunar Surface

Since SPENVIS does not have the feature to simulate the radiation environment specifically at the lunar surface, the OLTARIS tool [126] (developed and managed by NASA) was used for analyzing this phase of the mission. OLTARIS was used to evaluate the GCR environment at the lunar surface and also to simulate

the radiation environment during an SPE event. It is important to note that OLTARIS uses the HZETRN radiation transport code [96] to evaluate various quantities such as delivered dose, differential and integral flux/fluence along with shielding. An important advantage of OLTARIS to evaluate the radiation environment is that it also includes the contribution provided by lunar albedo, obtained by transport of the incident radiation through a slab model of lunar regolith. OLTARIS models are based on real observations performed at the Moon using the CRaTER instrument [110], which make it an invaluable resource for estimating the radiation environment in the vicinity of the Moon.

The typical workflow for OLTARIS simulations is shown in Figure 4.9. The actual steps that were followed, along with the inputs used in the online tool at each step are documented in Appendix E.

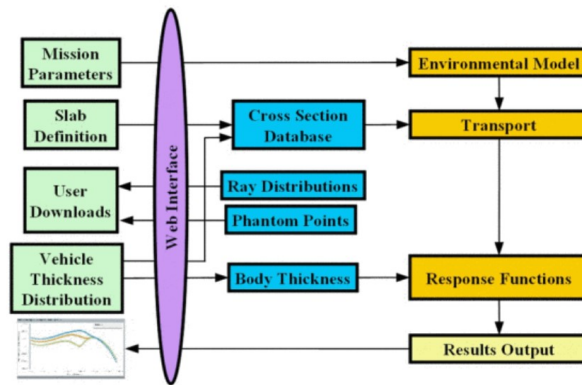


Figure 4.9: Typical OLTARIS Workflow [126]

To emulate the shielding provided by the rover, an Aluminum sphere of 1.5 mm ( $\sim 0.4 \text{ g/cm}^2$ ) shielding thickness was chosen. For the GCR environment on the lunar surface, the BON 2020 model [127] was used, specifically at the historical solar minimum of 2010. Since solar activity and GCR flux are anti-correlated, this setup led to high estimation of GCRs, particularly because the 2010 Solar minimum was observed to be unusually deep compared to previous minima [130, 80, 116]. The GCR spectrum included ions from  $Z=1$  to 28 (H to Ni) and the mission duration was set to 14 (Earth) days. The GCR spectrum was transported by OLTARIS using 1D HZETRN radiation transport. The doses and LETs were computed by OLTARIS in Silicon (Si).

GCR differential flux at the external boundary of the vehicle i.e. when the effect of the shielding is absent, can be seen in Figure 4.10. It is apparent that the incident cosmic radiation is composed mainly of protons and alpha particles. In contrast the flux of neutrons is seemingly negligible. Peak proton flux occurs at an energy of about 380 MeV/nucleon whereas the peak alpha particle flux occurs at a lower energy of about 200 MeV/nucleon.

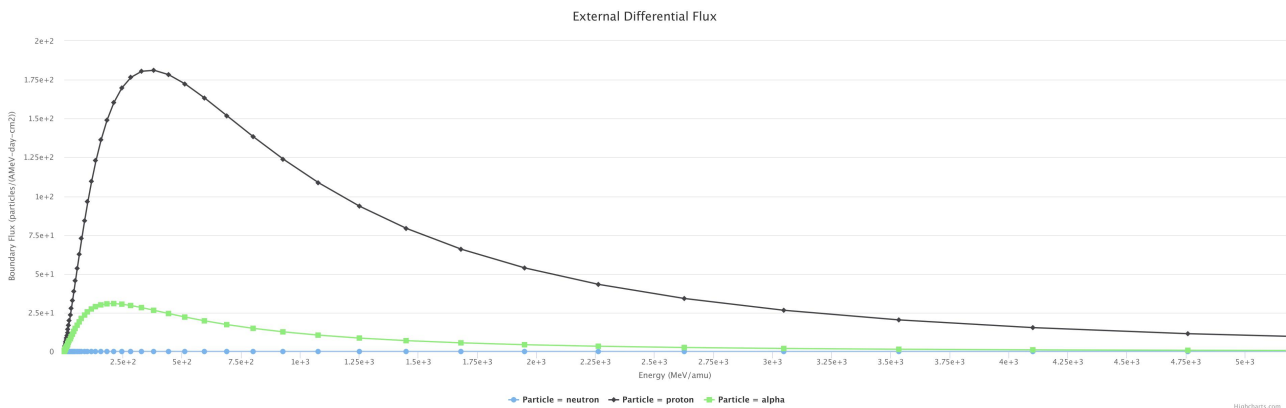


Figure 4.10: GCR differential flux at boundary

The doses obtained during the mission due to GCRs was found to be a minuscule 2.88 mGy at a dose rate of

0.21 mGy/day. Approximately 75% of the TID is contributed by freespace GCRs, while lunar albedo makes up the other 25%.

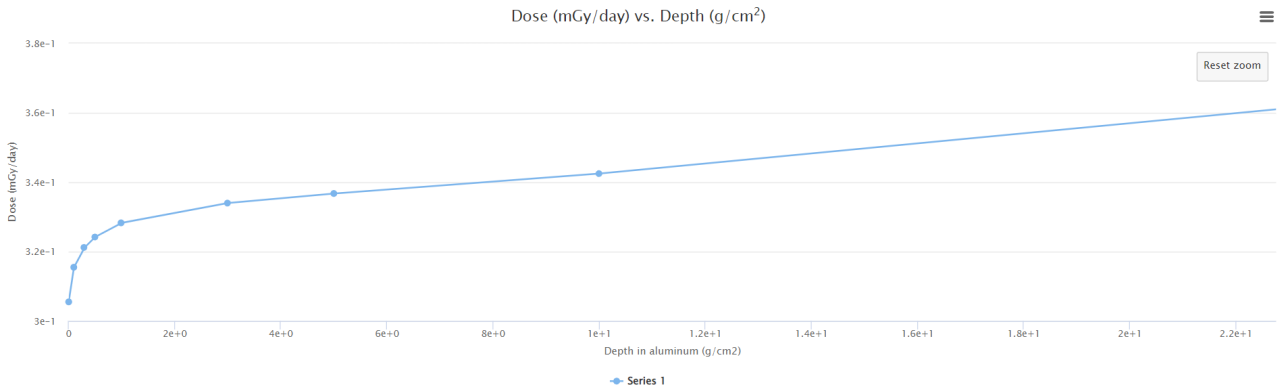


Figure 4.11: GCR dose v depth curve

The dose deposited at a shielding depth of 1.5 mm aluminum is about 0.32 mGy/day due to GCRs at the lunar surface. It is important to note that the dose deposited by GCRs actually goes up with an increase in shielding depth to a certain extent, thereafter decreasing monotonically. This trend (seen in Figure 4.11) can be attributed to fragmentation and the generation of secondaries, including high LET nuclei from neutrons produced within the shielding [39]. Similar results were obtained for the transport of GCRs at the lunar surface by [38] and for deposition of GCR dose in the ISS [30]. It can be seen from Figure 4.12 that most of the accumulated dose is due to protons and alpha particles, the primary constituents of cosmic rays.

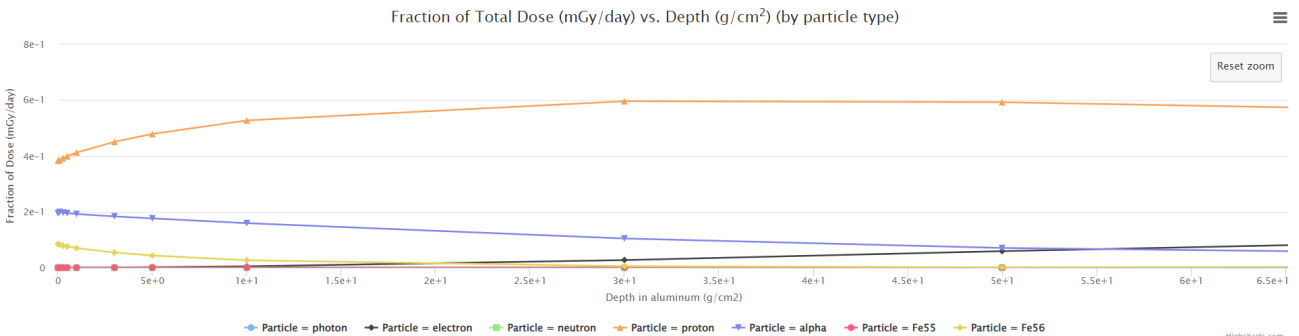


Figure 4.12: GCR dose v depth curve: contribution of various particles

The albedo flux at the boundary i.e. without the vehicle can be seen in Figure 4.13. As expected, neutron flux dominates the rest at low energies (up to ~0.075 MeV/amu). This consists of thermal, epi-thermal, slow and intermediate neutrons [38, 116]. Above 0.075 MeV/amu, the albedo flux consists mainly of photons, peaking at about 0.125 MeV/amu and declining steadily thereafter.

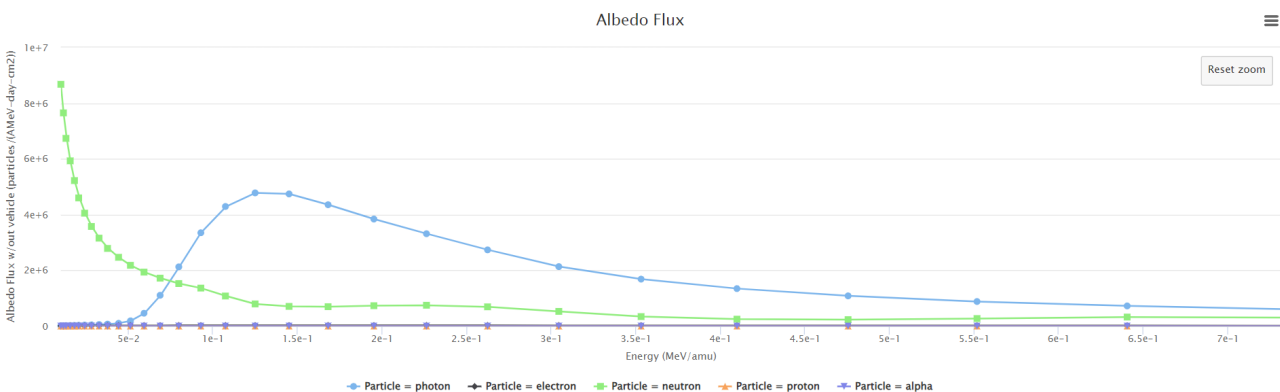
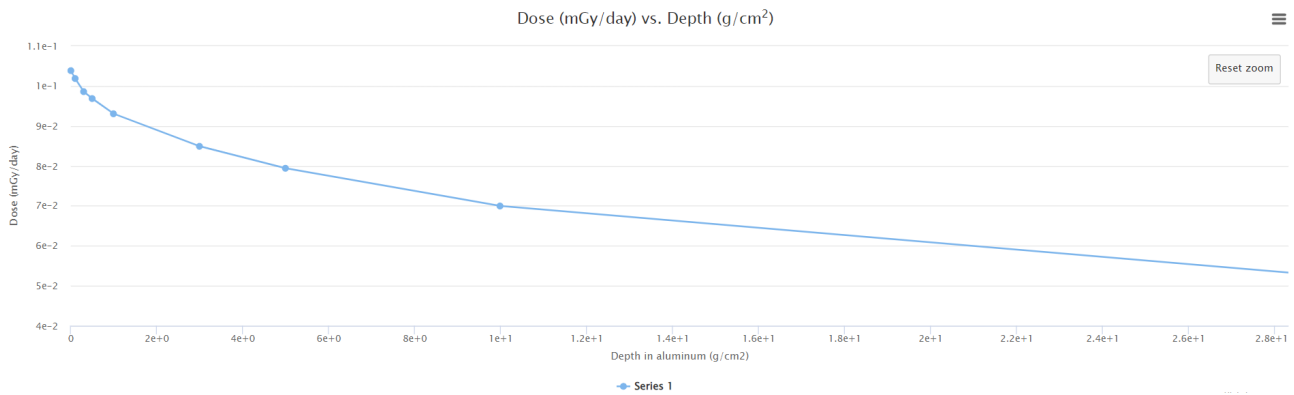


Figure 4.13: Lunar albedo flux

For lunar albedo, it is seen that the dose goes down monotonically with increase in shielding depth. The dose deposited by lunar albedo near the surface, at a shielding depth of 1.5 mm aluminum is about 0.098 mGy/day. Hence, the albedo particles can be blocked quite effectively by the Aluminum chassis, thereby shifting the burden of detecting the majority of albedo dose to the Daughterboard FGDOS of the Radiation Payload.



**Figure 4.14:** Lunar albedo dose v depth curve

Most of the albedo dose comes from protons and electrons. Pions, alpha particles, positrons and photons provide minor dose contributions, as seen in Figure 4.15. Despite the fact that protons make up a low proportion of the albedo flux, they still have high impact on the dose deposited, as compared to photons and neutrons.

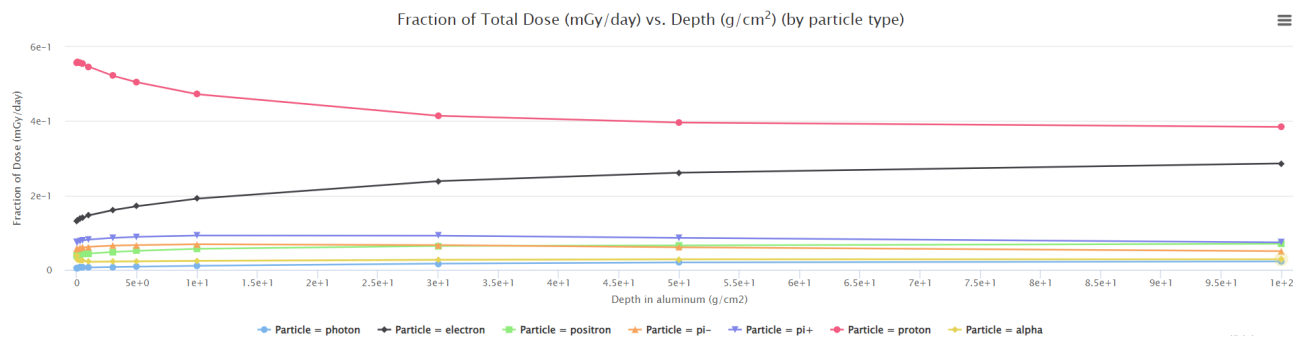


**Figure 4.15:** Lunar albedo dose v depth curve: contribution of various particles

While the probability of occurrence of an SPE during the Lunar Zebro Mission is difficult to anticipate at present, it would be extremely interesting to observe the characteristics and effects of such an SPE. Hence, an historical SPE event was simulated with OLTARIS, namely the 1972 King event [74]. This is an event of historic interest since it happened between the Apollo 16 and 17 missions and would have posed the threat of acute radiation sickness had a human spaceflight mission been in flight at the time [101].

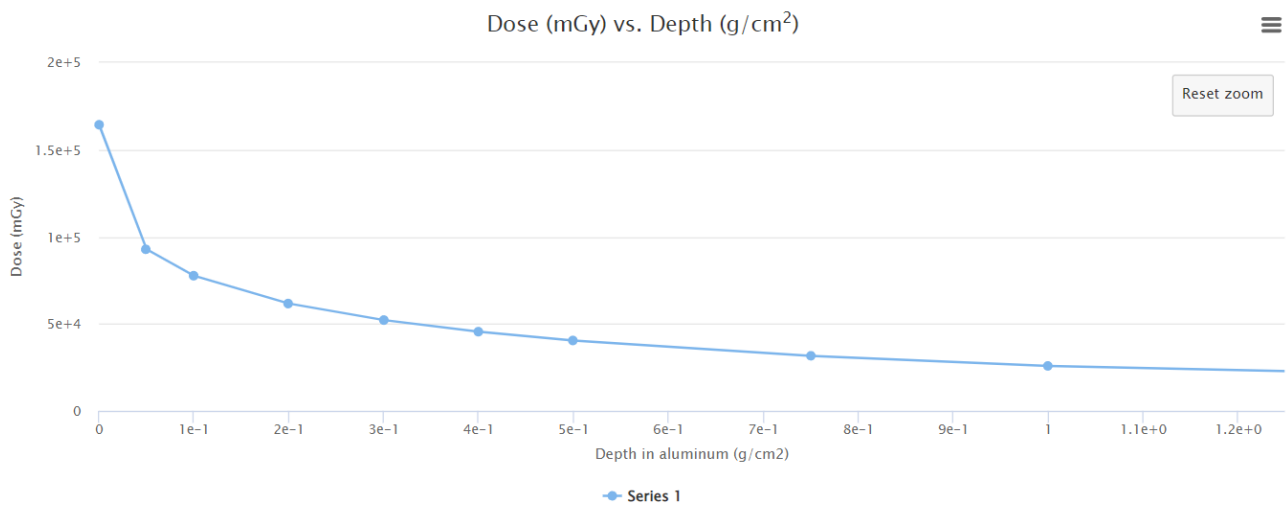


**Figure 4.16:** SPE dose v depth curve

The dose depth curve indicates that about 45.48 Gy of dose is accumulated for a shielding depth of  $0.4 \text{ g/cm}^2$ . It can be seen in Figure 4.17 that the majority of dose deposited at low shielding depths is contributed by solar protons, with solar electrons being the other main contributor at much higher shielding depths.

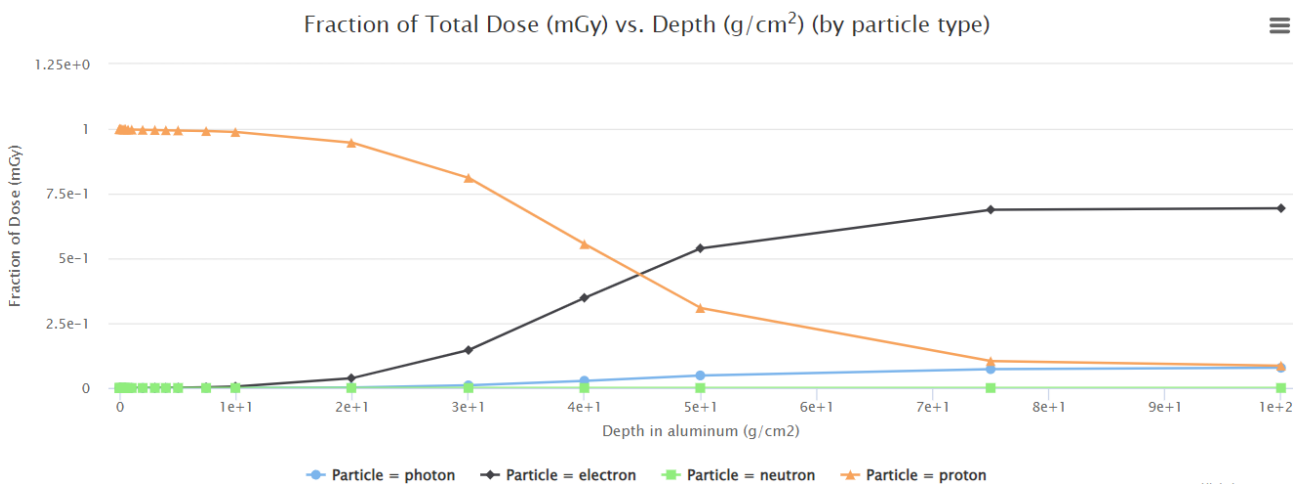


**Figure 4.17:** SPE dose v depth curve

### 4.2.3. Assumptions and limitations

The following limitations were observed in the model setup and the analysis methodology, which could have introduced errors and uncertainty in the test results:

- Spherical shielding models were used for the evaluation of flux and dose at the Radiation Payload. In reality, the rover would offer variable shielding along different directions. The use of sector shielding analysis techniques using tools such as Geant4 or FASTRAD is advisable to evaluate this.
- It is important to note that the presence of the vehicle (and the shielding it provides to the internal subsystems) is ignored for transport of lunar albedo particles in OLTARIS to a large extent in calculating the total deposited dose. This is the case for the GCR environment calculations. For SPE calculations, the albedo is taken to be zero based on the assumption of total blockage by the vehicle [126].
- In the tools currently used for radiation assessment, static models of the radiation environment are being used to evaluate for an environment which in reality is temporally dynamic in nature. Hence, the results obtained in this work do not necessarily capture the time dependent behavior of the radiation environment. Only in specific cases such as the simulation of SPEs and historic GCR levels is this limitation alleviated.

- The fluxes and fluences of SEPs are assumed to be isotropic in SPENVIS. However, this is not always true, especially in the initial stages of an SPE event [43]. Similarly, assumptions of isotropy are applicable for GCR fluxes in interplanetary space but not in the close vicinity of the Moon, due to the obstruction posed by the body of the Moon.
- The AP8 and AE8 models are based on cumulative averages of data collected over a long term. As such, these models are most appropriate for missions that spend more than 6 months in LEO. For shorter missions such as Lunar Zebro, statistical variations and uncertainties can be significant due to the short time interval of exposure to trapped particles [43].
- The mission was assumed to begin Jan 2024, but the launch date is subject to change. Hence, the analysis should be periodically updated based on new estimates of the project timeline. Of highest importance is the magnitude of solar activity at the time of the mission, which would dictate the nature and characteristics of the space radiation environment encountered by the rover and Radiation Payload.

#### 4.2.4. Results & Discussion

The following results can be gathered from the mission radiation environment modelling and analysis discussed heretofore:

1. Table 4.3 provides a summary of the expected radiation exposure during various mission phases, as derived from the analysis using SPENVIS and OLTARIS. The ispace user guide indicates a TID of 10 krad (100 Gy) behind 2 mm of Al shielding [67]. The results obtained by the analysis methods described here yielded total mission dose of about 99.8 Gy behind 1.5 mm of Al shielding and about 30 Gy behind 3.5 mm of Al shielding respectively. The latter being the estimate that includes aggregated shielding provided by the lander and rover to the Radiation Payload. On the lunar surface, only the shielding provided by the rover is considered relevant. Moreover, the exact shielding from the lander is still yet to be confirmed. Therefore, the doses expected behind 1.5mm of Al shielding for the duration of the mission are provided in Table 4.3.

Mission Phase	Radiation Sources	Dose after shielding (in Si)
LEO & VAB passage & Transit	Electrons, Protons, GCRs, SEPs	99.8 Gy (30 Gy behind 3.5mm Al shielding)
Lunar Surface	GCR & SEPs, Lunar albedo	2.88 mGy at 0.206 mGy / day
Lunar Surface	SPE event – Aug 1972	45.48 Gy

**Table 4.3:** Summary of mission doses and dose rates (behind 1.5 mm Al shielding)

2. A comparison of the results of the radiation environment models and data analysis presented here to historic mission observations from scientific instruments (discussed in section 2.2) can be gauged from Table 4.3 and Table 4.4. The dose rates expected on the lunar surface (from LND) and in Lunar orbit (from CRaTER) are in close agreement with the estimates from OLTARIS. In LEO, the observations from DOSTEL (outside the ISS) provide an estimate of the expected dose rates. With reference to the dose rates and fluxes in Earth orbit, RADOM and L4M results reaffirm that most of the mission dose will be accrued in LEO and VAB crossing, with the interplanetary dose rates being about the same as the dose rates in lunar orbit <sup>4</sup>. This is also the case for the interplanetary environment beyond 1 AU, as shown by the results for Mars cruise. Due to the Martian atmosphere, the dose rates on the Martian surface are lower than that on the Moon.

<sup>4</sup>As mentioned in section 2.2, the transit dose measurements from RADOM were lower than expected due to various factors such as spacecraft shielding and spectrometer dead time

Mission Phase	Mission Environment	Radiation source	Dose rate	Data source
Earth orbit	LEO	SEPs, GCRs, trapped	33.6 mGy/day	DOSTEL [14]
Earth orbit	VABs	Trapped protons + electrons	2.4 Gy/day	RADOM [32]
Cis-lunar transit	VAB crossing	Trapped protons + electrons	Total dose = 0.24 Gy	L4M [27]
Cis-lunar transit	Interplanetary	GCRs and SEPs	0.31 mGy/day; Total transit dose = 1.3 Gy	RADOM – transit & capture [32]
Lunar orbit	Interplanetary	GCRs and SEPs	0.5 mGy/day	CRaTER [116, 80]
Lunar surface Ops	Lunar surface	GCRs, albedo, SEPs	0.32 mGy/day	LND [159]
Mars transit and orbit	Interplanetary	GCRs and SEPs	0.24 - 0.48 mGy/day	MARIE and MSL - RAD [158]
Martian surface	Mars surface	GCRs and SEPs, secondaries	0.21 mGy/day	MSL-RAD [158]

**Table 4.4:** Dose results from historic data

3. From a scientific perspective, it is desirable for the Radiation Payload to be activated and to begin operating in LEO itself, given the sizeable dose forecasted for the initial part of the mission.
4. The Radiation Payload should be powered ON as long as possible during all mission phases in space to maximize the measurements time and the scientific return from the Lunar Zebro mission.
5. The sampling rate of the Radiation Payload should be increased during VAB crossing to acquire data with a higher time resolution, to fully capture the effect of high doses and dose rates on the sensor frequency, expected in this time period.
6. In the transit phase (post VAB passage) and in lunar orbit, the sampling rate can be reduced since the expected dose rates are very low, leading to low accumulated doses over a given time period. Depending on the time duration of the transit, some power saving measures may also be implemented on the radiation Payload, such as using the Low Power Mode (LPM) on the MSP430 MCU [139] or going in and out of sleep mode periodically. Since the FGDOS on the Daughterboard will experience relatively lower shielding than the Main Board FGDOS, it would be beneficial to acquire data from the external sensors more frequently in this mission phase.
7. On the lunar surface, the Radiation Payload should perform measurements at a high resolution. Hence, the Radiation Payload should be operated at high sampling rates over a considerably long measurement window in order to acquire adequate data such that statistically significant results can be obtained and noise can be filtered out in post processing as much as possible. This is necessitated by the very low dose rates (about 0.2 - 0.5 mGy/day) that are expected during lunar surface operations, as exemplified by Figure 4.18 from recent results of the CRaTER micro-dosimeter.
8. In the event of an SPE, the sampling rate of the Payload should be raised again, since significant dose accumulation is expected, depending in the strength and nature of the event. In case it is decided that the rover's subsystems are to powered OFF to protect them, the Radiation Payload should still be powered ON and allowed to function independently, storing data on it onboard memory. If this is deemed infeasible, the Radiation Payload should be switched to passive mode.
9. When considering the different radiation species and environments that will be encountered during the mission, the salience and significance of the distributed detection architecture of the Radiation Payload comes to the fore. Given that the Daughterboard FGDOS will have lower shielding, it is suited to detecting doses from SEPs and lunar albedo particles, in addition to GCRs. Since the chassis of the rover would provide shielding to the Main Board FGDOS, it is better suited to detecting doses from GCRs. As such, on analysing the data from the internal and external FGDOSs, some conjectures about the shielding effectiveness and relative abundance of various radiation particles can be surmised. This aspect can be explored in a more quantitative and defined manner with the use of detailed radiation transport models, as discussed in the next section.

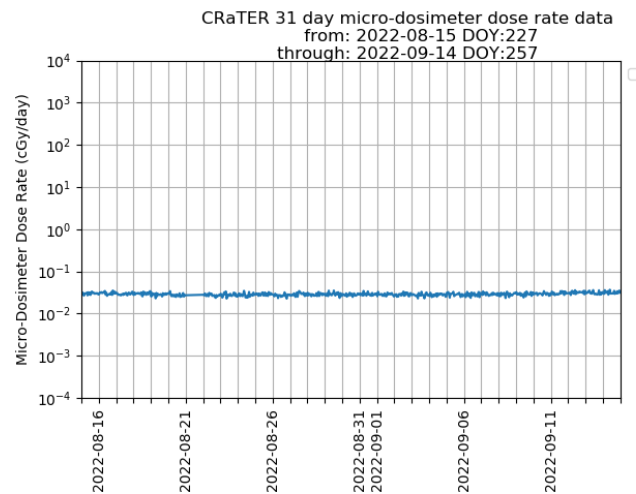


**Figure 4.18:** Dose rates from crater microdosimeter [146]

### 4.3. Radiation Transport Simulations using Geant4

Once the expected radiation environment has been derived and analyzed, the next logical step is to model the interaction of the environment with science instruments and their requisite detectors. Results from previously flown science instruments [87, 159, 116] and simulation studies [38, 93] have indicated that the radiation environment near the lunar surface is a rich mixture of primary cosmic rays and solar energetic particles, which give rise to a whole host of secondaries ranging from protons and electrons to neutrons, photons, pions etc. Such conditions can be very difficult to replicate in an experimental setting. This serves as the motivation for building models where mixed radiation fields can be repeatedly simulated in a virtual environment. To ensure accurate and valid results, such models need to be verified with other computational models and validated with experimental results as much as possible. To model the interaction of the LZ Radiation Payload with the rich radiation fields on the Moon, it was ascertained that Monte Carlo based radiation transport simulations could be conducted [122]. Such simulation models have previously been set up and validated for other instruments [79, 80]. The preparation of such a model for the Radiation Payload would constitute considerable progress toward the global payload science scheme described in Figure 4.1.

A complete and comprehensive characterisation of the lunar radiation environment would consist of information regarding particle types, energies, fluxes, angular and spatial distribution of primary and secondary radiation and LET spectra, among other quantities. With a radiation dosimeter, such extensive characterisation is not feasible based on mission observations alone. However, if a holistic radiation transport model of the science instrument containing the payload and its spacecraft platform can be created, the mission observation data can function as an input to this model, thereby enabling the aforementioned characterisation to a large extent. Derivation of such rich characterisation from simple dose measurements via the creation of transport models has been demonstrated in recent studies [79, 75]. Several Monte Carlo radiation transport models have been developed for predicting the radiation environment at planetary surface and sub-surface levels. Thus, it is possible to include phenomena such as regolith shielding and albedo generation in transport models concerning the Radiation Payload, resulting in the ability to simulate scientific measurements with a model that is highly representative of mission conditions.

The Moon consists of various features such as rilles, craters, lava tubes, ridges, boulders, basins and maria [28], that can modulate the effective radiation field in proximity [93]. The modulation or influence of these Selenographic landscape features is relevant for shielding from exposure to cosmic rays and SPEs. This influence can also be used to see the effect of *space weathering* on lunar regolith as a result of exposure to energetic particles [80]. Physically, the modulation is manifested in the form of secondary radiation in the vicinity of the lunar surface, which can be sensed and measured with in-situ instruments. Dobynde and Guo [38], reported that the secondaries generated at the lunar surface are mostly isotropic in nature, while sub-surface secondaries preferentially propagate deeper into the Moon. The secondary flux increases at first with soil depth and later reduces beyond a depth of about 1 m. As alluded to previously, secondary generation reflects attributes of the soil such as composition and density distribution, which may lead to

indicators regarding the presence of sub-surface water ice. Hence, it is extremely interesting to explore how the Radiation Payload and Lunar Zebro could be used for such scientific investigations.

In conjunction with estimates of primary sources that are based on expected environments, transport simulations can be performed to model and simulate the response of the Radiation payload and its detector to the aforementioned radiation fields made up of primary and secondary radiation on the Moon. On a larger scale, such models would include simplified representations of the aforementioned lunar landscape features. The features themselves would be made up of mixtures of chemical elements and compounds which approximate the composition<sup>5</sup> of lunar regolith according to samples retrieved in the past [100]. The results from these simulations can also be fed into the design process to produce more sophisticated iterations of the Radiation Payload. Accordingly, a set of preliminary radiation transport models were developed as a foundation to enable more extensive modelling in the future. In this section, these models are described with some preliminary results and validation.

#### 4.3.1. Simulation Methodology & Plan

The Geant4 toolkit (introduced in subsection 2.1.4) was used for creating and simulating transport models of the Radiation Payload. A virtual linux machine with an installation of Geant4 (version Geant4.11.0.1)<sup>6</sup> created by LP2i Bordeaux [65] was used for this purpose. To verify the correct installation and usage of this virtual machine, the in-built basic examples (B1-B5)<sup>7</sup> provided in Geant4 were compiled and executed. It was verified that usage of the input files provided with the installation led to outputs that matched expected results.

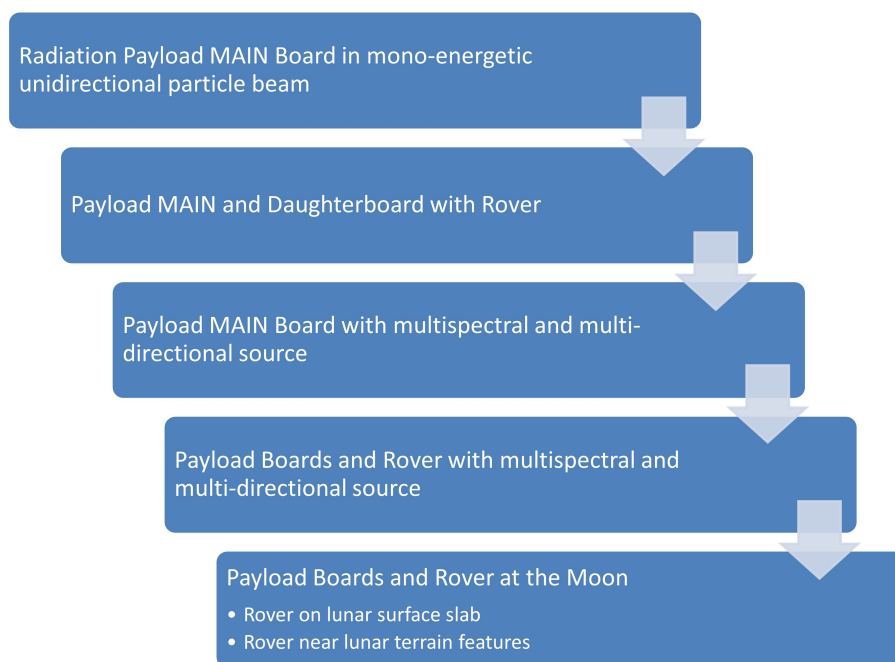


**Figure 4.19:** Plan for Radiation Payload Modelling with Geant4

A plan (shown in Figure 4.19) was sketched out to model the Radiation Payload and its interaction with the lunar radiation environment in a systematic and structured manner. This would enable iterative improvements in the simulation and modelling process such that the accuracy and fidelity of the models can be improved over time. It would also enable the addition of new elements and features over time such that the models can be extended to include more mission phases and radiation sources, or to draw upon more sophisticated theoretical and empirical radiation environment models that may become available in the near future. Additionally, the use of sophisticated data analysis and visualization methods is fairly straightforward to implement. The plan was created with the intention that modeling complexity would be added

<sup>5</sup><https://sites.wustl.edu/meteoritesite/items/the-chemical-composition-of-lunar-soil/>

<sup>6</sup><https://extra.lp2ib.in2p3.fr/G4/>

<sup>7</sup><https://geant4-userdoc.web.cern.ch/UsersGuides/ForApplicationDeveloper/html/Examples/BasicCodes.html#>

in layers and the results would be verified and validated at each level.

A basic model was set up and simulated to work out the model setup in Geant4, including various aspects such as geometry creation and placement, material assignment, scoring, run and event sequencing, primary source creation, source placement and graphical visualization. The model geometry consisted of a Silicon box which was bombarded with protons directed along the normal to one of its faces, originating from one end of the cuboid world volume. This is depicted in Figure E.23. The general workflow which was followed for the simulations in this section is shown in Figure 4.20. Hereon, the models outlined in Figure 4.19 are described with a brief presentation of the results derived from them.

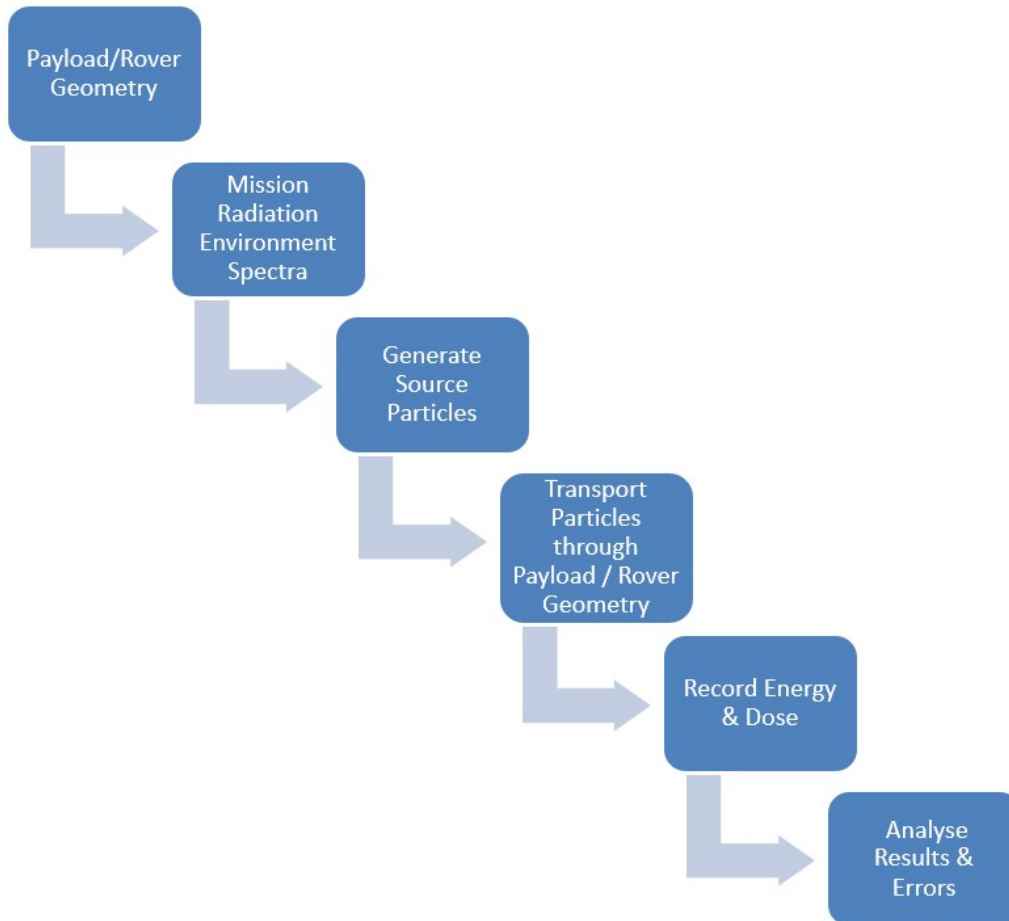


**Figure 4.20:** Workflow used for Geant4 simulations (based on [82])

#### 4.3.2. Radiation Payload MAIN Board in mono-energetic proton beam

The first model in the plan depicted in Figure 4.19 involves a simplified model of the Radiation Payload MAIN Board, with irradiation in the form of a mono-energetic beam of protons.

The FGDOS chip and payload MAIN PCB were modelled using "box" shapes in Geant4, similar to the approach described in [79]. The PCB was assigned the custom material FR4, created as a mixture of epoxy and silicon dioxide. The FGDOS chip was modelled as a solid block of Silicon, neglecting the intricate constituents of the SoC. Geometrical dimensions were specified to be identical to actual Radiation Payload dimensions. The model geometry thus obtained was contained within a cubic envelope of side 100 cm, which was contained in a world volume that exceeded the envelope by 20% in all directions. To simulate vacuum, the envelope was assigned the material "G4\_Galactic". Figure 4.21 shows the geometry setup inside the translucent blue world volume. A 5 x 5 x 1 mm block of Silicon representing the FGDOS was designated the scoring volume, for calculation of the amount of dose deposited per run. Additionally, the mean squared error in deposited dose was also calculated, as shown in Table 4.5.

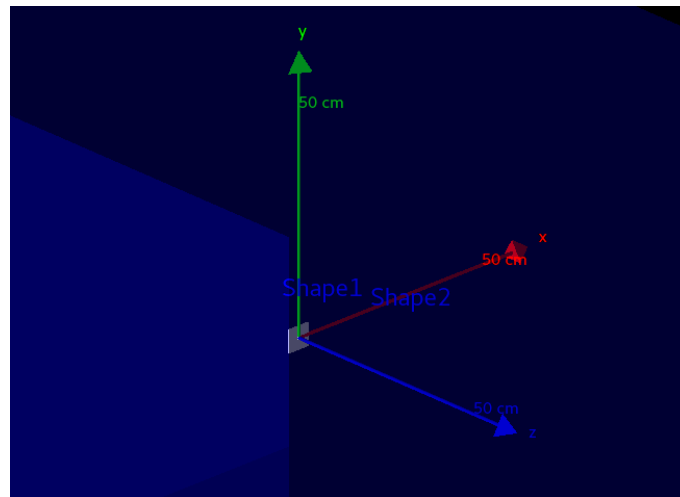


**Figure 4.21:** Radiation Payload MAIN Board simplified geometry

The QBBC physics list in Geant4 was used with all models covered in this section, since it has been found to include most interactions and processes that are relevant for space radiation related applications [82]. The primary source was specified to be a 10 x 10 cm square cross-sectioned beam of protons with a kinetic energy of 200 MeV. This beam cross-section was chosen on the basis of the field size used for irradiation tests at HPTC, as described in section 5.1. Generation of secondary protons, gammas (in green) and electrons (in red) as a result of primary protons (in blue) impinging on the Payload MAIN Board is illustrated by Figure 4.22.

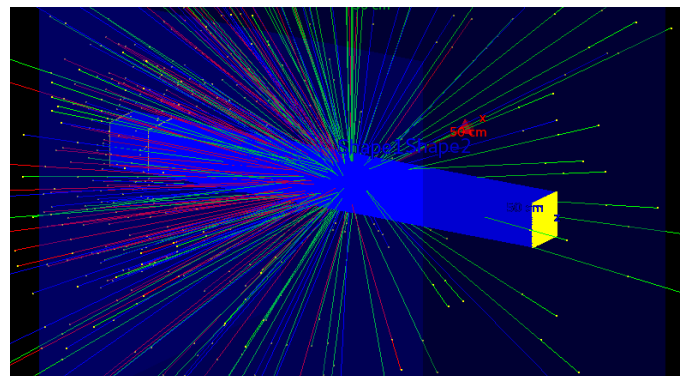


**Figure 4.22:** Generation of secondaries from proton interaction with simplified Payload board

The number of primary protons was increased from 1E3 to 1E6 and the dose deposited in the sensitive volume i.e. the FGDOS was recorded. The results are provided in Table 4.5.

# of primary particles	Cumulated dose in scoring volume (nanoGy)	RMS error (nanoGy)	Relative error (%)
1E3	4.31	3.05	70.8 %
1E4	62.76	12.75	20.3 %
1E5	555.24	60.09	10.8 %
1E6	5834.10	149.62	2.6 %

**Table 4.5:** Dose deposition results in MAIN Board FGDOS from large field proton beam irradiation

Comparing the dose deposited for 1E6 protons with normalized fluence from a typical proton irradiation run using large field at HPTC, the error in deposited dose was found to be approximately 0.4 %. This serves as validation of the model setup, enabling the creation of more involved simulations in subsequent subsections. In addition to the large 10 x 10 cm field, the pencil beam used for Radiation Payload V1 performance tests (described in section 5.6) was also simulated at a beam energy of 200 MeV, as shown in Figure 4.23. As

expected, the same number of primary particles leads to larger dose depositions in the case of the pencil beam, as evidenced by the values in Table 4.6.

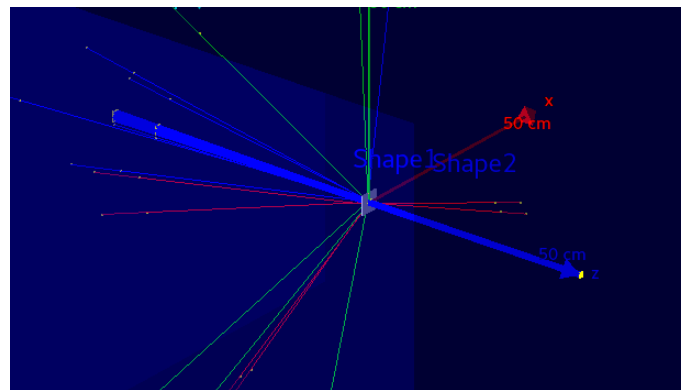


**Figure 4.23:** Pencil beam of protons incident on Radiation Payload MAIN Board

# of primary particles	Cumulated dose in scoring volume (nanoGy)	RMS error (nanoGy)	Relative error (%)
1E3	869.44	36.15	4.2 %
1E4	9108.96	165.69	1.8 %
1E5	94260.80	657.25	0.7 %

**Table 4.6:** Dose deposition results in MAIN Board FGDS from pencil beam irradiation

#### 4.3.3. Payload MAIN and Daughterboard with Rover

In flight configuration, the Radiation Payload will be assembled with the rover such that the MAIN Board is housed within the rover's chassis, while the Daughterboard is mounted to the Solar Panel Plate (SPP) outside the chassis.

Within the Geant4 environment, the Daughterboard was created to be identical to the MAIN Board, and was positioned at the centre of the SPP for convenience. For simplicity, the SPP was kept at a deployment angle of  $90^\circ$ , its likely configuration while harvesting solar power near polar latitudes [68]. The SPP was modelled as a thick plate (box shape) made up of Silicon Carbide (SiC), with a density of  $2.0 \text{ g/cm}^{-3}$ , as specified by the manufacturer<sup>8</sup>. Silicon box shapes representing the MAIN Board FGDS and the Daughterboard FGDS volumes were used as scoring volumes in turn. Figure 4.24 provides a wire-frame view of the model geometry. The two payload boards and respective FGDS chips can be seen clearly. The long plate represents the SPP, while the box like structure represents the chassis of LZ.

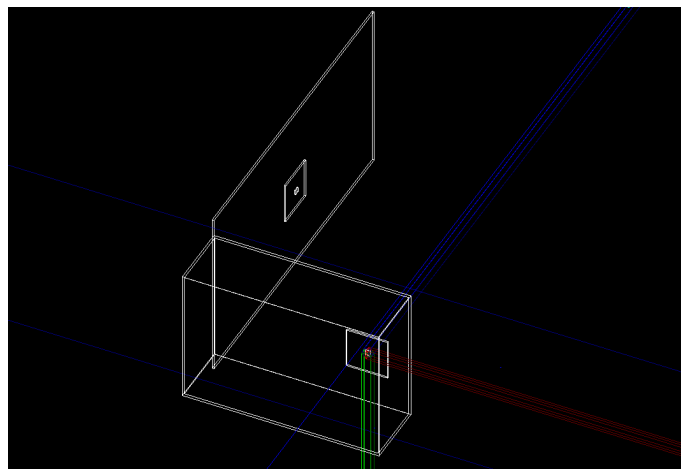


**Figure 4.24:** Wire-frame view of simplified LZ rover with Radiation payload MAIN and Daughter boards

<sup>8</sup>The LZ SPP is actually a plate made of ceramic matrix composite (CMC), with Carbon fibres impregnated in a Silicon matrix. Using physical properties mentioned in the material datasheet, this was approximated as SiC in Geant4

The QBBC physics list was used for all simulations performed using this model. The number of primaries was varied from  $1E3$  to  $1E6$ , until the relative RMS error in deposited dose fell below 10 %. The source was again specified as a  $10 \times 10$  cm large field proton beam.

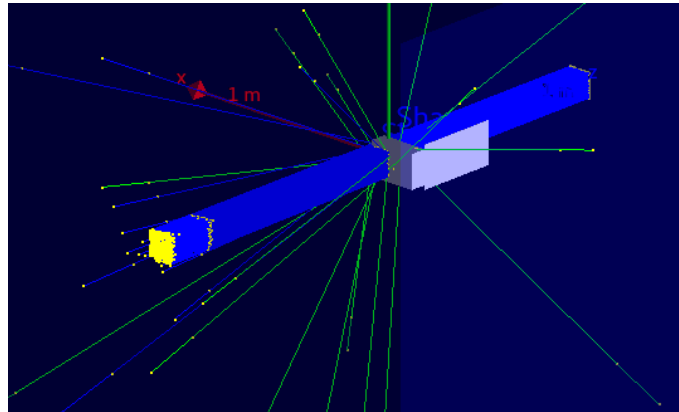


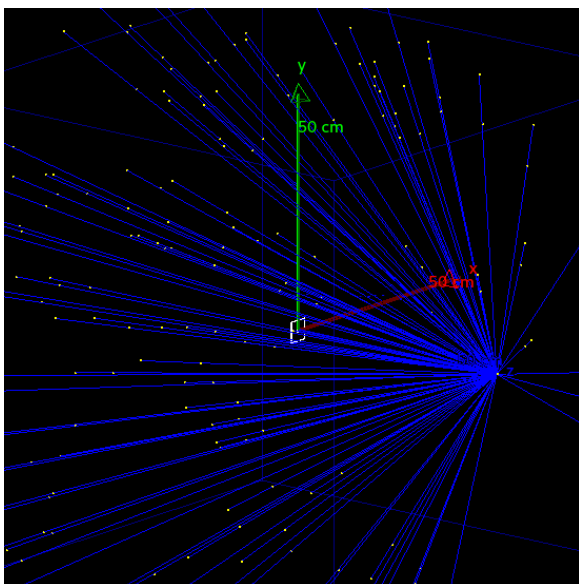
**Figure 4.25:** Simplified model of LZ rover exposed to proton beam

#### 4.3.4. Payload MAIN Board with multi-spectral and multi-directional source

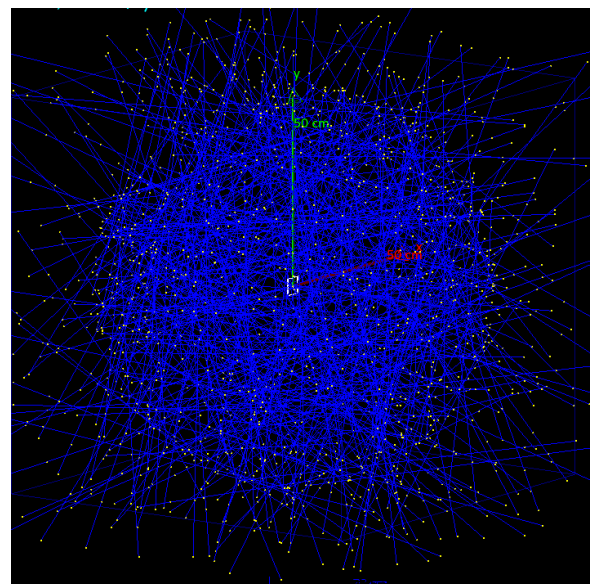
The geometry and materials used in this model were identical to subsection 4.3.2. Two kinds of primary source specifications were used:

- Spherical surface with isotropic angular distribution
- Point source with cosine angular distribution

The primaries were sampled from a histogram of the GCR spectrum representing interplanetary radiation environment obtained using SPENVIS. The data was input in the form of a SPENVIS generated macro, using the "general particle source" functionality in Geant4. Figure 4.26 depicts the geometry and source setup for the two source specifications.



**(a)** Point source with cosine distribution



**(b)** Spherical isotropic source

**Figure 4.26:** Multi-spectral, multi-directional sources with payload MAIN Board

As shown by Table 4.7, the number of primaries that could be simulated with available computational resources were not adequate to generate results with relative error in dose deposition lower than 10%. Since the models in following subsections involve more complicated configurations and larger world volumes, the results presented hereon are focused mainly on the demonstration of the models themselves whereas numerical values are intended to be purely indicative in nature.

# of primary particles	Cumulated dose in scoring volume (nanoGy)	RMS error (nanoGy)	Relative error (%)
1E5	3.73	2.22	59.5 %
1E6	34.44	7.22	20.9 %
1E7	595.79	243.63	40.9 %
1E8	5253.46	581.68	11.1 %

**Table 4.7:** Dose deposition results in MAIN Board FGDOS from GCR spectrum based point source with cosine distribution

#### 4.3.5. Payload Boards and Rover with multi-spectral and multi-directional source

The geometry and materials used in this model were identical to subsection 4.3.3. Again, two kinds of primary source specification were used, as shown in Figure 4.27.

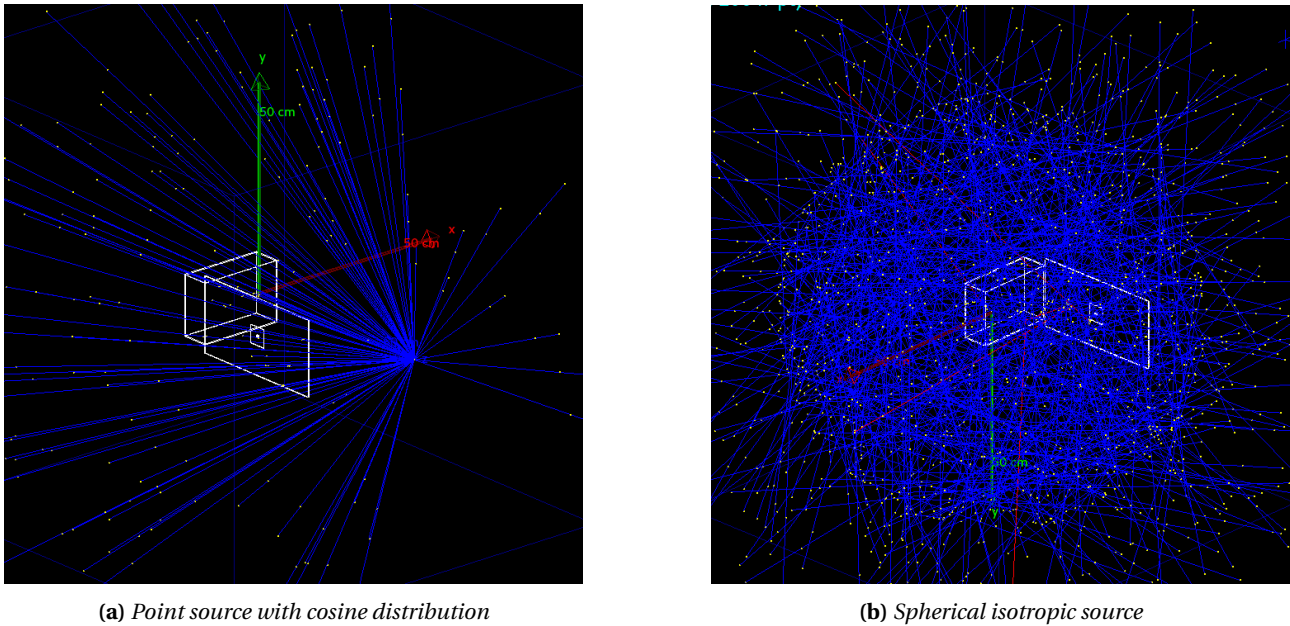


**Figure 4.27:** Multi-spectral, multi-directional sources with payload MAIN Board

The number of primaries that could be simulated with available computational resources were not adequate to generate statistically significant results. However, given more computational power this model can be used to judge the effectiveness of shielding of the simplified rover chassis. It can also be used to get an indication of the difference in dose deposition and observations between the Radiation Payload MAIN and Daughterboard FGDOS detectors.

#### 4.3.6. Rover on the Moon

Rover and payload geometry, materials and primary radiation source placement were incrementally modelled in the previous simulations. To have a consolidated model that is representative of mission conditions, it was decided to include a rudimentary representation of the Moon's surface along with the simplified LZ rover.

The composition and arrangement of the rover chassis, SPP and payload boards was identical to the previous sub-section. This model of the rover was placed over a slab intended to represent the lunar surface. The composition of the slab was based on soil composition provided in [88], with omission of the constituents having weight fractions less than 0.5%. Using the approach presented in [38] in an adapted form, only the first layer of lunar soil (having a depth of 22 cm with  $1.76 \text{ g cm}^{-3}$  density) was modelled. The lateral dimensions were chosen to be 10 m each, such that the rover would be sufficiently small compared to the slab. The chassis of the rover was placed 3 cm above the slab to account for the height provided by LZ's C-shaped legs.

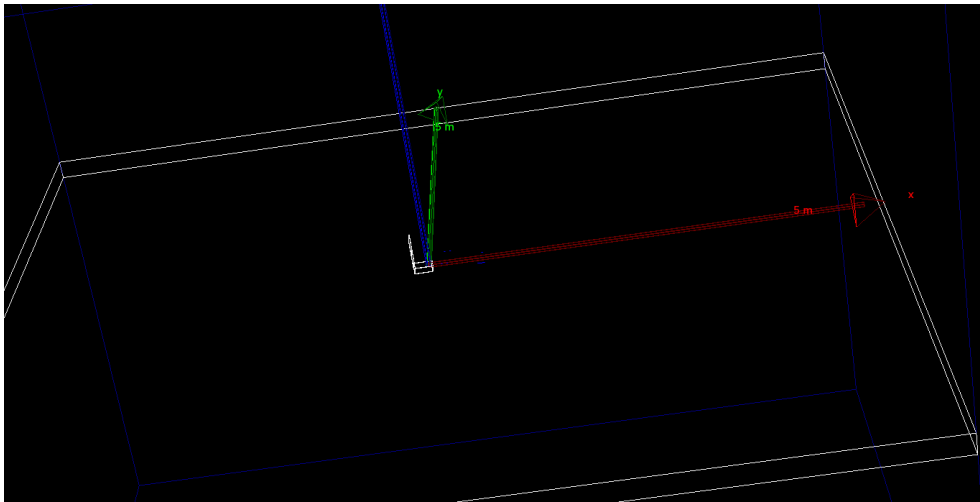


**Figure 4.28:** *Wire-frame view of rover on a lunar regolith slab*

The Silicon box shapes representing the MAIN Board FGDOS and the Daughterboard FGDOS volumes were used as scoring volumes / dose detectors. The QBBC physics list was used for all simulations performed using this model. The primary source was based on the interplanetary GCR spectrum generated using SPENVIS (discussed in section 4.2). The macro file which was used as the input for this model can be found in Appendix E. A point source with cosine angular distribution was used, which can approximate the incidence of particles from an isotropic source on a plane surface [38].

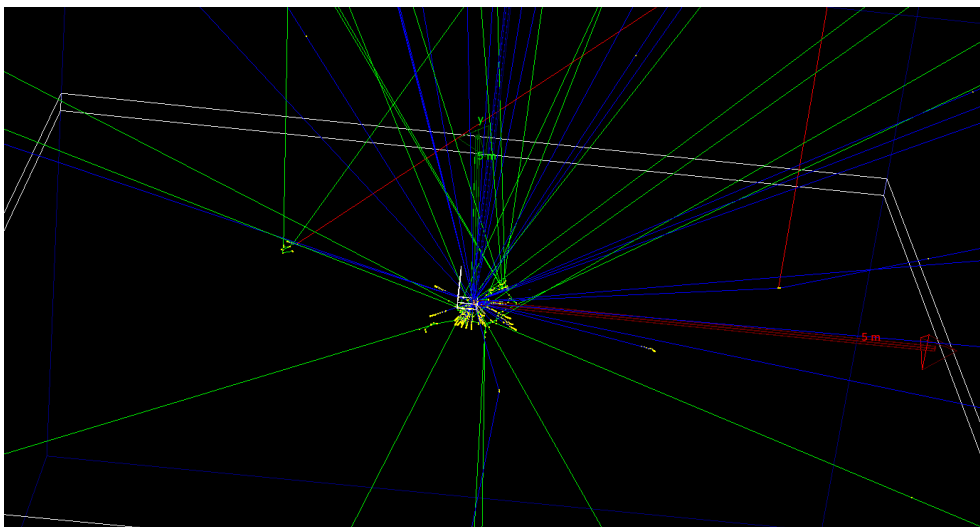


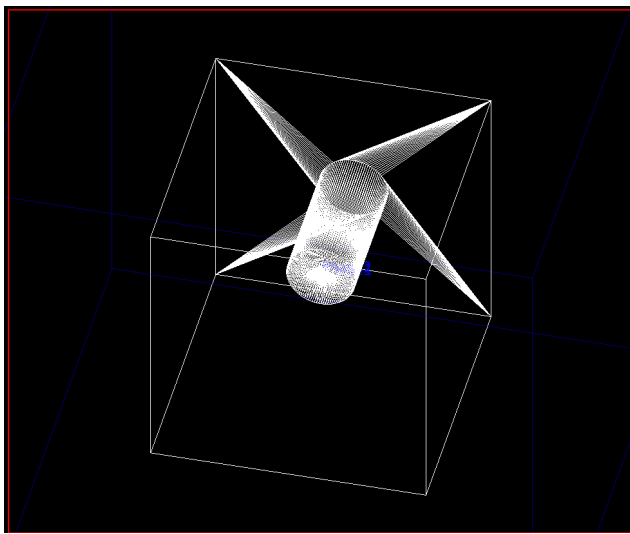
**Figure 4.29:** *Rover on lunar regolith slab: Exposure to point GCR spectrum with cosine angular distribution from point source*

Not enough primaries to generate noticeable dose deposition in the FGDOS detectors could be simulated, due to computational constraints. However, given more computational resources, this model could be used to simulate scientific observations of the Radiation Payload amidst lunar surface operations in the vicinity of relatively flat and uniform terrain. This model can also be improved by adding more layers of regolith (with appropriate elemental composition), to increase the depth of the lunar slab.

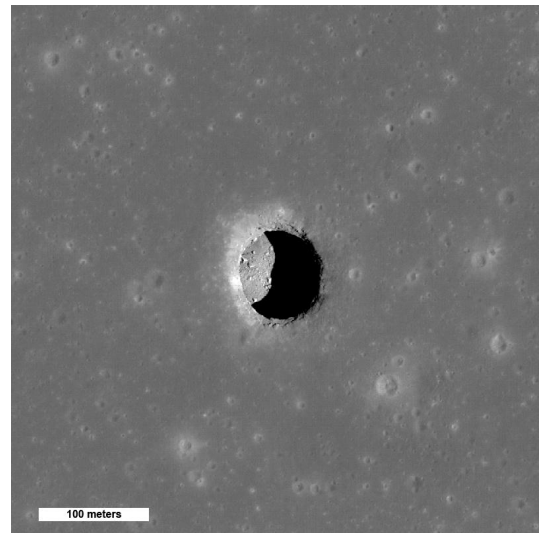
#### 4.3.7. Rover inside a Lunar Lava Tube

The final step is the creation of a consolidated model which can be used to simulate the radiation environment in the vicinity of interesting lunar landscape features, primarily the interaction of the rover and Radiation Payload with this mixed radiation field such that scientific observations in such conditions can be predicted to a certain extent. To illustrate this concept, a simplified vertical hole lava tube was created in Geant4 and the LZ rover was placed inside it, as shown in Figure 4.31. Lava tubes on the Moon are thought to

be promising locations for the establishment of lunar habitats and storage depots, since they offer shielding from ionizing radiation and micro-meteoroids, as well as a relatively stable thermal environment compared to the lunar surface [35, 93]. Figure 4.30b depicts a pit crater of about 100 m depth which serves as the vertical entrance to a lava tube at Mare Tranquillitatis on the Moon<sup>9</sup>.



(a) Vertical lava tube geometry in Geant4



(b) Mare Tranquillitatis pit (source: NASA JPL)

**Figure 4.30:** Vertical entrance of a lunar lava tube

The geometry and setup of the lava tube was adapted from the work described in [93]. Consequently, the rudimentary vertical lava tube was constructed using a cylinder, 5 m deep and 2.5 m in diameter, subtracted from a cubic slab of lunar regolith of side 10 m. Soil composition was left unchanged from subsection 4.3.6. The horizontal part of the lava tube was not included, for simplicity. The complete geometry setup is shown in Figure 4.30a.

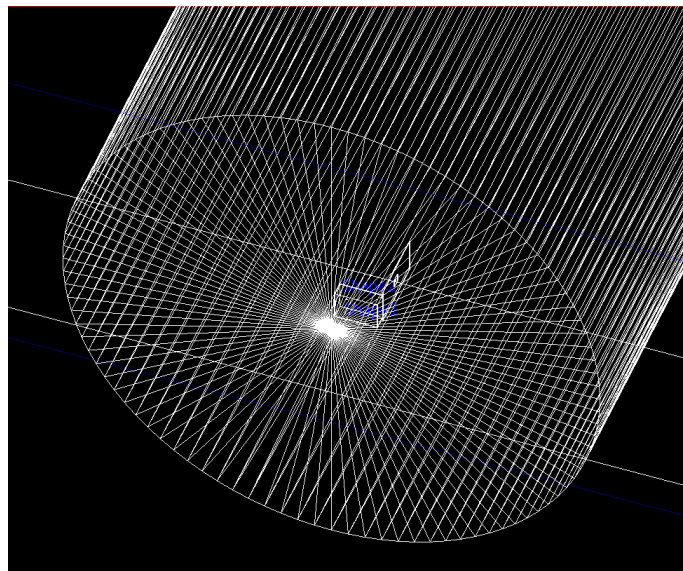


**Figure 4.31:** LZ rover positioned inside the lava tube entrance

This model highlights the immense scientific value that the Radiation Payload can offer in terms of detecting the modulation and shielding offered by lunar landscape features to the radiation field in their immediate vicinity. This is exemplified by Figure 4.32, which depicts the rover ensconced in the lava tube, shielded from incident GCR protons. Secondary photons (in green) and scattered protons (in blue) in the bulk of soil

<sup>9</sup><https://photojournal.jpl.nasa.gov/catalog/PIA13518>

surrounding the lava tube can also be observed. The model can also be extended to include multiple LZ rovers constituting a swarm, to simulate spatially distributed dose measurement and radiation mapping on the Moon, especially in the vicinity of interesting features of its terrain.

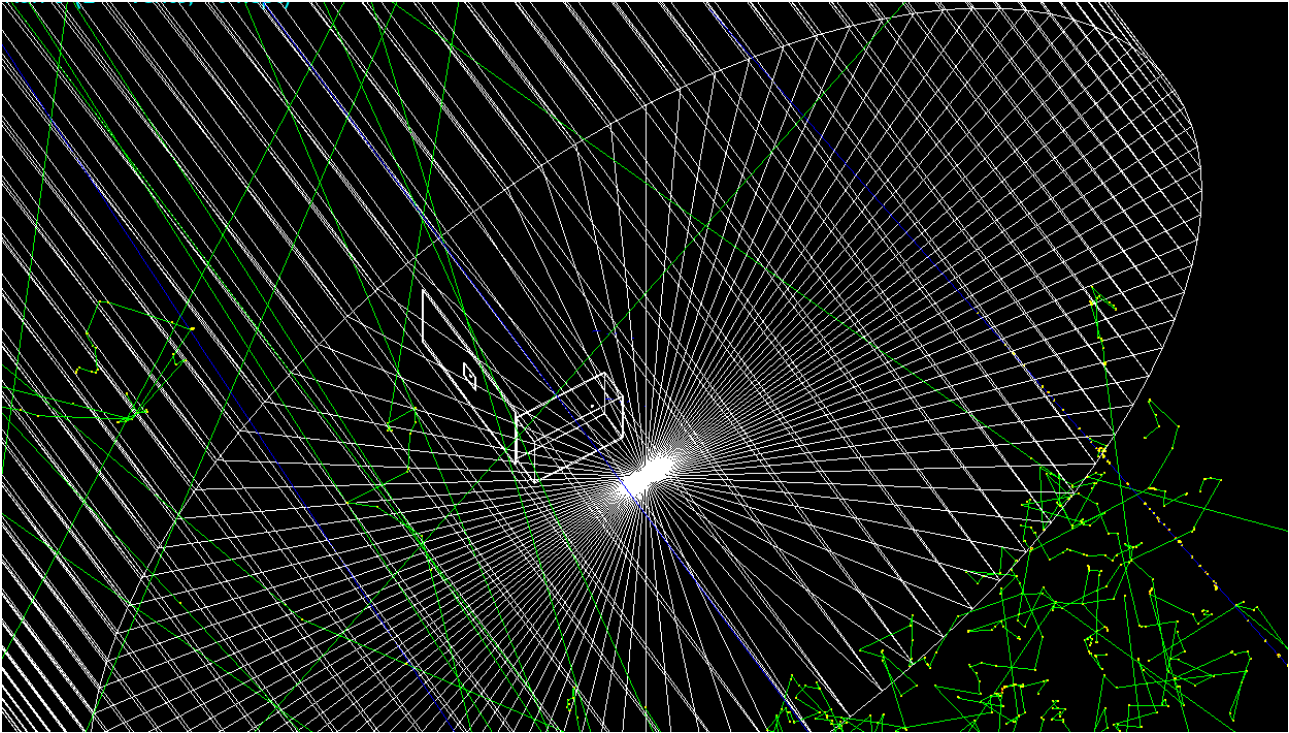


**Figure 4.32:** Rover shielded from incident radiation within the lava tube

#### 4.3.8. Assumptions and limitations

The the assumptions and limitation associated with radiation transport simulations and modelling covered in this section, are listed below:

1. Monte Carlo algorithms use pseudo random number generators which can pass tests of randomness. It is virtually impossible to generate truly random numbers using a computer. Hence, the sampling from cross-section or interaction PDFs is not truly random in a formal sense [155]. This can be compensated by increasing the number of samples to achieve statistically significant results. However, due to lack of high performance computation resources, the number of runs and source particles had to be lowered to comply with time constraints. Some modifications also had to be made to the model geometry for this reason. For instance, the size of the world volume, the lunar slab and lava tube had to be limited in order to save on computation time. For better results, these geometric entities should be enlarged so as to be considered infinitely large compared to the size of the LZ rover.
2. The use of biasing or involved sampling techniques was not applied in the simulations performed so far. However, these techniques may be useful for reducing the computation time and for enforcing bounds on the input spectra such that only particles of interest are transported.
3. Several simplifications and assumptions went into creation of the Radiation Payload model. Only the PCB and the FGDOS chip were included, the geometry was simplified by ignoring other payload components. The FGDOS chip was approximated to be a Si block. The PCB was assigned a custom defined 'FR4' material based on a mixture of  $SiO_2$  and epoxy. Similarly, the rover chassis geometry was simplified to the extent that it was taken to be a plain Aluminum box with walls of 1.5mm thickness. The other subsystems of the rover were neglected for the purpose of these simulations and so was the MLI insulation. For the SPP, only a single deployment angle was considered. In principle, changing the deployment angle could introduce variations in the dose measured by the Daughterboard FGDOS, due to variation in the local shielding with in a given solid angle w.r.t. the rover.
4. The dependence of the results on the choice of physics list in Geant4 was not explored. Based on results from literature, physics lists such as *FTFP\_BERT\_HP*, *QGSP\_BERT\_HP*, *QGSP\_BIC\_HP* and

*Shielding* may also be applied [82]. Model performance and effectiveness varies with particle type and energy ranges. As such, it may be useful to do an abbreviated comparison of different models in the expected energy range of various particles in the input spectra obtained from SPENVIS. Moreover, inherent limitations in the Geant4 toolkit regarding particle and ion interactions naturally apply to the models discussed here as well [3].

5. Since primary source particles were created from SPENVIS generated data, the errors associated with radiation environment models used in SPENVIS were propagated to radiation transport models as well.
6. More detailed design information and test data for the FGDOS is needed in order to make a realistic model of sensor response in Geant4. In the models presented here, the FGDOS has simply been abstracted as an ideal virtual detector with perfect response.
7. Due to time constraints, the simulation plan was not realized entirely. However, the models presented here provide an excellent foundation for more extensive modelling and simulation studies in the future.

#### 4.3.9. Conclusions & Recommendations

The main conclusions that can be derived from radiation transport modelling and simulations are presented below, in conjunction with recommendations for further development and investigation:

1. A rudimentary model of the Radiation Payload MAIN Board (including the FGDOS chip) was set up using Geant4 and the incidence of protons in square field beam was successfully simulated. The dose deposited in the volume of the FGDOS was computed for various proton fluences and the results were validated with experimental data.
2. Simplified radiation transport models of the Radiation Payload assembled into the LZ rover were successfully set up and demonstrated. Additionally, various multi-directional radiation sources were modelled, based on GCR spectra derived from SPENVIS. Simulations performed using this model can be used as a proof of concept for the spatially distributed detection scheme of the Radiation Payload. Expected measurements from the MAIN and Daughter FGDOS sensors can be simulated to create models of the modulations described in the overall science scheme (shown in Figure 4.1). It was demonstrated that the effects of regolith interaction and its induced effects on Radiation Payload measurements can be modelled using Monte Carlo simulations. This constitutes tangible progress on various building blocks of the Radiation Payload science scheme described in section 4.1,
3. The sensitivity of dose deposition in the FGDOS chips, on the elemental composition and density of lunar regolith can also be investigated. On a related note, this can be done to see the effect that the predicted/estimated soil composition might have on Radiation Payload observations. More lunar terrain features such as horizontal lava tubes, craters and boulders can also be included. Similarly the effect of rover configuration and positioning on the dose detected by various FGDOS sensors can be studied.
4. Once system level testing of the LZ rover with mixed radiation fields has been performed, the experimental results can be compared with an adapted version of the radiation transport model in order to validate it and improve it. In this case, the input primary sources would have to be changed to match the characteristics of the mixed fields which are provided by the test facility [66].
5. It would be extremely interesting to create a detailed model of at least the analog part of the FGDOS SoC, to increase transport model fidelity and to enable improved validation with radiation test results in the future. Ideally a model of the sensor response can be constructed so that effects such as sensitivity variation with energy and TID induced degradation can be modelled using Monte Carlo simulations. Once validated, this would result in tremendous savings in beam time required for FGDOS characterisation.
6. The radiation transport model can be expanded to include a rough representation of the lunar lander spacecraft, such that incident radiation during various mission phases prior to rover deployment can be simulated. If time-dependent radiation environment data is available, the transport models can be upgraded to investigate the time evolution of scientific measurements from the Radiation Payload.

# 5 Verification & Validation

This chapter describes the verification and validation efforts that were undertaken in the scope of this thesis project. Hence, it carries over from the work described in chapter 3 and goes on to describe parts of the synthesis phase of the systems engineering process. The results from the verification and validation activities are also presented herewith, along with a discussion of the implications, which is continued in the next chapter.

## 5.1. FGDOS Radiation Characterization & Performance Testing

The Floating Gate Dosimeter based FGD-03F sensor was tested against proton beam radiation to map out the behavior of the sensor and to characterize its performance w.r.t. incident radiation at various energies and dose rates. This test campaign was carried out at the Holland Proton Therapy Centre (HPTC) on three separate occasions - March 8, March 24 and April 12, 2022. The testing efforts described in these section were built upon the work of de Meyere, documented in the thesis named - "Floating Gate Dosimeter Characterization" [90]. An overview of the entire test campaign is given in Table 5.1. The first two test days are covered in [90]. Hereon, a synthesis and amalgamation of the observations and results from the last three test days is presented.

Test Day #	Date	Test Purpose	TID accumulated – in air (Gy)
1	16/12/2021	Sensor basic functioning	124 Gy
2	24/02/2022	Different energy levels	>35 Gy
3	08/03/2022	Higher energies & dose rates	>90 Gy
4	24/03/2022	Low dose rates and sensor properties	>36 Gy
5	12/04/2022	Other dose rates and missing data	>35 Gy
		TOTAL	>320 Gy

**Table 5.1:** FGDOS Proton Beam Characterization: Test Campaign Summary

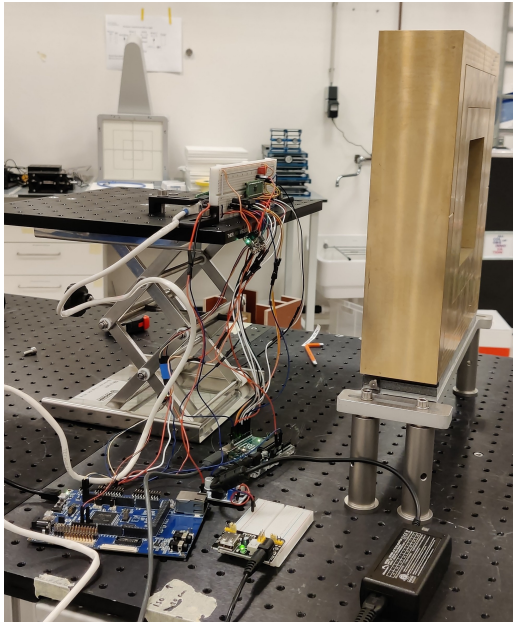
The main objective of this proton beam test campaign was to study the behavior of the FGDOS sensors under irradiation and to characterize its performance, especially its sensitivity to incident radiation. Since the sensitivity of the sensor is the main parameter that can be used to obtain TID values from sensor output, the main focus of the test campaign was placed on obtaining and analyzing the sensitivity and its variation w.r.t. the energy levels and dose rates of the incident proton beam.

### 5.1.1. Test Setup

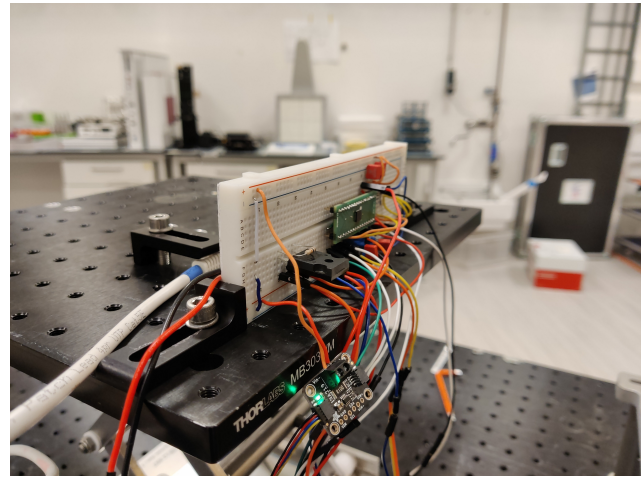
The test setup and data acquisition software that was used in the proton beam tests is an adapted version of the setup used in [90]. The setup consisted of:

- An FGD-03F QFN breakout PCB - *Sensor 2*
- FGD-03F DIL package prototype - *Sensor 1*
- Arduino Uno R3 microcontroller board
- Solderless breadboard with jumper wires
- Voltage decoupling capacitors
- MOSFET to switch power to the FGD-03F breakout
- SAM V71 board used to log power measurement data
- INA219 sensor breakout boards
- FGD-02F Evaluation Board
- DC/DC Step Up for recharging the FGD-02F Evaluation board
- 12V Power adapters
- USB cables
- Laptops for data acquisition and logging

Figure 5.1a and Figure 5.1b show the test setup mounted and ready for irradiation in the beam line at HPTC.



(a) side view of test setup



(b) Close up view of DUT

**Figure 5.1:** FGDOS radiation characterisation test setup

### FGDOS configuration

In order to meaningfully compare the results obtained with results from previous tests conducted in December 2021 and February 2022 [90], most settings and configurations for the FGDOS sensors were left unchanged. Hence, the shortest window factor corresponding with 4096 pulse per window was used, a recharge voltage of about 16.5 V was used for the internal charge pump and the clock frequency (WCK) was maintained at 31250 Hz. The sensor configuration details are shown in Table 5.2. For most tests, the sensor was configured in HI SENS mode with a target frequency of about 90 kHz and a threshold frequency of about 50 kHz. The sensors were mostly operated in active mode and sensor 1 and 2 were read alternately, once every 600 ms approximately.

Attribute	Value
Supply	5V – from Arduino Regulator via power adapter and HPTC socket
Readout interface	SPI through Arduino
Sensor Mode	Active / Passive
Sensitivity Modes	HI SENS / LOW SENS
Window Clock Frequency	31250 Hz
Window Pulses	4096
Window factor	7.63
Recharge Mode	Auto recharge from internal pump
Recharge voltage	16.5 V
SPI Frequency	5 MHz
Recharge Target Frequency - HI SENS	90000 Hz (85937.5)
Recharge Threshold Frequency - HI SENS	50000 Hz (46875)
Recharge Target Frequency - LOW SENS	180000 Hz (179687.5)
Recharge Threshold Frequency - LOW SENS	140000 Hz (132812.5)

**Table 5.2:** FGDOS configuration details

### Beam Line Setup

The beam line setup is shown in Figure 5.2. The beam line at Holland PTC consists of several elements. Protons originate from the cyclotron and are directed into the experiment room through an exit port consisting

of apparatus for controlling the beam energy and intensity. Hereafter, the proton beam passes through the Beam Monitor, a scatter foil, thin/thick scattering rings, bronze collimators and finally impinges on the device under test (DUT) i.e. the Breadboard with the two FGDOS chips mounted on it.

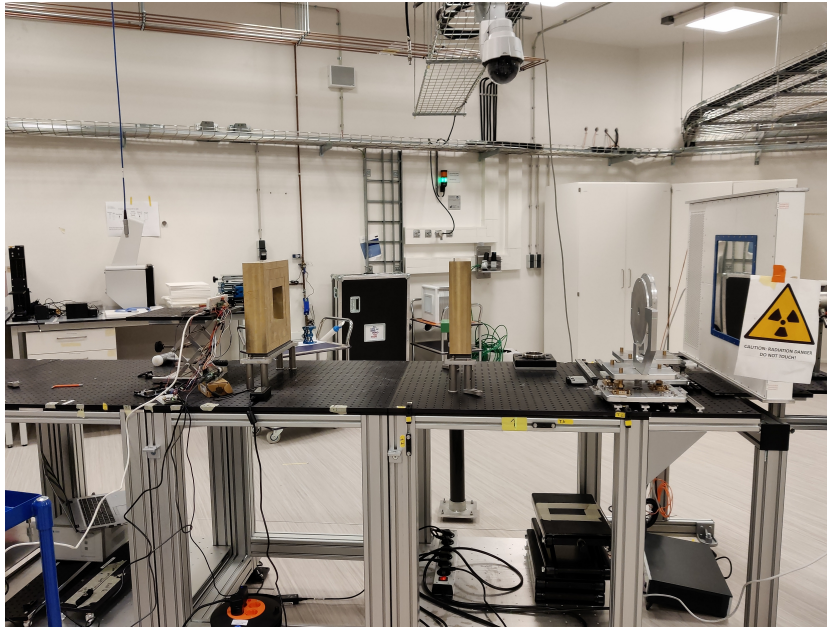


**Figure 5.2:** HPTC Beam Line Setup

### 5.1.2. Test Levels

The energy levels which were used for testing over the course of the entire proton beam testing campaign are shown in Table 5.3 and the dose rates are shown in Table 5.4. In essence, three different beam energies were used based on the availability of calibrated beam line setups at HollandPTC. "Energy at DUT" refers to the calibrated average kinetic energy of the protons that reach the FGDOS sensors.

Energy Code	Beam Nominal Energy (in MeV)	Energy @ DUT (in MeV)
A	100	70
B	150	120
C	215	200

**Table 5.3:** Test levels: Beam Kinetic Energy

The dose rates at each of these energies were limited by the minimum and maximum beam intensity that could be provided by the cyclotron. To keep track of these levels, each energy and dose rate value was assigned a unique code, alphabets A,B,C for the energies and numbers 1-14 for the dose rates.<sup>1</sup>

<sup>1</sup>The dose rate codes are not in strictly ascending or descending order since intermediate dose rate levels were added between tests based on the feasibility of obtaining that specific dose rate from the cyclotron at a given energy level.

Dose Rate Code	Dose rates @ target in air ( in Gy/min)	Dose rates @ target in air ( in Rad/s)
1	0.05	0.08333333
2	0.1	0.16666667
3	0.6	1
4	1.84	3.06666667
5	0.72	1.2
6	0.85	1.41666667
7	1	1.66666667
8	1.5	2.5
9	3	5
10	4.8	8
11	0.01	0.01666667
12	0.001	0.00166667
13	0.005	0.00833333
14	0.5	0.83333333

**Table 5.4:** Test levels: Dose rates

According to these codes, the test runs conducted on each test day are summarised in the tables Table 5.5 to Table 5.7. These tables provide information regarding the nature of incident radiation for each run (the energy and dose rate), irradiation duration, TID for each individual run, sensitivity configuration of the FGDOS and the purpose of any given run.

Run #	Test Code	Beam Energy (MeV)	Beam Energy at Target (MeV)	Dose rate at target (in air) (Gy/min)	Approx Run time (min)	Dose acc. at target - TID (in Air) (Gy)	Sensor Settings	Test Purpose
<b>SET 1</b>								
1	C4	215	200	1.84	3	5.52	HI SENS	Observe annealing from previous test day
2	A3	100	70	0.6	10	6	HI SENS	High sensitivity baseline at 70 MeV
3	A3	100	70	0.6	10	6	LOW SENS	Low sensitivity baseline at 70 MeV
4	A2	100	70	0.1	10	1	HI SENS	Dose rate variation
5	B2	150	120	0.1	10	1	HI SENS	Energy variation at constant dose rate
6	C2	215	200	0.1	10	1	HI SENS	Energy variation at constant dose rate
<b>SET 2</b>								
1	B3	150	120	0.6	10	6	HI SENS	Baseline test - TID degradation
2	C3	215	200	0.6	10	6	HI SENS	Energy variation at constant dose rate
<b>SET 3</b>								
1	B5	150	120	0.72	10	7.2	HI SENS	Dose rate variation
2	C5	215	200	0.72	10	7.2	HI SENS	Energy variation at constant dose rate
3	C6	215	200	0.85	5	4.25	HI SENS	Medium dose rate at 200 MeV
4	C7	215	200	1	3	3	HI SENS	Medium dose rate at 200 MeV
5	C8	215	200	1.5	3	4.5	HI SENS	Medium dose rate at 200 MeV
6	C4	215	200	1.84	3	5.52	HI SENS	Medium dose rate at 200 MeV
7	C9	215	200	3	3	9	HI SENS	High dose rate at 200 MeV
8	C10	215	200	4.8	3	14.4	HI SENS	High dose rate at 200 MeV
<b>SET 4</b>								
1	B3	150	120	0.6	5	3	HI SENS	Baseline test - TID degradation

**Table 5.5:** Test run overview: 8 March

Run #	Test Code	Beam Energy (MeV)	Beam Energy at Target (MeV)	Dose rate at target (in air) (Gy/min)	Approx Run time (min)	Dose acc. at target - TID (in Air) (Gy)	Sensor Settings	Test Purpose
<b>SET 1</b>								
1	B3	150	120	0.6	5	3	HI SENS	Baseline test - Test setup functioning
2	A2	100	70	0.1	5	0.5	HI SENS	Medium dose rate at 70 MeV
3	A14	100	70	0.5	5	2.5	HI SENS	Dose rate variation
4	A6	100	70	0.85	5	4.25	HI SENS	Dose rate variation
<b>SET 2</b>								
1	B3	150	120	0.6	5	3	HI SENS	Baseline test - TID degradation
2	B12	150	120	0.001	10	0.01	HI SENS	Very low dose rate at 120 MeV
3	B13	150	120	0.005	10	0.05	HI SENS	Very low dose rate at 120 MeV
4	B1	150	120	0.05	5	0.25	HI SENS	Low dose rate at 120 MeV
5	C11	215	200	0.001	9	0.009	HI SENS	Very low dose rate at 200 MeV
6	C1	215	200	0.05	9	0.45	HI SENS	Low dose rate at 200 MeV
<b>SET 3</b>								
1	B3	150	120	0.6	5	3	HI SENS	Baseline test - TID degradation
2	B3	150	120	0.6	5	3	LOW SENS	Low sensitivity baseline at 120 MeV
3	B3	150	120	0.6	5	3	PASSIVE	Passive mode at 120 MeV
4	B3	150	120	0.6	9	5.4	HI SENS	Full sensor freq characteristic
<b>SET 4</b>								
1	C3	215	200	0.6	5	3	HI SENS	Energy variation at constant dose rate
2	C3	215	200	0.6	5	3	LOW SENS	Low sensitivity baseline at 200 MeV
3	C3	215	200	0.6	5	3	PASSIVE	Passive mode at 200 MeV
4	C3	215	200	0.6	5	3	HI SENS	Full sensor freq characteristic

**Table 5.6:** Test run overview: 24 March

### 5.1.3. Methodology

Throughout each irradiation run, the following parameters were monitored for each sensor:

1. Time elapsed
2. Sensor frequency
3. Reference frequency
4. Temperature
5. Recharge count
6. Power consumption

Sensitivity was computed from the slope of a line fit to the sensor frequency within the linear dynamic range (LDR). The sensitivity was calculated using Equation 5.1. For irradiation runs which included recharges, the sensitivity for each discharge interval was calculated separately and an average sensitivity value was reported for the entire run.

$$S = \frac{\Delta f_{sens}}{\Delta t \times d} \quad (5.1)$$

where S represents the sensitivity in kHz/Gy, d is the dose rate in Gy/s,  $\Delta f_{sens}$  represents the fall in the frequency in time interval  $\Delta t$ .

### Test Procedure

The step-by-step test procedure which was followed during the proton beam tests can be found in [120]. Sensor and power consumption data was logged before and after the tests at the test facility to verify the functioning of the setup. Pre-test and post-test data was later compared to discover if any permanent changes in the behavior of the test article(s) was caused by exposure to radiation during a specific test day.

### 5.1.4. Observations

Categorized by areas of sensor behavior and performance, the observations from the tests in March and April are presented below.

Run #	Test Code	Beam Energy (MeV)	Beam Energy at Target (MeV)	Dose rate at target (in air) (Gy/min)	Approx Run time (min)	Dose acc. at target - TID (in Air) (Gy)	Sensor Settings	Test Purpose
<b>SET 1</b>								
1	B3	150	120	0.6	5	3	HI SENS	Baseline test - Test setup functioning
2	A11	100	70	0.01	9	0.09	HI SENS	Low dose rate at 70 MeV
3	A1	100	70	0.05	9	0.45	HI SENS	Dose rate variation
4	A12	100	70	0.001	9	0.009	HI SENS	Very low dose rate at 70 MeV
5	A13	100	70	0.005	9	0.045	HI SENS	Dose rate variation
6	A3	100	70	0.6	3	1.8	HI SENS	<i>Rapid Recovery</i> effect at 70 MeV
7	A3	100	70	0.6	3	1.8	HI SENS	<i>Rapid Recovery</i> effect at 70 MeV
<b>SET 2</b>								
1	B3	150	120	0.6	5	3	HI SENS	Baseline test - TID degradation
2	B11	150	120	0.01	9	0.09	HI SENS	Low dose rate at 120 MeV
3	B14	150	120	0.5	3	1.5	HI SENS	Dose rate variation
4	C14	215	200	0.5	3	1.5	HI SENS	Energy variation at constant dose rate
<b>SET 3</b>								
1	B3	150	120	0.6	3	1.8	HI SENS	<i>Rapid Recovery</i> effect at 120 MeV
2	B3	150	120	0.6	3	1.8	HI SENS	<i>Rapid Recovery</i> effect at 120 MeV
3	B3	150	120	0.6	3	1.8	HI SENS	<i>Rapid Recovery</i> effect at 120 MeV
4	C3	215	200	0.6	3	1.8	HI SENS	<i>Rapid Recovery</i> effect at 200 MeV
5	C3	215	200	0.6	3	1.8	HI SENS	<i>Rapid Recovery</i> effect at 200 MeV
6	C3	215	200	0.6	3	1.8	HI SENS	<i>Rapid Recovery</i> effect at 200 MeV
<b>SET 4</b>								
1	B3	150	120	0.6	2	1.2	PASSIVE	Passive mode at 120 MeV
2	C3	215	200	0.6	2	1.2	PASSIVE	Passive mode at 200 MeV
3	C3	215	200	0.6	5	3	HI SENS	Full sensor freq characteristic
<b>SET 5</b>								
1	B3	150	120	0.6	3	1.8	HI SENS	Baseline test - TID degradation
2	B11	150	120	0.01	5	0.05	LOW SENS	Low Sens mode at 120 MeV
3	B2	150	120	0.1	3	0.3	LOW SENS	Low Sens mode at 120 MeV

Table 5.7: Test run overview: 12 April

### Sensor characteristic & performance

The linear characteristic of the sensor in the LDR was confirmed. The frequency characteristic of the FGDOS over an extended frequency range of 240 kHz to 50 kHz can be seen in Figure 5.3. Both the LDR and the non-linear regions of the FGDOS's operational domain can be perceived. It's important to note that the initial flat region in the frequency was due to an error with the cyclotron that resulted in the absence of protons for a short period of time. Ignoring this region, the drop in sensor frequency with the delivery of dose to the FGDOS is clearly visible. This run was used to confirm the correct functioning of the test setup in the beginning. Figure 5.5 shows the recharge characteristic of the FGDOS over an extended recharge range. It can be seen that the recharge profile becomes increasingly non-linear as the frequency grows beyond the LDR upper bound. A series of successive recharges within the LDR can be seen in Figure 5.5.

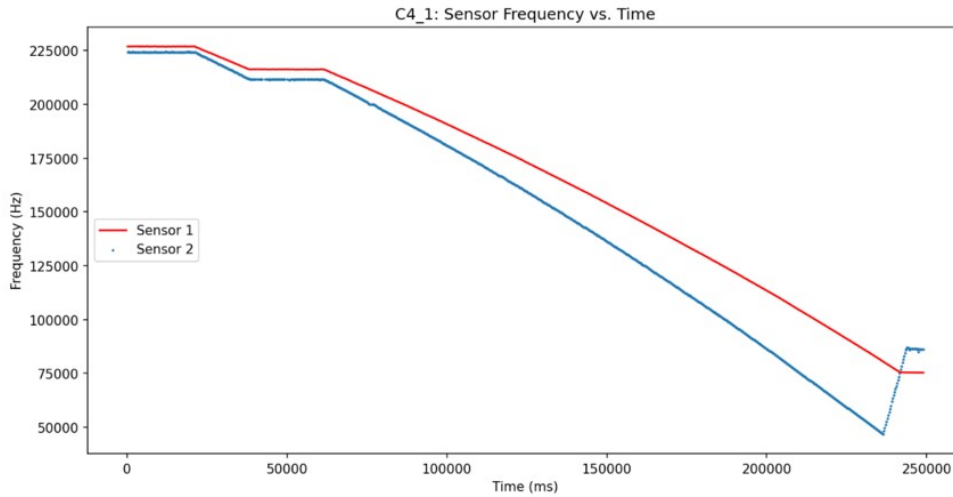


**Figure 5.3:** FGDOS characteristic over extended frequency range

Of the two sensors that were tested, Sensor 2 was found to be consistently more sensitive than Sensor 1. Sensors 1 and 2 are based on the same technology but have different types of packaging. Sensor 1 is an older prototype and Sensor 2 belongs to the chip version that is currently available commercially [90]. As such, Sensor 2 is the type of detector which will be used for the Radiation Payload. Hence, it is the point of focus of this characterisation campaign and the discussion of observations and results mainly revolve around sensor 2.

Several discrepancies were noticed during the proton beam tests. These discrepancies were mainly related to the operation of the beam monitor and the cyclotron at the test facility and led to short time intervals in which the testing had to be halted and some test plans had to be adapted in light of time constraints.

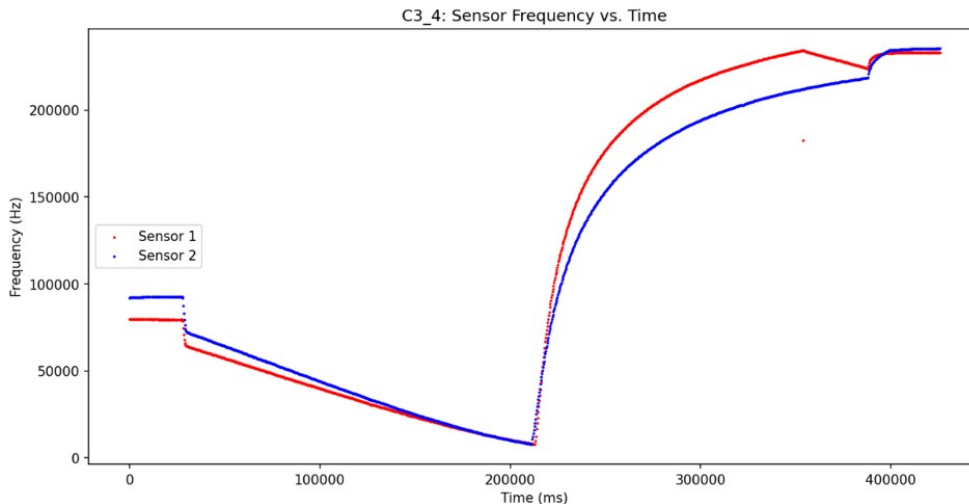


**Figure 5.4:** FGDOS recharge characteristic over extended frequency range

### High sensitivity mode - HISENS

The typical sensitivity in HISENS mode was observed to be about 33-38 kHz/Gy initially at low energies (70 & 120 MeV) and about 48-55 kHz/Gy at 200 MeV. This is lower than the 70 kHz/Gy reported in the product data sheet [117], but in agreement with test results reported in scientific literature [34, 4]. The power consumption in HISENS mode was observed to be about 19-22 mW for each sensor at first, which rose progressively with the addition of TID to the sensors. The effect of TID induced degradation on sensitivity can be seen in Figure 5.12.

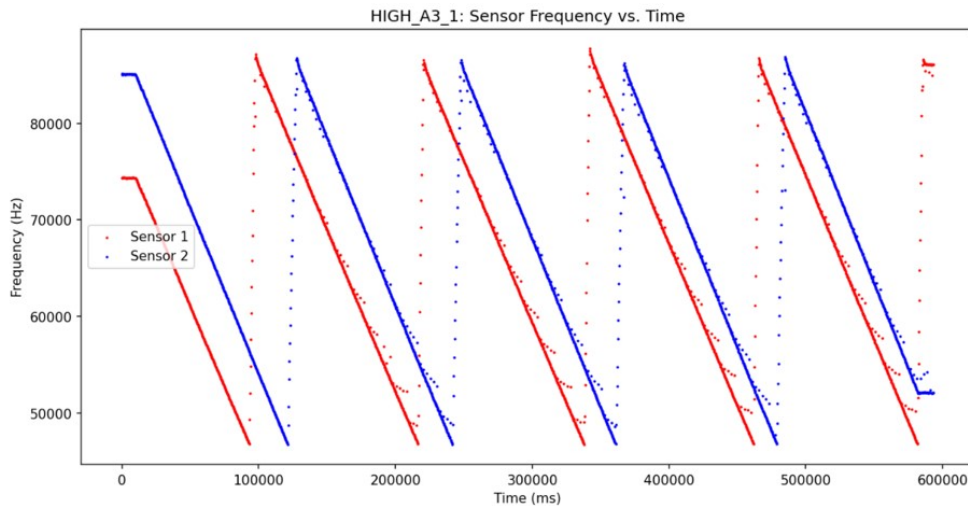
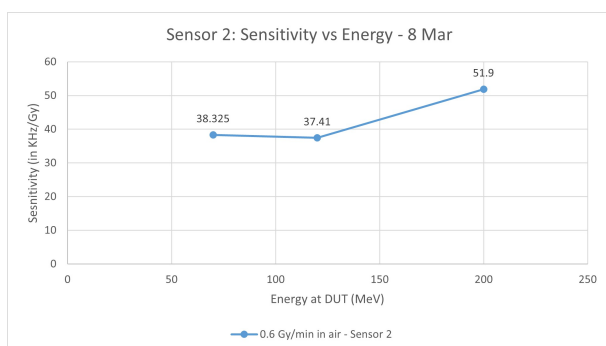


**Figure 5.5:** Frequency characteristic within LDR - HISENS Mode

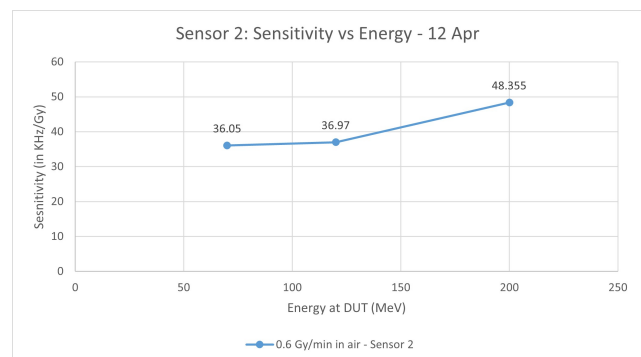
The typical operational characteristic of the FGDOS under irradiation at a constant dose rate is portrayed in Figure 5.5. The sawtooth pattern is composed of downward sloping lines that correspond to a discharge until the frequency threshold is reached. This is followed by a fast recharge (the dotted upward sloping curves) which bring the frequency back to the target level. This process repeats several times, the number of recharges in a given time interval being dependent on the magnitude of the dose rate as well as effective sensitivity of the sensors.

### Effect of beam energy and dose rate on sensitivity

The FGDOS sensitivity (to ionizing dose) is seen to increase with rise in beam energy level, as shown in Figure 5.6. This observation is congruent with the findings reported by Danzeca et al after proton beam testing in 2014 [34]. The increasing trend was noticed for both the HISENS and LOWSENS modes of the sensor.



**(a)** Sensitivity variation with Beam Energy



**(b)** Sensitivity variation with Beam Energy

**Figure 5.6:** Variation of FGDOS sensitivity with beam energy - HISENS mode

The sensitivity is also seen to vary with changing dose rate of the incident proton beam. However, no consistent trend can be inferred from the test results. To isolate the effect of energy variation, the data is plotted

separately for different beam kinetic energy levels - for 70 MeV (Figure 5.7), 120 MeV (Figure 5.8) and 200 MeV (Figure 5.9). Sensitivity data points from different test days have not been compared directly in light of TID related effects.

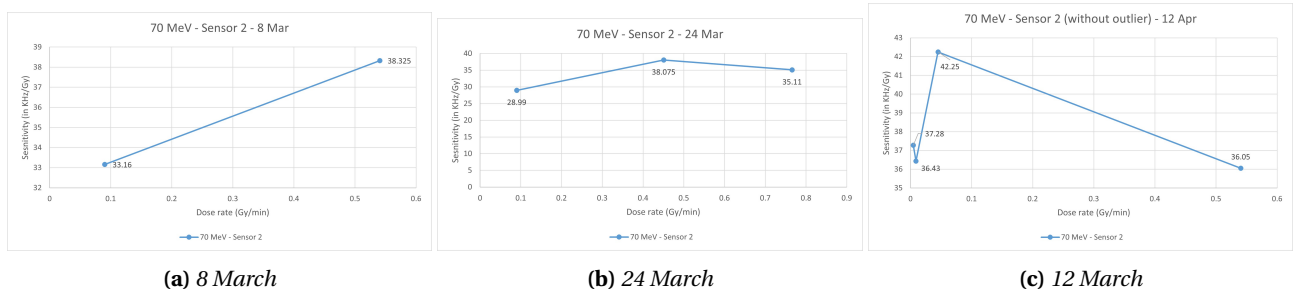


**Figure 5.7:** Variation of FGDOS sensitivity with dose rate at 70 MeV

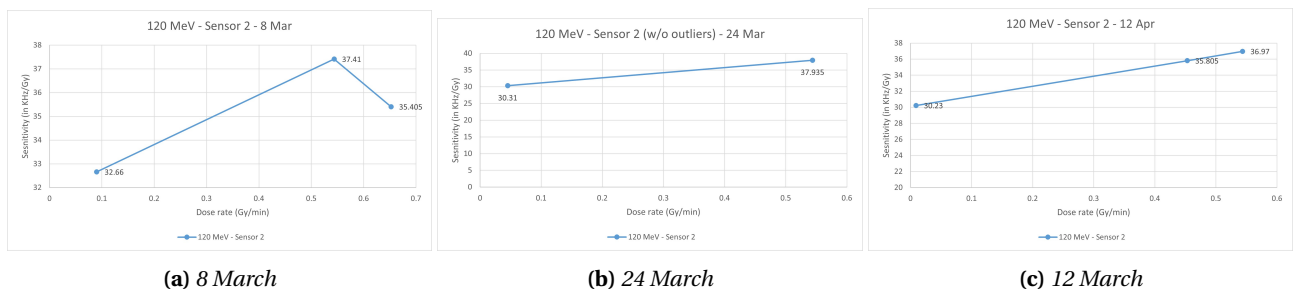


**Figure 5.8:** Variation of FGDOS sensitivity with dose rate at 120 MeV

As seen most notably in Figure 5.9a, the sensitivity vs dose rate trend oscillates back and forth, implying that small random variations in the sensitivity may be at play, caused by errors relating to the test setup, the beam arrangement, beam characteristics or methodology of data collection and analysis. These factors have been elaborated at the end of this section. As such, it can be asserted that there is no systematic dependency of the sensitivity of the FGDOS on the dose rate of incident radiation.

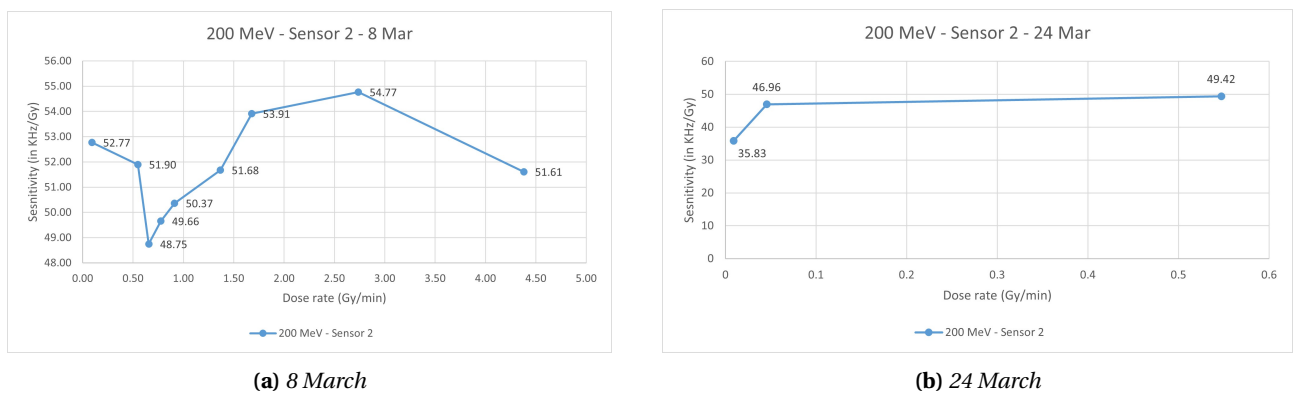


**Figure 5.9:** Variation of FGDOS sensitivity with dose rate at 200 MeV

### Low sensitivity mode - LOWSENS

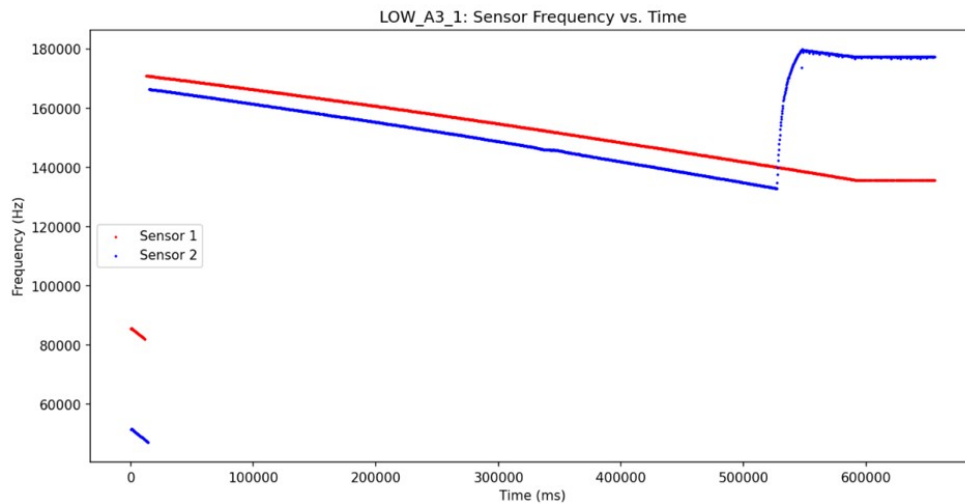


**Figure 5.10:** Frequency characteristic in LDR - LOW SENS Mode

The typical sensitivity in LOWSENS mode was observed to be about 6-7 kHz/Gy initially. The effect of TID induced degradation on sensitivity can be seen in Figure 5.11. Despite the limited number of data points, it can be seen that the sensitivity in LOWSENS mode also exhibits a rising trend with respect to the kinetic energy of incident protons (seen in the orange curve in Figure 5.11).

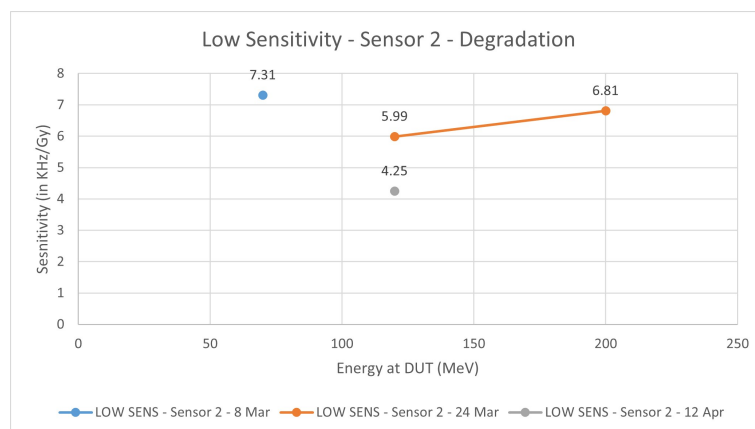


**Figure 5.11:** Sensitivity variation with Beam Energy - LOW SENS Mode

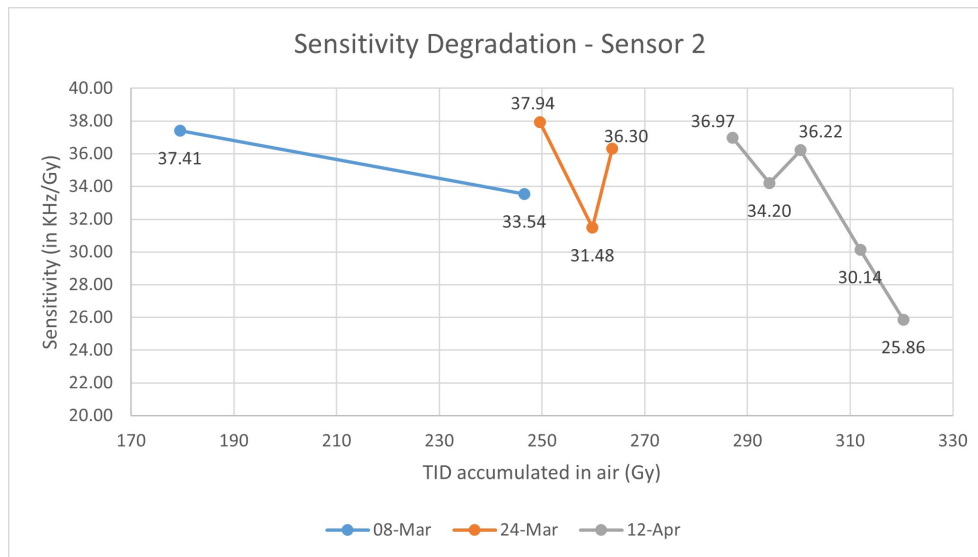
### TID induced degradation

Figure 5.12 shows the change in sensitivity of sensor 2, as it progressively accumulated TID over the three test days. The sensitivity was computed and compared for baseline energy and dose rate levels, to remove any variation in the sensitivity that may be a result of variation in these beam parameters. FGDOS sensitivity is seen to deteriorate with rise in TID, in line with expectations. The degradation is due to multiple factors reported in previous studies:

- Trapping of charge carriers in the field oxide results in reduction in the electric field across the floating gate and oxide. The trapped holes also increase the rate of recombination of electrons that are released by ionizing radiation [34].
- Deterioration of the readout circuitry of the FGDOS SoC i.e. fall in the threshold voltage of the readout n-MOSFET [20].
- Displacement damage in the field oxide caused by proton collisions [34].

Overall, a sensitivity degradation of about 31 % was seen over a TID range of about 180-320 Gy. Curiously, it can be seen that the sensitivity shows an increase at the beginning of each test day. This is believed to be the result of annealing of trapped charges [34, 23] in the time interval between successive test days, or

long term annealing [4]. Annealing on a shorter time scale was also observed. The sensitivity seemed to grow moderately between successive recharges of the sensor in a given run. This is referred to as short term annealing [4]. The data shown in the plot was collected during baseline tests (at 120 MeV and 0.6 Gy/min).



**Figure 5.12:** Sensitivity degradation with TID

The power consumption of the sensors was seen to progressively increase as the test campaign went on and the sensor accumulated more and more TID. At the end of the test campaign, the power consumption had risen by a factor of four. For consistency with the sensitivity degradation curve, the power consumption data shown in Figure 5.13 was collected only during the baseline runs at 120 MeV and 0.6 Gy/min. In practice, it was seen that the power consumption remained agnostic to the energy/dose rate of irradiation.

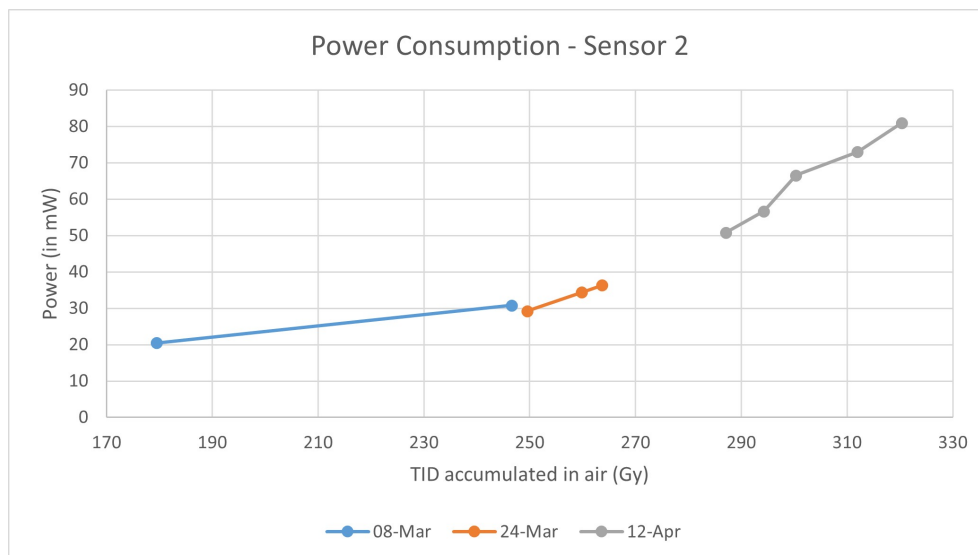


**Figure 5.13:** Increase in FGDOS power consumption with TID

The sensors continued to function until the end of the test campaign. Thus, the 'breaking point' of the sensors in terms of TID was not reached by virtue of the 320 Gy delivered to the FGDOS chips. In an extensive study published by Rizzo et al. [106], it was reported that the analog and digital circuits of the FGDOS could continue functioning up until a TID of approx. 840 Gy and 420 Gy respectively [106].

### Rapid Recovery Effect

After the accumulation of significant TID (about 150 Gy) the sensors exhibited an interesting, previously unseen behavior which is referred to as the *Rapid Recovery* hereafter. In the *Rapid Recovery* effect, the sensor frequency is seen to rise immediately ("recovery") after irradiation stops, thus leading to a profile that looks similar (yet slower) to a recharge at first glance. Soon after, the frequency levels off at a higher value. This is referred to as the "level-off". When irradiation is resumed, the frequency drops steeply ("drop-off") to nearly pre-recovery values. All three parts of the *Rapid Recovery* effect can be clearly appreciated in Figure 5.14.

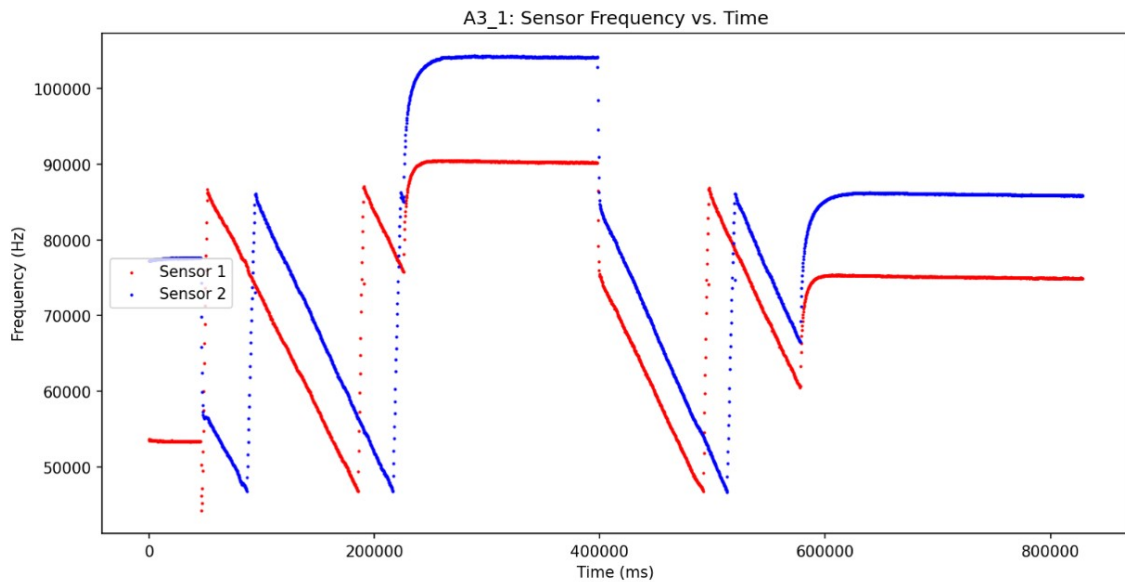


**Figure 5.14:** *Rapid Recovery* effect observed at 70 MeV

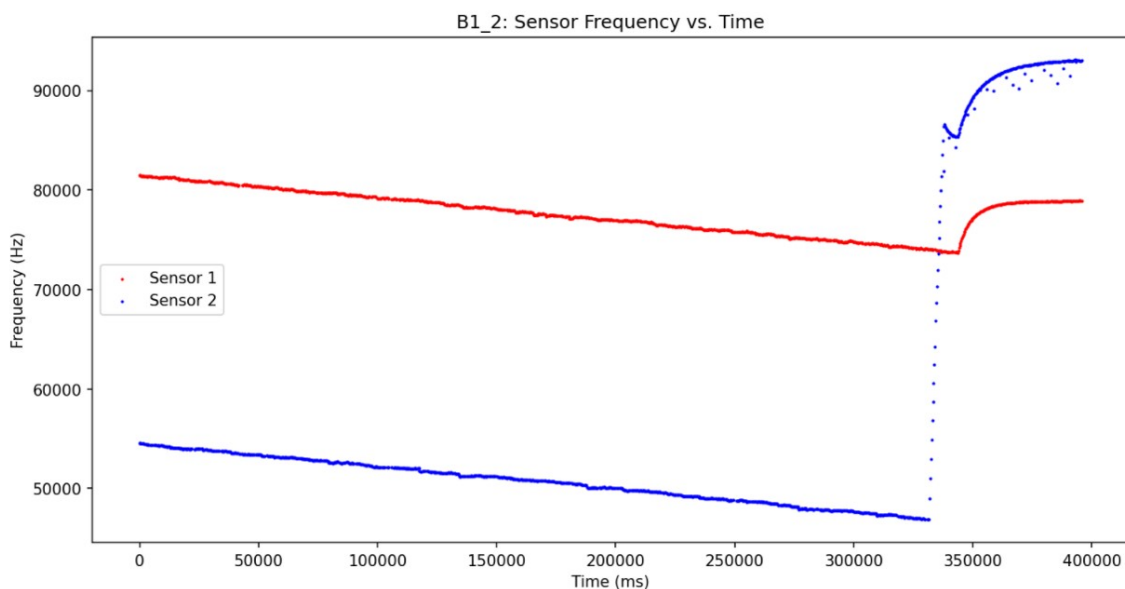


**Figure 5.15:** *Rapid Recovery* effect observed at 120 MeV

In Figure 5.15, an interesting occurrence of the *Rapid Recovery* can be seen in Sensor 2. This *Rapid Recovery* occurs immediately after the sensor recharges to the target frequency. Once irradiation ceases, the 'recovery' pushes the sensor frequency beyond the target value. This indicates that the *Rapid Recovery* happens independently of the charging control circuitry of the FGDOS.

Owing to the structure and working principle of the FGDOS as explained in [34], [20], the *Rapid Recovery* could be attributed to one of the following elements. The possible role of these elements in this effect is discussed below, with the aim of isolating the most probable cause.

- **Charging circuitry:** The charging circuitry of the FGDOS is made of a p-MOSFET that injects charge onto the floating gate such that the sensor frequency rises up to its target value. It is unlikely that the *Rapid Recovery* effect is associated with this element since it was observed that the recharging process continued to function correctly during and between irradiation runs even after the *Rapid Recovery* effect was first noticed. Also, the amount of frequency rise seen in the *Rapid Recovery* effect was unrelated to the target or threshold frequencies, which implies that the *Rapid Recovery* is not caused by a 'misfiring' of the recharge mechanism that is triggered after irradiation stops.
- **Floating Gate/ Sensing circuit:** It could be the case that an accelerated recombination of charges takes place after irradiation stops. Leading to a reduction in the rate of charge neutralisation on the floating gate. It could also be speculated that the *Rapid Recovery* is precipitated by an increased rate of charge trapping in the field oxide beyond certain TID levels. This line of reasoning implies that the incidence of protons was somehow 'releasing the trapped charges at an increased rate'. A rate which subsequently plummeted as soon as the protons stopped impinging. However, these speculations fail to convincingly explain the *Rapid Recovery* effect in its entirety, which casts doubts over the involvement of the sensing circuit in the production this phenomenon.
- **Readout circuitry:** The readout circuitry of the FGDOS consists of an n-MOSFET whose drain current is fed to a current to frequency converter to provide frequency values. It might be the case that the *Rapid Recovery* is a caused by the drain current going up, as a result of the release of residual charges post irradiation. In a discussion of the *Rapid Recovery* effect with CERN researchers, it was posited that a factor associated with the readout circuitry might be the most feasible explanation for the *Rapid Recovery* effect. However, the presence of an apparent bottleneck does not seem to be the cause.

The *Rapid Recovery* effect had not been noticed previous to this study. However, it is most certainly not a "one-off" since further testing conducted on an FGDOS chip from a separate batch served to reproduce the *Rapid Recovery* effect. This is discussed further in section 5.6. The need for a viable explanation as to the onset of the *Rapid Recovery* effect at high TID levels calls for further investigation into this phenomenon.

### Single Event Effects and other anomalies

Throughout the test campaign, no latchups occurred in the FGDOS or elsewhere in the constituent elements of the test setup. This shows that the FGDOS can comfortably function without latchups up to the expected mission doses (listed in Table 4.3), with ample margin. However, multiple SEEs were observed during the test campaign. The result of one such SEE is evidenced by the plots in Figure 5.16.

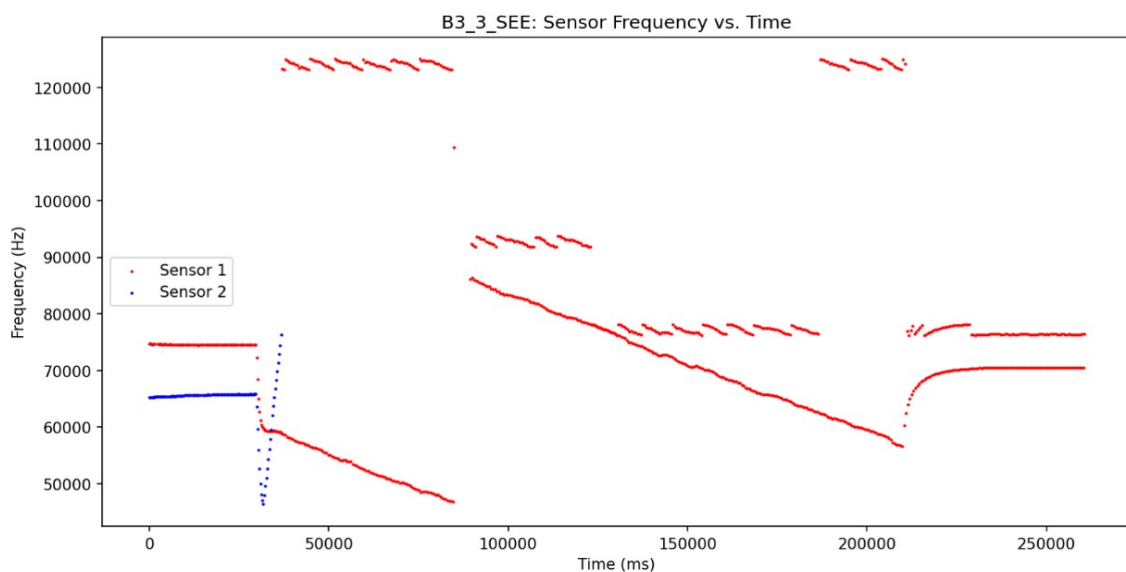


**Figure 5.16:** *SEE in FGDOS*

It is apparent that the frequency values from Sensor 2 (in blue) suddenly disappear around the 50 s mark. This disappearance coincides with dubiously high frequency values being read out from Sensor 1 (in red), in addition to intermittent values which lie within expected bounds. This anomaly is not resolved until

the sensor is reset by virtue of power cycling. Subsequently, in the next irradiation run, the values seen in Figure 5.17 were received which indicate that sensor 2 was recharged to a very high value lying outside its LDR.

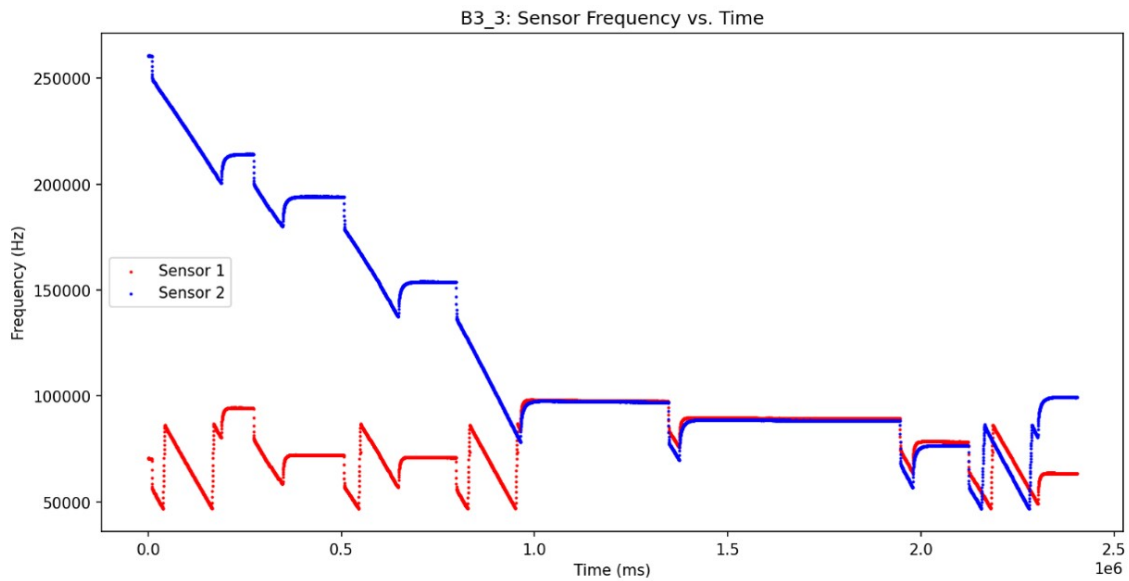


**Figure 5.17:** Post SEE readout and irradiation

Upon further examination, it becomes apparent that the SEE may be localized in the readout registers of the FGDOS. As illustrated by Figure 5.17, the frequency of Sensor 2 increased greatly after the FGDOS was re-initialized. Supposedly, when the SEE occurred, the values in the register designated for storing sensor 2 frequency stopped updating, which caused the recharge control circuitry to interpret this as a case of low frequency and to erroneously inject charge on the floating gate of Sensor 2.

Occasional spikes and dips in the sensor and reference frequencies were observed when scanning the readout from the FGDOS sensors. Some of these were found to coincide with spikes/dips in the temperature measured by the internal temperature monitor of the FGDOS. Some such effects have been attributed to non-destructive SEEs in the digital registers of the FGDOS SoC [90, 34]. However, other spikes and dips lying outside the nominal noise limits of the frequency were also noticed, even when the temperature readings were constant. A definite cause for these anomalies has not been identified. Since the SPI registers in the FGDOS SoC are refreshed with each readout cycle, the soft SEEs are not a cause for concern.

### Noise & Resolution

At very low dose rates, it was seen that the unprocessed response of the sensor under irradiation could not be distinguished from the inherent noise in the sensor frequency. When the sensitivity was computed using linear regression at very low dose rates, it yielded uncharacteristically high sensitivity values, since the drop in sensor frequency is extremely gradual and the slope of the linear fit was being skewed by noise in the frequency. An example of a test run performed at very low dose rate is provided in Figure 5.18. Because of limitations on the maximum irradiation time per run, the sensor frequency dropped by an amount that is no larger than the deviations in frequency due to sensor noise. To overcome this, the duration of the irradiation runs at very low dose rates should be extended sufficiently. This could be achieved with the use of a Co-60 source. Another potential approach is to filter the sensor output before computing the sensitivity slope [19]. In conjunction, it would also be prudent to minimize the noise generated by various sources in the test setup such as the readout board, electrical connections, oscillator for the clock signal used by the FGDOS and other components that were mentioned in [90].

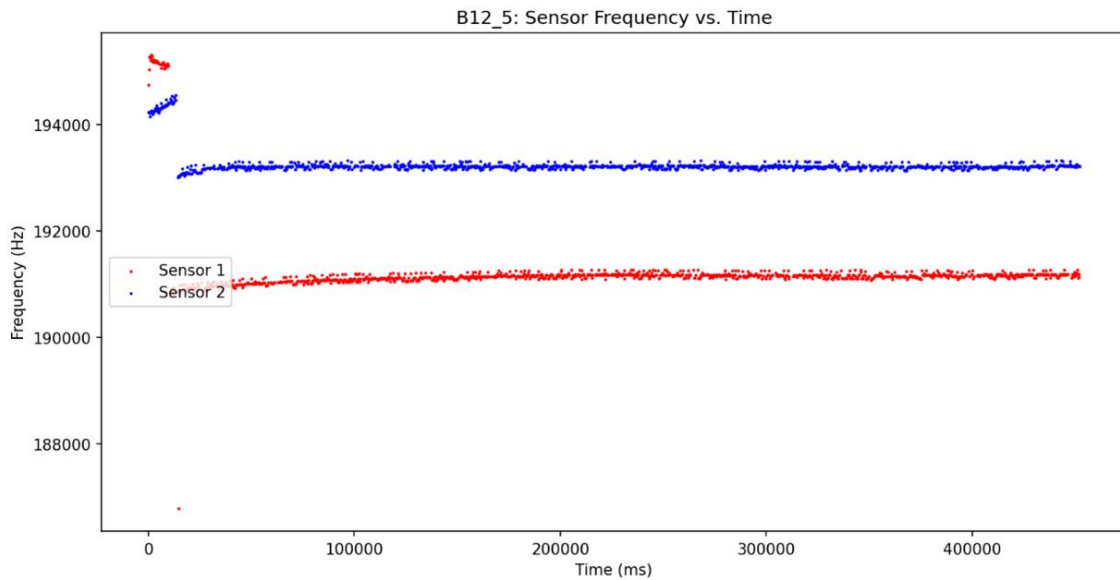


**Figure 5.18:** *Sensor response at very low dose rate (1 mGy/min)*

### 5.1.5. Assumptions and limitations

The following assumptions and limitations were associated with the test setup and methodology, with the consequences and implications stated below:

- Due to beam time constraints and other limitations posed by the test facility, enough runs to yield statistically significant results about the relationships between beam energy and sensitivity, dose rate and sensitivity, could not be executed.
- Even though the test runs were set up to observe individual effects and phenomena in a systematic manner, an interplay between TID effects, annealing and temperature effects could not be completely eliminated. In practical terms, it is difficult to decouple these effects while analyzing the test results and making inferences about the dependence of FGDOS sensitivity on energy, dose rate and other parameters.
- No temperature compensation was applied on the acquired test data since it was noticed that the temperature remained fairly constant during the tests.
- The influence of supporting apparatus and the test equipment on the radiation dose provided to the DUTs was neglected.
- The energy, flux and dose rate of the proton beam was assumed to be constant over each test run. In practice, the beam emitted from a cyclotron is not exactly constant and uniform over time. This could have been a cause for a portion of the noise that was observed in the sensor frequency.
- The profile of the proton beam over the 100 X 100 mm square field was assumed to be uniform. In reality the beam had a profile with a uniformity of 90% or more within the square field.
- Electronic noise in the sensor interfacing circuitry could have been caused by the jumper wires, solderless breadboard and the Arduino board and power supply. Variations in the flux or intensity of the beam could also have contributed to the noise.

### 5.1.6. Results and Conclusions

The results from the tests presented in this section can be summarized as follows:

1. The sensitivity of the FGDOS is seen to increase with kinetic energy of the incoming proton beam. Whether this sensitivity inflation with energy is a general phenomenon needs to be verified by testing against other types of radiation sources. While this is a useful trend to note, the exact relation could not be described mathematically since the number of test runs conducted and the number of energy levels used were not sufficient to come up with statistically significant results. A dependence of the sensitivity on beam energy was reported previously in proton beam testing [34]. However, this observation needs to be verified using various beam energy levels. As alluded to in section 5.6, the energy dependence may vary between sensor specimens and it may also be affected by the TID endured by

the dosimeter.

2. A conclusive correlation between the dose rate of incoming radiation and sensitivity could not be established. This is despite the observations that the sensor sensitivity was seen to vary with changing dose rate at a constant beam energy. In a discussion with researchers from CERN, it was suggested that the observed variation could be a statistical phenomenon that could be pinned down given enough test runs. A negative relation between dose rate and sensitivity was seen at some proton energy levels in HISENS mode, in the experiments in [34]. But this observation was not reproduced in subsequent testing done by the researchers in various studies since then [18, 23, 19].
3. The FGDOS sensor can occasionally exhibit anomalous behaviors such as sudden dips or spikes in sensor frequency and temperature. Based on the occurrence of two such events (on Feb 24 and Apr 12 respectively), one kind of anomalous behavior could be attributed to Single Event Effects (SEEs) in the readout circuitry of the FGDOS chip. When such SEEs occur, power cycling of the device is needed to restore the FGDOS to nominal behavior. Other SEEs in the FGDOS temperature monitor circuit have been noticed, but these are resolved automatically when the SPI registers are rewritten on the next readout cycle. When post processing the payload data, the effects of the SEEs discussed here can be identified and isolated in a straightforward manner.
4. Based on the observed sensitivities w.r.t energy, using a single point sensitivity of approx 35 kHz/Gy could lead to errors in operational TID measurement of about 17% at low energies and up to 56% at high energies.
5. To account for the sensitivity degradation of the sensor with TID, a sensitivity equation could be formulated with a TID dependent decay term, similar in form to:

$$Sensitivity = S_{nominal} \times [1 + S(TID)] \quad (5.2)$$

However, the decay term cannot be precisely derived at this point due to the lack of test data and uncertainty caused by annealing, sensitivity variation with beam energy, dose rate etc. Such an expression should be derived independently for the HISENS and LOWSENS modes. More testing and perhaps a Monte Carlo method based radiation transport model of the FGDOS SoC could provide more insight into this behavior. As a first approximation, the calibration curve developed by Bruccoli et al could be used to estimate the sensitivity decay [18]. This includes the caveat that possible variations in sensitivity due to energy or intensity of incident radiation are not fully captured.

6. Based on the tests performed up to this point, the exact pre-flight calibration profile required to completely characterize the sensor and prepare it for the lunar mission cannot be finalized. This is because the full envelope of expected particle types, energies, fluxes and dose rates could not be utilized within practical constraints and limitations associated with the test facility.
7. For space applications, the FGDOS should almost always be operated in HI SENS mode. This is due to the fact that the dose rates and fluxes generally observed in the space environment are very low, especially in the interplanetary phase of missions. In order to have an appreciable drop in the sensor frequency under the effect of radiation exposure, it is important that the sensitivity be sufficiently high such that the frequency drop can be confidently distinguished from sensor noise.
8. The noise levels of the sensor frequency should be minimized by the use of a large FGDOS window factor in the sensor configuration (as demonstrated in [90]) as well as other electronic noise reduction techniques. Table 5.8 shows a summary of the noise levels obtained in various studies. The use of a precise external oscillator that is robust to the extremes of the space environment may also be interesting to explore for the provision of the window clock (WCK) signal to the FGDOS. To experimentally determine the resolution of the sensor in measuring dose, irradiation runs with long durations at very low dose rates can be performed with a Co-60 source. This would also serve as a better approximation of the mission radiation environment.

Source	Noise level (HISENS mode)
Sealicon FGD-03F Datasheet [117]	75 Hz
Bruccoli et al, 2019 [19]	0.5 mGy (approx. 15 Hz-20 Hz)
de Meyere, 2021 [90]	60-90 Hz
Lunar Zebro Payload	TBD

**Table 5.8:** FGDOS noise and resolution estimates from various sources

9. To ensure the usefulness and statistical significance of the mission results, the readout rate of the sensor should be set to a high frequency. The Lunar 4M mission payload sampling rate was set to once every 5 mins [27]. For the Radiation Payload in the Lunar Zebro Mission, a higher sampling rate of once per min for each sensor may be advised. This sampling rate can be increased further in the mission phases where the expected dose rates are extremely low.
10. Despite the rise in power consumption with TID, the FGDOS at the core of the Radiation Payload is bound to remain within power constraints (discussed in subsection 3.1.9, given the estimated total mission exposures expressed in Table 4.3).
11. The response of the sensor to low dose rates delivered for a high duration of time is not known, since such tests cannot be performed with a cyclotron. This is an important caveat since this condition would be in place for major intervals of the lunar mission, once the rover passes through the VABs.
12. It can be recommended that an identical Ground Model of the Radiation Payload, using FGDOS chips from the same batch as the flight model chips, should be characterized and tested fully against various radiation sources, over the full TID range of that sensor, in order to obtain calibration curves and performance data for the flight model sensors, targeted toward post processing and analysis of the payload mission data. Even though there may be variations between the ground and flight sensors, it can be assumed that sensors from the same batch would exhibit fairly similar behavior, as reported by [22, 18]. To account for sensitivity variations due to energy, pre-flight characterization could be performed at various energy levels that lie within the envelope of the expected environment. Thereafter, the effective sensitivity could be derived using a weighted average of the sensitivities at various energy levels, based on relative flux of particles in each energy band. In a similar fashion, the aforementioned TID decay calibration curve could be constructed pre-flight, using a certain batch of FGDOS chips.
13. Since the dose rates are expected to be very low in the mission, the error introduced during the recharge process can be considered negligible and a low recharging voltage such as 16V or 16.5V can be comfortably used.
14. On the advice of FGDOS developers and researchers from CERN, anomalies such as SEUs and subtle characteristics in the response of the FGDOS to radiation could be investigated better in a mixed field facility such as CHARM [66].

### 5.1.7. Open Questions

In addition to these results and conclusions, some questions still remain unanswered. As such, these can be subjected to further investigation:

- The cause of the so called *Rapid Recovery* effect is yet unknown. At this juncture, it can be speculated that the effect is related to the degradation of the readout n-MOS in the FGDOS SoC.
- The origin and frequency of SEE-like phenomena can be studied further, including the derivation of SEU cross-sections for sensors from various batches.
- The shielding and modulation to incoming particles provided by the packaging of the sensor chip to the inner sensitive volume needs to be studied further and quantified. If more detailed information about the layout and construction of the FGDOS chip can be obtained, a geometric model for radiation transport simulations could be set up.
- The behavior of the sensor at negative temperatures and the variation of sensor response with thermal cycling needs to be observed. Most importantly, the response of the sensor to simultaneous incidence of ionizing radiation in a changing thermal environment needs to be investigated via testing. This is explored further in section 5.2 and section 5.3.
- Another interesting aspect for investigation is the response of the FGDOS to sudden bursts of ionizing radiation over short time intervals. Most of the research done on the FGDOS so far has been conducted at relatively constant dose rates. Behavior of the sensor when bombarded with neutrons at various energies would also be interesting.

## 5.2. FGDOS Temperature Characterization

The sensor and reference frequencies of the FGDOS vary considerably with the temperature of the chip [117, 18]. This is due to a shift in the output characteristics of the MOSFETs in the FGDOS SoC induced by variation in temperature [135]. Since the Radiation Payload is expected to encounter extreme temperatures during flight, it was decided to perform a test to characterize the behavior of the FGDOS sensor w.r.t. temperature.

To correct acquired sensor frequency data for temperature effects, the manufacturer advises the use of one of two approaches; (a) compensation assuming a linear relation between the sensor and reference frequencies as the temperature changes, or (b) using a look up table produced in advance by mapping out the sensor behavior over the expected temperature range. The look up table based approach is considered more accurate and can be performed on ground during post processing of the Radiation Payload data [23]. The FGDOS chip contains an internal temperature monitor for this purpose, with a range of  $-40$  to  $125$  °C [117]. However, this temperature sensor has a resolution of  $1$  °C, which has been reported to be too coarse when compared against the sensitivity of the frequencies to temperature fluctuations [90]. Moreover, the temperature indicated by the internal monitor has to be calibrated in advance with an external temperature reference, since each chip may have a different temperature offset w.r.t the actual absolute temperature.

### 5.2.1. Test setup

The setup for the temperature characterization test is depicted in Figure 5.19, with its constituent elements described below:

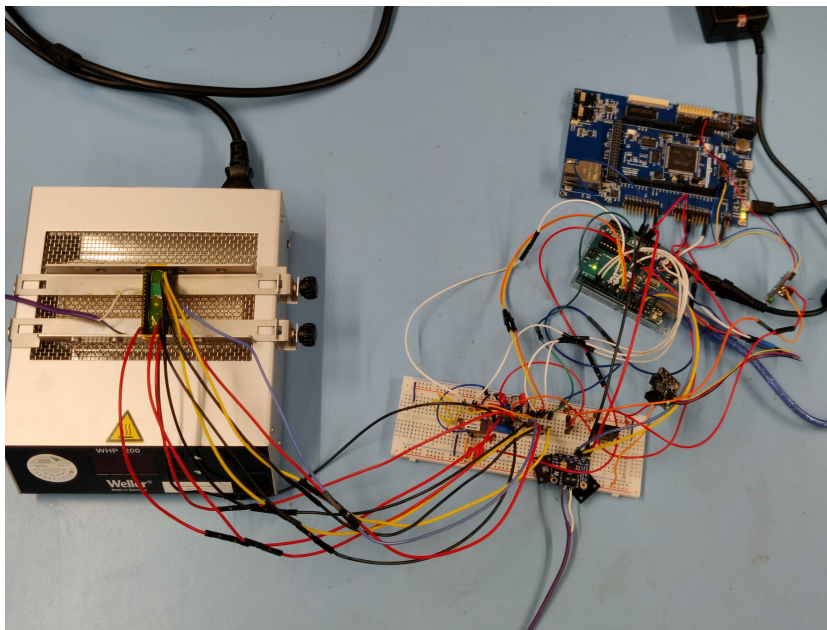


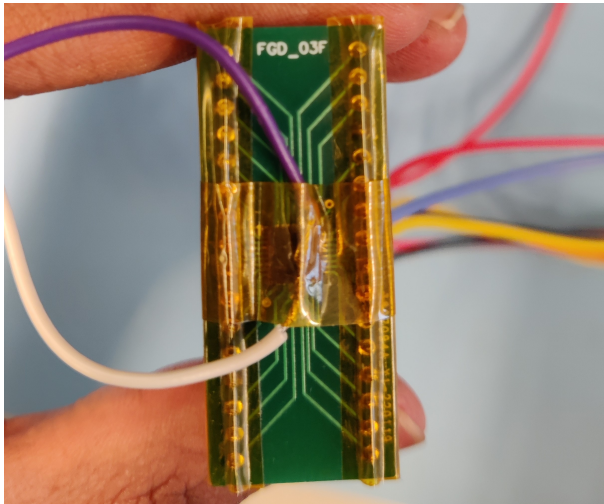
**Figure 5.19:** *Temperature characterization test setup*

1. The test article was an FGD-03F sensor breakout PCB with a new QFN packaged FGDOS chip [117] soldered on it. Only Sensor 2 of this chip was connected and used for this test.
2. A DIL package FGD-03F sensor chip was used to measure ambient temperature with the same circuitry that is used by the internal temperature monitor of the FGDOS.
3. An Arduino Uno R3 development board was used to control and read out the FGD-03F breakout as well as the thermocouple breakout.
4. A solder-less breadboard was used to make connections between various electronic components, with the use of DuPont style jumper wires.
5. An Infrared Heater was used to provide heat flux to the test article. The heater used for this purpose was a Weller WHP 200 with a heating range of  $50$  -  $400$  °C [149]<sup>2</sup>. The FGD-03F breakout was clamped

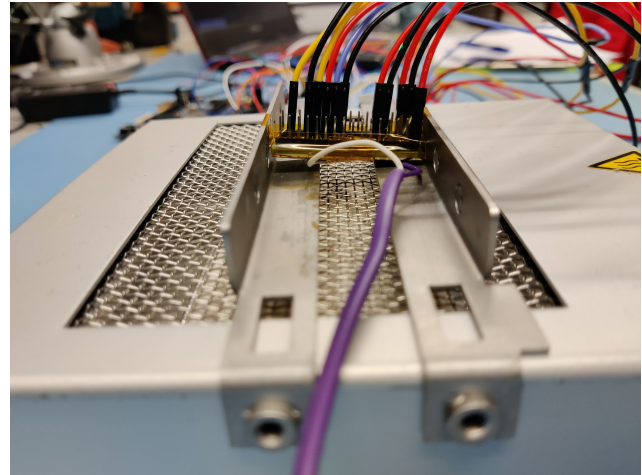
<sup>2</sup>It is to be noted that this range refers to the temperature very close to the heater lamp itself and is not necessarily the temperature range that can be obtained by objects placed between its clamps

above the wire mesh of the WHP 200 such that FGDOS chip was facing the incident IR flux. This is shown in Figure 5.20b.

6. An E-type thermocouple was affixed to the surface of the FGDOS chip with Kapton tape to provide measurements of the surface temperature of this chip, as shown in Figure 5.20a.
7. An MCP9600 breakout board from Adafruit<sup>3</sup> was used to readout the thermocouple voltage using a built-in ADC and to compensate such that a temperature value on the Celsius scale could be obtained over an I2C connection to the Arduino. The MCP9600 contains a built in cold junction.



(a) Thermocouple affixed to FGDOS chip



(b) FGD-03F Breakout clamped in IR Heater fixture

**Figure 5.20:** Temperature characterisation test setup - alternate views

### 5.2.2. Test Levels

The test levels for this test are tabulated in Table 5.9. Accounting for the offset in the FGDOS internal temperature monitor, the actual temperature range to which the FGDOS chip was subjected is 22-107 °C.

Temperature Reference	Min Temperature °C	Max Temperature °C
IR Heater Setting	50	400
FGDOS Internal Temperature Monitor (raw measurement / offset compensated)	85/22	170/107
E-Type Thermocouple (measured)	22	158

**Table 5.9:** FGDOS Temperature Characterization Test Levels

### 5.2.3. Methodology

#### Test Procedure

The test procedure which was followed during the temperature characterization test can be found in [121]. The temperature characterization test can be thought of as consisting of three main phases:

1. Ambient temperature measurement: Initially, it was assumed that the internal temperature monitor of the FGDOS was at thermal equilibrium with the surroundings and the entire chip would be at a uniform temperature. This implies that the surface temperature of the FGDOS chip (where the thermocouple was affixed) would be identical to the temperature measured by the internal monitors. Measurements were recorded at this stage before any heat input was provided.
2. Heating: In this phase, the test article was taken from ambient temperature to the highest possible setting of the IR Heater. This heating was performed in multiple steps. Essentially, the heater setting was increased by a fixed amount and allowed to remain at this set point until the temperature readings stabilized i.e. the setup reached steady state w.r.t the heater and the surroundings. This led to the highest reading of the FGDOS internal temperature monitor and thermocouple. The setup was allowed to dwell at this setting until the temperature readings stabilized at this peak.

<sup>3</sup><https://www.adafruit.com/product/4101>

3. Cooling: Once the highest temperature setting was reached by the IR heater, the internal temperature monitor and thermocouple, the heater setting was reduced to the lowest point, initiating a cooling phase which lasted until temperature readings stabilized to ambient levels.

Prior to the actual test, a checkout of the setup was performed to ensure that all equipment, sensors and test articles were working as expected and the data acquisition and logging system was also checked out to ensure that test data could be successfully recorded and stored. The heating characteristic and levels of the IR Heater were observed by clamping the thermocouple in the intended location of the DUT and by observing its output at different settings of the heater. The thermocouple was calibrated at room temperature in advance, using a FLUKE 714 Thermocouple Calibrator<sup>4</sup>. The offset between the Calibrator readout and the readout from the MCP9600 was found to be about  $0.9\text{ }^{\circ}\text{C}$ , which lies well within the error bounds for an E-Type<sup>5</sup>.

#### 5.2.4. Observations

The following observations were made during the temperature characterization test:

- The maximum temperature that could be achieved during the test was measured to be  $170\text{ }^{\circ}\text{C}$  by the internal monitor and  $158\text{ }^{\circ}\text{C}$  by the thermocouple. The reading of the internal monitor equates to  $107\text{ }^{\circ}\text{C}$ , accounting for the initial offset. The ambient temperature in the room remained relatively constant at about  $21\text{--}22\text{ }^{\circ}\text{C}$ . This was recorded by the internal monitor of Sensor 1, as shown by the red scatter plot in Figure 5.22.

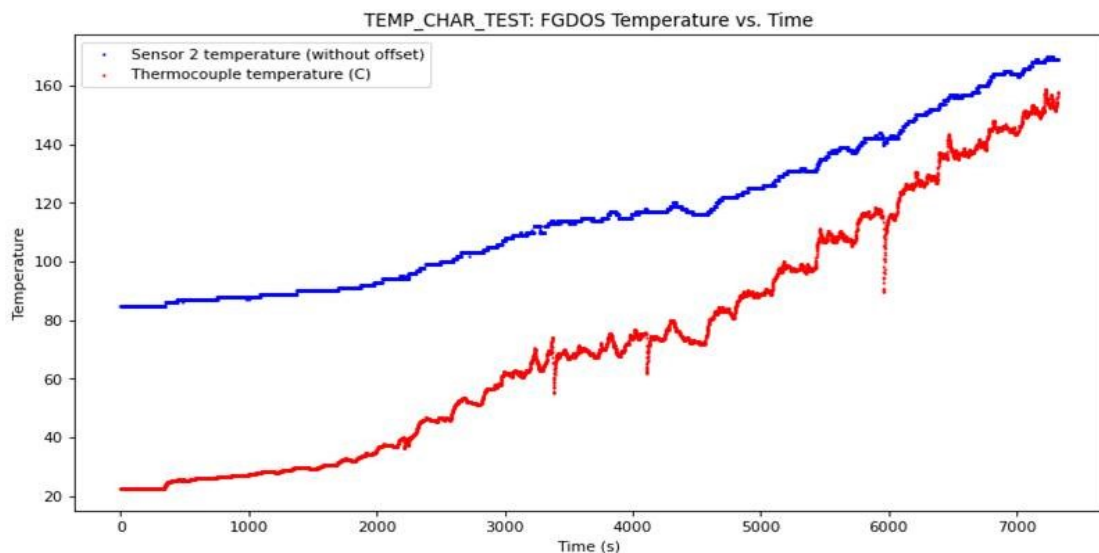


**Figure 5.21:** Temperature measured by the FGDOS internal monitor and the thermocouple during the heating phase

- The temperature measured on the surface of the FGDOS chip differs from the temperature measured internally by the in-built temperature monitor. However, the reading from both sensors show a similar trend as seen in Figure 5.21. This shows that both monitors experienced a similar heat flux over time, as shown by the blue plot in Figure 5.22, but the disagreement in absolute temperature measurements varies considerably as the temperature deviates increasingly from ambient levels. The thermocouple is seen to reach a higher final temperature than the internal temperature monitor.

<sup>4</sup><https://www.fluke.com/nl-nl/product/kalibratie-instrumenten/temperatuurkalibrators/fluke-714>

<sup>5</sup><https://tempsens.com/blog/type-e-thermocouple>

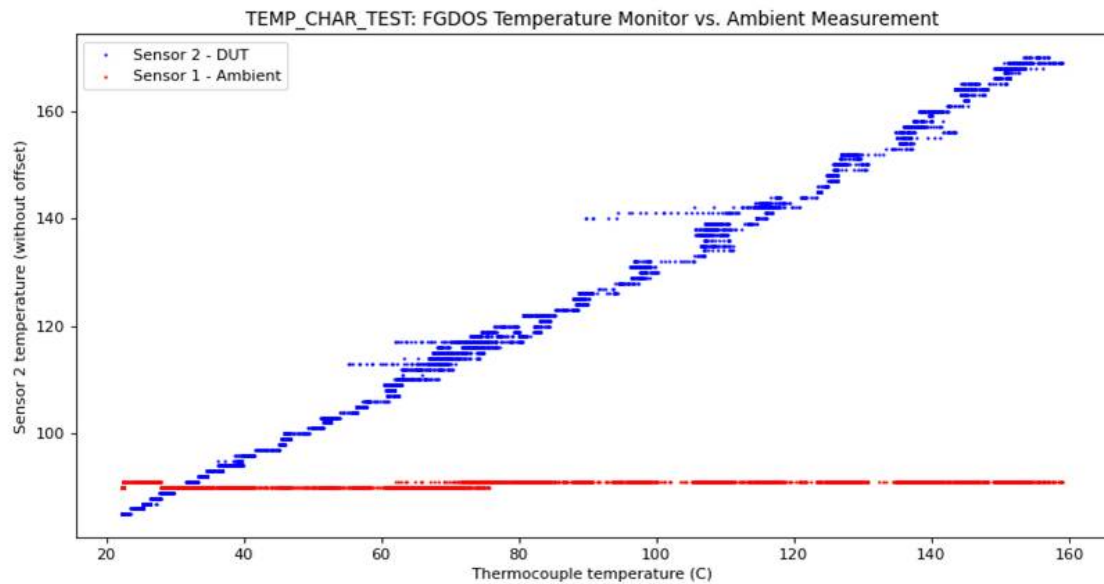


**Figure 5.22:** Correlation between FGDOS internal temperature monitor readings and thermocouple measurements over the heating phase. Sensor 1 recorded the ambient temperature

- The sensor frequency goes down as the temperature rises. Similarly, the reference frequency also reduces. This is shown in Figure 5.25. This confirms the basic trend in frequencies w.r.t temperature. As reported in [18], the gradient of reduction of the sensor frequency is different (steeper) from the gradient of reduction for the reference frequency. As shown in Figure 5.25, these gradients also vary over the temperature range in a subtle manner. Figure 5.23 shows that the sensor and reference frequencies of the FGDOS decrease monotonously with an increase in temperature. However, the rate at which they decrease i.e. the slope of the downward trend is not the same for the sensor and reference frequency. This is substantiated by the time history plot in Figure 5.25.

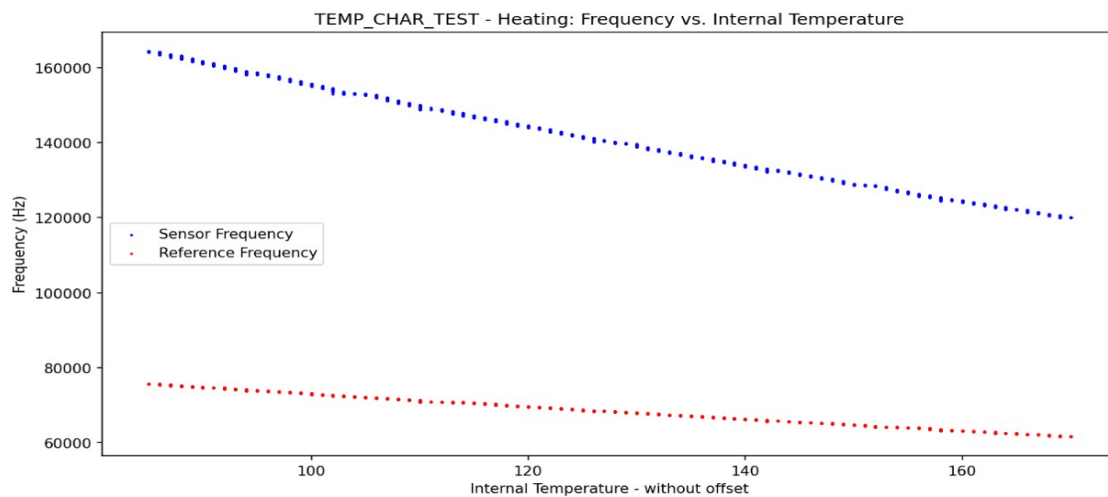


**Figure 5.23:** Variation of Sensor and reference frequencies with temperature

- The power consumption of the FGDOS did not vary appreciably over the duration of the temperature characterization test. This can be seen clearly in the time history plot of sensor power consumption in Figure 5.24.

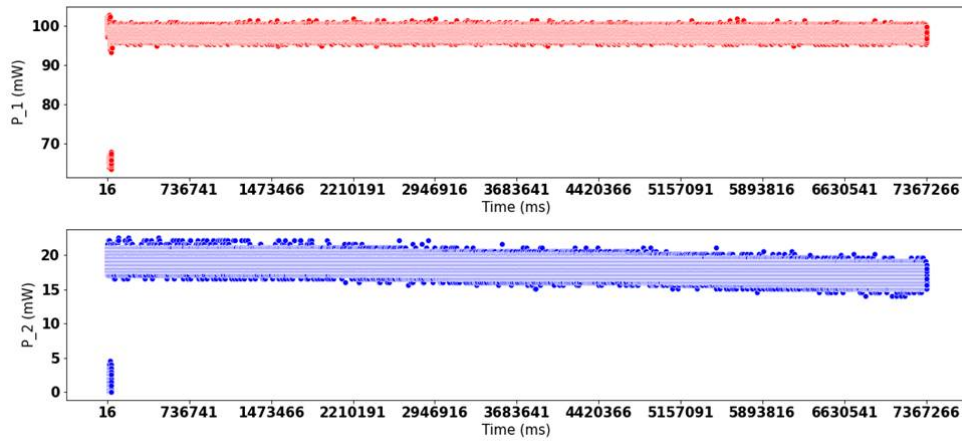


**Figure 5.24:** FGDOS Sensor power consumption during the heating phase. Sensor 2 (in Blue) was the DUT while Sensor 1 showed high power consumption due to TID degradation from previously conducted proton beam tests

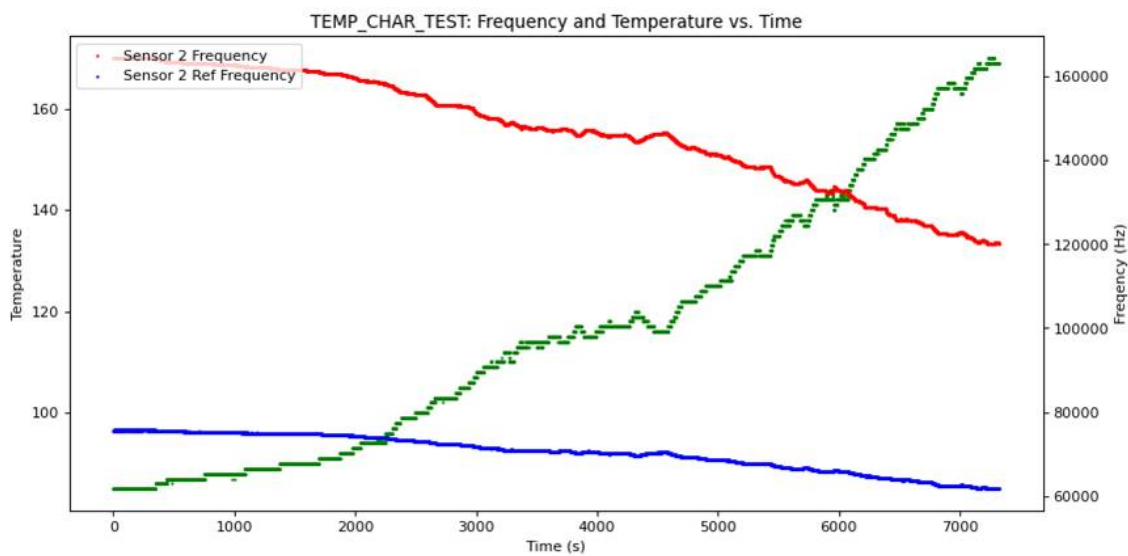


**Figure 5.25:** Evolution of sensor frequency, reference frequency and temperature (in green) during the heating phase

### 5.2.5. Limitations and assumptions

The following limitations were observed in the test setup and the test methodology, which could have introduced errors and uncertainty in the test results:

- The test article could not be subjected to temperatures below ambient i.e. the test setup could not perform cooling. The maximum temperature that could be reached by the setup was restricted to about 160 °C.
- The temperature characterization test described here was performed at a certain working point i.e. base value of the sensor frequency at ambient temperature. This value would change under irradiation as the sensor accumulates TID, within the LDR. Brucoli et al. reported that the temperature characteristic of the FGDOS varies slightly with the working point [23]. This variation was not investigated in the present work. Similarly, the change in frequency vs temperature gradient with change in temperature was not investigated in the present work. Hence, the temperature dependence may be a second order effect but it is approximated to be a first order in this study.
- As seen in the temperature plot of the thermocouple w.r.t time, the thermocouple readings were seen to be very sensitive as evidenced by the fluctuating nature of the temperature output. The output from the IR Heating lamp was not strictly constant over time. This could also have led to fluctuations in the measured temperature.
- The thermal interface between the thermocouple and the FGDOS chip may not be perfectly conductive, thereby rendering the chip temperature to be slightly different from that measured by the ther-

mocouple. The thermocouple is an analog sensor whereas the internal temperature monitor is digital and has a coarser resolution. This leads to a deterioration of the correlation between the temperatures measured by these sensors, as apparent in Figure 5.22.

- The gradient of temperature rise or fall during the test run could not be controlled precisely with the test setup that was used.

### 5.2.6. Results & Conclusions

The following conclusions can be derived from the temperature characterisation performed on the FGDOS:

1. The FGDOS chip can survive and function outside the operational temperature range advertised in [117]. The range of temperature characterisation was extended on top of previous efforts documented in [23]. However, the extent to which this allowable temperature range can be extended needs to be tested with a setup capable of subjecting the test article to more extreme temperatures. The TVAC test described in subsection 5.7.3 can serve this purpose.
2. The temperature measured by the internal monitor of the FGDOS chip is different from the surface temperature of the chip. However, in a gradually varying thermal environment such as the expected lunar mission conditions, it is foreseeable that the chip would reach near steady state for sizeable time intervals, so that it may be considered a thermal lumped mass. From an engineering standpoint, the temperature measured by the internal temperature monitor cannot be replicated by measuring the surface of the FGDOS chip. Hence, if the temperature of the chip is to be measured at higher resolution, another method is needed. This is explored further in section 5.3.
3. The relationship between the sensor frequency and reference frequency is approximately linear w.r.t varying temperature, as described by the manufacturer [117]. This is shown by Figure 5.25. The linear relationship between the sensor and reference frequencies for the DUT at the given starting frequency is captured by Equation 5.3 where  $f_{Sens}$  and  $f_{Ref}$  have units of Hz. The linearity<sup>6</sup> was calculated to be of 98.3% for the fit indicated by the line shown in Figure 5.25, which corresponds to the slope and intercept in the equation below:

$$f_{Sens} = 3.197 \cdot f_{Ref} - 78061.97 \quad (5.3)$$

This approach can be used to compensate sensor frequency readings by using the reference frequency readings in conjunction with readings from the internal temperature monitor. It is to be noted that a look up table (LUT) based approach could also be followed and would be more accurate in practice, as described in [23]. In a discussion with researchers from CERN, it was advised that the temperature compensation could be done solely on the basis of the reference frequency. In this regard, the internal temperature monitor readings could be used to monitor the health of the FGDOS and to provide a way of diagnosing any abrupt changes or SEEs that occur in the frequency registers of the FGDOS. The merits and utility of the internal temperature monitor from the perspective of Radiation Payload operations are discussed further in section 5.3.

4. The power consumption of the FGDOS chip does not appear to have an appreciable dependence on the temperature of the chip. This characteristic is favorable for the mission application since the Radiation Payload is expected to experience high thermal extremes. Having a relatively stable power requirement during these different thermal conditions would produce less stress on the upstream power management and distribution faculties of the rover.
5. The performance of the FGDOS under the effect of simultaneous incidence of ionizing radiation and thermal environment variation needs to be tested, since this would emulate the mission conditions more accurately. To the knowledge of the author, such tests have not been conducted yet. Hence, a test (described in section 5.3) was designed and executed to investigate this phenomenon. At this point, it is not known whether large temperature variations would affect the sensitivity of the FGDOS sensor to ionizing radiation. It can be presumed that the combined effect of temperature variation and radiation incidence would influence the LDR and recharging process of the sensor. Hence, it would be prudent to restrict the LDR of the sensor such that a sufficient margin is present to account for these affects. It was previously noticed that the linear range can be extended upwards to increase

<sup>6</sup>The linearity would be higher if spikes and dips in the frequency had been filtered out

the amount of TID that can be measured between two successive recharges [90]. However such an extension may not be prudent in light of the combined temperature and radiation effects discussed here. For instance, the sensor may recharge to the target frequency at a high temperature. As this temperature reduces, the sensor frequency would rise, thereby rendering the sensor outside the linear range. Similarly, at the lower temperatures, the sensor could be discharge to levels which would lie below the recharge threshold at ambient temperature. To combat this, temperature dependent recharge target and threshold frequency configuration could be added in the sensor control software. Another way to accomplish this would be to configure the recharge levels based on the current reference frequency values which would be compared against the base (ambient level) reference frequency values.

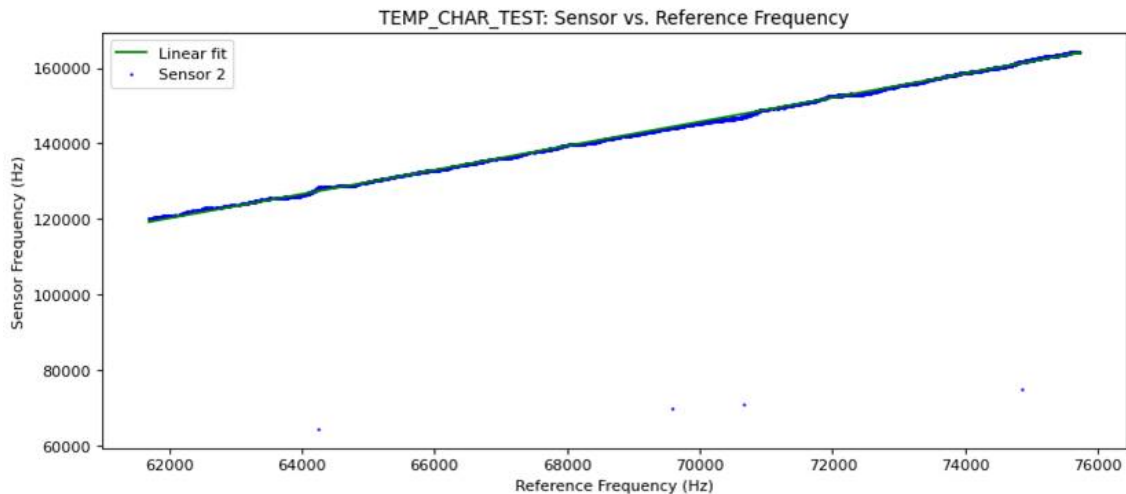


**Figure 5.26:** Relationship between sensor and reference frequency with temperature variation. A linear fit approximating this relation is shown by the green line

6. Temperature characterization and calibration of the FGDOS sensor on the FM of the Radiation should be performed pre-flight since it is important to decouple the effects of temperature variation and incident ionizing radiation, on the sensor and reference frequencies.
7. Considering the transferability of these results to the lunar mission application, some distinctions become apparent. The temperature variations during the mission would be much more gradual than the test conducted here. However, the magnitude of temperature swings is expected to be more extreme [47]. The effect of thermal cycling between such extremes on the operations and performance of the FGDOS sensor is not yet known. This could also be a matter of interest for the TVAC test mentioned in section 5.7.
8. To supplement the internal temperature monitor, an external temperature sensor with higher precision may be used on the Radiation Payload. At first glance, it may seem like an external temperature sensor may not experience a temperature which is completely representative of the conditions within the FGDOS chip. Since the internal temperature monitor is embedded within the integrated circuit (IC), it provides a measurement which is a more accurate representation of the temperature of the sensors in the chip. This also means that the external sensor would be slower to respond to temperature fluctuations within the chip. If the external temperature sensor is mounted on a PCB along with the FGDOS chip, it may be possible to get it to experience a temperature similar to the chip by mounting it very close to the sensor or underneath it, along with the use of a large ground plane to provide thermal connection between the two and to raise the thermal inertia of the PCB. This approach is explored in section 5.3.

### 5.3. FGDOS Sensor Characterization: Simultaneous Irradiation and Temperature variation



**Figure 5.27:** *Experiment room arrangement during testing at HPTC*

#### 5.3.1. Aim & Rationale

Another test of the FGDOS FGD-03F module was conducted to observe the behavior of the sensors under exposure to radiation whilst simultaneously being subjected to a varying temperature. Ideally, the combined effect of temperature change and irradiation could be characterized as the superposition of the behavior of the sensor under irradiation and temperature change taking place separately. However, it is important to study the actual behavior of the sensor to obtain a characterization that closely approximates real world applications.

This test was also designed to overcome some of the limitations present in the test setup and methodology of the temperature characterisation presented in the previous section.

#### 5.3.2. Test Setup

The experimental setup used for this test is conveyed by the schematic shown in Figure 5.28. The setup consisted of the following elements:

- Daughterboard PCBs with FGD-03F and thermally bonded Peltier modules
- Arduino Uno microcontroller boards
- n-MOSFET based custom made peltier supply boards
- Relay array modules
- DC power supply
- INA219 power monitor breakout boards
- FGD-02F Evaluation Board
- DC/DC Step Up for recharging the FGD-02F Evaluation board
- 12V Power adapters
- USB cables
- Laptops for data acquisition and logging

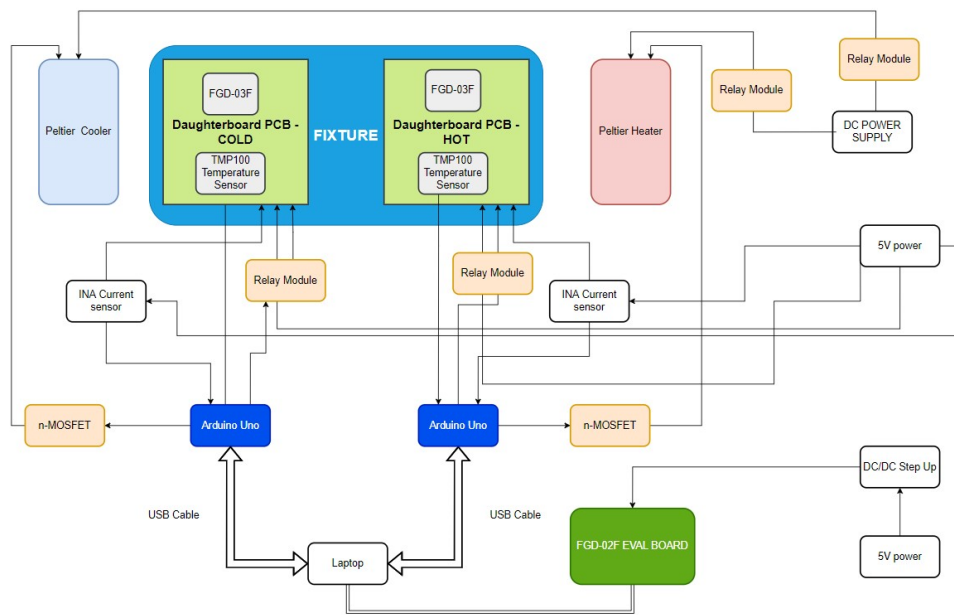
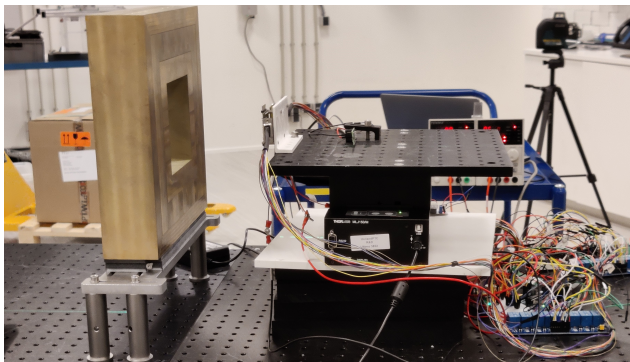
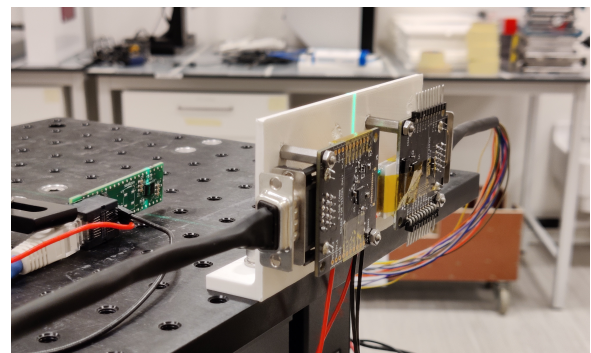


Figure 5.28: Setup schematic

Figure 5.29a and Figure 5.29b show the setup at the outset of the experiment. Custom fixtures were 3D printed to firmly hold the DUTs in place during the experiments. Two Daughterboard specimens were used for the test. One of these was bonded to the hot side of peltier module using thermal paste and is hereafter referred to as the "HOT board". The other specimen was bonded to the cold side of a different peltier module and is termed the "COLD board".



(a) Experimental setup side view



(b) DUTs mounted on test fixture

Figure 5.29: Experiment setup at HPTC

### 5.3.3. Test Levels

A summary of all test runs performed on test day is provided in Table 5.10. This information includes the purpose of each run, the beam characteristics and the temperature profile for the HOT and COLD boards.

Run #	Test Code	Beam Energy (MeV)	Beam Energy at Target (MeV)	Dose rate at target (in air) (Gy/min)	Approx Run time (min)	Dose acc. at target - TID (in Air) (Gy)	Sensor Settings	Test Purpose	Thermal Profile - HOT Board	Thermal Profile - COLD Board
<b>SET 1</b>										
1	A3		70	0.6	5	3	HI SENS	High sensitivity baseline at 70 MeV	Constant - ambient temperature	Constant - ambient temperature
2	B3		120	0.6	5	3	HI SENS	Baseline test - TID degradation	Constant - ambient temperature	Constant - ambient temperature
3	C3		200	0.6	5	3	HI SENS	High sensitivity baseline at 200 MeV	Constant - ambient temperature	Constant - ambient temperature
4	B2		120	0.1	3	0.3	HI SENS	Medium dose rate	Constant - ambient temperature	Constant - ambient temperature
5	B11		120	0.01	9	0.09	HI SENS	Low dose rate	Constant - ambient temperature	Constant - ambient temperature
6	B12		120	0.001	9	0.009	HI SENS	Very low dose rate	Constant - ambient temperature	Constant - ambient temperature
<b>SET 2</b>										
1	B3		120	0.6	5	3	LOWSENS	Low sensitivity baseline at 120 MeV	Constant - ambient temperature	Constant - ambient temperature
2	B3		120	0.6	8	4.8	HI SENS	Passive mode & Full sensor freq characteristic	Constant - ambient temperature	Constant - ambient temperature
<b>SET 3</b>										
1	B3		120	0.6	8	4.8	HI SENS	Thermal baseline	Linear	Linear
2	B3		120	0.6	8	4.8	LOWSENS	Thermal baseline in low sensitivity mode	Linear	Linear
3	B3		120	0.6	8	4.8	HI SENS	Thermal effect on Full freq characteristic	Linear	Linear
4	B3		120	0.6	8	4.8	HI SENS	Thermal cycling effect on Full freq characteristic	Sawtooth	Gradual recovery from cold spike
5	B3		120	0.6	8	4.8	HI SENS	Thermal cycling effect	Sawtooth	Oscillation
6	B3		120	0.6	8	4.8	HI SENS	discontinuous temperature rise effect	Staircase	Constant - ambient temperature
7	B3		120	0.6	8	4.8	PASSIVE	thermal effect on passive mode	Staircase	Constant - ambient temperature
<b>SET 4</b>										
1	B2		120	0.1	5	0.5	HI SENS	thermal effect on medium dose rate	Linear	Linear
2	B11		120	0.01	8	0.08	HI SENS	thermal effect on low dose rate	Linear	Linear
5	B12		120	0.001	8	0.008	HI SENS	thermal effect on very low dose rate	Sawtooth	Oscillation
6	B3		120	0.6	5	3	HI SENS	Extreme thermal variation	Linear	Spike and oscillation
<b>SET 5</b>										
1	B3		120	0.6	3	1.8	HI SENS	TID Baseline & Thermal Degradation	Constant - ambient temperature	Constant - ambient temperature
<b>Cumulative TID</b>						<b>66.79</b>				

**Table 5.10: Irradiation & temperature characterization: Test run summary**

### 5.3.4. Methodology

The test was carried out in three different stages:

1. Pre-test temperature characterisation.
2. Radiation characterisation at constant temperature.
3. Simultaneous irradiation and temperature variation.

Throughout each test run, the following parameters were monitored for all sensors:

1. Time elapsed
2. Sensor Frequency
3. Reference Frequency
4. FGDOS Internal Temperature
5. Recharge count
6. Voltage
7. Current consumption
8. Power consumption
9. PCB Temperature
10. Actuation status for relays connected across - Peltier power supply, Daughterboard supply and FGDOS SPI connections
11. Peltier control I/P

#### Pre-Test Temperature Characterization

Prior to the experiment at HPTC, mock tests were carried out without irradiation to characterize the thermal coupling between the peltier modules and the PCBs and to check the quality of the thermal interface between these. Another objective of these tests was to characterize the temperature profiles to be used during the tests. These profiles were monitored using the TMP-100 temperature sensor mounted on the Daughterboard as well as the internal temperature monitor of the FGDOS.

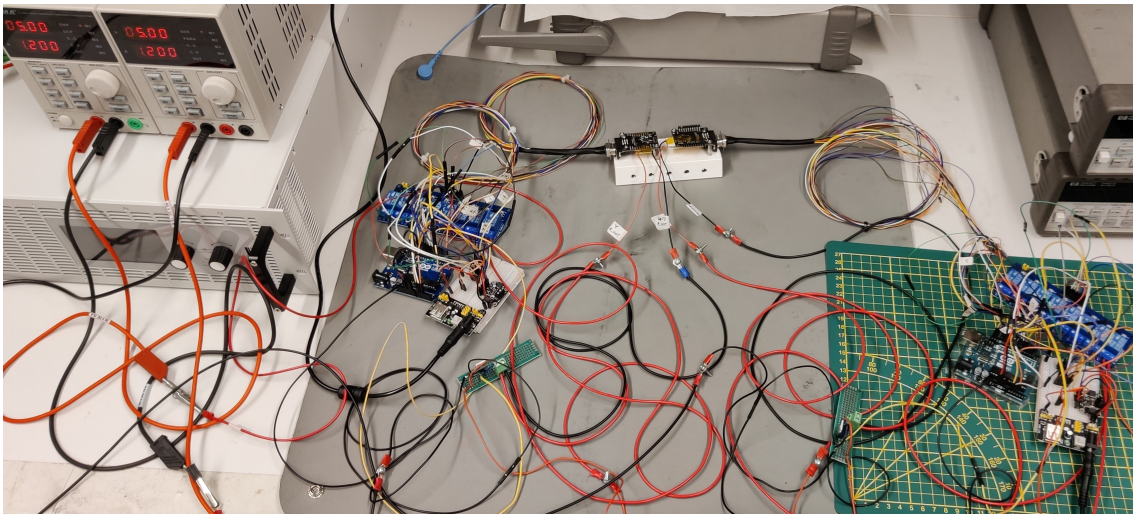


**Figure 5.30:** - Radiation & Temperature change: Pre-test characterization setup

As described in section 5.2, the primary means of temperature characterisation is the sensor vs. reference frequency characteristic, which can be approximated as a linear relationship. Additionally, since this relationship can be assumed to have the same slope at different working points of the sensor (different sensor frequencies at ambient temperature)<sup>7</sup>, the slope of the linear fit can be used as the sole parameter for temperature characterisation and compensation. The following heating temperature profiles were used with the HOT board for the purpose of temperature characterisation prior to irradiation:

- Constant heating power
- Quasi-linear

<sup>7</sup>This assumption is based on information provided by the manufacturer in the product's datasheet

- Sawtooth
- Staircase/Rising sawtooth

Each profile will be discussed separately below. For the pre-test runs, the accuracy of compensation was quantified by calculating the *average compensation error* i.e. the mean of the deviation between the frequency at room temperature (base frequency) and the frequency values obtained after temperature compensation. In principle, perfect compensation would imply that the average compensation error would be no larger than the signal noise in the base frequency itself.

- **Constant heating power:** When the peltier heater is supplied with constant power, it produces a linear rise in temperature for a short interval of time. This profile was mainly experimented with to check the responsiveness of heat transfer and to verify the functionality of the test setup. The effect of temperature rise is a reduction in the sensor and reference frequencies as expected, and demonstrated in Figure 5.31. The green curve represents the temperature of the PCB, whereas the red and blue curves represent the sensor and reference frequency signals.

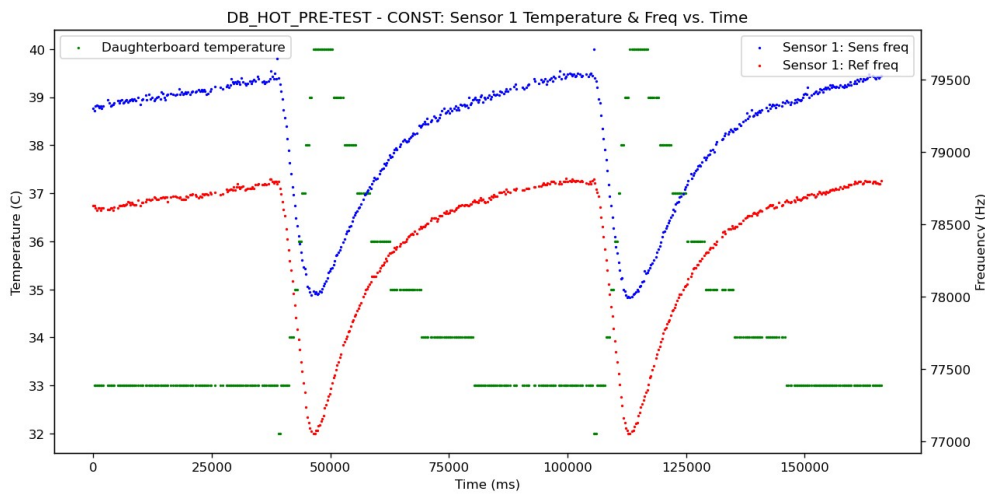


**Figure 5.31:** Pre-test temperature characterization: Constant heater power

- **Quasi-linear:** The quasi linear temperature profile (as seen in Figure 5.32) is made up of a near-linear rise in board temperature, followed by cooling to ambient temperature as a result of natural convection. This profile has been termed 'Quasi-linear' because it was observed that the temperature rise became increasingly non-linear with increase in the upper temperature limit.

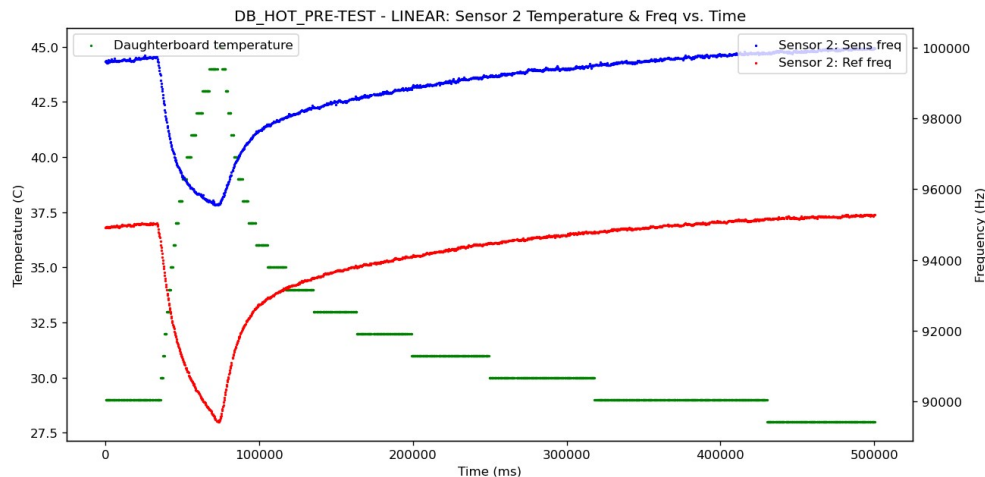


**Figure 5.32:** Pre-test temperature characterization: Quasi-linear profile

- **Sawtooth:** The sawtooth profile consists of repeated cycles of enforced heating and natural convective cooling between a lower and upper bound, as shown by the green curve in Figure 5.33.

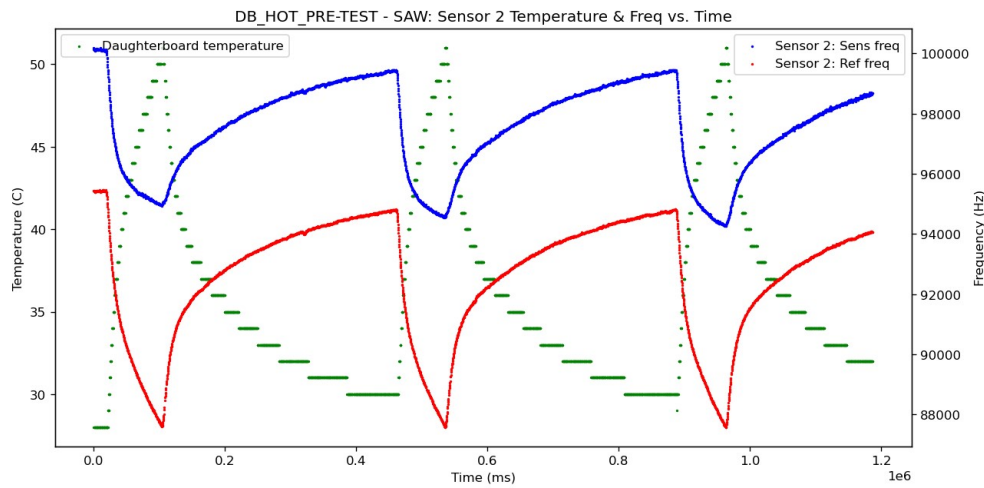


**Figure 5.33:** Pre-test temperature characterization: Sawtooth profile

- **Staircase/ Rising sawtooth:** The staircase profile involves heating up of the board by a certain step size, followed by a small fixed time interval of convective cooling. This sequence is repeated until a threshold temperature is reached. In practice, it was observed that the temperature intervals could not be maintained at a constant value for more than 2-3 s, hence this profile is better understood as a rising sawtooth pattern, as shown in Figure 5.34.

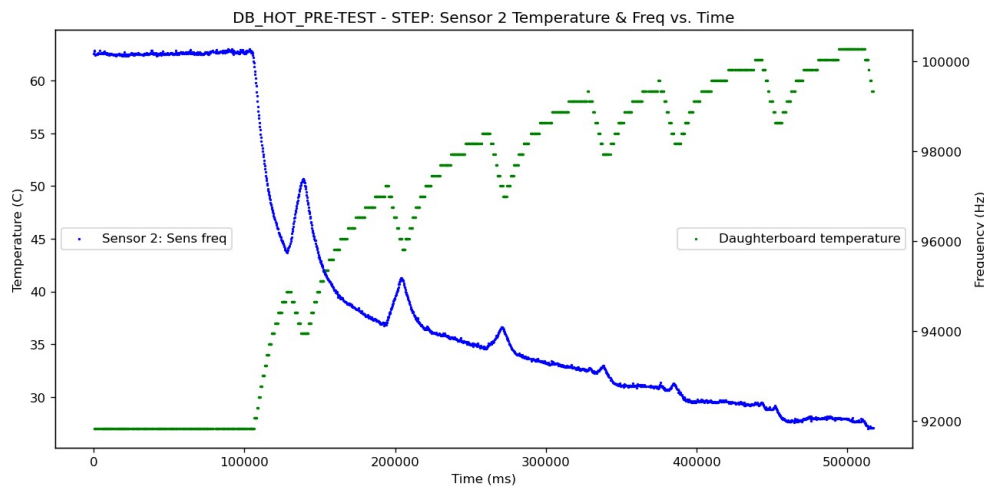


**Figure 5.34:** Pre-test temperature characterization: Rising sawtooth profile

In the frequency characteristic, it can be seen that intermittent partial cycling of temperature causes the characteristic to deviate from its ideal linear form, as shown in Figure 5.35. The cluster of curves in the lower left end is indicative of a lag between the temperature being measured by the internal temperature monitor and the instantaneous temperature of the sensor and reference MOSFETs embedded in the FGDOS SoC. This non-ideal behavior can likely be alleviated by ensuring a more uniform distribution of heat throughout the chip.

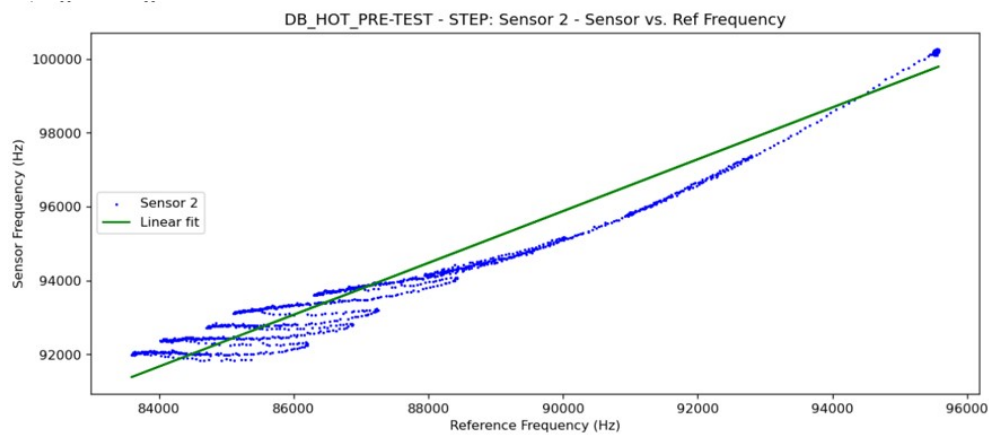


**Figure 5.35:** Pre-test temperature characterization: effect of cycling on sensor v ref freq characteristic for staircase profile

In the case of the sawtooth profile, it was seen that the characteristic assumed a saddle-like shape, shown in Figure 5.36. Each temperature cycle results in a different saddle curve, which is conceivable due to the inherent noise in the frequency readouts, which prevents the variation of frequencies w.r.t temperature from being a one-to-one function. The saddle curvature itself may be a result of rapid and non-uniform heating and cooling of the FGDOS chip.

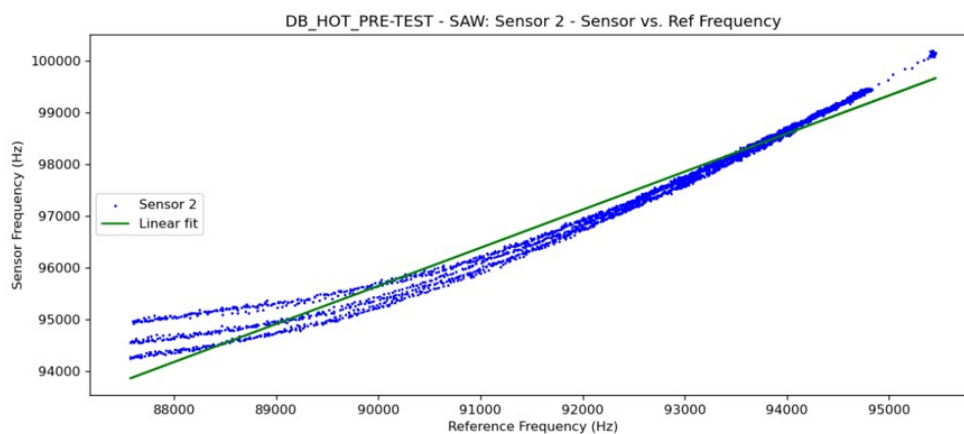


**Figure 5.36:** Pre-test temperature characterization: effect of cycling on sensor v ref freq characteristic for sawtooth profile

The following cooling temperature profiles were used with the COLD board for the purpose of temperature characterisation prior to irradiation:

- **Constant cooling power:** In this profile, constant power was supplied to the cooling peltier for a short interval of time, resulting in linear temperature reduction. The constant cooling power profile was only used to demonstrate the effectiveness of heat transfer between the peltier cooler and the cold board, and to verify the predictable rise in sensor and reference frequencies that is caused by cooling. Again, the green curve represents PCB temperature while the blue curve represents the sensor frequency signal.

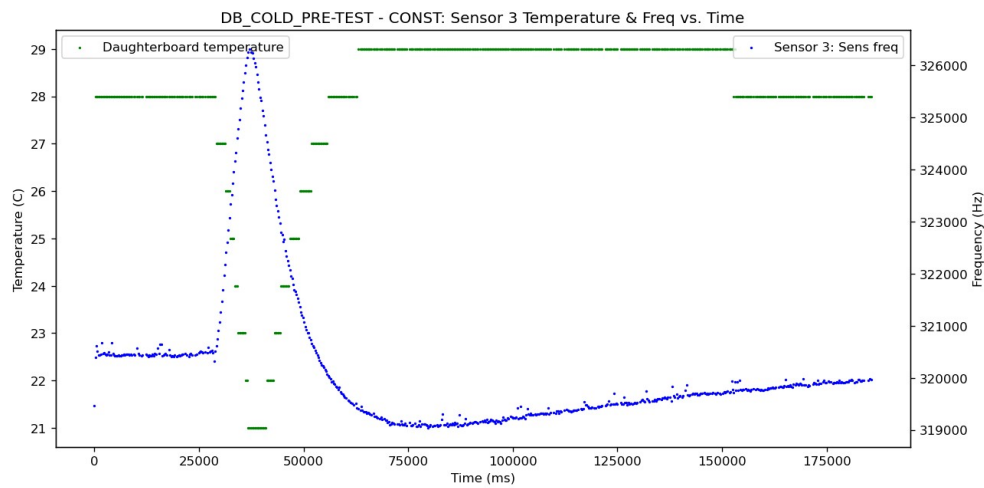


**Figure 5.37:** Pre-test temperature characterization: Cold spike

- **Quasi-linear with oscillation:** This profile was aimed at producing a linear drop in temperature, which can be seen in Figure 5.38. However, due to the nature of the thermal interface between the peltier and the COLD board i.e. the lack of a sufficient heat sink, as soon as the cooling was concluded, the peltier tile would release heat into the COLD board, causing an oscillation to occur in the temperature profile, and the frequency as a consequence.

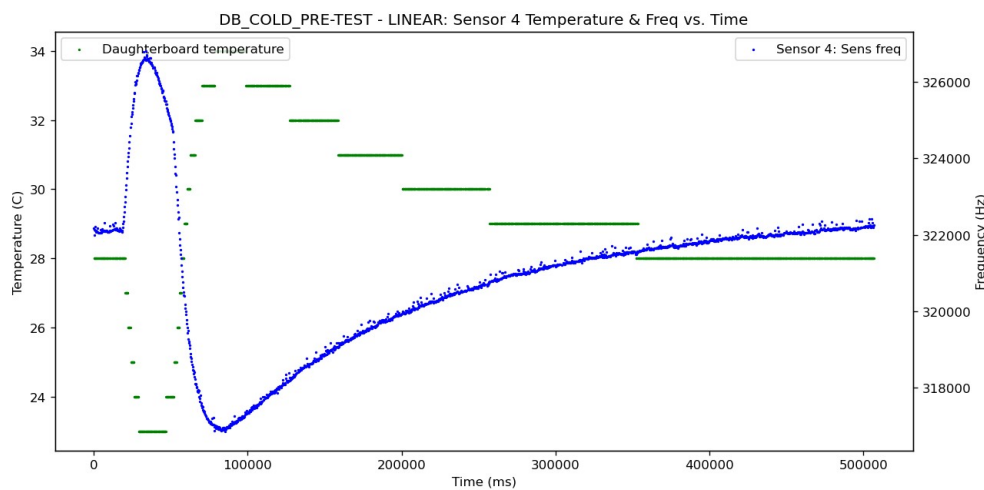


**Figure 5.38:** Pre-test temperature characterization: Quasi-linear with oscillation

- **Maximum cooler power with oscillation:** This profile consists of maximum heat removal that the peltier cooler can achieve at a supply voltage of 5V and the temperature oscillation that follows after the minimum achievable temperature has been reached.

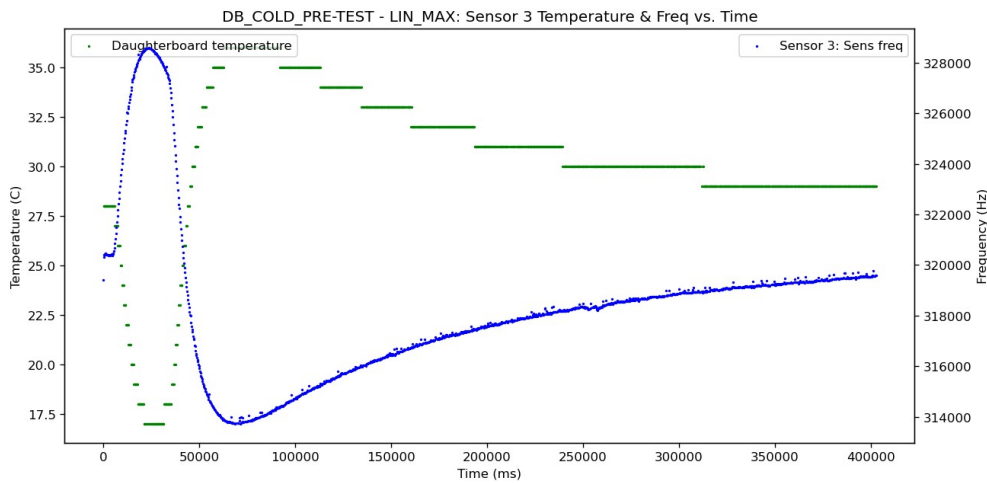


**Figure 5.39:** Pre-test temperature characterization: Quasi-linear with oscillation

- **Cold Spike:** This profile was induced with the use of electronic freeze spray<sup>8</sup> on the FGDOS chip. As evidenced by the plot in Figure 5.40, the spray ejecta cause the temperature to drop suddenly, resulting in a spike in the sensor and reference frequencies, as seen in Figure 5.41.

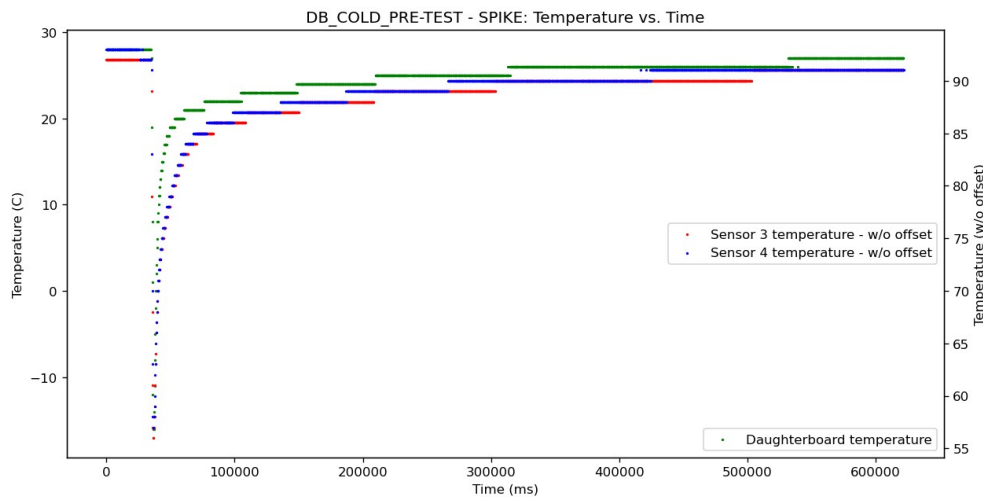


**Figure 5.40:** Pre-test temperature characterization: Cold spike

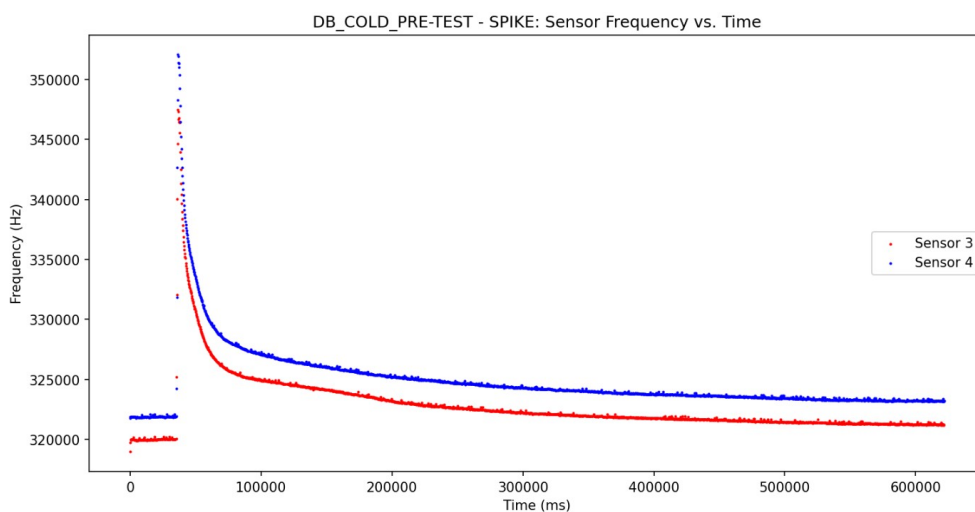


**Figure 5.41:** Pre-test temperature characterization: Cold spike

<sup>8</sup><https://www.chemtronics.com/ultimate-guide-to-diagnostic-freeze-spray>

The raw and compensated signals are plotted for comparison in Figure 5.42. The compensation for the cold spike profile was seen to be effective as it resulted in an average compensation error of about 160 Hz which corresponds to a relative error of 0.05% in sensor frequency. This lies within the typical unfiltered noise band of sensor frequencies, as discussed in section 5.5.

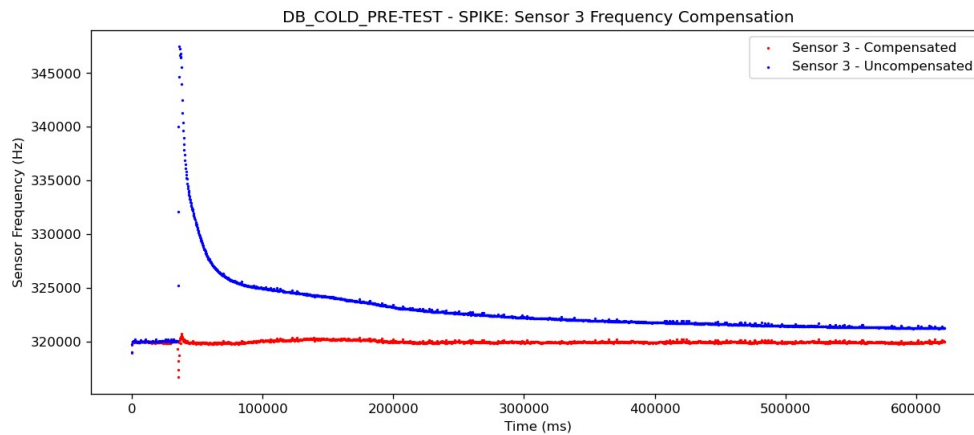


**Figure 5.42:** Pre-test temperature characterization: Cold spike

These profiles were always accompanied with natural convection which brought the temperature of the PCBs (and the FGDOS) back to ambient levels in a gradual manner.

The results from all the temperature characterisation runs are summarized in Table 5.11. Whereas sensors 2, 3 and 4 yield a characterized slope that varies only minimally for each profile, sensor 1 shows a large spread in the distribution of the calculated slopes, including an unexpected negative slope for the staircase profile (visually expressed by Figure C.2). Hence, anomalous behavior was observed on the part of sensor 1 during the characterisation runs. Therefore, the characteristic slope calculated for the constant profile was used for compensation later on in the case of sensor 1. The average slope calculated over all applicable profiles was used for the rest of the sensors.

#	Profile	s1		s2		s3		s4	
		slope	intercept	slope	intercept	slope	intercept	slope	intercept
1	CONST	9.27E-01	6.45E+03	1.06E+00	-9.30E+02	3.79E+00	2.92E+03	5.00E+00	-1.01E+05
2	QUASI-LINEAR	5.37E-01	3.76E+04	8.25E-01	2.13E+04	3.59E+00	1.95E+04	5.01E+00	-1.02E+05
3	SAWTOOTH	1.74E-01	6.59E+04	7.36E-01	2.94E+04				
4	LINEAR MAX					3.81E+00	1.30E+03	4.94E+00	-9.58E+04
5	STAIRCASE	-4.49E-01	1.15E+05	7.02E-01	3.27E+04				
6	SPIKE					3.91E+00	-6.79E+03	5.18E+00	-1.16E+05
	<b>Average</b>	2.97E-01	5.63E+04	8.30E-01	2.06E+04	3.77E+00	4.23E+03	5.03E+00	-1.04E+05

**Table 5.11:** Pre-test temperature characterization results (s1 denotes sensor 1)

Temperature compensation efforts revealed that the quality of compensation (and temperature characterisation) was influenced by several factors. The severity of temperature gradients i.e. the rate of temperature change in a given interval of time influences how uniformly heat is distributed throughout the FGDOS SoC. If the temperature changes too quickly, there isn't enough time for heat to be distributed uniformly throughout the chip. This can cause the sensor and reference MOSFETs, as well as the internal temperature monitor to be at different instantaneous local temperatures, causing the frequency and temperature readout values to be out of sync temporarily as far as the effect of temperature is concerned. The presence of gradient reversals and abrupt temperature changes leads to similar effects. When constructing the temperature effect calibration curve (sensor vs ref frequency plot shown in Figure 5.26), the influence of the aforementioned factors is seen most prominently when the thermal profile the FGDOS is subjected to involves rapid cycling. Based purely on the temperature dependence, cycling would cause the reference and sensor frequencies to oscillate between two fixed values, along the ideal calibration line. But because of inherent noise in the frequencies, the values that are assumed by each frequency signal w.r.t. temperature do not constitute a one-to-one function. This situation on a repeated basis, combined with non-uniform heat distribution, results

in a poor linear fit between the sensor and reference frequencies when the temperature is cycled rapidly. For instance, the compensation of the sawtooth profile shown in Figure 5.43, results in a signal which still possesses some artifacts of the raw frequency signal, especially when the temperature gradient is seen to reverse. By contrast, when the temperature change is gradual, the compensation quality is improved, as exemplified by Figure 5.42. Here, even though there is a large freezer spray induced spike, the subsequent return of the FGDOS to steady state by virtue of natural convection causes the quality of compensation to improve considerably, bar a small artifact of the spike which can still be noticed.

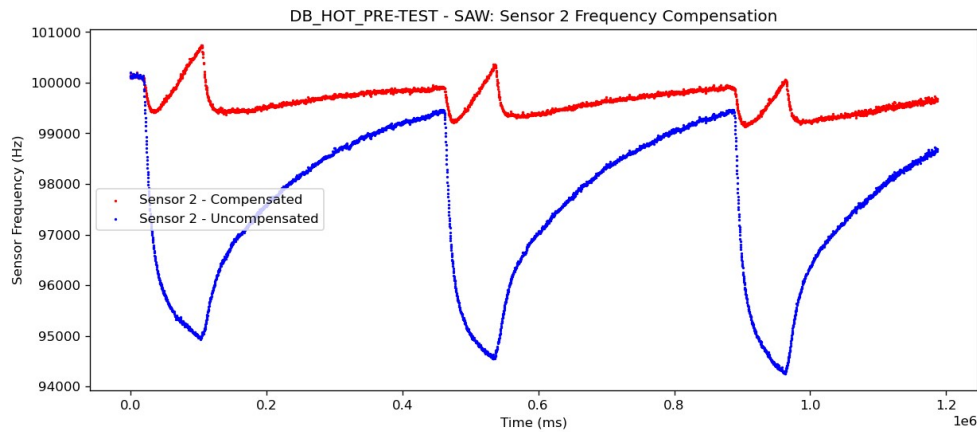


**Figure 5.43:** Pre-test temperature characterization: Sawtooth profile compensation

The anomalous behavior of sensor 1 during the pre-test temperature characterisation is recounted by the plots in Figure C.2. Before the start of radiation characterization, it was noticed that the TMP-100 sensor on the COLD board stopped functioning. This failure could have been a soldering fault compounded by the freezer spray used during pre-test temperature characterisation.

### Radiation Characterization

Radiation characterization consisted of proton beam irradiation runs at the three separate calibrated energy levels shown in Table 5.3. Various dose rates were also used to gauge the variation in FGDOS sensitivity with dose rate. The energy levels and dose rates were selected such that sensor performance could be contrasted with the results from previous tests (section 5.1).

Sensitivity was computed from the slope of a line fit to the sensor frequency within the LDR. The sensitivity was calculated using Equation 5.1, in the time interval between two sensor recharges. In irradiation runs where multiple recharges were observed, the sensitivity for each interval between two successive recharges was computed and the average of these sensitivities was reported as the overall sensor sensitivity for the run.

### Simultaneous Irradiation and Temperature Variation

In the main portion of the test, temperature change of the FGDOS chip was enforced in conjunction with the impinging of protons on the FGDOS and depositing dose in the floating gate field oxides. In post-processing of the FGDOS readout obtained for these runs, the sensor frequency signal was compensated using calibration line slope calculated during pre-test characterization described previously. Variation of this slope due to change in the sensor frequency working point or temperature was assumed to be negligible. The sensitivity of the compensated signal was calculated using linear regression on the unfiltered signal readout from the FGDOS. Compensated sensitivity was compared to average sensitivity computed at constant temperature and baseline energy/dose rate in advance (during the radiation characterization part of the test).

From Equation 5.1 which relates the measured TID to drop in sensor frequency and sensitivity, it follows that the relative error in TID measurement is equivalent to the relative error in FGDOS sensor sensitivity (S), neglecting the error involved in frequency sampling in the readout circuitry of the FGDOS. Hence, the relative error in sensitivity determination was computed to gauge the effectiveness of compensation under

simultaneous irradiation and temperature change:

$$\frac{\Delta TID}{TID} = \frac{\Delta S}{S} \quad (5.4)$$

### Test Procedure

The step by step procedure which was followed during the test can be found in [119]. For pre-test temperature characterisation runs, the procedure boiled down to initiation of heating/cooling and enforcement of a given thermal profile during the course of each run. The thermal control was initiated after FGDOS readout had been established for a few seconds. In the radiation baseline characterisation runs, the thermal control apparatus was powered off and all irradiation runs were performed at ambient temperature. Following this, the procedure for irradiation runs was repeated, with the thermal control apparatus powered on and the selection on an appropriate thermal profile according to Table 5.10. A solitary run was performed in the end, at relatively constant temperature, to assess the effects of thermal variations on the FGDOS chips.

### 5.3.5. Observations

For irradiation at constant ambient temperature, the effect of beam energy on sensitivity was observed to be much gentler compared to the tests described in section 5.1. The effect of dose rate continued to be non-appreciable. In total, about 65 Gy of TID was accumulated by the test specimens during this test.

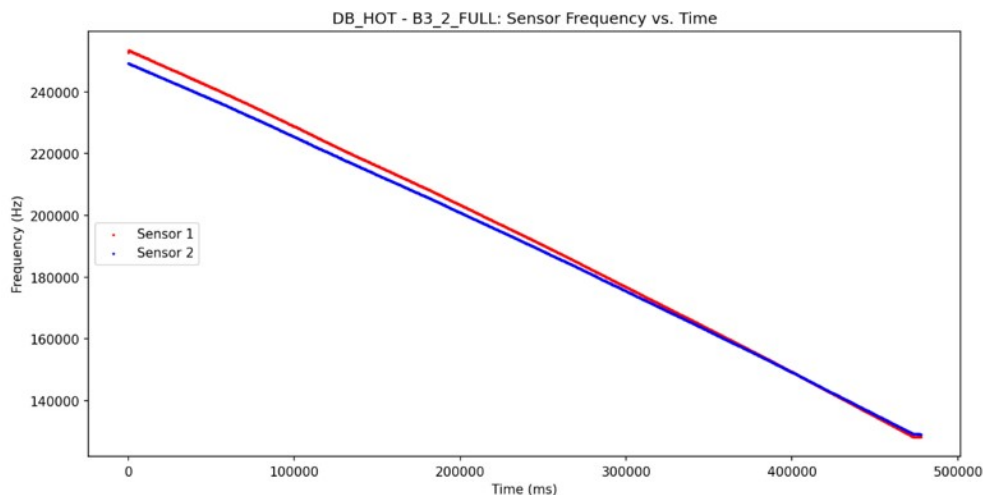


**Figure 5.44:** Radiation characterisation: Extended frequency characteristic

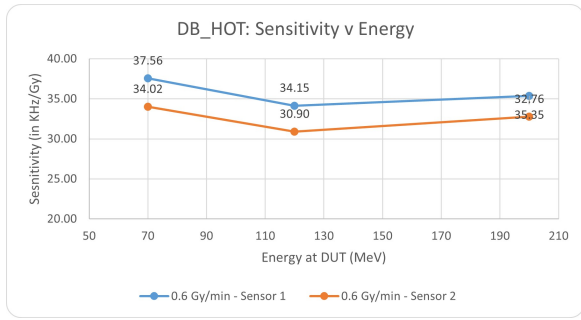
The extended frequency characteristic of the HOT board sensors is displayed in Figure 5.44. At baseline beam parameters, the sensor sensitivity in HISENS mode was observed to be about 31-38 kHz/Gy. The corresponding power consumption was approximately 43-46 mW for each FGDOS SoC. In LOWSENS mode, the average sensitivity was observed to be about 6 kHz/Gy with a power consumption of about 22-25 mW in general<sup>9</sup>.

### Effect of energy and dose rate on sensitivity

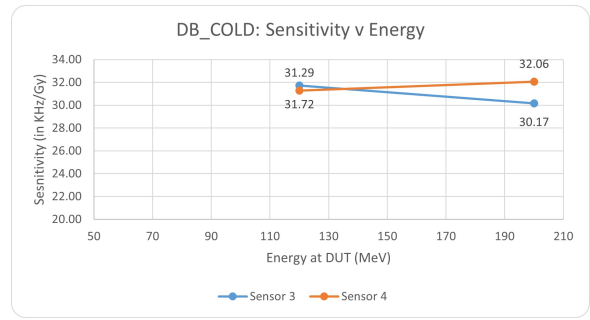
Variation in FGDOS sensitivity with beam energy can be seen in Figure 5.45. The sensitivities depicted in Figure 5.45 were calculated at constant temperature and baseline dose rate of 0.6 Gy/min. For the HOT Board, the sensitivity goes down when the energy is increased from 70 to 120 MeV, but it grows with further rise in energy to 200 MeV. Interestingly, for the COLD board, opposing trends were seen for Sensors 3 and 4, which were contained in the same FGDOS chip. Overall, it can be surmised that the change in sensitivity is marginal compared to similar tests described in section 5.1. It might be posited that the change in sensitivity might be due to statistical variations rather than the presence of a definite underlying cause. The different observed trends may be caused by a difference in the FGDOS chips that were used for these tests. Concretely, the FGDOS chip used for the test discussed in section 5.1 had already accrued in excess of 150 Gy of

<sup>9</sup>The power consumption figures quoted here also include the marginal power required by the TMP-100 sensor which was present on the Daughterboard PCBs

TID. It may be possible that the dependence of sensitivity on beam energy grows stronger as TID increases. However, this claim is speculative in nature and remains to be verified by controlled experimentation.



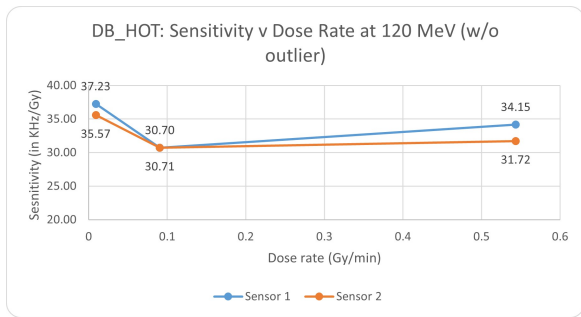
(a) HOT board sensitivity trend



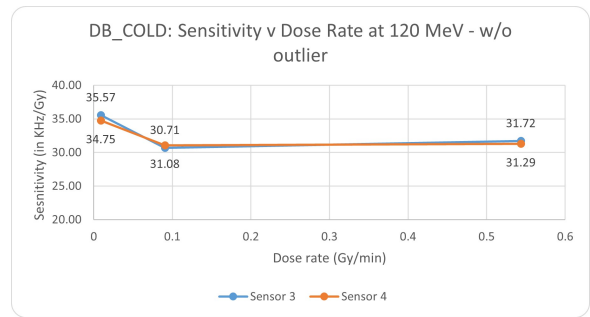
(b) COLD board sensitivity trend

Figure 5.45: Dependence of FGDOS sensitivity on beam kinetic energy

Similar to previous tests, FGDOS sensitivity did not show a systematic variation with the dose rate. The plots in Figure 5.46 show that the sensitivity for all four irradiated sensors decreases at first, then increases gently with further rise in the dose rate. This bolsters the previously presented conclusions that the sensitivity can be considered independent of the dose rate of incident radiation, within certain bounds of error.



(a) HOT board sensitivity trend

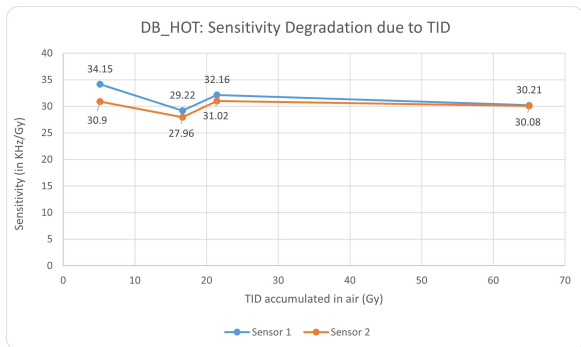


(b) COLD board sensitivity trend

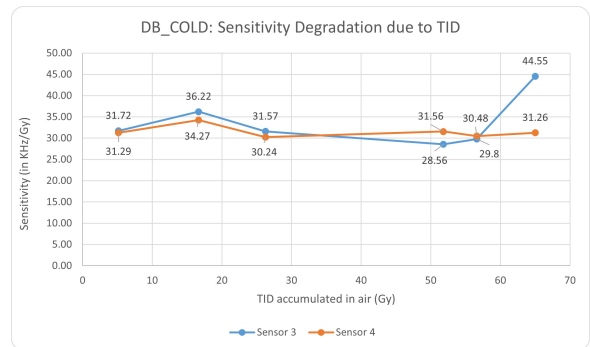
Figure 5.46: Dependence of FGDOS sensitivity on dose rate of irradiation

Hence, for new FGDOS chips from a batch, the sensitivity of sensor frequency to dose seems to be relatively independent of the energy and dose rate of incident radiation, at least for protons. This property needs to be verified with other radiation sources too. It would be most desirable to have this be proved experimentally, since invariance of the sensitivity with the nature of incident radiation would certainly be a desirable characteristic for the Radiation Payload to possess.

**TID induced degradation**



(a) HOT board sensitivity degradation



(b) COLD board sensitivity degradation

Figure 5.47: Degradation of FGDOS sensitivity as a function of accumulated TID

The noticeable rise in sensor 3 sensitivity in Figure 5.47b is an outlier corresponding to erratic sensor 3 behavior which was seen toward the conclusion of the test. This notion is supported by the rise in power consumption displayed by the last data point in Figure 5.48b. This occurrence may have been caused by an SEE in the sensor or thermally induced damage to Sensor 3. Thermal damage to the entire FGDOS SoC seems unlikely in this case since any permanent thermal degradation was not observed in the neighbouring sensor 4. Any other probable causes could not be identified.

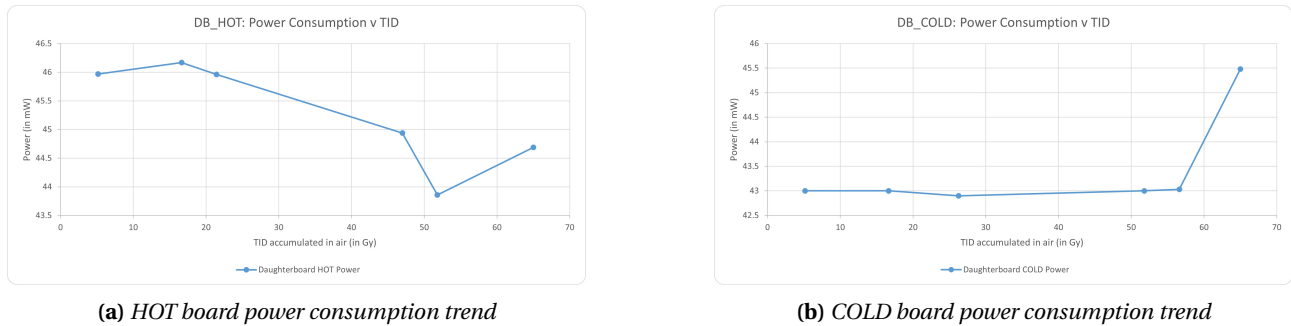


**Figure 5.48:** Evolution of average power consumption as a function of TID

### FGDOS Passive Mode

The passive mode of the FGDOS was tested, following failed attempts on previous test days in March and April 2022. This was done using two different approaches. As a consequence, two big time interval gaps in the frequency data can be seen in Figure 5.49. The first gap corresponds to the SPI lines (between the FGDOS and the Arduino board) being disconnected, the sensor continues to measure dose and a recharge is triggered once the SPI lines are connected again and s3 frequency drops below the threshold limit. The second gap corresponds to the 5V supply being switched OFF. As soon as the voltage drops, dubious data starts streaming in over the SPI lines, but the values are restored to normal as soon as the voltage is reconnected. As such, the dubious values can be easily discriminated and discarded. Hence, this run serves as a demonstration of operating the FGDOS in the passive mode, albeit within the dose limit contained within the LDR, since recharges cannot be affected if the FGDOS is not receiving power.

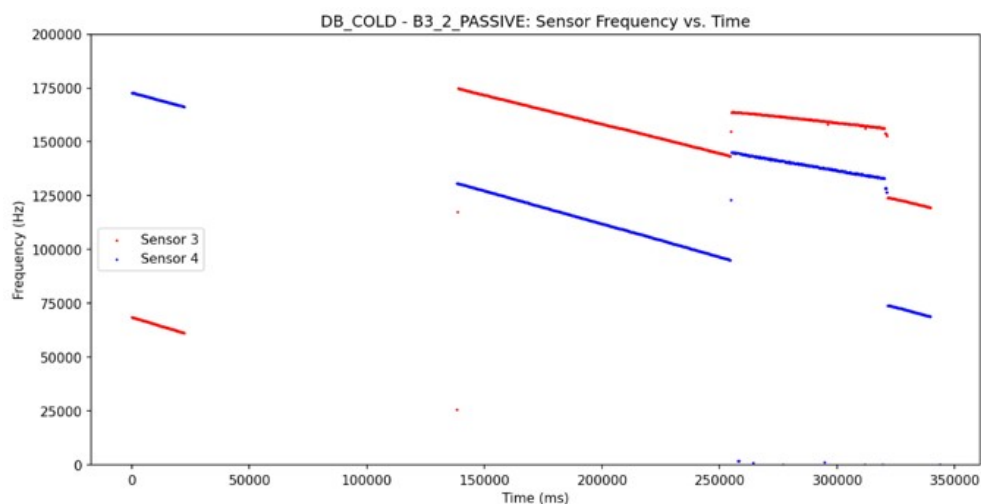


**Figure 5.49:** Passive mode baseline

### Temperature Effect & Measurement

The close agreement between the measurements of the external TMP-100 and the internal temperature monitors embedded in the FGDOS chip demonstrates that the indicated sensor temperature is essentially the temperature of the thermal pad of the FGD-03F chip. As a consequence, the PCB on which the FGDOS is soldered can be designed with a GND pad below the FGDOS QFN package having a similar temperature. Furthermore, the placement of a high resolution temperature sensor on this GND pad, close to the FGDOS

would allow for high precision temperature measurements of the FGDOS sensors, which may be used to enrich the temperature characterisation and compensation of frequency data in light of temperature variation.

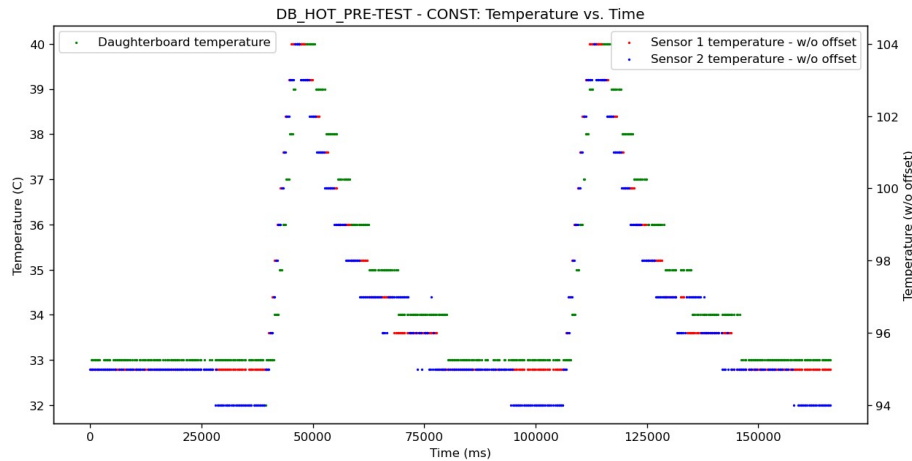


**Figure 5.50:** Comparison of external (Daughterboard) and internal (FGDOS) temperature readings

### Combined effect of irradiation & temperature change

When the temperature of the FGDOS is varied in presence of ionizing radiation, two kinds of coupling between the effects of temperature change and irradiation on sensor frequency values are observed:

- **Constructive coupling:** When the temperature of the FGDOS rises, the sensor frequency decreases. Under irradiation, the rising temperature makes for a higher reduction rate of sensor frequency. Hence, based purely on the raw readout from the FGDOS, the combined effect makes it look like the sensor has an 'apparent sensitivity' which is higher than the sensitivity at constant temperature. The fall of sensor frequency becomes non-linear in nature w.r.t time/dose.
- **Destructive coupling:** When the temperature of the FGDOS goes down, the sensor frequency goes up. This tends to diminish the frequency fall caused by irradiation. Hence, the apparent sensitivity seems to be lower than the sensitivity at constant temperature. The sensor frequency change is also non-linear in most cases.

The nature of this coupling depends on the relative strength of the irradiation dose rate and the gradient of the temperature profile. In principle, this coupling should be a linear super-position of the effect of irradiation and the effect of temperature change. The key to decoupling these effects is to use the reference frequency signal, which is insensitive to radiation but dependent on temperature. The extent to which these effects can be successfully decoupled is quantitatively described shortly.

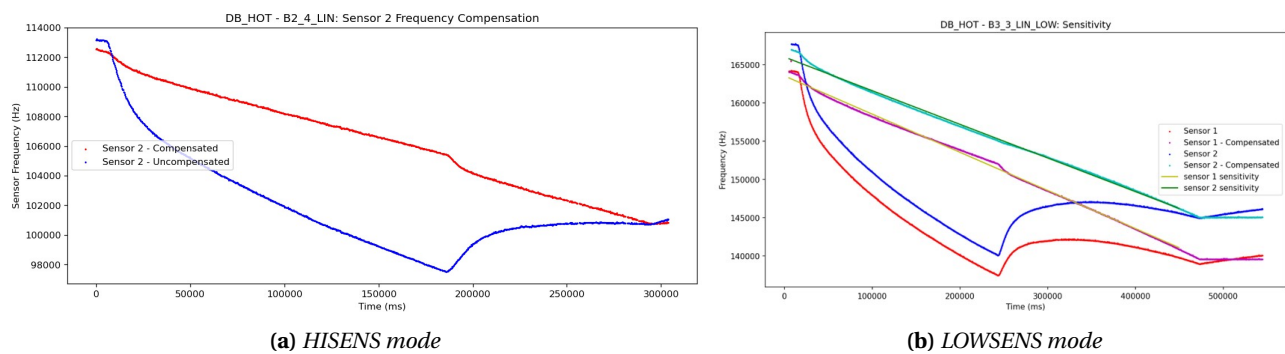
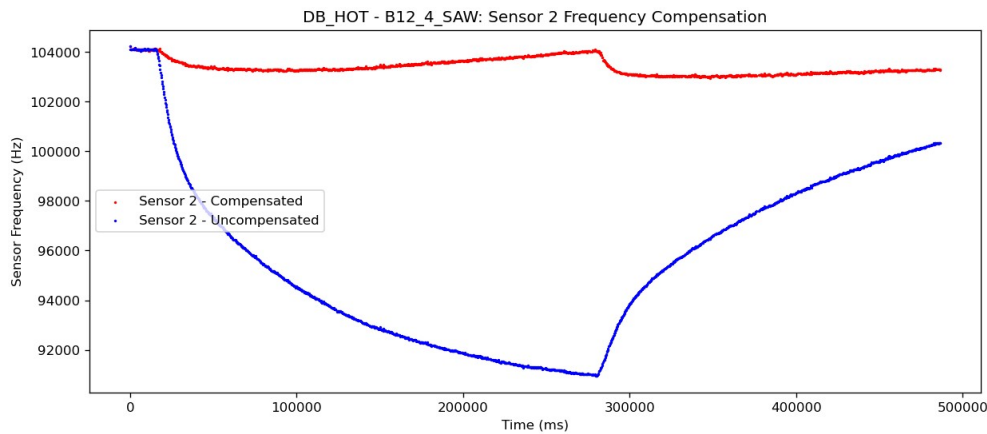


**Figure 5.51:** Compensation for quasi-linear temperature profile at medium dose rate

For the quasi-linear temperature profile, the temperature was varied from about 30 - 60 °C and the compensation was seen to work effectively with average sensitivity error of about 15-17 %. Figure 5.51 shows the compensated and uncompensated signals, with the linear fit for sensitivity estimation superimposed.

This was verified for LOWSENS mode as well, as shown by Figure 5.51b, where the compensation error was about 8-9 %.

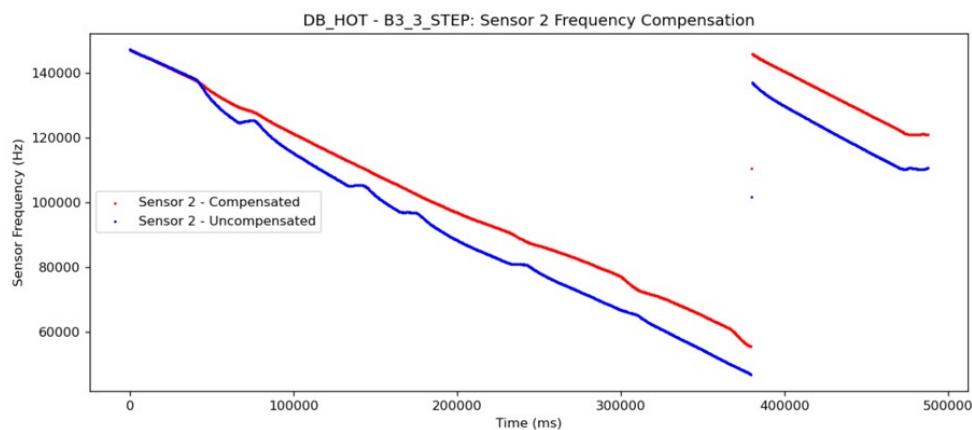
At very low dose rates of about 10 mGy/min, the temperature effect completely overshadowed the sensor frequency drop induced by irradiation. A sawtooth profile run was executed at a dose rate of 1 mGy/min to simulate rapid temperature change in the FGDOS while being exposed to interplanetary ionizing radiation environments, as discussed in section 4.2. Based on radiation tests at ambient temperature, it was already known that such low dose rates could not be measured within the time duration allowed by HPTC for each run. The addition of oscillating temperatures made the detection of TID at such low dose rates even more difficult, as shown in Figure 5.52. Artifacts of the temperature variation can be spotted clearly in the compensated signal represented by the red curve.



**Figure 5.52:** Compensation of the effect of sawtooth profile at very low dose rate

The recharge target and threshold frequencies for the FGDOS are defined at room temperature. When the temperature changes, the target and threshold remain the same, but the sensor frequency starts to vary. Figure 5.53 shows an important implication of temperature change on the behavior of the FGDOS. When the FGDOS is at an elevated temperature, recharges can be triggered prematurely, as shown by the blue curve in Figure 5.53. The red curve shows the compensated frequency value i.e. what the frequency would be at ambient temperature.

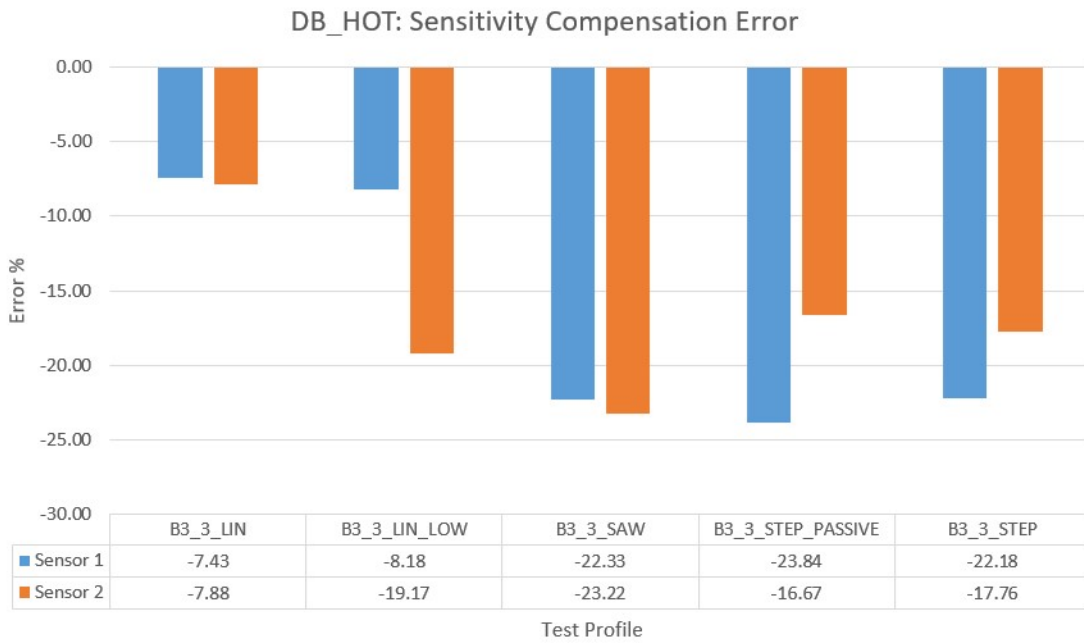
The recharge process is seen to take the compensated sensor frequency beyond the target value. Therefore, the recharge process is effectively altered by temperature change as well. To get highly accurate recharging, it would be necessary to dynamically tweak the recharge target and threshold on the basis of the current FGDOS temperature/reference frequency. Alternatively, the target and threshold could be adjusted in advance such that deviations in recharging at non-ambient temperatures aren't large enough to drag the sensor frequency outside the LDR.



**Figure 5.53:** Compensation of the effect of staircase profile on s2 frequency

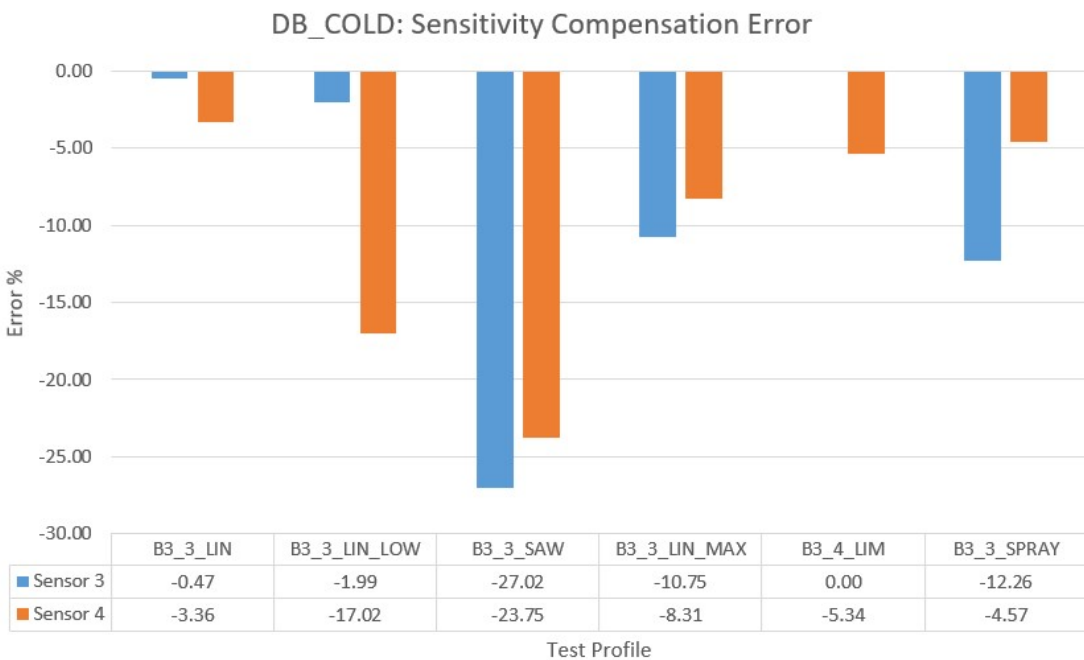
**Temperature Compensation Effectiveness**

Figure 5.54 and Figure 5.55 show an overview of the compensation effectiveness under irradiation, for various temperature profiles, for the HOT and COLD boards respectively. Using the expected vs compensated sensitivity as metrics, these plots communicate the extent to which the effect of temperature change and irradiation occurring simultaneously can be successfully decoupled in a practical manner.



**Figure 5.54:** Summary of temperature compensation error for the HOT Board

It was observed that the compensated sensitivity was always lower than the original sensitivity, hence the errors shown here are negative in sign. The COLD board showed more accurate results in general, given that the temperature ranges it was exposed to were smaller in comparison to the HOT board.



**Figure 5.55:** Summary of temperature compensation error for the COLD Board

The observations made about temperature effect compensation, during pre-test temperature characterisation are seen to resurface. The compensation effectiveness is observed to be acceptable for the quasi-linear profiles (computed sensitivity errors are within 10%). However, when rapid thermal cycling, steep temperature gradients or gradient reversals are present, the compensation errors climb to higher values, going as high as 25% in some cases. It should be noted that the calculation for compensated sensitivity did not account for the change in sensitivity between different runs or the degradation in sensitivity caused by TID. Another factor which was not considered was the change in the frequency vs temperature gradient with the working point of the sensor. It was reported by Brucoli et al that the rate at which the sensor frequency decreases with increase in temperature, changes slightly with the starting value of the sensor frequency at room temperature [23]. Hence, the error values reported in this section should be interpreted as the worst case compensation error. The actual compensation error would be lower in all likelihood, provided that the moderating factors mentioned here are taken into account in the post processing of sensor data.

### Temperature change during passive mode

The HOT Board was subjected to a rising sawtooth/staircase profile under irradiation at baseline levels. The FGDOS was periodically placed in passive mode, to observe whether temperature change would adversely affect the dose measurement and whether compensation could be adequately performed in post processing. In context of Radiation Payload operations, this run was aimed at emulating situations where the payload would be in safe mode<sup>10</sup> for extended time periods involving appreciable thermal change and cycling. The original (blue) and compensated (red) signals from s2 are shown in Figure 5.56.

The aforementioned dubious frequency values read in passive mode are seen again in the two time intervals corresponding to the 5V supply being disconnected. The spurious data from these periods can be ignored as such. In the intermediate active mode data, it is apparent that the compensation works acceptably, demonstrating that consequences of this operational scenario can be adequately tackled during post-processing of mission data.

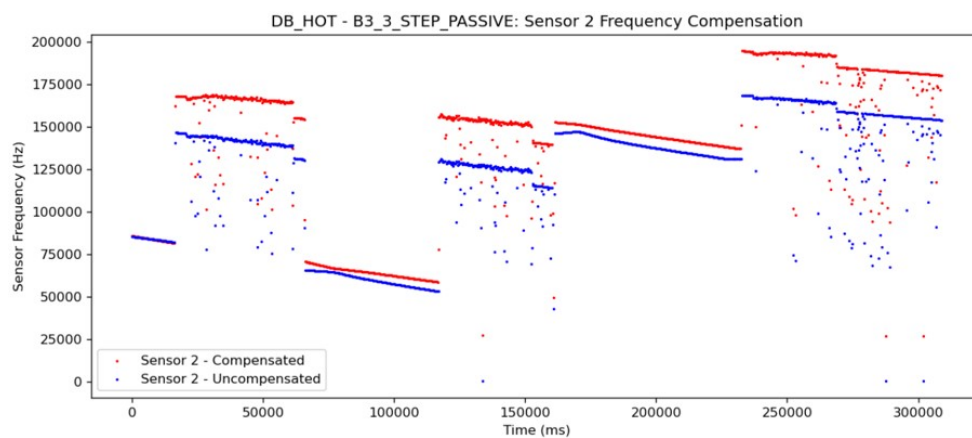


**Figure 5.56:** Simultaneous temperature change and irradiation for FGDOS in passive mode

### Extreme temperature variation

The FGDOS chips were subjected to a run which entailed exposure to the most extreme temperature values that could be achieved with the experimental setup, this was done partly to ascertain the functionality of the FGDOS and to see the effects of extreme variation on sensor frequency compensation. The HOT board was subjected to temperatures ranging from 24 to 93 °C. The COLD board was subjected to freezer spray which caused the temperature of the FGDOS to drop abruptly at first to about -15 °C, followed by a gradual convective natural heating to ambient temperature. Figure 5.57 saliently illustrates the basis of temperature compensation for the FGDOS. Initially, when the proton beam is turned on, the FGDOS is at a constant temperature. The sensor frequency (blue curve) descends linearly while the reference frequency is unchanged. As soon as the temperature starts to rise, both frequencies start to decrease, albeit with different gradients. Past the 300 s mark, the apparent sensor frequency goes low enough to trigger a recharge. Afterwards, as

<sup>10</sup>see 3.2.4 for a description of the operational modes of the Radiation Payload

the temperature starts to fall, the reference frequency immediately begins to rise, but the sensor frequency continues to fall due to radiation dose (albeit at a gentler rate owing to the destructive coupling mentioned earlier). This part of the test demonstrated that temperature extremes from at least  $-15$  to  $93$  °C could be survived by the FGDOS while providing useful dose measurement data. This run also substantiates an observation made in section 5.2. The FGDOS SoC can still operate satisfactorily outside its advertised operational temperature range, to a certain extent. The absolute maximum allowable temperature needs to be revealed with the help of an experimental setup that can subject the FGDOS to higher temperatures than described here.

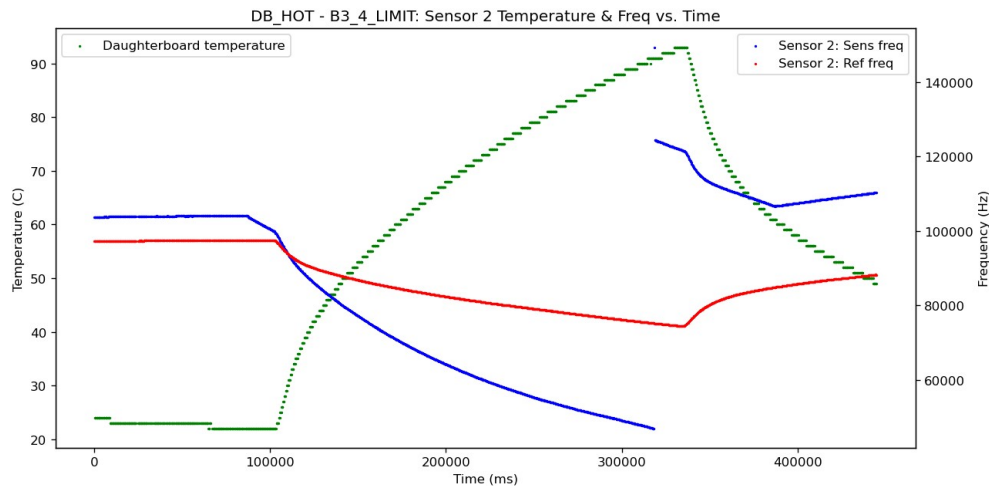


**Figure 5.57:** Extreme temperature variation run

### Thermally induced degradation

After the completion of the test runs with irradiation and temperature change, an "irradiation only" run was carried out to check whether the repeated thermal stresses the FGDOS chips were subjected to had resulted in any permanent effects. It was observed that sensor 3 started producing very noisy and irregular sensor frequency values (shown by the red scatter plot in Figure 5.58), albeit the reference frequency from sensor 3 remained unaffected as such.

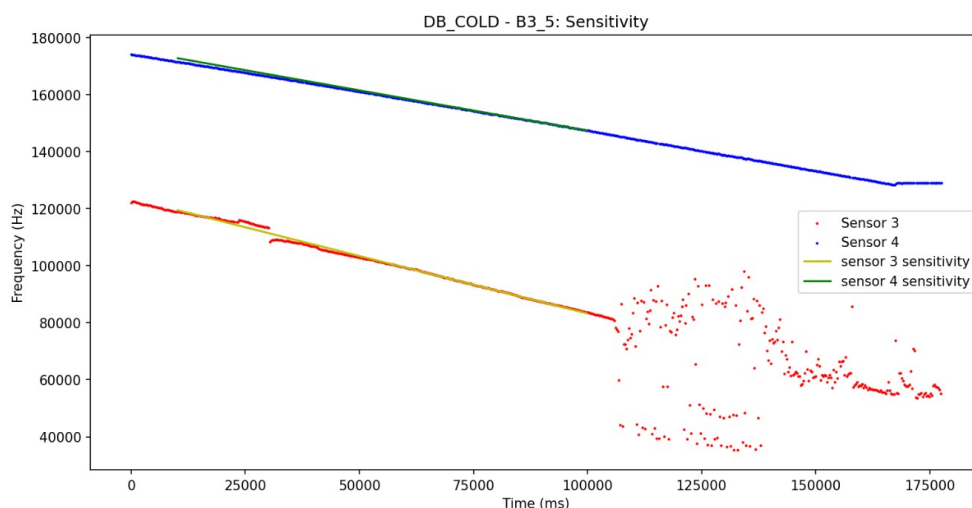


**Figure 5.58:** Post test thermal degradation run

All other sensors being tested did not show any signs of permanent damage caused by either irradiation or temperature change (as shown by the blue curve in Figure C.4). Hence, estimations regarding the presence of any definite thermal fatigue or thermally induced residual effects on the FGDOS could not be made.

### 5.3.6. Limitations and assumptions

The following limitations and assumptions are associated with the tests described in this section:

- It is possible that the steep temperature gradients and fast thermal cycling enforced with peltier modules led to situations in which the entire FGDOS chip may not have heated up or cooled down uniformly. Hot spots or cold spots in the chip could compromise the temperature characteristic of the FGDOS. Given the limited number of temperature sensors available, and the unanimous nature of their response, the occurrence of uneven temperature distribution over the FGDOS chip was neglected.
- The sizing of the peltier modules and the construction of the temperature profiles was based on simple, back of the envelope calculations concerning the peltier power, thermal conductance of the paste and the heat capacity of the FGDOS chip, combined with experimentation and trials. A detailed thermal mathematical model was not implemented. Hence, the temperature gradients and overshoots in the temperature profiles could not be strictly controlled.
- A detailed quantitative analysis of the frequency variation w.r.t temperature gradients was not conducted, but this might yield further insight into thermal characteristics of the FGDOS.
- It was assumed that the peltier modules did not affect the dose delivered to the FGDOS modules by the incident proton beam.
- The proton beam was considered to be homogeneous over its entire cross-section and to be delivering a relatively constant dose rate over the duration of each run.
- The gradient of temperature change during each test run could not be controlled precisely. A test setup with more sophisticated thermal control capabilities is recommended to this end.
- Intra-batch variations among the FGDOS chips were neglected, as justified by the findings of Brucoli et al [18].

### 5.3.7. Results & Conclusions

Observations, inferences and findings from the characterisation of the FGDOS under simultaneous irradiation and temperature change lead to the following conclusions:

1. The effect of irradiation on sensor frequency can be successfully decoupled from the effect of temperature variation with high accuracy, for moderate temperature gradients and largely monotonic variation in temperature. The decoupling is still effective for stronger gradients and exotic temperature profiles, but suffers in accuracy, especially if the uniform heating/cooling of the whole FGDOS chip cannot be ensured. This may be alleviated using a LUT for compensation in favor of the sole reliance on the sensor vs reference frequency calibration characteristic. The application of filtering techniques to the sensor and reference frequency data prior to compensation may yield even better compensation results. In summary, the change in sensor frequency can be expressed as a linear combination of the reduction caused by the delivered dose and the increase/decrease in reference frequency caused by temperature fall/rise.
2. When it comes to post-processing of Radiation Payload data, specifically the FGDOS readout, the simultaneous irradiation and temperature variation tests revealed some important aspects:
  - Kinks (sharp twists or bends) in the frequency signals can indicate incidence of ionizing radiation or change in temperature. More appropriately, kinks can indicate an abrupt change in the temperature gradient or dose rate, thereby serving as an additional aid for post processing of FGDOS data.
  - Temperature change may interfere with the need and effectiveness of the recharge process. Hence, it is advisable to do periodic online updates of the recharge target and threshold based on the current reference frequency, or to have the recharge bounds configured such that there is adequate margin and the sensor frequency stays within the LDR.
  - In practice, the occurrence of recharging, temperature variation, irradiation, annealing of trapped charges and the *Rapid Recovery* effect<sup>11</sup> can produce effects on the sensor frequency that appear to be the same at first glance. To distinguish between these requires judicious use of the characteristics of the FGDOS and its various features. As demonstrated in this section, the irradiation

<sup>11</sup>see section 5.1 and section 5.6

and temperature influences can be isolated using the reference frequency and the temperature monitor readings. Change in reference frequency beyond the expected noise band should act as the trigger for temperature compensation, performed according to a pre-constructed LUT. Recharges can be easily isolated using the recharge register of the FGDOS. It is more difficult to isolate the effects of annealing and the novel *Rapid Recovery* phenomenon. A plausible approach is to observe the time-scale over which frequency variation occurs. While *Rapid Recovery* is an immediate effect, annealing of trapped charges is known to be a slow acting phenomenon. So far, it has also been seen that the *Rapid Recovery* effect only starts to appear after considerable TID has been accumulated by the FGDOS, as described in section 5.6.

3. Based on test results, it is advisable to set up the thermal design of the Radiation Payload such that the temperature is kept relatively stable, heat is distributed uniformly over the entire surface of the PCBs and heat transfer with other subsystems and the surroundings occurs at a gradual rate. These conditions would make the application of temperature compensation on the payload data easier and more effective.
4. Given the limitation associated with proton beam irradiation at HPTC, it would be very interesting to perform this test using another radiation source such as gamma rays. With a Co-60 source, a different regime of dose rates could be explored. Most importantly, the achievable duration of irradiation is much longer with Co-60 sources, opening up the opportunity to test with gradual temperature gradients and multiple cycles of heating and cooling over an extended interval of time [37]. This would undoubtedly permit a better approximation of mission conditions.
5. On a related note, the temperature profiles and thermal control could also be developed further to achieve more defined and sophisticated profiles. These profiles could simulate mission conditions accurately if they are based off of the results from thermal-vacuum testing of the rover (mentioned in section 5.7) or a validated geometrical thermal model (as mentioned in Figure 3.2.2).
6. For pre-flight characterisation of the FGDOSs used in the Radiation Payload FM, a largely monotonously varying thermal profile which covers the full range of expected temperatures during the mission is advisable. The most suitable setting for this is a TVAC chamber where heat transfer is by virtue of irradiation (to approximate mission conditions) and the rate of temperature change is deliberately slow to allow the FGDOS to attain quasi-steady state. Subsequently, a look up table should be constructed, relating the sensor frequency at each temperature to the corresponding reference frequency, which would be used for compensation during post processing of mission data.
7. The occurrence of anomalies in s1 during pre-test characterisation and s3 during the thermal degradation check highlight the importance of the inherent dual modular redundancy built into the FGDOS SoC. Despite the presence of this feature, it may be worthwhile to go one step further and to include an extra FGDOS chip on the MAIN board of the Radiation Payload. Along with the Daughterboard, this would effectively result in triple modular redundancy (TMR), with a total of six FGDOS sensors distributed over three chips. From a systems perspective, the addition of an FGDOS chip would be advisable as long as it complies with the power and telemetry constraints imposed on the Radiation Payload. Based on current requirements and constraints, it seems that the payoff of including an extra chip is extremely favorable compared to the added resource consumption.

## 5.4. Radiation Payload Prototype Functional Testing

The Radiation Payload PCBs were tested according to the steps described in this section.

### 5.4.1. Inspection & Post soldering

Once the bare PCBs were delivered by the manufacturer, visual inspection was carried out to check for quality and workmanship, and to identify any manufacturing defects that may have been introduced in the process. This is shown in Figure 5.59a. Bare boards are already tested by Eurocircuits BV, however an electrical test was performed after delivery to act as an additional check.

Post soldering, a visual inspection of the soldered joints was performed under a microscope. The PCBs were thoroughly cleaned with IPA to remove residual solder flux and other debris. Figure 5.59b shows the Radiation Payload Main PCB V1 after all required components had been soldered on, while Figure 5.60 shows two views of a Daughter board specimen assembled with extra connectors for purposes of debugging

and testing.



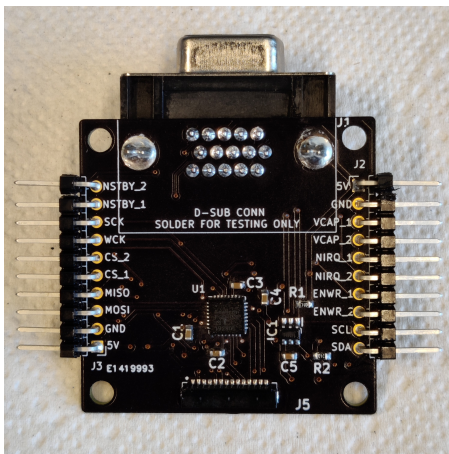
(a) Panelized Bare PCBs being inspected upon delivery



(b) Soldered PCB

Figure 5.59: MAIN Board assembly

The visual inspection was repeated and followed by an electrical continuity check on all soldered joints, component leads, PCB pads and connectors. This was done to ensure the integrity of the soldered joints, to check for inadvertent electrical shorts and to check that the solder had flown effectively to bond with component leads and solder pads on the PCB. The connectors were manually tested for their mechanical strength to ensure that they were properly affixed to the board. The PCBs were carefully broken off from the panel and later inspected under a microscope for cracks and rough edges.



(a) Front view



(b) Rear view

Figure 5.60: Assembled Daughterboard PCB

#### 5.4.2. Electronics & S/W functional testing

After completion of the soldering process and thorough inspection of the assembled PCB, they were tested electrically in an incremental manner:

- Voltage check: Regulated 5V supply was provided as input to the PCB at the appropriate breakout pins, and it was ensured that intended components received 5V as the input voltage. Overcurrent protection was used during this process, to prevent damage to the PCB. It was verified that the LDO was functioning correctly and producing a 3V supply for some of the components on the PCB. The board was also checked for protection against electrical shorts.
- The DF13 payload interface connector was tested next. Connection wires were crimped and assembled with a DF13 wire housing, which was then inserted into the DF13 socket on the Main Board.

Electrical continuity between the wires and the soldered leads of the connector was verified. This is shown in Figure 5.62a.

- The voltage level shifter was tested by providing 5V supply and a 5V signal SPI signal. It was observed that the 5V signal was translated into a 3V signal, as desired.
- The FGDOS chip was tested using the "FGDOS DEBUG" header pins included in the design of the Main and Daughter boards on the DM. The sensor was read out and nominal values were seen for the sensor and reference frequencies, as well as the temperature monitor in the FGDOS chip. An Arduino with a small test script was used for the purpose of reading out the sensor.
- The MSP430 MCU was tested using the "MCU DEBUG" pins over the Spy-by-Wire (SBW) interface, using the MSP430EXPFR5969 LaunchPad [140]. Firmware for functional testing of the MCU was flashed to the MCU via the eZ-FET emulator on the Launchpad and the UART backchannel connection was used to print a preset string to the Serial Monitor [139]. The setup for this test is shown in Figure 5.61.

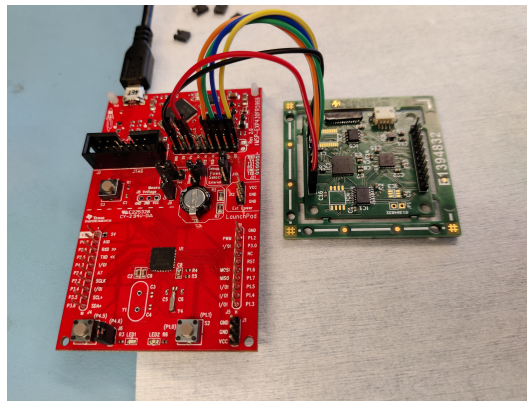
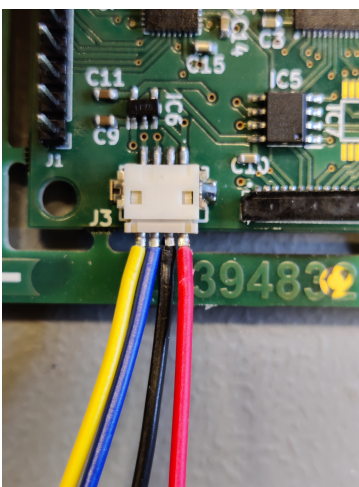
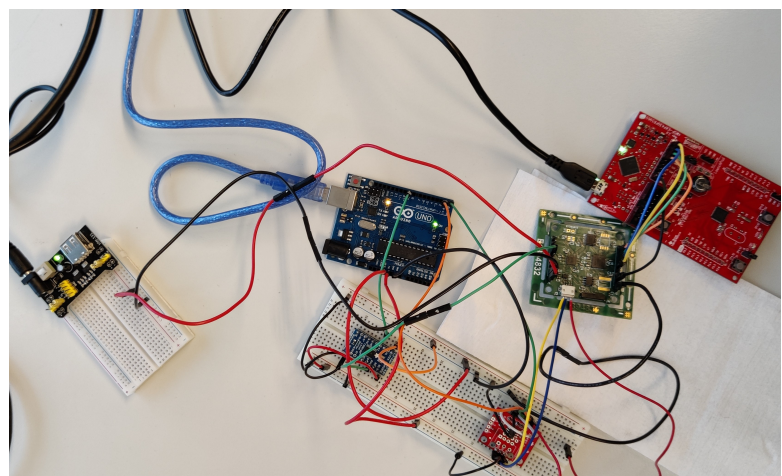


**Figure 5.61:** MCU being tested via interface with an MSP430 LaunchPad development board

- Readout of the FGDOS chip through the MCU was tested as well. For this test the WCK signal to the FGDOS was provided from an Arduino, through a level shifter to bring the signal down from 5V to 3.3V level.
- The RS485 transceiver was tested next to verify that UART signals from the MCU were being translated to the required non-inverting and inverting voltage signals over the RS-485 data bus. For this purpose, an Arduino was fed the output signals from the payload, through an RS485 transceiver breakout board, which translated the data bus signals back into UART. The baud rates of the signal transmission from the payload MCU and reception on the Arduino were matched at 9600 baud. Figure 5.62b shows the test setup.



**(a)** Payload Connector Testing



**(b)** RS485 communication test setup

**Figure 5.62:** PCB Electrical testing

Once it was verified that the payload PCBs were soldered successfully and that all components were functioning correctly, the assembled boards were thoroughly inspected and cleaned.

## 5.5. Radiation Payload Performance Testing

Having cleared preliminary functional tests and inspection, the Radiation Payload prototype was tested to gauge the performance and to characterize some important performance parameters that are relevant to payload operations. Specifically, these performance tests were split into three individual tests, which are described hereon:

1. Noise characterisation, power consumption & temperature measurement
2. Daughterboard interfacing
3. Radiation detection and dose measurement

The results from the first two tests are presented in the following subsections. The radiation detection and dose measurement performance test has been described extensively in section 5.6.

### 5.5.1. Noise Characterisation, Power consumption & Temperature Monitor Calibration

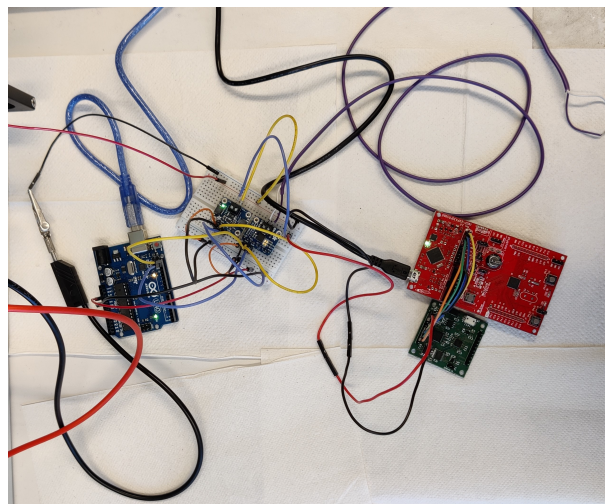


**Figure 5.63:** Setup for noise characterisation, power consumption and temperature monitor calibration test

The prototype was powered in two different ways. First, it was connected to a regulated 5V supply from an LDO, sourced from an electrical socket. This was supposed to approximate the power supply from the rover in operational configuration. Second, a DC laboratory power supply was used to power the board and data was acquired separately to get a benchmark estimate of the expected noise levels. The frequency, power and temperature data were collected for about 25 mins in each run, all while the FG DOS was configured for HISSENS mode with a window size of 4096 pulses.

The noise in the sensor frequencies was observed to be about 8-9 % higher when supplied from the LDO. Figure 5.64 shows comparisons between the sensor frequency distribution based on the power source, for both FG DOS sensors in the chip. The corresponding time history plots can be found in Figure C.5 and Figure C.6. As remarked by de Meyere, the frequency distribution appears to be bi-modal in nature [90]. However, the relative strength of the two peaks was found to be skewed more heavily. This may well be caused by the difference in the setups used for these tests. It is important to note that an abstract electronic model of the FG DOS, such as the one presented in [22] is needed for detailed analysis and prediction of the electronic noise levels in the FG DOS circuitry and its dependence on the noise of the power supply. Such an analysis is considered outside the scope of this thesis.

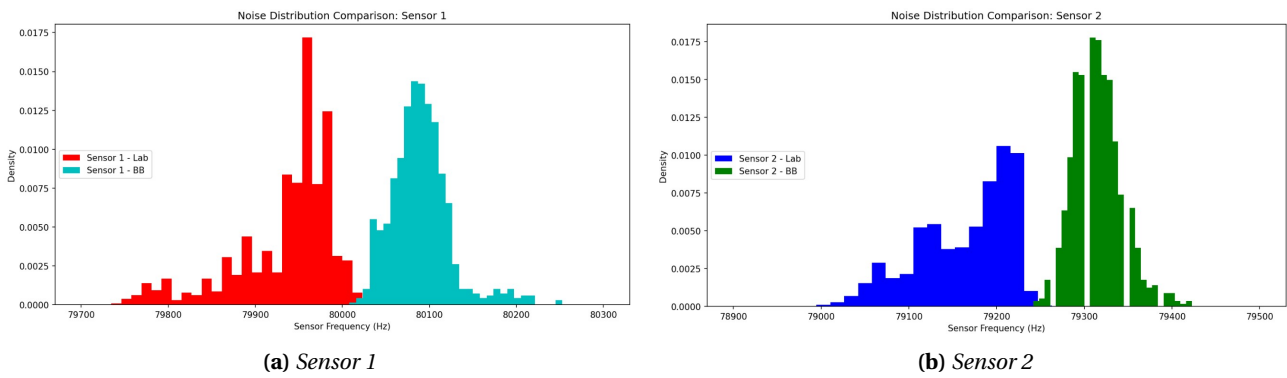


**Figure 5.64:** Raw sensor frequency noise distribution: effect of power supply

The sensor frequencies collected under power from the DC supply were filtered using a moving average filter, similar to the approach described in [22] and [90]. A window size of about 40s was used to calculate the moving average<sup>12</sup>.

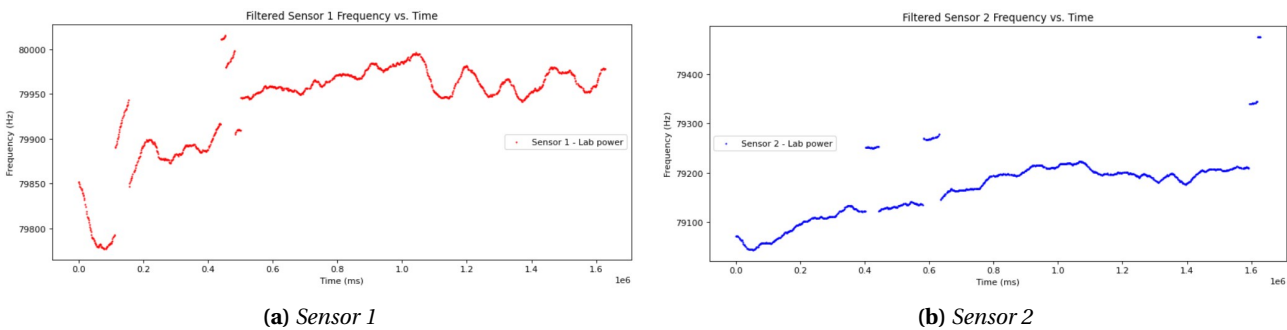


**Figure 5.65:** Filtered sensor frequencies

It was noticed that the moving average was being skewed by the presence of a small amount of spikes/dips. These outliers were subsequently removed to clean up the frequency signal. The noise in the resulting filtered signal is visually displayed in Figure 5.66, after subtraction of the raw frequency signal from the filtered signal.

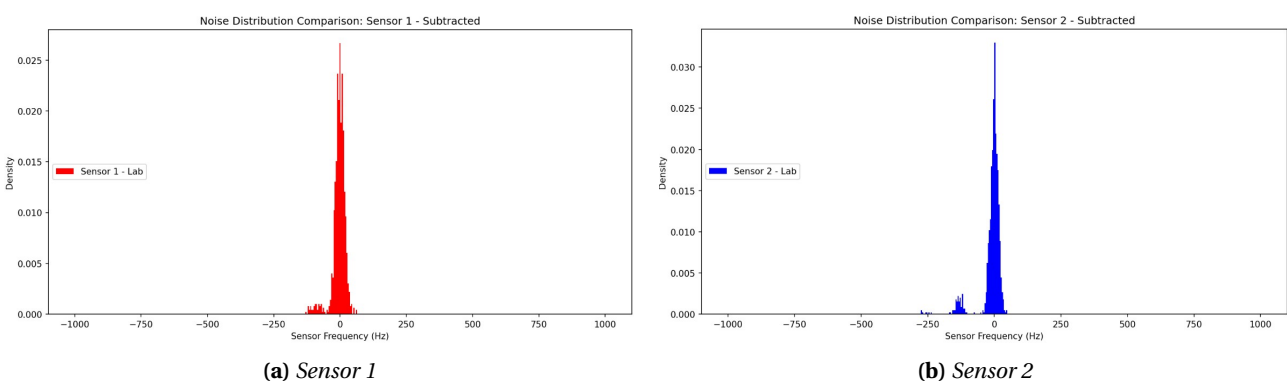


**Figure 5.66:** Filtered sensor frequencies with raw signal subtracted

The results from the noise tests are summarized in Table 5.12. A  $3\sigma$  estimate of the noise is reported, which comes out to be about 75-123 Hz when considering the filtered signals from both sensors. This is commensurate with the noise reported in the FGD-03F datasheet [117]. This noise level equates to a dose measurement resolution of about 2.14 - 3.51 mGy, considering an average sensitivity value of 35 kHz/Gy. It is known that the noise can be lowered by enlarging the sampling window beyond the lowest value of 4096

<sup>12</sup>this translates to about 30 data points of successively logged frequency values

pulses. This was previously demonstrated in [90]. It is important to appreciate that the two sensors in the same chip can have different noise characteristics (as apparent in Table 5.12), necessitating pre-flight noise characterisation for all Radiation Payload sensors individually. As an additional noise reduction measure, the implementation of a simple LC filter on the incoming 5V supply line is recommended for V2 of the Radiation Payload [135].

Noise Calculation method	s1- $\sigma$ (Hz)	s1-3 $\sigma$ (Hz)	s2- $\sigma$ (Hz)	s2-3 $\sigma$ (Hz)
Raw signal	134	402	211	633
Moving average filter - [40s] window	51	153	62	186
Filtered + outliers removed	25	75	41	123

**Table 5.12:** Radiation Payload performance: Sensor noise characterization (s1 refers to sensor 1)

The power consumption of the prototype board was measured to be approximately 43 mW on average, as shown in Figure 5.67a. Considering that the power consumption of a single FGDOS sensor is about 20-22 mW [90, 18], the test demonstrates that more than 95 % of the power required by the Radiation Payload is due to the FGDOS detector. The distribution of the power consumption is shown in Figure 5.67a. The instantaneous power consumption varies between 41-46 mW, which could be due to the cyclic nature of the FGDOS readout scheme in the current firmware.

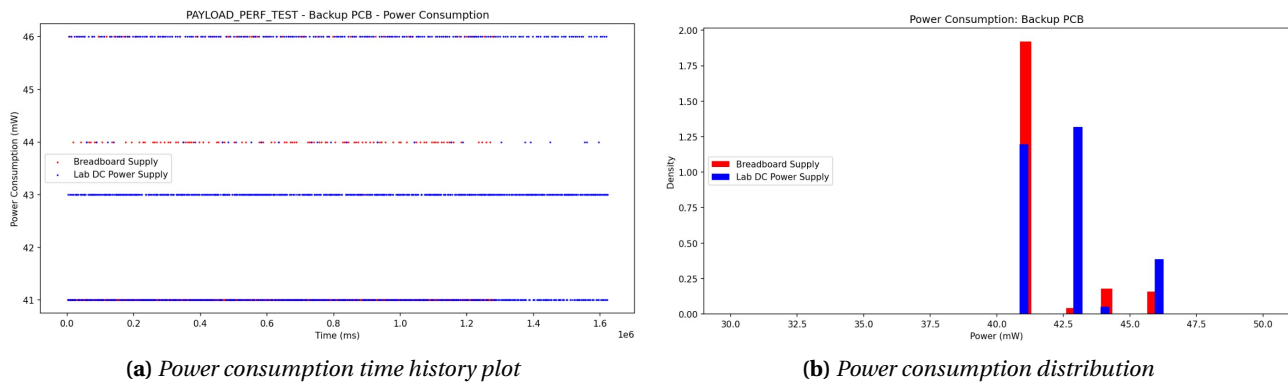


**Figure 5.67:** Payload prototype power consumption

Measurements of ambient temperature from the internal temperature monitor were compared to corresponding measurements made by an E-type thermocouple. As expressed in section 5.2, the calibration of the internal temperature sensors of the FGDOS consists of an offset between the integer value stored in the temperature register and the absolute value of the actual temperature on the Celsius/Kelvin scale<sup>13</sup>. For the FGDOS soldered on the Radiation Payload MAIN V1, this offset was found to be 66 on average, as apparent in Figure 5.68.

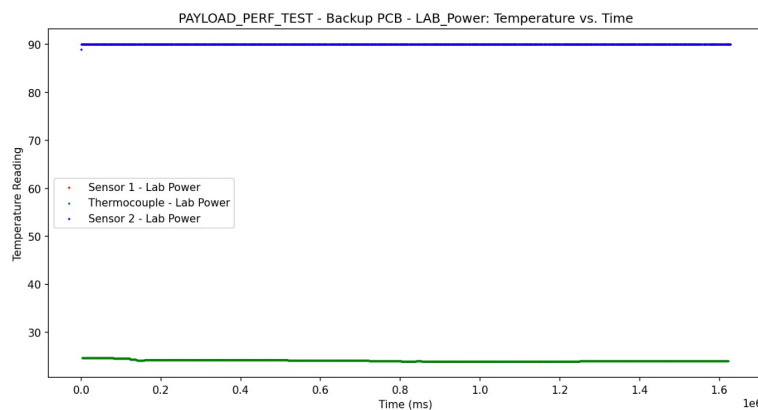


**Figure 5.68:** FGDOS temperature monitor calibration

<sup>13</sup>The Celsius scale is used here for convenience and consistency

### 5.5.2. Daughterboard Interface Test

An interface test was performed to verify the ability of the Radiation Payload Main board to communicate with and read out the Daughterboard. Before this interface test, the Daughterboard was tested individually to verify its design and to ensure proper assembly and soldering of the PCB. This was carried out by reading out the FGDOS on the Daughterboard with a setup similar to Breadboard-A, as shown in Figure 5.69.

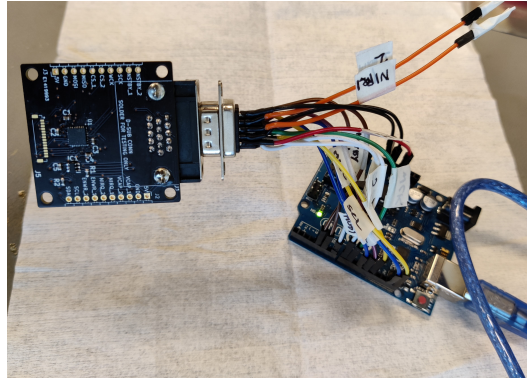


**Figure 5.69:** *Daughterboard unit testing*

Figure 5.70 shows the setup used interface testing. The test consisted of a relatively simple process in which the two boards were connected using a mock interface cable harness and the data was read out from all four FGDOS sensors over a serial port, using a slightly modified version of the firmware for the MSP430 MCU.

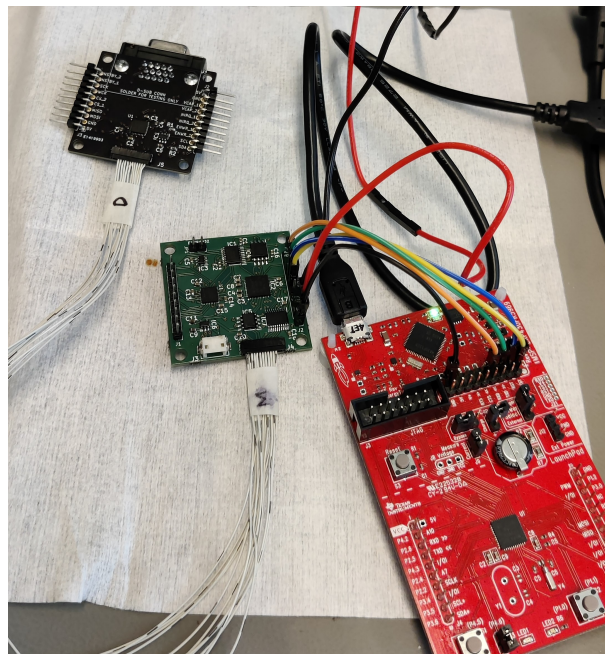


**Figure 5.70:** *Daughterboard Interface test setup*

The test was executed successfully, demonstrating the functioning of the complete V1 electronic system design. This test also serves to prove the architectural concept of spatially distributing the radiation measurement over two separate electronic boards (and two separate FGDOS SoCs). Owing to the modularity of the design and knowledge of the FGDOS SoC, full validation by means of a dedicated test is concerned superfluous. Instead, it might be interesting to achieve this using a Monte Carlo radiation transport model of the Radiation Payload boards, as described in section 4.3.

## 5.6. Radiation Payload Performance Testing: Proton Beam Irradiation

### 5.6.1. Aim & Rationale

As a part of the functional and performance testing of the Radiation Payload prototype, it was tested against proton beam radiation to calibrate the FGDOS that lies at its core and to gauge the performance of the payload in its detection of protons at various beam kinetic energies and dose rates. This test also served as an extension of the previously discussed FGDOS radiation characterisation and calibration campaign (section 5.1). This is justified because the radiation from various sources expected during the mission is predominantly composed of protons, as discussed in chapter 2 and section 4.2. Since, the main objective of this test was to demonstrate the payload prototype's ability to detect and measure ionizing radiation, a pencil beam of protons targeted on the FGDOS chip was used for irradiation. Large fields were ruled out since the test was not aimed at conducting radiation hardness assurance (RHA) testing of the payload prototype. RHA tests were precluded by limits imposed on the maximum duration of irradiation runs at HPTC.

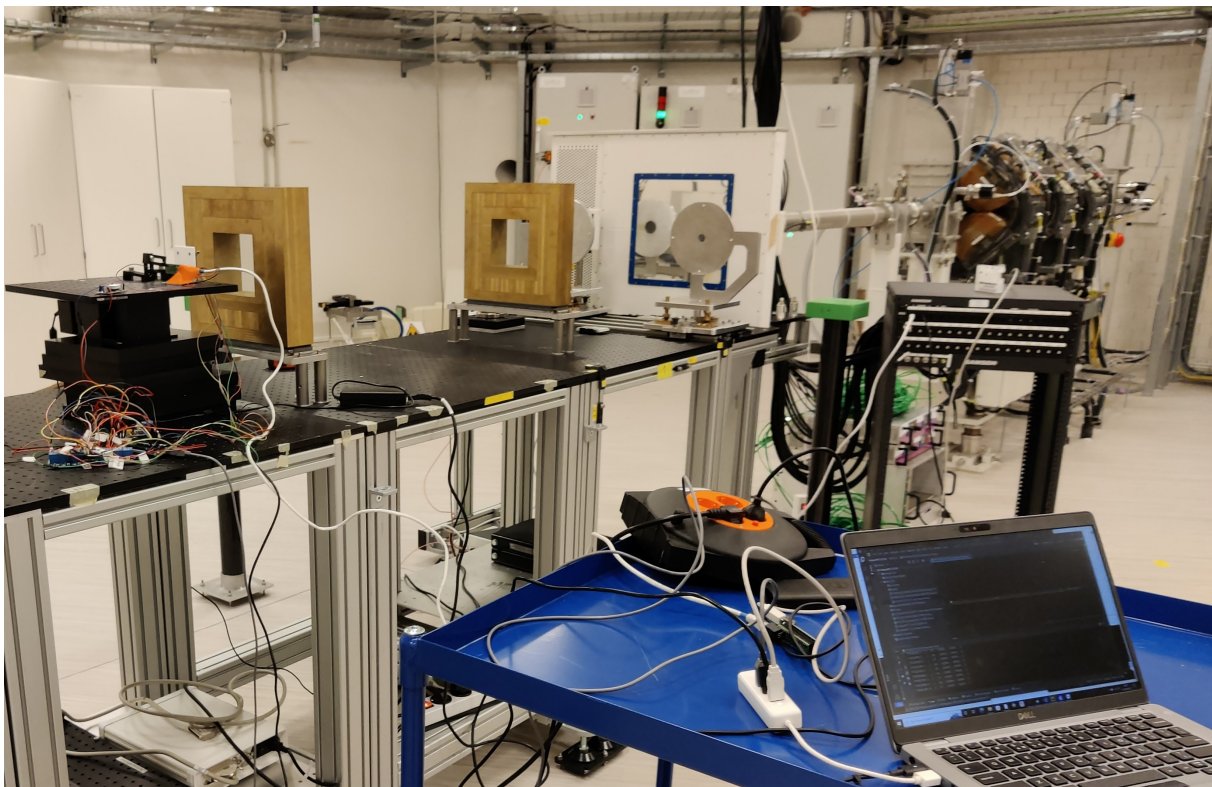


**Figure 5.71:** *Radiation Payload performance testing at HPTC*

### 5.6.2. Test Setup

The Radiation payload performance test setup is illustrated by the schematic shown in Figure 5.72a and the setup of the experiment room at HPTC is shown in Figure 5.71. The setups for the DUT and the beam line were similar to those delineated in section 5.1. The most important distinction was that the irradiation was performed in the form of a pencil beam of protons, which led to the exclusion of scatter rings. The use of a pencil beam also made it necessary to align the test article along the beam path accurately, as depicted by Figure 5.73a.

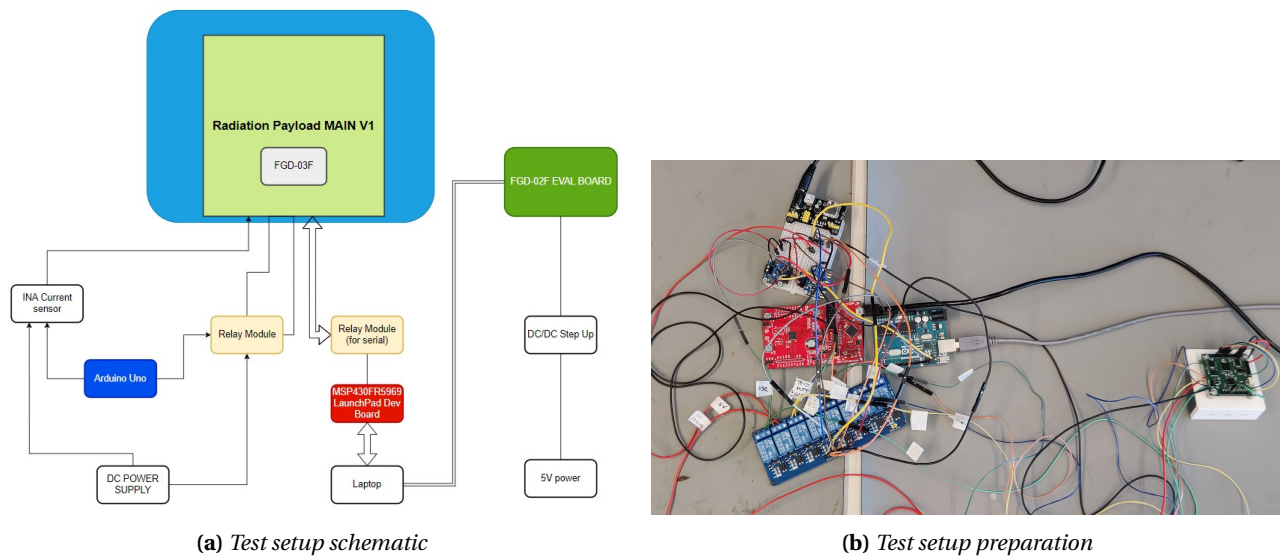
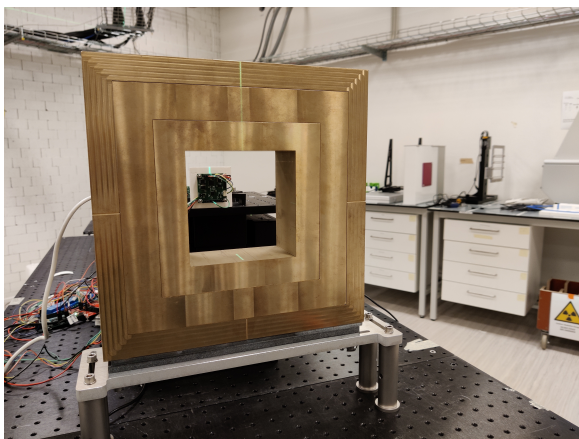


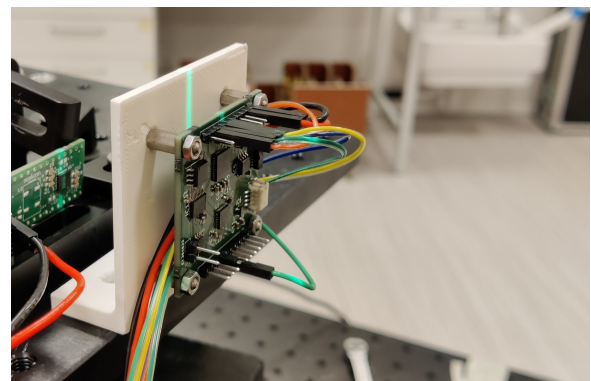
**Figure 5.72:** Close up views of payload performance test setup

The setup consisted of the following elements:

- Radiation Payload MAIN V1
- MSP430FR5969 LaunchPad Development board
- Arduino Uno microcontroller board
- Relay array module
- DC power supply
- INA219 power monitor breakout boards
- FGD-02F Evaluation Board
- DC/DC Step Up for recharging the FGD-02F Evaluation board
- 12V Power adapters
- USB cables
- Laptops for data acquisition and logging



(a) View along the beam path



(b) Payload board mounted on fixture

**Figure 5.73:** Close up views of payload performance test setup

### 5.6.3. Test Levels

The choice of pencil beam enabled the use of a much wider range of beam energy levels and dose rates than previously available. These levels have been presented in Table 5.13 and Table 5.14.

Energy Code	Beam Energy (in MeV)
A	70
B	120
C	200
D	100
E	160
F	244

**Table 5.13:** *Payload performance test: Beam kinetic energy levels*

Dose Rate Code	Dose rates at target in air (in Gy/min)	Dose rates at target in air (in rad/s)
2	0.1	0.17
3	0.6	1
6	0.85	1.42
7	1	1.67
9	3	5
15	0.02	0.03
16	0.12	0.20
17	1.7	2.83
18	0.15	0.25
19	6.2	10.33
20	12.4	20.67
21	18.6	31.00
22	24.8	41.33
23	31	51.67

**Table 5.14:** *Payload performance test: Dose rate levels*

A holistic summary of all radiation runs conducted during the test can be found in Table 5.15. An indication of the purpose of each run is also provided, along with the sensor settings used in correspondence. The test plan was divided into seven sets according to the purpose of the irradiation runs within that set or the beam energy used in the set.

#### 5.6.4. Methodology

Throughout each test run, the following parameters were monitored for both sensors:

1. Time elapsed
2. Sensor Frequency
3. Reference Frequency
4. FGDOS Internal Temperature
5. Recharge count
6. Payload voltage
7. Current consumption
8. Power consumption
9. Actuation status for relays connected across - payload power supply and UART connections

Prior to the performance test at HPTC, mock tests were carried out to ensure proper functioning of the test setup and successful data acquisition and logging. The main focus of the performance test data analysis was obtaining and analyzing the sensitivity and its variation w.r.t the energy levels and dose rates of the incident proton beam. After the test, a post test run was carried out to identify any permanent damage to the payload prototype caused by irradiation.

#### Test Procedure

The step-by-step procedure that was used to conduct the test can be found in [123]. As far as the irradiation runs are concerned, the procedure that was followed was identical to the FGDOS radiation characterisation

tests discussed in section 5.1.<sup>14</sup>.

Run #	Test Code	Beam Energy (MeV)	Beam Energy at Target (MeV)	Dose rate at target (in air) (Gy/min)	Approx Run time (min)	Dose acc. at target - TID (in Air) (Gy)	Sensor Settings	Test Purpose
<b>SET 1</b>								
1	A3	70	70	0.6	8	4.8	HI SENS	High sensitivity baseline at 70 MeV
2	A7	70	70	1	8	8	HI SENS	High dose rate at 70 MeV
3	A9	70	70	3	6	18	HI SENS	Dose rate variation
4	A3	70	70	3	3	9	HI SENS	High dose rate at 70 MeV
5	A9	70	70	3	6	18	HI SENS	High dose rate at 70 MeV
6	A2	70	70	0.1	5	0.5	HI SENS	Medium dose rate at 70 MeV
<b>SET 2</b>								
1	B7	120	120	1	8	8	HI SENS	Energy variation
2	B3	120	120	0.6	8	4.8	HI SENS	Baseline test - TID degradation
3	B6	120	120	0.85	8	6.8	HI SENS	Dose rate variation
4	B16	120	120	0.12	3	0.36	HI SENS	Medium dose rate at 120 MeV
<b>SET 3</b>								
1	B3	120	120	0.6	5	3	HI SENS	Baseline test - TID degradation
2	C6	200	200	0.85	3	2.55	HI SENS	Energy variation
3	C17	200	200	1.7	1	1.7	HI SENS	Dose rate variation
<b>SET 4</b>								
1	B3	120	120	0.6	5	3	HI SENS	Baseline test - TID degradation
2	B3	120	120	0.6	5	3	LOWSENS	Low sensitivity baseline at 120 MeV
3	B3	120	120	0.6	5	3	PASSIVE	Passive mode at 120 MeV
<b>SET 5</b>								
1	D3	100	100	0.6	5	3	HI SENS	High sensitivity baseline at 100 MeV
2	D18	100	100	0.15	3	0.45	HI SENS	Dose rate variation
3	D6	100	100	0.85	3	2.55	HI SENS	Medium dose rate at 100 MeV
4	D7	100	100	1	2	2	HI SENS	High dose rate at 100 MeV
<b>SET 6</b>								
1	E3	160	160	0.6	5	3	HI SENS	High sensitivity baseline at 160 MeV
2	E6	160	160	0.85	5	4.25	HI SENS	Medium dose rate at 160 MeV
3	E7	160	160	1	2	2	HI SENS	High dose rate at 160 MeV
<b>SET 7</b>								
1	B3	120	120	0.6	5	3	HI SENS	Baseline test - TID degradation
2	F19	244	244	6.2	2	12.4	HI SENS	Energy variation
3	F20	244	244	12.4	1	12.4	HI SENS	High dose rate exposure
4	F21	244	244	18.6	1	18.6	HI SENS	Very high dose rate exposure
5	F22	244	244	24.8	1	24.8	HI SENS	Dose rate variation
6	A15	70	70	0.02	5	0.1	HI SENS	Very low dose rate exposure
7	B3	120	120	0.6	5	3	HI SENS	Baseline test - TID degradation
8	F23	244	244	31	0.7666667	23.7666667	HI SENS	Extremely high dose rate exposure
<b>Cumulative TID</b>						<b>153.30</b>		

**Table 5.15:** Radiation Payload V1 Performance Testing: Summary of test runs

### 5.6.5. Observations & Inferences

#### Sensor characteristics

The characteristic of the sensor over the entire dynamic frequency range, under irradiation at constant dose rate can be seen in Figure 5.74. The yellow and green lines depict a linear fit to the frequency values within the LDR of sensors 1 and 2. Thus, both the non-linear and linear segments of the frequency characteristic can be clearly appreciated, based on the  $V_{gs} - I_d$  trend of the readout n-MOS of the FGDOS [34]. In line with previous observations, a stray spike in sensor 1 frequency is seen toward the tail end of the run.

The sensitivity of the FGDOS sensors in the LDR in high sensitivity mode was found to be about 32-37 kHz/Gy. In low sensitivity mode, the sensitivity was found to be about 6 kHz/Gy. The LOWSENS characteristic (restricted to its LDR) is portrayed in Figure 5.75.

<sup>14</sup>Since a pencil beam was used for irradiation instead of a large field, switching beam energy levels was relatively quick as it did not involve rearrangement of certain elements in the beam line setup

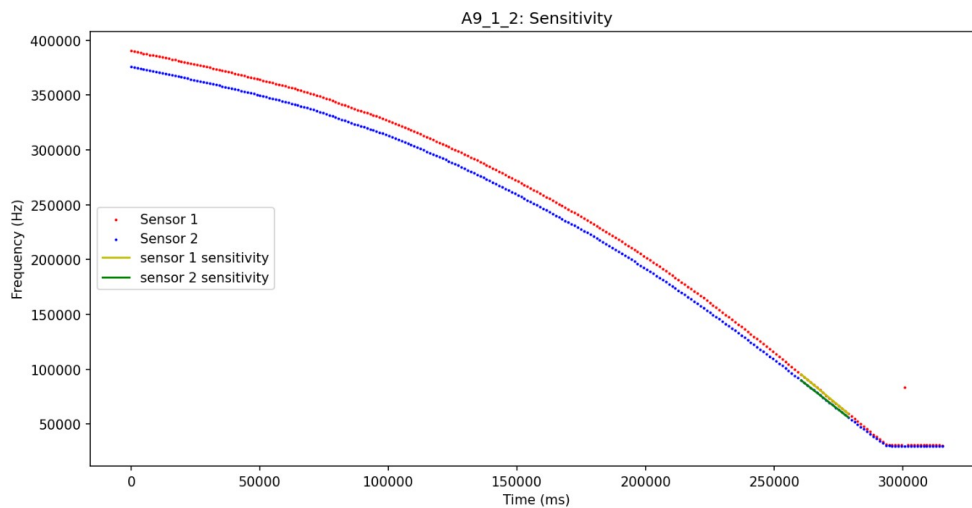


**Figure 5.74:** Payload Performance: HISENS characteristic over full frequency range

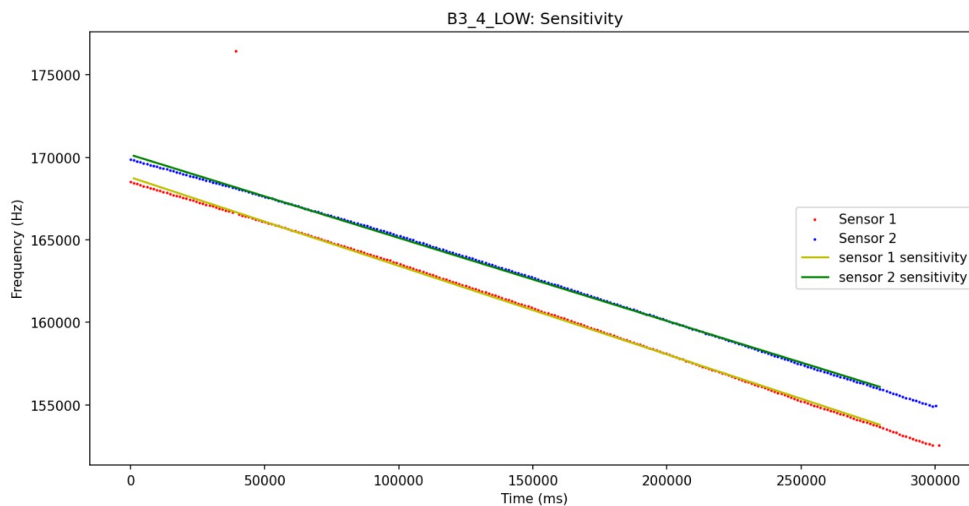


**Figure 5.75:** Payload Performance: LOWSENS characteristic

Payload power consumption was about 44 mW on average. This dropped to about 21 mW when the FGDOS was configured for LOWSENS mode. As elucidated in section 5.5, the power draw measurements indicate that almost all of the payload power consumption stems from the FGDOS SoC. Apart from the variation in FGDOS power consumption due to TID, the power consumed by the payload for a given FGDOS configuration does not vary considerably in the midst of radiation dose detection.

#### Effect of energy and dose rate on sensitivity

Figure 5.76 shows the trend of sensitivity with varying energy, at three different dose rates. Apart from the high sensitivity at 120 MeV and 0.85 Gy/min (which can be regarded as a spurious data point), it can be seen that the sensitivity increases gradually with increase in the beam energy. However, the strength of this trend is not as intense as seen in previous tests (described in section 5.1).

Figure 5.77 shows the variation in FGDOS sensitivity with changing dose rate. To isolate the energy dependence, the tests were carried out for each energy level separately. While some trends can be seen in the plots for 120 MeV, 160 MeV and 200 MeV, overall it can be seen that no systematic trend exists in the sensitivity of either sensor as the dose rate changes. This is exemplified by the plots where more data points are available i.e. at 100 MeV and 244 MeV. In line with previous results (section 5.1), it can be posited that dose sensitivity is independent of the dose rate of incident radiation.

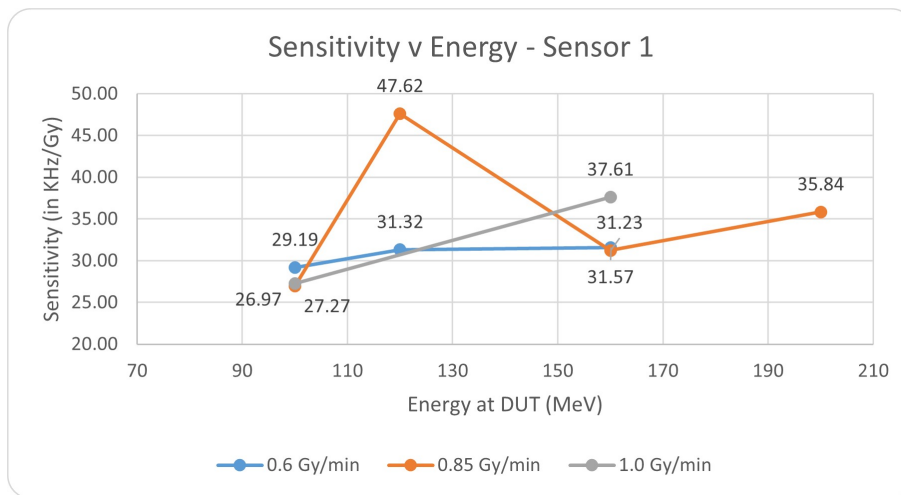
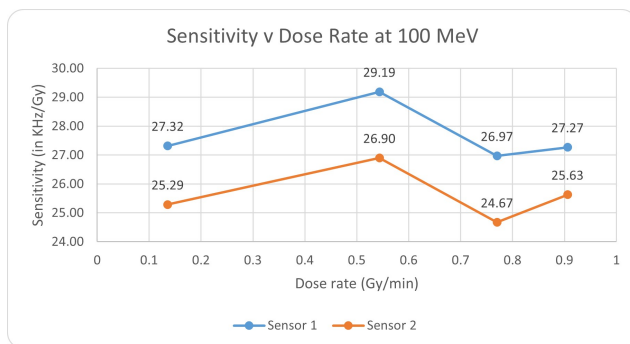
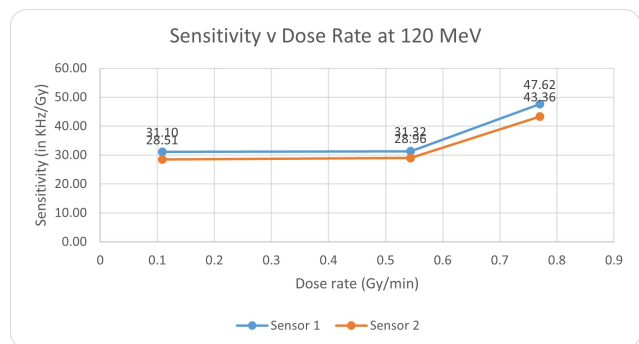


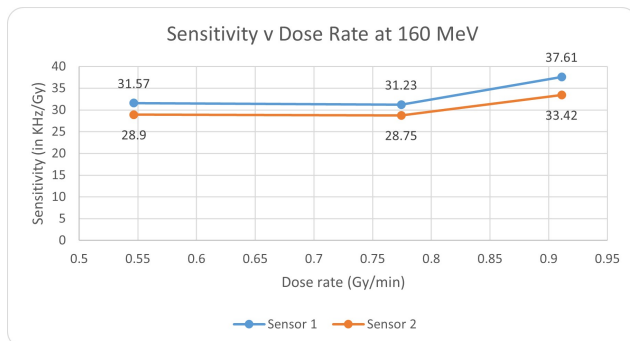
Figure 5.76: Payload Performance: Sensitivity variation with beam kinetic energy



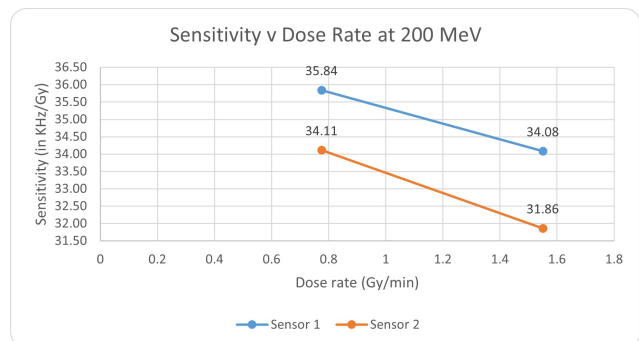
(a) 100 MeV



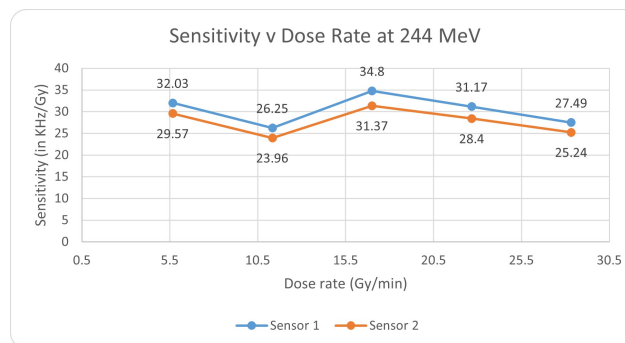
(b) 120 MeV



(c) 160 MeV



(d) 200 MeV



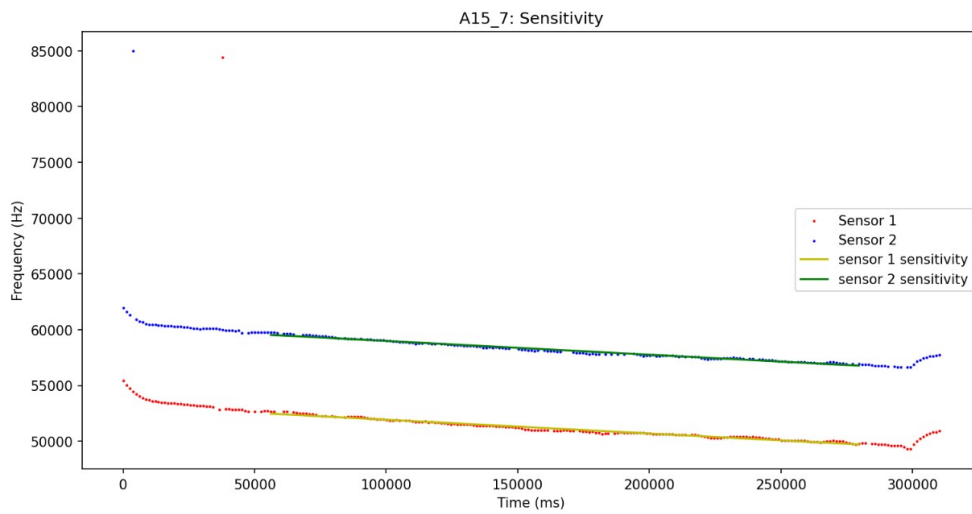
(e) 244 MeV

Figure 5.77: Payload Performance: Sensitivity variation with dose rate at various beam energies

### Measurement resolution

The inherent noise in the the payload prototype's frequency signals was previously characterised and discussed in subsection 5.5.1.

During radiation testing, it was sought to practically assess the resolution at which the payload can perform dose measurements. However, the lowest dose rate which could be obtained with the pencil beam was limited at the lower end by the minimum beam intensity that could be supplied by the cyclotron. For the current energy levels, the minimum dose rate that could be achieved was about 0.02 Gy/min at 70 MeV, portrayed in Figure 5.78. As discussed previously, the irradiation duration constraints at HPTC imply that sensitivity cannot be measured accurately at very low dose rates from the raw unfiltered output of the FG-DOS sensors. this is due to the fact that the dose accrued within 8-9 minutes at very low dose rates does not precipitate an appreciable frequency drop as compared to the noise band of the sensor frequency. This can be overcome by the use of a moving average filter to increase the effective dose resolution of the FG-DOS. Since filtering is a post processing technique and it bears no influence on the raw signals from the FG-DOS in operation, the dose resolution is better tested using long duration irradiation runs, which might be possible with another source such as gamma rays from Co-60.



**Figure 5.78:** Payload Performance: measurement at low dose rate (0.02 Gy/min)

Additionally, the lowest dose rate at 120 MeV that could be used was 0.12 Gy/min, with the corresponding FG-DOS response shown by the plots in Figure 5.79. The flat segment in the curves on the right half of the plots represents a time interval in which the beam was not available.

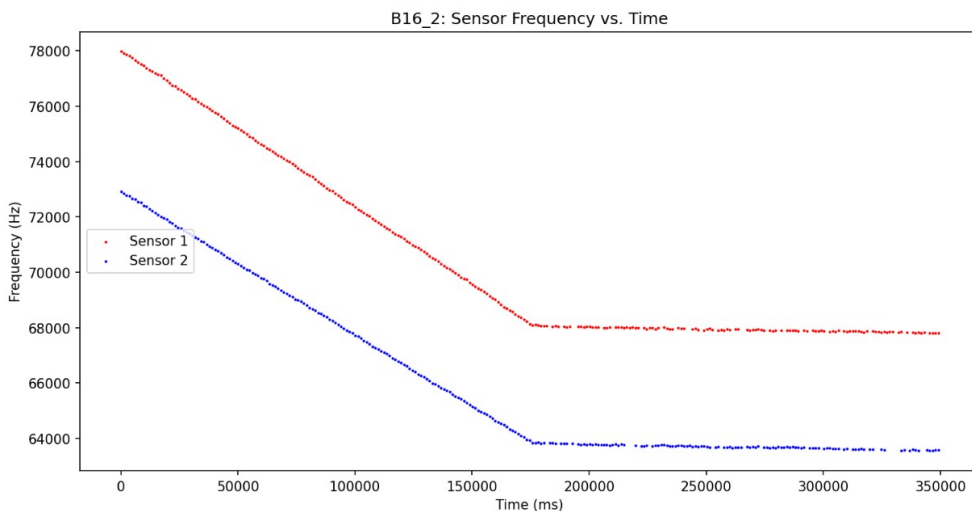


**Figure 5.79:** Payload Performance: measurement at medium dose rate (0.12 Gy/min)

### Sensor response to very high dose rates

To check the response of the FGDOS under protons arriving at a very high dose rate, a series of runs were performed, each consisting of one discharge cycle for the FGDOS. These test were carried out a beam energy of 244 MeV, since this energy allowed for high dose rates of an unprecedented magnitude which could not be achieved at other energies or with a large field<sup>15</sup>. The sensor frequencies have been shown in Figure 5.80, along with lines fitted to the data points lying within the LDR, for purpose of calculating the sensitivity. The corresponding sensitivity values can be viewed in Figure 5.77e. It is to be noted that the dose rates shown there approximate the dose deposited at target in Si, whereas the captions in Figure 5.80 refer to the dose rates at target in air.

For each dose rate, the FGDOS is seen to operate nominally, although the toward the end, the sampling rate begins to appear too coarse to obtain enough data points within the LDR to yield accurate sensitivity estimation using linear regression. Most importantly, it was seen that exposure to extremely high dose rates did not cause any anomalies or unexpected behavior in the FGDOS. This demonstrates that the Radiation Payload would still be able to perform dose measurements in the face of unprecedented events such as SPEs, where high radiation doses can be delivered within short time periods.

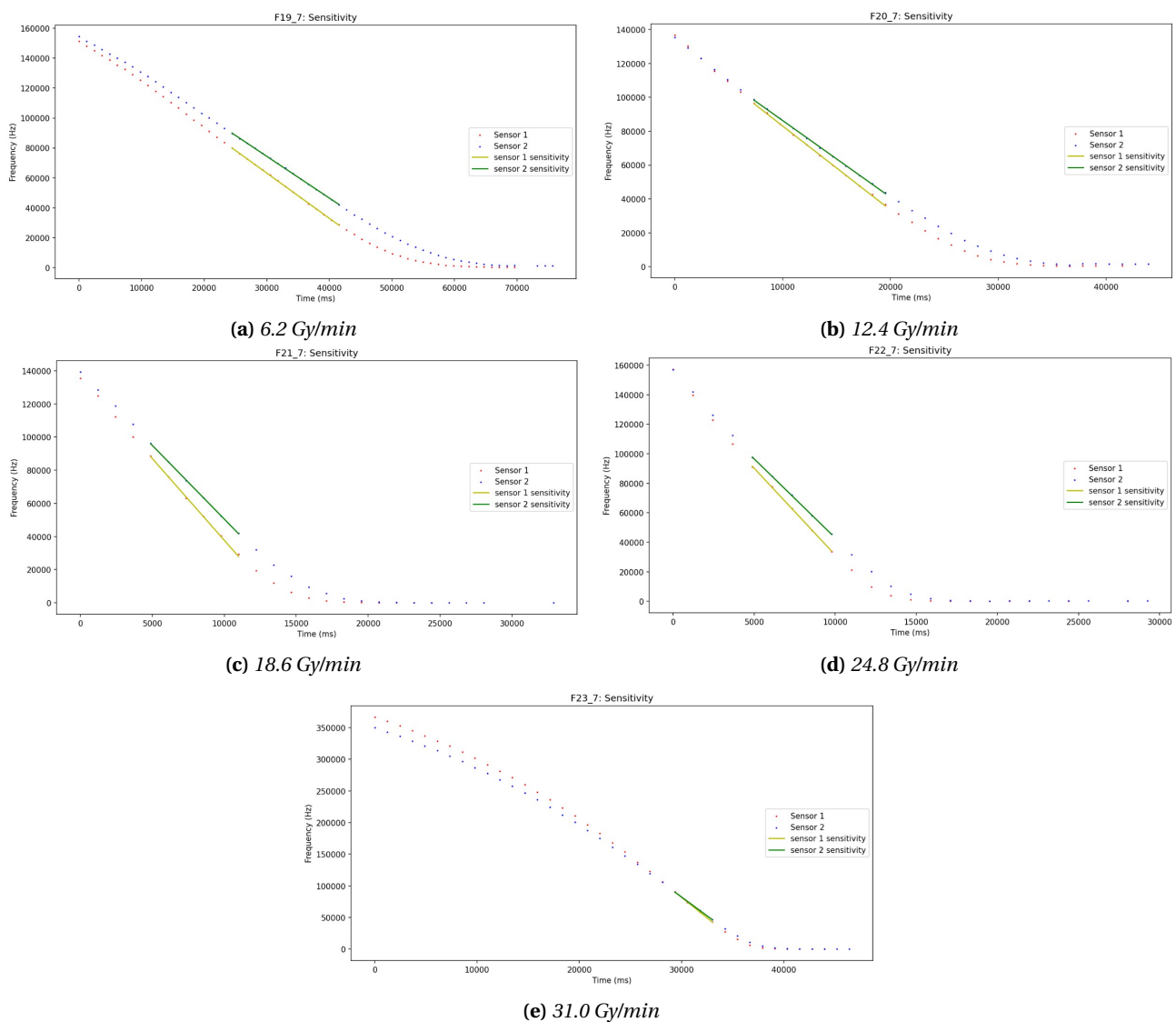


**Figure 5.80:** Payload Performance: FGDOS response to very high dose rates at 244 MeV

Overall, practical bounds on dose rate measurements as created by two factors. The minimum dose rate which can be measured is dictated by the resolution of the FGDOS sensors and the sampling rate i.e. how

<sup>15</sup>Dose rates as high as 5000 Gy/min could be obtained if the cyclotron was pushed to its maximum beam intensity levels

frequently the FGDOS registers are read out. This is expressed by:

$$d^*_{min} = \text{Dose resolution} \times \text{Sampling rate} \quad (5.5)$$

In Equation 5.5,  $d^*_{min}$  refers to the lowest measurable dose rate. The maximum detectable dose rate practically depends on the size of the LDR chosen for the FGDOS, the sampling rate as well as the sensitivity, assuming that at least two data points within the LDR are required for dose measurement. This is expressed by:

$$d^*_{max} = \frac{\text{LDR}}{\text{Sensitivity}} \times \text{Sampling rate} \quad (5.6)$$

In Equation 5.6,  $d^*_{max}$  refers to the highest measurable dose rate.

### TID induced degradation

Since a sizeable amount of TID was delivered to the FGDOS on the Radiation Payload, the degradation induced by TID on FGDOS sensitivity (in Figure 5.81) and FGDOS power consumption (in Figure 5.82) could be studied. To maintain consistency, only sensitivity values computed for irradiation runs at baseline levels were used to gauge the degradation. The sensitivity drops by about 11-12 % over TID of about 127 Gy. Comparing the relative sensitivity drop in TID results from Figure 5.81 and Figure 5.13, it is clear that TID induced degradation in sensitivity is a non-linear effect. The degradation is observed to accelerate with continued TID accumulation.

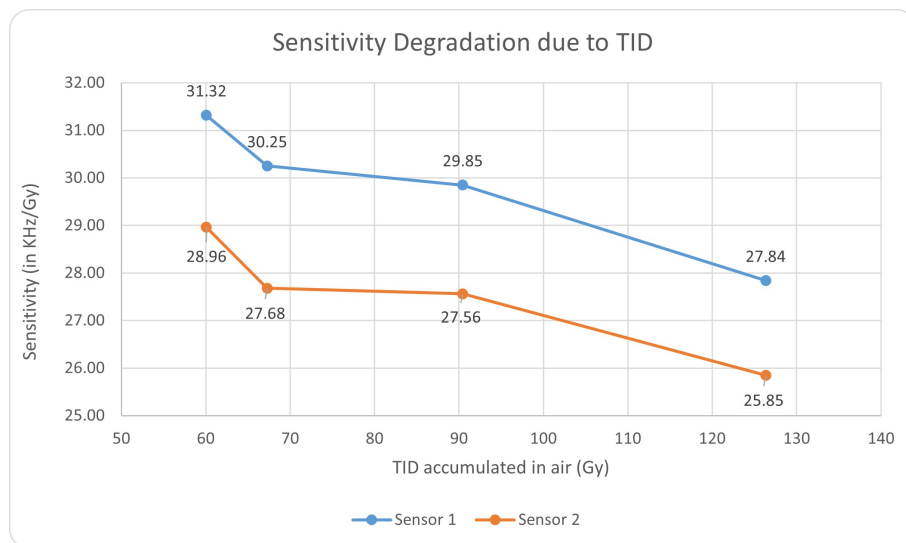


**Figure 5.81:** Payload Performance: Sensitivity degradation with TID

The power consumption did not vary considerably for the TID accumulated through the course of all irradiation runs. This observation was expected since previous tests showed that the power consumption started to grow noticeably between a TID of 190-210 Gy (as shown in Figure 5.13).

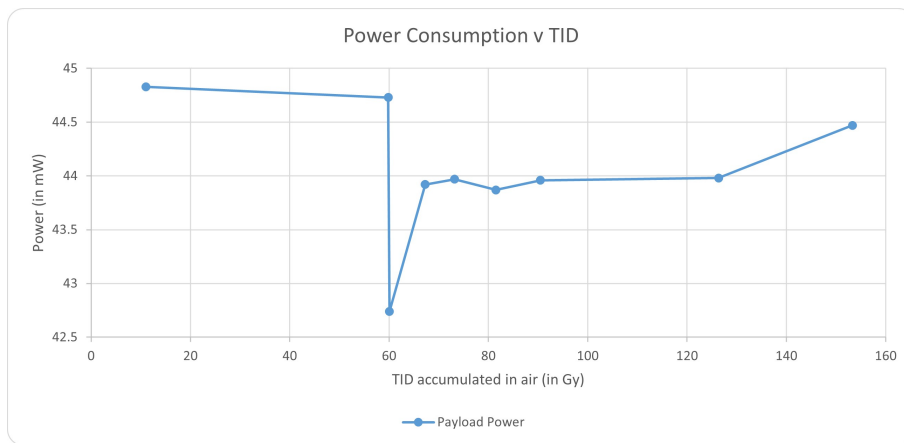
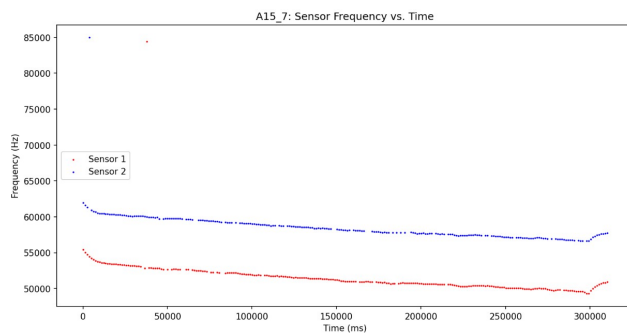


**Figure 5.82:** Payload Performance: Change in power consumption with TID

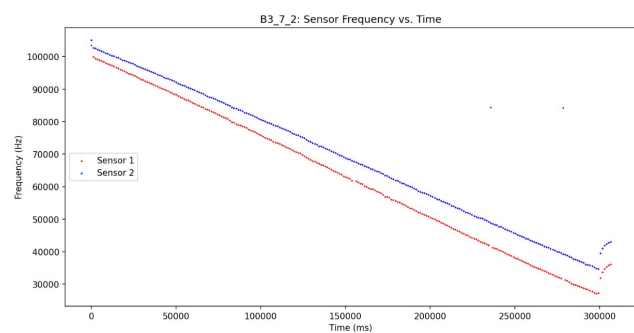
### **Rapid Recovery effect**

Toward the tail end of the Radiation Payload performance test, the *Rapid Recovery* (previously observed during FGDOS characterisation in section 5.1), was observed on two separate irradiation runs. This occurred when the FGDOS had accumulated a TID of approximately 126 Gy, comparable to the 180 Gy accumulated when the effect was first noticed during the tests in March 2022.

The distinction between this occurrence of *Rapid Recovery* and the previous example (Figure 5.14 & Figure 5.15) is that the rebound magnitude is lower. It can be argued that this is due to the TID accumulated by the payload's FGDOS being lower. The implication being that the *Rapid Recovery* effect grows in magnitude and prominence along with the aggregation of TID in the FGDOS. The matter of engineering importance here is that each FGDOS chip may have a *threshold TID* which marks the onset of the *Rapid Recovery* phenomenon. As long as the TID expected for the operational life/duration of use of an FGDOS is below this threshold, the *Rapid Recovery* effect may not be a relevant concern.



**(a)** Rapid Recovery at medium dose rate



**(b)** Rapid Recovery at low dose rate

**Figure 5.83:** Payload Performance: Rapid Recovery effect

A gradual drop in the sensor frequencies was captured after the conclusion of the last irradiation run, shown in Figure 5.84. This may appear to be a *Rapid Recovery* associated 'drop-off' at first glance, but it's unlikely since drop-offs have only been observed to coincide with irradiation so far. Other potential causes of this frequency fading might be short-term annealing of trapped holes or charge leakage from the buried gate [18].

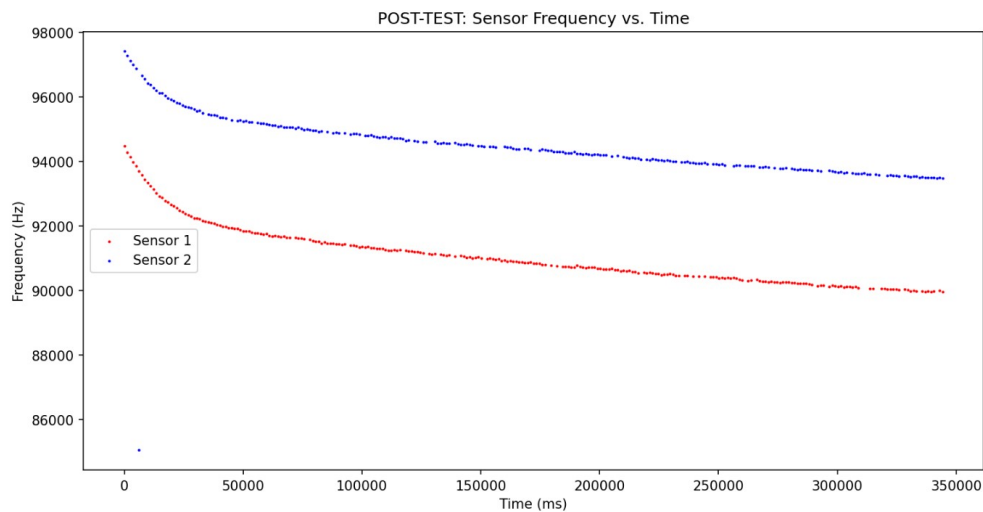


**Figure 5.84:** Payload Performance: Post test frequency fading

### Temperature monitoring

The test setup was maintained at ambient temperature for the entirety of the test duration. Hence, the payload was operated at a relatively constant temperature, eliminating the need for temperature compensation of frequency signals. As expected, the internal temperature monitor of the FGDOS recounted this stable temperature levels, shown by a sample of acquired temperature data in Figure 5.85.

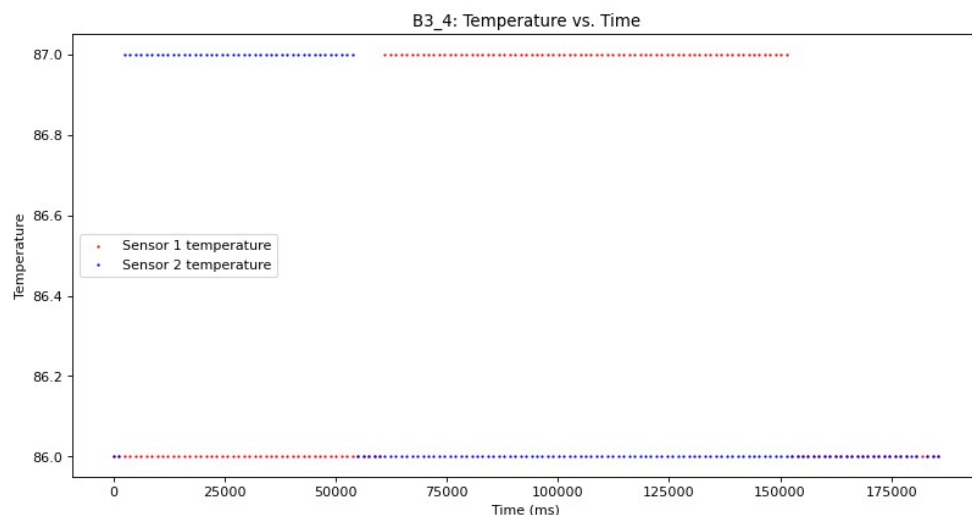


**Figure 5.85:** Payload Performance: Temperature monitoring

### Anomalies

It was observed prior to the test that the automatic recharge system of the FGDOS chip soldered on Radiation Payload Main V1 was malfunctioning, causing continuous injection of charge on the floating gate which led to extremely high sensor frequency values at the beginning of the test. This drove the sensor frequency outside its LDR. This issue was dealt with by disabling the automatic recharge in the configuration of the FGDOS. Thereafter, the recharge process was controlled manually albeit still using the charge pump embedded in the FGDOS. This was achieved by resetting the recharge voltage to its least allowable value of 14.5 V, enabling the recharge and later disabling it by re-configuring the FGDOS. Needless to say, this procedure was carried out between irradiation runs to prevent the loss of dose measurements, with one exception, where the recharge process was executed during irradiation so that it may be recorded and analyzed, as shown in Figure 5.86. The recharge characteristic appears to be similar to that of a nominally operating FGDOS.

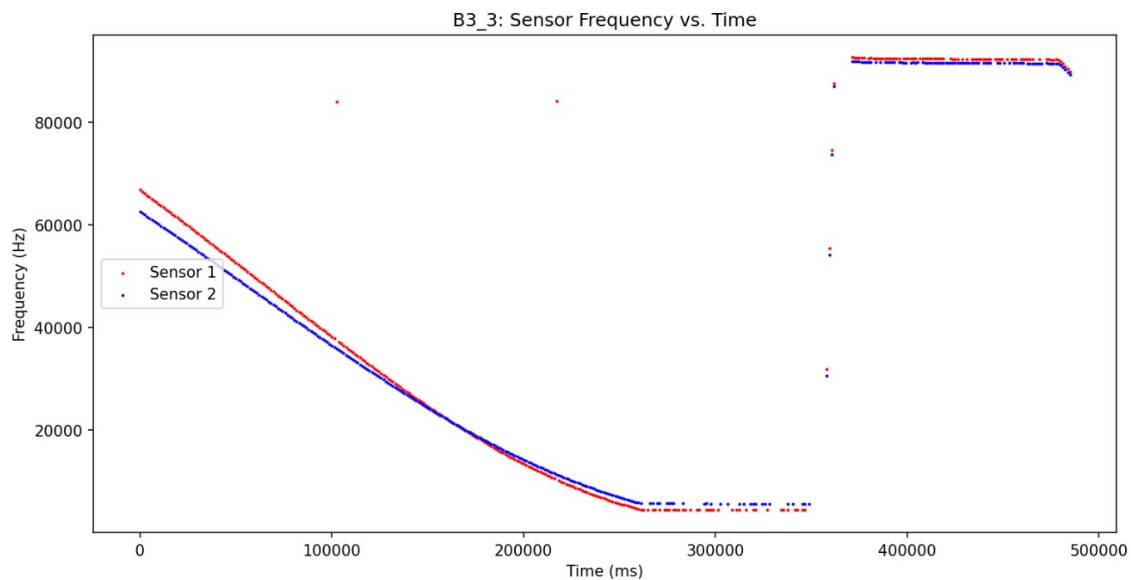


**Figure 5.86:** Payload Performance: Recharge characteristic at 14.5 V recharge voltage

Similar to previous tests, occasional spikes and dips in the frequencies and temperature values were observed during the test. The nature of these anomalies was temporary and they could be identified and filtered out of the test data reliably. A plausible explanation for these 'blips' has been provided in [22], [34], where the investigators chalked it up to SEEs in the FGDOS's digital registers which store frequency and temperature readout from the analog part of the chip.

The passive mode of the FGDOS was tested to simulate payload operations during lunar night (in an accelerated manner), when the Lunar Zebro rover would be in hibernation.

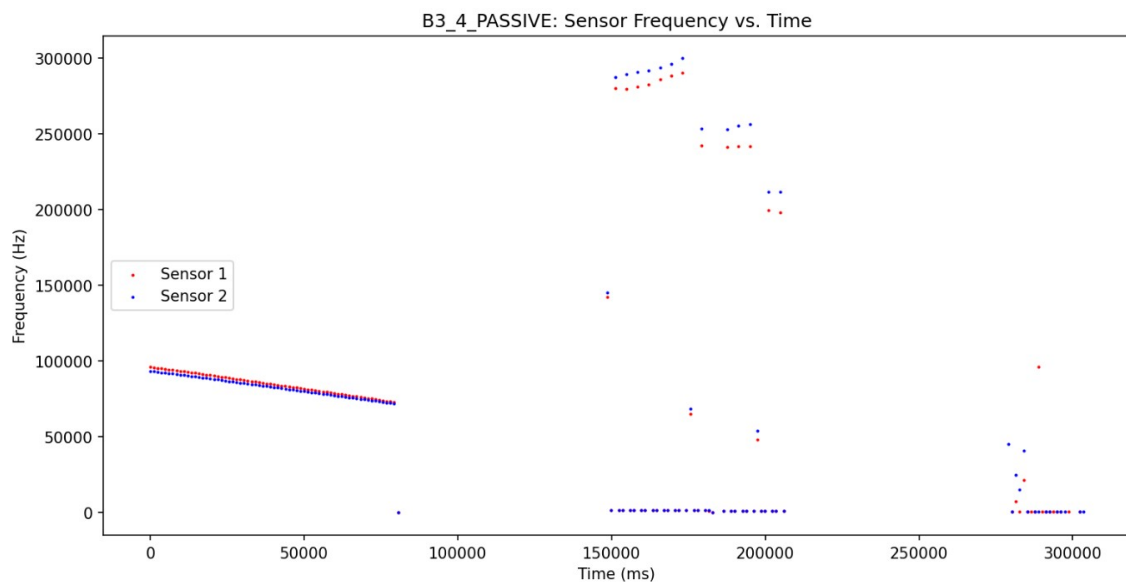


**Figure 5.87:** Payload Performance: Passive mode

Passive mode was initiated by simply turning off the 5V supply to the payload board. Similar to previous tests, once the power supply was reconnected, spurious frequency values started coming through over the SPI lines<sup>16</sup>. The issue had to resolved by power cycling the payload. Meanwhile, the temperature readings were seemingly accurate and sensible throughout this episode (Figure C.9). This situation was resolved by power cycling the payload board and restoring all electrical connections. A potential solution to this problem rests in executing passive mode using the method described in section 5.3.

<sup>16</sup>These values oscillated between two extremes repeatedly, from 0 Hz to about 200-300 kHz

### 5.6.6. Limitations and assumptions

The following limitations and assumptions were associated with the test, which may have introduced minor uncertainties and errors in the test results:

- The pencil beam was considered to be homogeneous over its entire cross-section and that this cross-section engulfed the entire sensitive volume of the FGDOS. It was also assumed that the pencil beam delivered a relatively constant dose rate over the duration of each run.
- The alignment of the DUT w.r.t the pencil beam path was considered sufficiently accurate and any alignment errors were neglected. This was checked with the help of a trial run in the beginning of the test.
- The attenuation of the kinetic energy of protons in the pencil beam as they approached the DUT from the beam monitor was neglected. As such, the nominal energy of the beam was taken to be the beam energy at DUT.
- Due to time constraints, a dedicated campaign aimed at characterizing the energy dependence of sensitivity could not be conducted. As such, there are not enough data points in the results presented here to draw statistically significant conclusions about the exact nature of this relationship or to derive a mathematical expression for it. However, best efforts were made to draw inferences about the overall trends in sensitivity such that more targeted tests can be performed in the future.

### 5.6.7. Results & Conclusions

The Radiation Payload performance test gave rise to the following conclusions:

1. The ability of the Radiation Payload prototype to detect and measure ionizing radiation was successfully demonstrated. Hence, major aspects of the design of the payload were verified by testing. The requirements which were verified by this test can be found in the verification matrix (Table 3.4). The corresponding requirements IDs are also stated below for reference:
  - RADPAY-FUNC-1.2
  - RADPAY-FUNC-1.3
  - RADPAY-FUNC-1.4
  - RADPAY-PERF-1.1
  - RADPAY-PERF-1.2
  - RADPAY-PERF-1.4
  - RADPAY-PERF-1.7
  - RADPAY-INT-1.3
2. The characterisation envelope of the FGDOS was extended, especially at very high dose rates and additional proton energies. The dependence of FGDOS sensitivity w.r.t energy and dose rate was investigated with a new chip specimen. It was verified that the sensitivity shows no systematic variation with change in the dose rate. Increasing the beam energy led to higher sensitivities, but the gradient was gentler than previously observed. This suggests that there might be batch variations or TID dependent variations in the energy trend. As noted in previous sections, the energy dependence may be affected by TID aggregation, accounting for the discrepancy in the trends between the payload test and FGDOS radiation characterization (see section 5.1) done previously. It remains to be seen whether the sensitivity depends considerably on the nature of incident radiation particles.
3. The *Rapid Recovery* effect was reproduced with an independent setup and test specimen. The idea that there may be a threshold TID beyond which this phenomenon comes into prominence was advanced. This creates the possibility that the *Rapid Recovery* effect and its ramifications can be avoided for the Radiation Payload, given that the total expected mission dose (from Table 4.3) is lower. However, it should be kept in mind that the flight model of the payload would also have to undergo pre-flight characterisation. So the total TID for characterisation and mission operations should be lower than this speculated *Rapid Recovery* threshold. Moreover, this threshold TID may also be subject to sample and batch variations, however this is yet to be explored given the relatively recent discovery of this phenomenon.
4. The procedure, test levels and analysis executed for the payload performance test provide a useful template for construction of a suite of pre-flight characterisation profiles for the flight model of the Lunar Zebro Radiation Payload. Accordingly, some guidelines and rules of thumb can be laid out

based on the results presented here. For instance, the cumulative TID of the pre-flight characterisation should be restricted such that the flight version of the FGDOS does not have a high probability of crossing the *Rapid Recovery* threshold during the mission. Another salient takeaway is that a pencil beam is highly useful for characterising the FGDOS detector without affecting any other electronic components on the payload boards. Doing this with alternate radiation sources would necessitate the use of custom lead shielding.

5. The observations and results from this test show that it would be feasible as well as useful to have a Ground Model (GM) of the Radiation Payload which can be subjected to additional testing and characterisation efforts and continued char during flight and future. The test also goes to show the importance of obtaining raw measurement data from the payload (as a part of the rover's telemetry) and post-processing it on the ground. The use of onboard processing or modification of FGDOS frequency values should be discouraged.

## 5.7. Environmental Testing

An environmental test campaign was planned in collaboration with Lunar Zebro. The objective of the campaign was to test the engineering model Belka 2 at qualification levels, such that the rover's design could be validated against vibration and launch loads, for electromagnetic interference and compatibility, vacuum, thermal loads and cycling, exposure to lunar regolith and for hardness with respect to the space radiation environment. Since these tests were going to be performed at a system level, the Radiation Payload would be included in the rover such that it would also be exposed to the aforementioned environments, albeit in an integrated form.

Owing to schedule delays experienced by the Lunar Zebro team in functional testing, integration and assembly, the environmental test campaign was delayed beyond the timeline of this thesis project. Nevertheless, a brief description of various tests in the planned campaign that concern the Radiation payload, and the implication of each of these test for the evaluation and validation of the payload design has been provided hereon. Other than these tests, a locomotion test for the rover in a test bed filled with lunar regolith simulant has also been planned. This test would provide indications as to how much exposure the payload Daughterboard would have to electrostatically charged lunar dust particles when the rover is traversing over the lunar surface.

### 5.7.1. Functional Tests

In the environmental test campaign, the Radiation Payload will be subjected to functional tests before, during and after each environmental test, in order to verify the functionality and integrity of the payload hardware and software, under the influence of the harsh (simulated) extremes of the mission environment. The functional tests would also be carried out multiple times within the scope of each environmental test, between successive test runs or in correspondence with different test levels and profiles. It is planned that the functional tests would be commanded and performed by LZ Test Engineers present on site, using a custom developed GUI Based application that facilitates choosing and running various commands from the list provided in Table B.1.

Before the environmental tests, the functional test would also be performed as a part of the integration of the Radiation Payload Subsystem into the Lunar Zebro rover. This would result in the verification of the requirements stated below, which are described in the verification matrix (Table 3.4).

- **RADPAY-INT- 1.1**
- **RADPAY-INT- 1.6**
- **RADPAY-INT- 1.8**
- **RADPAY-INT- 1.9**

### 5.7.2. Mechanical loads: Vibration and Shock Testing

To verify that the rover and its subsystems are able to withstand structural loads caused by launch, separation and deployment, the rover will be tested against mechanical loads. This is planned to be carried out in the form of a random vibration test and a shock test using the shaker tables at Royal NLR <sup>17</sup>.

<sup>17</sup><https://www.nlr.org/capabilities/environmental-testing/>

This test would result in the verification of the following requirement(s):

- **RADPAY-RAMS-1.3**

### **5.7.3. Thermal-Vacuum Test**

A thermal vacuum test has been planned to check the survival of the rover and its subsystems under the extreme thermal conditions that it will be exposed to in the mission. Of special interest are the extremely cold conditions at the lunar South pole. Another objective of this test is to validate thermal models such that they can be used to simulate the temperature and heat distribution over the entire rover, under different constraints and operating conditions. The TVAC test would also entail exposure to high vacuum.

Hence, the payload subsystem would also be tested for exposure to vacuum and to check its functional integrity with respect to extreme temperatures and thermal cycling. This test also presents an opportunity to significantly extend the thermal characterisation envelope of the FGDOS. The limits of the extended envelope would essentially be the temperature extremes that would be faced during the mission. In addition to the Main Payload PCB, the Payload Daughterboard prototype would also be included in the TVAC test setup. This would be done in an improvised manner, with the Daughterboard mounted underneath the rover's Solar Panel Plate (SPP) and its readout being transmitted and recorded over a separate DAQ channel. This addendum to the TVAC test was proposed in order to mitigate one of the critical risks that were identified in Table D.1 during the preliminary risk analysis for the Radiation Payload.

The TVAC test would enable the verification of the system requirements stated below, which are described in the verification matrix (Table 3.4).

- **RADPAY-RAMS-1.4**
- **RADPAY-RAMS-1.6**
- **RADPAY-RAMS-1.7**

### **5.7.4. Radiation Hardness Assurance**

To ensure that the rover and its subsystems can survive exposure to the space radiation environment during the mission, a radiation hardness assurance test has been planned. The scope of the tests has not been finalized, but early indications are that the test could be split into system level testing under mixed radiation fields at a facility such as CHARM [66]; supplemented by more conventional tests for TID, SEUs and SELs, against a Co-60 and/or proton source.

Successful completion of the TID, SEU and SEL tests for the Radiation Payload would ensure that it can reliably perform its functions during the entirety of the mission, enabling the fulfillment of the science mission objectives presented in subsection 3.1.2. These tests can also be conducted for the payload on subsystem or component level, if sufficient time and resources are available. Otherwise, system level testing is advisable, provided that intermediate functional testing can be performed in an isolated manner and carefully prepared diagnostic procedures are available in the event of failures or unexpected test outcomes.

From the POV of developing payload capabilities and extending the characterisation envelope of the FGDOS, system level testing under mixed field environments would be extremely interesting. The results from such a test could also be used for partial validation of Monte Carlo radiation transport models of the Radiation Payload, as discussed in section 4.3.

The RHA tests would result in the verification of the system requirements stated below, which are described in the verification matrix (Table 3.4).

- **RADPAY-RAMS-1.1**
- **RADPAY-RAMS-1.2**
- **RADPAY-RAMS-1.8**
- **RADPAY-RAMS-1.9**
- **RADPAY-RAMS-1.10**

# 6 Conclusions

The first half of this chapter presents the conclusions and results of the work performed in this thesis. The research work can be thought of as being directed along three intertwined branches, which are described in the first three sections. The second half of this chapter, i.e. section 6.4 presents a synthesis of the conclusions as a means to answer the research questions which were investigated under the scope of this project.

## 6.1. Radiation Payload Development

In accordance with a systematic V-model based approach, payload systems engineering activities were carried out. The objectives of the science mission were postulated and a mission definition was created. This was followed by identification and analysis of stakeholders and their requirements. This led to the technical system requirements being defined. A summary of the technical system requirements was provided in Table 3.4 with the current status of verification of each requirement. As described in section 5.7, a substantial portion of the *RAMS*, *Functional* and *Performance* requirements will be verified during the upcoming environmental test campaign, at system level. Prior to that, some interface requirements will be verified during integration of the Radiation Payload prototype with Belka-2, the engineering model (EM) of the LZ rover. As for the yet unverified performance requirements, these would be verified in the future with the development of the next iteration i.e. version 2 (V2) of the Radiation Payload, which is envisioned to be the first EM. Front end systems engineering also consisted of the identification and definition of interfaces, the definition and tracking of technical budgets and formation of a work breakdown structure (WBS). Risk management in a qualitative and quantitative manner was also initiated, using a risk register and by identifying the most critical technical risks. The biggest technical challenges for payload development were identified to be: (a) noise reduction in the sensor frequency to enable fine resolution dose measurements on the lunar surface, and (b) thermal survival of the FGDOS module on the Daughterboard.

A high level system architecture of the Radiation Payload subsystem and its relationship with the rover was defined. The concept was turned into a consolidated design which was manifested as the first prototype of the Radiation Payload. Mechanical, electronic and software design and implementation activities were performed to achieve this, as a part of the decomposition phase of the systems engineering process. Mechanical design and verification consisted of geometrical design of the circuit board, the preparation of a CAD model of the prototype and its integration into the CAD assembly of the rover as well as preliminary thermal analysis. Electronic design started with the construction of a system level electronic architecture, followed by breadboarding, circuit design, component selection and PCB design. Software design started with the construction of a system level CDHS architecture, the creation of a functional breakdown. Software development was divided into two parts, the payload subsystem firmware and a driver application intended for the rover's OBC. A comprehensive list of commands and telemetry was drafted and a high level design for the driver App was proposed. Payload operational modes and operational flow were defined in accordance with the mission definition, system architecture and requirements.

The Radiation Payload prototype was manufactured and assembled, including the payload *MAIN* and *Daughter* boards. Preparations were made to enable integration and assembly of this prototype with the rover in the near future. The prototype was subjected to a regime of tests at component and subsystem level to verify proper functioning and operation. This included individual tests of the electronic components as well as readout, interface and communication tests with the payload subsystem firmware. Further tests were carried out to verify the performance of the prototype boards with respect to requirements concerning noise & resolution, power consumption, temperature monitoring, interface and general design. Noise tests revealed the necessity of further noise reduction measures for future versions of the payload and the application of simple filtering techniques for post processing of frequency data. Ultimately, the performance of the Radiation Payload w.r.t. radiation detection and dose measurement was successfully demonstrated using proton beam irradiation.

## 6.2. Radiation Environment Modelling and Transport Simulations

The lunar mission was split into multiple phases, based on the radiation environment and primary source(s). Subsequently, the expected environments and exposure for various phases of the lunar mission were extracted using the SPENVIS and OLTARIS toolkits.

The SPENVIS model yielded the expected exposure and fluxes in Earth orbit and during the cis-lunar transit. The dominance of trapped particles toward dose exposure was confirmed and the nature of exposure from the VABs was shown in terms of the integral and differential fluxes of electrons and protons. The peak as well as total flux from solar protons and solar ions was derived, in addition to the spectrum of GCR protons. Spherical shielding was approximated to about 1.5 mm of Al for the rover chassis, an additional 2 mm for the lunar lander spacecraft, and the dose depth curve for the entire mission was derived, yielding about 30 Gy of exposure. Considering only the rover shielding, the exposure is inflated to about 99.8 Gy, which stands in close agreement with typical guidelines published by launch providers concerning TID [8, 67].

The fluxes, spectra and exposures at the lunar surface for shielded as well as unshielded (boundary) configurations were obtained using OLTARIS. This allowed for the creation of a baseline specification for the expected dose levels during lunar surface operations, which was later used to identify some required performance specs (noise and resolution), that the Radiation Payload must match in order to successfully characterize the radiation fields at the surface of the Moon. Moreover, the results from OLTARIS's transport simulations provided a first order estimate of the influence of the rover's chassis shielding on the dose measurements that would be acquired by the Radiation Payload. The fluxes and dose rates on the lunar surface create a challenge for the Radiation Payload in terms of the demand for precise dose resolution. The influence of lunar regolith on the the radiation environment near the surface can be directly appreciated in the form of albedo and secondary particles. It can be predicted that the occurrence of an SPE during lunar surface operations would result in a large amount of dose exposure which would be detected by the Radiation Payload.

Based on historic data from in-situ measurements, Table 4.4 shows a compilation of the expected radiation dose exposure for various mission phases, corresponding to various sources and environments. The results derived and analyzed in section 4.2 show good agreement with historic data, which serves as validation of the analysis and methods applied here. The results presented in this work could function as inputs for the specification of the radiation environment for Lunar Zebro and it can be used to come up with test levels for radiation hardness assurance as well as the specification of radiation design margins for various subsystems on the rover.

Monte Carlo based radiation transport simulations were performed using the Geant4 simulation toolkit [1]. A simple model of the Radiation Payload consisting of the PCB board and the FGDOS was created. The dose deposited in the detector due to impinging protons was computed. Secondary generation and scattering was observed and the model was validated with experimental results from large field proton beam irradiation at HollandPTC. This baseline model was expanded in a systematic manner, according to the simulation plan depicted in Figure 4.19. A simplified representations of the LZ rover, mainly its Al chassis and solar panel plate were added, in order to create a consolidated model which can be used to predict Radiation payload scientific observations in a wide variety of rover configurations, radiation sources and environmental settings. Accordingly, a rudimentary model of the lunar surface was simulated, which was later augmented by positioning the rover inside a vertical hole lunar lava tube. Due to time constraints and the lack of high performance computing resources, the simulation plan could not be executed entirely in great detail, but a promising foundation has been laid to enable extensive simulation and modelling work in the future. These models can be used to study the influence of lunar terrain features and regolith on the local radiation field in the vicinity of the rover. It is envisioned that the transport models can be expanded to simulate radiation field mapping through spatially distributed dose measurements by a swarm of LZ rovers.

## 6.3. FGDOS Characterization & Testing

Proton beam irradiation tests were performed to characterize the behavior of the FGDOS sensor. A correlation of the sensitivity of the sensor w.r.t. energy of incident radiation was identified, but no meaningful trend could be deciphered between sensitivity and dose rate. An unexpected phenomenon, hereby coined

as *Rapid Recovery* was noticed once a significant amount of TID had been accumulated. While a concrete cause of the *Rapid Recovery* effect could not be singled out, it can be reasonably argued that the effect is concerned with TID induced degradation of the readout n-MOS circuitry of the FGDOS. SEEs were observed and localized to the frequency readout registers of the FGDOS SoC. The noise performance of the sensor under irradiation could not be satisfactorily verified due to limitations on the irradiation duration imposed by the test facility. The cause of noise in sensor frequency and design modifications for noise reduction are topics that require further investigation, along with directed testing to compute the SEE cross-section of the FGDOS. No latches were observed during the entire test campaign. Methods and techniques for compensating for the energy dependence, sensitivity enhancement and discrimination of incident particle species were recommended based on test results as well as recent findings in literature [106, 21].

The Radiation Payload performance test mentioned earlier served as a further extension of the characterisation envelope of the FGDOS. The *Rapid Recovery* phenomenon was recreated and variation of the FGDOS sensitivity at various energy levels and dose rates was explored. This confirmed the inference that FGDOS sensitivity is correlated with the energy of incident radiation, but largely independent of the dose rate. Passive mode operation of the FGDOS was also tested, in addition to the characterisation of degradation induced by TID. This degradation is seen to manifest in the form of sensitivity decay and rise of power consumption of the FGDOS.

Temperature characterization tests were performed to verify that the reference frequency of the FGDOS can be used as a basis for temperature compensation. The tests also revealed additional margins in the allowable temperature range of the FGDOS SoC. The nature and source of measurements made by the internal temperature monitor were also probed. This revealed a gulf between the temperature measured by the internal monitor in contrast with the external surface temperature of the chip package. However, this was later resolved by showing that the temperature measured internally is indicative of the GND pad of the FGDOS chip, which can be successfully probed externally to obtain more precise and accurate temperature measurements using an external sensor.

Based on synthesis of the findings from the previous tests, a simultaneous irradiation and thermal characterization test was conducted to observe the behavior of the sensor in conditions that approximate an accelerated version of the mission conditions for the Radiation Payload. Most importantly, it was shown that the temperature and irradiation effects could be decoupled to a satisfactory extent using simple compensation and data processing techniques. It was found that the quality of compensation suffers in the face of rapid temperature change, thermal cycling and temperature gradient changes due to non-uniform local heat distribution within the body of the FGDOS chip. The lunar mission would presumably involve more gentle temperature gradients, thereby allowing for high quality compensation of FGDOS sensor frequency data. As such, the thermal challenge for the Radiation Payload lies in the absolute temperatures reached at extremities rather than the nature/gradient of temperature change during various mission phases. As long as the payload remains within operational temperatures, scientific observations can be collected reliably. Additional findings from this test led to operational considerations and guidelines for Radiation Payload configuration and operations during flight. All these findings and developments led to advances toward the definition of a pre-flight characterization profile for the Radiation Payload's FGDOS modules in the future.

## 6.4. Research Questions

The main research question for this research was formulated as stated below and decomposed into sub-questions. Hereby, a discussion is presented (based on the conclusions provided earlier) to answer these questions and to bring this study to a meaningful end.

### 6.4.1. RQ-1

**How can the lunar radiation environment be characterized using a miniaturized, low cost instrument that can be operated on board a nano-rover platform such as the Lunar Zebro ?**

On a holistic level, the science scheme shown in Figure 4.1 concisely captures how the Radiation Payload, based on the system architecture and design presented in chapter 3, and the detector testing and characterisation described in chapter 5, can be used to probe and characterize the lunar radiation environment (analyzed in chapter 4), while operating as a part of the Lunar Zebro nano-rover platform. The scheme pre-

sented in Figure 4.1 caters to the overall science goals and significance of the Lunar Zebro Science Mission by illustrating the inputs, processes and results associated with this scientific investigation. The main research question was decomposed into the following sub-questions, which will be individually answered hereon:

### RQ-1.1

#### **What should the characteristics and architecture of the instrument be?**

- *How can the FGDOS sensor be incorporated into the instrument?*
- *How should the instrument be incorporated into the nano-rover?*

By virtue of detailed design and production of a prototype, the architecture and system characteristics were discovered, demonstrated and verified. The FGDOS was incorporated as the primary detector of the Radiation Payload, within the context of a spatially distributed detection architecture, facilitated by supporting electronic components. The Radiation Payload itself was incorporated and integrated into the design of the rover as one of its subsystems. The definition of the payload subsystem, its design, its interfaces and relationship with other rover subsystems and functionality as a part of the larger rover system are explained visually in the form of the system architecture (Figure 3.4), electronic subsystem block diagram (Figure 3.13), the functional breakdown (Figure 3.2) , the S/W functional breakdown (Figure 3.16 and Figure 3.17), the CDHS architecture (Figure 3.15) and the functional flow diagram (Figure 3.3).

### RQ-1.2

#### **Can the instrument, integrated on the nano-rover platform, enable radiation measurement in the influence or vicinity of lunar landscape features such as lava tubes, craters and the lunar regolith?**

In relevant studies presented in literature, it has been shown that the influence of lunar landscape features on the radiation field at the surface can be detected. Given the radiation environment predictions described in chapter 4, the characteristics of the FGDOS, and knowledge about the position of the rover and its surrounding landscape, mission observations can be combined with predictions from radiation environment models and Monte Carlo simulations depicted in section 4.3 to derive rich and detailed results concerning the shielding and modulation properties of different lunar features. This was demonstrated using a series of preliminary radiation transport models in Geant4, ending with a scenario involving the rover inside a vertical hole lava tube on the Moon.

However, more sophisticated modelling efforts are required to obtain concrete results concerning secondary particle types, fluxes, energies and angular distributions in relation to the detection capabilities of the Radiation Payload in the vicinity of interesting lunar terrain features. Concerning more advanced characterisation capabilities such as discrimination of particle species and detection of single ions, further technological developments and design improvements are needed for the FGDOS and Radiation Payload respectively. It is advisable to augment the capabilities of the current Radiation Payload design by virtue of adding sensing elements for detecting thermal neutrons and/or a miniaturized spectrometer, if feasible within the bounds of technical constraints. Similar efforts to combine dosimetry data with radiation transport models in order to enable extensive characterisation of radiation fields in space have been reported recently [79, 75, 84], which provide encouragement for the prospects of the Radiation Payload. This approach needs to be validated experimentally, potentially in a facility that can offer mixed field radiation that approximates the composition of the radiation environment close to the lunar surface.

### RQ-1.3

#### **How can it be used to measure the radiation during various phases of the mission ?**

- *How should the instrument be configured and operated?*

Space radiation environment models were probed using the SPENVIS and OLTARIS toolkits to derive the environment characteristics that are expected for various mission phases that constitute the LZ mission. Based on current estimates that the rover will receive power during transit to the Moon, active time-resolved

measurements can be performed by the Radiation Payload starting in LEO, through VAB passage, cis-lunar transit and in lunar orbit before rover deployment on the surface of the Moon. From an engineering and operations standpoint, the operational flow diagram in Figure 3.19 illustrates how the Radiation Payload should be used during various mission phases, within the overall mission concept of Lunar Zebro or an equivalent mission to the lunar surface. The main part of the mission would involve nominal operations of the Radiation Payload, as the rover traverses and explores the lunar surface before going into hibernation for lunar night. During time intervals where power is unavailable, the passive mode dose measurement capabilities of FGDOS technology can be leveraged to get cumulative TID measurements.

Additionally, some operational considerations that would ensure maximisation of the scientific return from the payload have been provided in chapter 4 and chapter 5. These mainly concern configuration parameters of the FGDOS, design characteristics of the Radiation payload and the nature of the expected radiation environment during each mission phase.

#### **RQ-1.4**

##### **How can such an instrument be used to characterize the effectiveness of shielding of the nano-rover platform?**

First order estimates of the shielding effectiveness of the rover were already made using results from SPENVIS and OLTARIS. For the entire mission, the shielding effectiveness was approximated using the dose depth curve presented in Figure 4.8. A total mission dose of 99.8 Gy at the vehicle boundary (post lander spacecraft shielding) would be reduced to about 30 Gy by the rover's structure, considering a shielding of 1.5 mm of Al for the rover and 2 mm for the lander. At the lunar surface, the shielding was estimated by comparing the unshielded dose and flux at vehicle boundary to the respective shielded values. These preliminary estimates can be refined further using radiation transport simulations presented in section 4.3, which provide another means of studying the effectiveness of shielding w.r.t. to various particle types and intensities. To obtain the most accurate results based on detailed geometric models of the Lunar Zebro rover, a sector shielding analysis is needed.

Having considered these analytical and simulation approaches, the most practical way of characterising the shielding effectiveness in flight is to compare and contrast the mission observations from the sensors belonging to the FGDOS chips located on the chassis housed MAIN Board and the relatively exposed Daughterboard. This is a major driver for the spatially distributed detection architecture of the Radiation Payload.

In summary, a strong foundation for further development and engineering of the Radiation Payload has been established. Characterization and scientific investigation of the FGDOS detector was augmented and extended. The prediction of radiation environments for the Lunar Zebro mission was achieved in a preliminary manner, along with the initiation of radiation transport modelling of the payload which can be developed further along channels aimed at simulating FGDOS sensor response, payload interaction with the space environment and high-fidelity estimation of rover shielding. Collectively, this would enable extensive characterization and monitoring of the ionizing radiation environment on the Moon, leading to the achievement of the scientific objectives of Lunar Zebro's mission.

# 7 Recommendations for Further Work

Following the conclusions presented in the previous chapter, this chapter outlines some recommendations which are proposed for further investigation and development activities concerning the Radiation Payload and this research domain in general.

## 7.1. Lunar Zebro Radiation Payload

### 7.1.1. Payload Design & Development

The current design of the Radiation Payload can be iterated on to produce the next, improved version of the payload. From a systems engineering standpoint, the second iteration i.e. V2 would probably be an engineering model (EM), or another development model (DM). Upgrades can be made along the following channels:

- Similar to the SpaceRadMon instrument by CERN [160], a SRAM memory bank could be included for the detection of thermal neutrons, provided such an addition to the design can be made within power consumption and data handling constraints. This would enable the detection of thermal neutrons present in the lunar albedo [38]. If the architecture of the rover is altered in the future to a sufficient degree so as to allow much more liberal constraints for the payload w.r.t. mass, power and size, a linear energy transfer (LET) spectrometer such as the TimePix [57] would be an extremely valuable addition from a scientific point of view. Similar to the strategy used by RADOM [32], the flux measured using a spectrometer could be combined with measured dose rates to get a rough estimate of the type of incident radiation particles.
- Electronic COTS components which have more radiation testing results and greater radiation tolerance than the components in the current design can be selected. However, this is obviously contingent on the availability of these components in time for production of the next model of the rover and payload.
- The electronic architecture can be updated to include more functionality, redundancy and fault tolerance at the hardware level such that technical risks can be reduced further. At the same time, the importance of extensive testing should be prioritized over the addition of redundancy, since redundancy can lead to the needless addition of complexity to a subsystem which is intended to be simple and robust [16]. Some electrical connections in the rover's umbilical could be attributed to the Payload Subsystem so that it can be reprogrammed and checked out externally (without having to disassemble the rover) during ground based activities such as functional tests and diagnostic runs. In the same vein, more pins and connectors could be added to the MAIN and Daughterboard PCBs to ease testing and debugging.
- Payload S/W can be developed and refined further to add more flexibility and modularity. The code can also be improved in terms of readability and organization. The addition of some fault detection, isolation and recovery software would function to make the design more robust and operationally sound.
- Upon further iteration and examination of the data budget and software of the payload, it could become necessary to add a compression method to the payload data before storing it on the payload onboard memory or sending it to the rover's OBC. Additional security measures such as data encryption could be implemented to make the payload telemetry and commands more secure. It would be favorable however, to coordinate such an implementation with the general security approaches that would be implemented on other subsystems and the CDHS of the rover in general.

The activities carried out in the scope of this thesis were restricted to the Space Segment of the Lunar Zebro mission. However, during the mission, a critical role will be played by the Ground Segment in commanding and monitoring the rover through various mission phases. Most importantly, the Ground Segment will receive telemetry from the rover, including the scientific data gathered by the Radiation Payload. A pipeline needs to be established in order to monitor this data throughout the course of the mission, to store it on

ground and to distribute it to the PI and other scientific investigators. To facilitate the execution of the Lunar Zebro Science Mission and the aforementioned ground segment based functions, an interface or terminal dedicated to the Radiation Payload/Science Mission could be incorporated into the Lunar Zebro Mission Dashboard. This could be used by the rover operators as well as the Payload PI to monitor and oversee the status and operations of the payload.

### 7.1.2. Verification & Validation

In conjunction with design improvements, verification and validation activities also need to be performed along the following channels:

- From a mechanical standpoint, once the launch provider is finalized, more detailed FEM based analyses can be performed to ensure that the payload will structurally withstand flight loads and vibrations. This includes coupled loads analyses that could be performed in an integrated form with the rover and possibly even the lander spacecraft. Once the mission profile, schedule and landing site for the lunar mission is known, more detailed thermal simulations can be performed to verify that the Radiation Payload and its components stay within operating temperature ranges during various mission phases.
- The electronic design of the payload can be further analyzed by building SPICE models of the circuit and simulating the electrical behavior and noise characteristics of various payload components, especially the Floating Gate MOSFET [9]. This can lead to design modifications which would enable enhancement of the sensitivity as well as resolution of the Radiation Payload in terms of dose measurement. This is also relevant for the design of the FGDOS SoC itself, which consists of analog and digital circuits which can be improved further in light of the results presented in this study.
- Environmental testing of future models of the Radiation Payload to qualification and acceptance levels is to be performed to prove that the payload is flight-worthy.
- Further radiation testing can be performed on the Radiation Payload for characterizing its behavior and performance against various sources of ionizing radiation such as heavy ions and neutrons.
- For the flight model of the Radiation Payload, FGDOS chips which have been characterized for radiation and temperature variation in advance should be used. This characterization should preferably be done in a mixed radiation field facility, preferably at system or subsystem level [161]. The radiation testing approach should be tailored toward the COTS components and FGDOS SoC in the Radiation Payload [37].
- It is important to combine and coordinate the Radiation Hardness Assurance (RHA) testing of the Radiation Payload with the Lunar Zebro rover. It would be prudent to perform such testing in an integrated form at system level [161] since the actual radiation environment experienced by the payload will depend on the modulation provided by the rover, in the form of secondary radiation and shielding effects (as discussed in chapter 4).

### 7.1.3. Long Term Applications

Beyond the first Lunar Zebro mission to the Moon, the Radiation Payload also has applications which align with the long-term goals of Lunar Zebro. A few of these envisioned applications are described here in brief:

- The Radiation Payload (or most of its functionality, specifically the FGDOS radiation monitor) could be redesigned such that it is embedded into the main electronics carrier board of the rover, named the Motherboard. Hence, the FGDOS can be used as an in-built radiation monitor for the rover <sup>1</sup>.
- Swarms of Lunar Zebro rovers carrying the Radiation Payload could be used as a distributed system to intelligently probe and map the radiation environment on the Moon. Swarms of semi-autonomous Zebros could rapidly monitor dose rates, TID and other characteristics of the radiation environment at various locations, providing a spatial map of the radiation exposure levels in a certain region on the Moon. This is also applicable to other extra-terrestrial environs where the Zebro may operate, such as near Earth Asteroids (NEAs), comets and Mars [132]. This idea resembles the OLFAR concept that has been proposed to carry out radio astronomy on the Moon [77, 11]. Such swarms could be used for identifying radiation 'storm shelters' and for carrying out scientific measurements aimed at studying

<sup>1</sup>This approach has already been implemented by the Ubotica CogniSAT-XE1 CubeSat Board - <https://ubotica.com/product/specifications/>

the evolution of SPEs and GCRs over time, among other applications.

- The Radiation Payload, in a modified form, could also be used during combined Human - Zebro missions i.e. missions where a group of Zebro rovers is used in collaboration with crew for exploration activities, to detect and warn against radiation hazards. In this scenario, the Radiation Payload derivative would serve as a supplement to personal dosimeters/counters that astronauts are usually provided.
- The application of radiation mapping in hazardous conditions can also be extended to include the terrestrial Zebro. It is relatively straightforward to envision the integration of the Radiation Payload in the terrestrial counterpart of the Lunar Zebro. This would allow the rover to probe inaccessible areas in disaster mitigation and search and rescue scenarios in locations such as nuclear power plants or test facilities, where monitoring radiation levels via robotic means might prove to be instrumental.

## 7.2. Space Radiation Environment Modelling & Simulations

### 7.2.1. Space Environment Models

Concerning theoretical and semi-empirical models of the radiation environment for lunar missions:

- Based on the actual launch date and mission timeline, the modelling of radiation environments can be updated to get more accurate estimates of the expected mission conditions. Solar activity and phase of the solar cycle at that point in time should also be accounted for in order to estimate the modulation of GCRs and trapped particles (in the VABs) by solar wind.
- Newly developed models concerning the interplanetary radiation environment could be used to get a higher fidelity estimate for the cislunar transit phase than SPENVIS's "Near Earth Interplanetary" model. This mainly concerns the exposure due to GCRs.
- Given the nature of the radiation environment in interplanetary space, the findings from the cis-lunar and lunar orbital phases of the mission can also be used to estimate the radiation environment in the vicinity of other extra-terrestrial bodies in the terrestrial neighbourhood, such as Near Earth Asteroids and comets.

### 7.2.2. Radiation Transport Simulations

The following recommendations are made for further work on the aspect of modelling the interaction of radiation particles with the Radiation payload using Monte Carlo based transport simulations:

- According to the updated radiation environment calculations mentioned previously, the source spectra for radiation transport simulations can also be updated in Geant4 to provide more accurate and relevant results concerning the radiation particles incident on the Radiation Payload and the FGDOS sensor.
- The simulations can also be extended to cover a wider range of source particles, more detailed geometry and material definitions as well as various configurations of the rover w.r.t. the position of the solar panel, orientation of the chassis, integration into the deployment device and lander.
- A sophisticated model of the sensor response of the FGDOS could be developed. To this end, more detailed information concerning the physical composition and arrangement of the FGDOS chip would be needed. Such a model could be integrated with the space environment and radiation transport models, to derive a tool which can quickly yield a hypothetical estimate of the data generated by the FGDOS while operating in a wide range of radiation environments as well as exploration targets. If significant research efforts can be invested in this endeavor, a high fidelity 'digital twin' of the Radiation Payload could also be developed. Such a model could be used to predict and verify the performance of the Radiation Payload during experimental activities and the actual mission. This would allow for the prediction of payload measurements based on the predicted environments, rover configuration and mission profile. Such a tool could also be utilized for subsequent research into Lunar radiation monitoring and for payload integration into other spacecrafts.

## 7.3. FGDOS Testing & Characterization

From a scientific and engineering perspective, further research into the FGDOS technology and the product FGD-03F would presumably be a mainstay of research and development activities concerning the Radiation

Payload in the future:

- As mentioned in chapter 5, the ongoing characterization campaign should be extended to expose the FGDOS to irradiation from other sources such as gamma rays (Co-60), neutrons (Cf-252) and mixed fields [23], and to study the characteristics of its response to these sources.
- The behavior and performance of the FGDOS sensor is an area of active research. Collaborative efforts between Sealicon and CERN are currently underway to develop better versions of the FGDOS chip. New techniques to enhance the sensor sensitivity [106] and reduce the noise and power consumption [161] have been recently investigated. These methods and developments could be utilized to improve the performance of the design and simulation models of the Radiation Payload. It has been reported that the FGDOS sensor can be used to detect individual particles/ heavy ions as a modulation of the charge yield within the floating gate MOSFET circuitry [21]. If applied successfully, this technique could tremendously increase the scientific yield of the Radiation Payload. The design of the Radiation Payload could be revised to include these additional capabilities of the FGDOS sensor, as more research on its analog and digital electronic circuits takes shape in the near future.
- Sonification might be used as additional means to analyze and interpret the frequency data acquired during irradiation tests. While sonification was briefly experimented with in this project, visualization was used as the primary mode for perceiving and analyzing logged frequency and temperature data. Further use of sonification techniques may possibly reveal heretofore unnoticed variations in the sensor and reference frequencies, due to the multidimensional nature of audio and the innate ability possessed by humans to filter signals from noise [157]. This may enable further characterization of the sensor behavior<sup>2</sup>.

## 7.4. Outlook Toward the Future

During the period in which this project was carried out, the Engineering Model of the Lunar Zebro, named Belka 2, was being subjected to development testing. This was carried out as a precursor to an environmental test campaign, intended to verify the design against various requirements. This test campaign will include the DM of the Radiation Payload.

The next step for Lunar Zebro is to iterate the system architecture and design, based on the results of the test activities. This will lead to building and testing of an improved Engineering Model (EM) of the rover, followed by the Proto-Flight Model (PFM). It is envisioned that these rovers will include corresponding Engineering and Proto-Flight Models of the Radiation Payload, which will be subjected to qualification and acceptance tests whilst integrated into the rover. Following the EM, a design freeze must be initiated to finalize the design of the Radiation Payload, as well as its interfaces with the Lunar Zebro rover. This is to be done concurrently with back-end systems engineering activities geared toward the final validation and operations phase. Operational plans and considerations need to be finalized in coordination with the Ground Segment and Mission Operations teams of Lunar Zebro and the Mission Operations team of the launch provider/lander company. A *Radiation Payload Operations Manual* is to be drafted which documents and communicates the design and behavior of the Radiation Payload in a concise and easily digestible manner. The operations manual must mainly detail operational considerations related to the payload such as commands, software flows, modes of operations, telemetry description, error codes, troubleshooting methods etc.

During nominal mission operations at the Moon, it would be extremely interesting to note how the measurements vary as the rover traverses over the lunar surface and approaches craters and boulders. The key characteristic to be noticed would be modulation in the captured FGDOS sensor frequency data due to the influence of lunar albedo. Another interesting opportunity is to observe the relative shielding inside a lunar lava tube, as compared to the surface of the Moon. The validation of radiation transport models which were described in section 4.3 is an extremely valuable aspect of the post-processing of payload data. Another important part is to compare payload data with pre-flight predictions of the mission radiation environment, with the approach discussed in section 4.2, using theoretical and semi-empirical models. The mission observations from the Radiation Payload can be published in scientific literature. This is expected to engender

<sup>2</sup>An example of sonified Radiation Payload data can be found at [https://github.com/Abhi-2049/REDMOON/blob/main/Jupyter%20Notebooks/Sonification%20-%20B3\\_4\\_LIM%20-%20edited.wav](https://github.com/Abhi-2049/REDMOON/blob/main/Jupyter%20Notebooks/Sonification%20-%20B3_4_LIM%20-%20edited.wav)

further research and deliberation into monitoring, modelling and prediction of the lunar radiation environment.

While the mission is underway and the Radiation Payload is operational, one of the most scientifically interesting tasks is to compare the data delivered by the chassis-housed Main Board FGDOS sensors with the exposed Daughterboard sensors. Inferences concerning the shielding performance, radiation environments and sensor performance could be extracted as a result. It is expected that during the Lunar Zebro mission, the LRO's microdosimeter instrument would still be operational in lunar orbit [87]. This provides a privileged opportunity for comparison and calibration of the measurements made by the Radiation Payload w.r.t the observations of the teledyne micro-dosimeter [79] onboard the LRO. Comparisons could also be made to the information yielded by other radiation monitoring systems stationed in lunar orbit, such as the RadPC CubeSat currently under development [83]. Similarly, measurements acquired at the lunar surface can be compared against the observations made by other surface bound payloads such as NASA's LETS spectrometer [45]. This would yield validation of Lunar Zebro's Radiation Payload from an independent source in the same operational environment. Conversely, stark disagreements with the measurements made by other instruments in a similar environment would serve to reveal technical issues, subsystem faults or failures on the Radiation Payload. In the vicinity of other spacecrafts or payloads on the Moon, it is important to be mindful of sources of noise and attenuation, including passive shielding or radioactive sources such as RTGs.

Based on the results and lessons learned from the first Lunar Zebro mission, the second generation of the Radiation Payload can be engineered and tested, with an eye on collective sensing and characterisation of radiation fields using rover swarms. Consequently, the operations would also be aimed toward radiation environment and dose mapping using the rapid exploration capabilities of swarms. Such a system would also lend itself to more robustness and reduction of risks w.r.t. the achievement of the science objectives of the Radiation Payload. If the lifetime of the rover platform can be extended, even bigger scientific goals would become achievable. The evolution of solar activity over sizeable chunks of the solar cycle and the resultant modulation of cosmic radiation could be studied. With commercial lunar exploration efforts rising to a crescendo in the next decade, an exciting path lies ahead. Given the simplicity and flexibility of the Radiation Payload concept, design and architecture, it is also possible to deploy it on-board other miniaturized spacecraft platforms such as nano- and pico- scale satellites [131] or autonomous robots aimed at exploration of remote extra-terrestrial locations such as Jovian and Saturnian moons, comets and near Earth Asteroids [151, 49, 71, 114]. Such generalized efforts could rapidly accelerate our understanding of the space radiation environment and lead to the development of effective counter measures and technologies to mitigate its effects, enabling safe and effective robotic as well as crewed space exploration on an unprecedented scale.

# Bibliography

- [1] S. Agostinelli et al. “Geant4—a simulation toolkit”. In: *Nuclear Instruments and Methods in Physics Research Section A: Accelerators, Spectrometers, Detectors and Associated Equipment* 506 (3 July 2003), pp. 250–303. ISSN: 0168-9002. DOI: 10.1016/S0168-9002(03)01368-8.
- [2] Alessandra Menicucci. *AE4S15: Space Embedded Systems*. TU Delft Lecture Slides. Accessed: 2022-05-20. 2020.
- [3] J. Allison et al. “Geant4 developments and applications”. In: *IEEE Transactions on Nuclear Science* 53.1 (2006), pp. 270–278. DOI: 10.1109/TNS.2006.869826.
- [4] Maite Álvarez et al. “Total Ionizing Dose Characterization of a Prototype Floating Gate MOSFET Dosimeter for Space Applications”. In: *IEEE Transactions on Nuclear Science* 60.6 (2013), pp. 4281–4288. DOI: 10.1109/TNS.2013.2288573.
- [5] Arpana. *Units of ionising radiation measurement*. <https://www.arpana.gov.au/understanding-radiation/what-is-radiation/radiation/measurement>. Accessed: 2022-01-24. 2022.
- [6] Makoto Asai. “Geant4 applications in space”. In: *Astroparticle, Particle And Space Physics, Detectors And Medical Physics Applications*. World Scientific, 2008, pp. 719–728.
- [7] Astrobotic. *CUBEROVER PAYLOAD USER’S GUIDE*. Tech. rep. Astrobotic Technology, 2021.
- [8] Astrobotic. *PEREGRINE LUNAR LANDER - PAYLOAD USER’S GUIDE*. Tech. rep. Astrobotic Technology, 2020.
- [9] Rawid Banchuin and Rounsang Chaisricharoen. “The probabilistic modeling of random variation in FG MOSFET”. In: *2016 13th International Conference on Electrical Engineering/Electronics, Computer, Telecommunications and Information Technology (ECTI-CON)*. IEEE, 2016, pp. 1–5.
- [10] E.R Benton and E.V Benton. “Space radiation dosimetry in low-Earth orbit and beyond”. In: *Nuclear Instruments and Methods in Physics Research Section B: Beam Interactions with Materials and Atoms* 184 (1-2 Sept. 2001), pp. 255–294. ISSN: 0168583X. DOI: 10.1016/S0168-583X(01)00748-0. URL: <https://linkinghub.elsevier.com/retrieve/pii/S0168583X01007480>.
- [11] MJ Bentum et al. “A roadmap towards a space-based radio telescope for ultra-low frequency radio astronomy”. In: *Advances in Space Research* 65.2 (2020), pp. 856–867.
- [12] Eric Berger. *Liftoff: Elon Musk and the desperate early days that launched SpaceX*. HarperCollins UK, 2021.
- [13] T Berger et al. “The German Aerospace Center M-42 radiation detector—A new development for applications in mixed radiation fields”. In: *Review of Scientific Instruments* 90.12 (2019), p. 125115.
- [14] Thomas Berger et al. “DOSIS DOSIS 3D: Radiation measurements with the DOSTEL instruments onboard the Columbus Laboratory of the ISS in the years 2009-2016”. In: *Journal of Space Weather and Space Climate* 7 (2017). ISSN: 21157251. DOI: 10.1051/SWSC/2017005.
- [15] J Bouwmeester et al. “Design status of the Delfi-Next nanosatellite project”. In: *61st International Astronautical Congress, Prague, Czech Republic, 27 September-1 October 2010*. Citeseer, 2010.
- [16] Jasper Bouwmeester, Alessandra Menicucci, and Eberhard KA Gill. “Improving CubeSat reliability: Subsystem redundancy or improved testing?” In: *Reliability Engineering & System Safety* 220 (2022), p. 108288.
- [17] Riccardo Brambilla. *Conceptual Thermal Mathematical Rover*. Tech. rep. TU Delft: Lunar Zebro, Oct. 2022.
- [18] M Brucoli et al. “A complete qualification of floating gate dosimeter for CERN applications”. In: *2016 16th European Conference on Radiation and Its Effects on Components and Systems (RADECS)*. IEEE, 2016, pp. 1–4.

- [19] M Brucoli et al. "Investigation on passive and autonomous mode operation of floating gate dosimeters". In: *IEEE Transactions on Nuclear Science* 66.7 (2019), pp. 1620–1627.
- [20] M Brucoli et al. "Investigation on the sensitivity degradation of dosimeters based on floating gate structure". In: *2017 17th European Conference on Radiation and Its Effects on Components and Systems (RADECS)*. IEEE. 2017, pp. 1–4.
- [21] M. Brucoli et al. "Heavy-Ion Charge Yield Measurement by Floating Gate Dosimeters". In: *Radiation and its Effects on Components and Systems (RADECS)* (2021).
- [22] Matteo Brucoli. "Total ionizing dose monitoring for mixed field environments". PhD thesis. Université Montpellier, 2018.
- [23] Matteo Brucoli et al. "Floating gate dosimeter suitability for accelerator-like environments". In: *IEEE Transactions on Nuclear Science* 64.8 (2017), pp. 2054–2060.
- [24] H Bücker. "The Biostack experiments I and II aboard Apollo 16 and 17". In: *Life sciences and space research*. Elsevier, 1974, pp. 43–50.
- [25] Ben Bussey et al. "NASA's Lunar Discovery And Explorartion Program". In: *AGU Fall Meeting Abstracts*. Vol. 2019. 2019, PA54B–11.
- [26] Jarvis A. Caffrey and D. M. Hamby. "A review of instruments and methods for dosimetry in space". In: *Advances in Space Research* 47 (4 Feb. 2011), pp. 563–574. ISSN: 0273-1177. DOI: 10.1016/J.ASR.2010.10.005.
- [27] J. Cesari et al. "Floating gate dosimeter measurements at 4M lunar flyby mission". In: *IEEE Radiation Effects Data Workshop 2015-November* (Nov. 2015). DOI: 10.1109/REDW.2015.7336710.
- [28] Andrew Chaikin. *A man on the Moon: The voyages of the Apollo astronauts*. Penguin UK, 2019.
- [29] Greg Chavers et al. "NASA's Human Landing System: The Strategy for the 2024 Mission and Future Sustainability". In: *2020 IEEE Aerospace Conference*. IEEE. 2020, pp. 1–9.
- [30] Marc Andre Chavy-Macdonald et al. "High-accuracy simulations of the ISS radiation environment and applications to interplanetary manned missions". In: *IEEE Transactions on Nuclear Science* 60 (4 2013), pp. 2427–2434. ISSN: 00189499. DOI: 10.1109/TNS.2013.2273375.
- [31] Cypress Semiconductor Corporation. *Excelon™ LP 8-Mbit (1024K × 8) Serial (SPI) F-RAM*. <http://www.infineon.com/>. CY15B108QN-40SXI. 2016.
- [32] T. P. Dachev et al. "An overview of RADOM results for earth and moon radiation environment on Chandrayaan-1 satellite". In: *Advances in Space Research* 48 (5 Sept. 2011), pp. 779–791. ISSN: 0273-1177. DOI: 10.1016/J.ASR.2011.05.009.
- [33] TP Dachev et al. "Overview of the Liulin type instruments for space radiation measurement and their scientific results". In: *Life sciences in space research* 4 (2015), pp. 92–114.
- [34] S. Danzeca et al. "Characterization and Modeling of a Floating Gate Dosimeter with Gamma and Protons at Various Energies". In: *IEEE Transactions on Nuclear Science* 61.6 (2014), pp. 3451–3457. DOI: 10.1109/TNS.2014.2364274.
- [35] G De Angelis et al. "A radiation safety analysis for lunar lava tubes". In: *Proc. Lunar Plan. Sci. Conf. XXXIII, Lunar and Planetary Institute, Houston TX*. 2002, pp. 1417–1418.
- [36] Lunar Zebro Software Department. *Subsystem Message Layout Proposal*. Tech. rep. TU Delft: Lunar Zebro, 2022.
- [37] Stefano Di Mascio et al. "Towards defining a simplified procedure for COTS system-on-chip TID testing". In: *Nuclear Engineering and Technology* 50.8 (2018), pp. 1298–1305.
- [38] Mikhail I Dobynde and Jingnan Guo. "Radiation Environment at the Surface and Subsurface of the Moon: Model Development and Validation". In: *Journal of Geophysical Research: Planets* 126.11 (2021), e2021JE006930.

- [39] Marco Durante and Francis A. Cucinotta. "Physical basis of radiation protection in space travel". In: *Reviews of Modern Physics* 83 (4 Nov. 2011), p. 1245. ISSN: 00346861. DOI: 10.1103/REVMODPHYS.83.1245/FIGURES/39/MEDIUM. URL: <https://journals.aps.org/rmp/abstract/10.1103/RevModPhys.83.1245>.
- [40] Eberhard Gill. *AEAS12: Space Systems Engineering*. TU Delft Lecture Slides. Accessed: 2022-03-20. 2020.
- [41] *ECSS-E-ST-10-02C – Verification*. Tech. rep. European Cooperation for Space Standardization, 2018.
- [42] *ECSS-E-ST-10-03C – Testing*. Tech. rep. European Cooperation for Space Standardization, 2022.
- [43] *ECSS-E-ST-10-04C – Space environment*. Tech. rep. European Cooperation for Space Standardization, 2020.
- [44] *ECSS-E-ST-10-12C – Methods for the calculation of radiation received and its effects, and a policy for design margins*. Tech. rep. European Cooperation for Space Standardization, 2020.
- [45] Eddie Semones. *Radiation Dose Monitoring for Future NASA Programs*. [https://indico.cern.ch/event/782801/contributions/3471009/attachments/1910315/3156321/ed\\_CERN\\_Symposium.pdf](https://indico.cern.ch/event/782801/contributions/3471009/attachments/1910315/3156321/ed_CERN_Symposium.pdf). Accessed: 2022-01-25. 2019.
- [46] Manfred von Ehrenfried et al. "Spacecraft, landers, rovers and payloads". In: *The Artemis Lunar Program*. Springer, 2020, pp. 48–74.
- [47] Erik Stalcup. *Lunar Thermal Environment*. [https://www.nasa.gov/sites/default/files/atoms/files/ericstalcup\\_lunar\\_thermal\\_environment\\_v2.pdf](https://www.nasa.gov/sites/default/files/atoms/files/ericstalcup_lunar_thermal_environment_v2.pdf). Accessed: 2022-10-14. 2021.
- [48] ESA, BIRA-IASB. *SPENVIS: SPace ENVironment Information System*. <https://www.spennis.oma.be/intro.php>. Accessed: 2022-02-03. 2022.
- [49] Peter Falke et al. "Cosmic ray dose monitoring using RadFET sensors of the Rosetta instruments SESAME and COSIMA". In: *Acta Astronautica* 125 (2016), pp. 22–29.
- [50] Norbert Frischauf et al. "NewSpace: new business models at the interface of space and digital economy: chances in an interconnected world". In: *New Space* 6.2 (2018), pp. 135–146.
- [51] E Garcia-Moreno et al. "Floating gate CMOS dosimeter with frequency output". In: *IEEE Transactions on Nuclear Science* 59.2 (2012), pp. 373–378.
- [52] Danny Gasman. *Payload Concept Design*. Tech. rep. Delft: Lunar Zebro, 2019.
- [53] Danny Gasman. *Phase B: Payload (5600)*. Tech. rep. Delft: Lunar Zebro, Feb. 2021.
- [54] R Gaza et al. "Orion EM-1 Internal Environment Characterization: The Matroshka AstroRad Radiation Experiment". In: *Applied Space Environments Conference (ASEC 2019)*. JSC-E-DAA-TN68618. 2019.
- [55] "S.P. George et al. *The linear energy transfer spectrometer for radiation measurements on the lunar surface*. URL: [https://inis.iaea.org/search/search.aspx?orig\\_q=RN:52087959](https://inis.iaea.org/search/search.aspx?orig_q=RN:52087959).
- [56] Carlos Granja and Stepan Polansky. "Mapping the space radiation environment in LEO orbit by the SATRAM Timepix payload on board the Proba-V satellite". In: *AIP Conference Proceedings*. Vol. 1753. 1. AIP Publishing LLC. 2016, p. 080006.
- [57] Carlos Granja et al. "The SATRAM Timepix spacecraft payload in open space on board the Proba-V satellite for wide range radiation monitoring in LEO orbit". In: *Planetary and Space Science* 125 (2016), pp. 114–129.
- [58] John P Grotzinger et al. "Mars Science Laboratory mission and science investigation". In: *Space science reviews* 170.1 (2012), pp. 5–56.
- [59] H.M. Doss. *Shields Up: What's Holding Up Human Travel to Mars?* <https://www.physicscentral.com/explore/action/shields-up.cfm>. Accessed: 2022-02-10. 2018.
- [60] David M Harland and Ralph Lorenz. *Space systems failures: disasters and rescues of satellites, rocket and space probes*. Springer Science & Business Media, 2007.

- [61] Donald M. Hassler et al. "Mars' surface radiation environment measured with the Mars science laboratory's curiosity rover". In: *Science* 343 (6169 Jan. 2014). ISSN: 10959203. DOI: 10.1126/SCIENCE.1244797/SUPPL\_FILE/HASSLER.SM.PDF. URL: <https://www.science.org/doi/abs/10.1126/science.1244797>.
- [62] D Heynderickx et al. "ESA's space Environment information system (SPENVIS): A web-based tool for assessing radiation doses and effects in spacecraft systems". In: 2005.
- [63] A. G. Holmes-Siedle et al. "RADFET dosimeters in the belt: The Van Allen Probes on day 365". In: *2013 14th European Conference on Radiation and Its Effects on Components and Systems (RADECS)*. 2013, pp. 1–7. DOI: 10.1109/RADECS.2013.6937363.
- [64] D. Hou et al. "Removing the dose background from radioactive sources from active dose rate measurements in the Lunar Lander Neutron Dosimetry (LND) experiment on Chang'E 4". In: *Journal of Instrumentation* 15 (1 Jan. 2020). ISSN: 17480221. DOI: 10.1088/1748-0221/15/01/P01032.
- [65] Sébastien Incerti et al. "The geant4-dna project". In: *International Journal of Modeling, Simulation, and Scientific Computing* 1.02 (2010), pp. 157–178.
- [66] A Infantino et al. "Dose gradient assessment at the new CERN CHARM irradiation facility". In: *Radiation Physics and Chemistry* 155 (2019), pp. 225–232.
- [67] ispace. *PAYLOAD USER'S GUIDE*. Tech. rep. ispace, 2020.
- [68] Jason James. *Detailed Design Document*. Tech. rep. TU Delft: Lunar Zebro, Feb. 2021.
- [69] Bongim Jun et al. "Intercomparison of Ionizing Doses From Space Shielding Analyses Using MCNP, Geant4, FASTRAD, and NOVICE". In: *IEEE Transactions on Nuclear Science* 67.7 (2020), pp. 1629–1636. DOI: 10.1109/TNS.2020.2979657.
- [70] Arijit Karmakar et al. "A Review of Semiconductor Based Ionising Radiation Sensors Used in Harsh Radiation Environments and Their Applications". In: *Radiation* 1.3 (2021), pp. 194–217.
- [71] Jun'ichiro Kawaguchi, Akira Fujiwara, and Tono Uesugi. "Hayabusa—Its technology and science accomplishment summary and Hayabusa-2". In: *Acta Astronautica* 62.10-11 (2008), pp. 639–647.
- [72] Paul Kessler et al. "Artemis Deep Space Habitation: Enabling a Sustained Human Presence on the Moon and Beyond". In: *IEEE Aerospace Conference*.
- [73] Y. Kimoto and A. Jaksic. "RADFET utilization for spacecraft dosimetry". In: *2004 24th International Conference on Microelectronics (IEEE Cat. No.04TH8716)*. Vol. 2. 2004, 657–659 vol.2. DOI: 10.1109/ICMEL.2004.1314914.
- [74] Joseph H King. "Solar proton fluences for 1977-1983 space missions". In: *Journal of Spacecraft and Rockets* 11.6 (1974), pp. 401–408.
- [75] CP Lambropoulos et al. "MIDAS: A Miniature Device for Real-Time Determination of the Identity and Energy of Particles in Space". In: *Space Weather* 18.3 (2020), e2019SW002344.
- [76] Wiley J Larson et al. *Applied space systems engineering*. CEI, 2018.
- [77] Maxim Liefaard et al. "Feasibility study of lufar". In: (2019).
- [78] Robert P Lin. "Observations of lunar shadowing of energetic particles". In: *Journal of Geophysical Research* 73.9 (1968), pp. 3066–3071.
- [79] Chadwick D Lindstrom et al. "Characterization of Teledyne Microdosimeters for Space Weather Applications". In: ().
- [80] M. D. Looper et al. "The radiation environment near the lunar surface: CRaTER observations and Geant4 simulations". In: *Space Weather* 11 (4 Apr. 2013), pp. 142–152. ISSN: 15427390. DOI: 10.1002/SWE.20034.
- [81] Lunar Zebro. *Lunar Zebro | Nano Rover TU Delft*. <https://zebro.space/>. Accessed: 2022-19-01. 2015.
- [82] Matthew Lund and Tatjana Jevremovic. "Enhanced GEANT4 Monte Carlo simulations of the space radiation effects on the International Space Station and Apollo missions using high-performance computing environment". In: *Acta Astronautica* 165 (2019), pp. 219–228.

- [83] Chris Major et al. "Overview of the Upcoming RadPC-Lunar Mission". In: *2021 IEEE Aerospace Conference (50100)*. 2021, pp. 1–7. DOI: 10.1109/AERO50100.2021.9438284.
- [84] M Malich et al. "A miniaturized radiation monitor for continuous dosimetry and particle identification in space". In: *Journal of Instrumentation* 17.01 (2022), p. C01066.
- [85] Maxim Integrated. *MAX3000E/MAX3001E/MAX3002–MAX3012 +1.2V to +5.5V, ±15kV ESD-Protected, 0.1µA, 35Mbps, 8-Channel Level Translators*. <http://www.maximintegrated.com/.MAX3001EEUP+>. 2008.
- [86] Maxim Integrated. *MAX3070E–MAX3079E - +3.3V, ±15kV ESD-Protected, Fail-Safe, Hot-Swap, RS-485/RS-422 Transceivers*. <http://www.maximintegrated.com/.MAX3078EESA+T>. 2016.
- [87] J. E. Mazur et al. "New measurements of total ionizing dose in the lunar environment". In: *Space Weather* 9 (7 July 2011). ISSN: 1542-7390. DOI: 10.1029/2010SW000641. URL: <https://onlinelibrary-wiley-com.tudelft.idm.oclc.org/doi/full/10.1029/2010SW000641>.
- [88] GW McKinney et al. "MCNPX benchmark for cosmic ray interactions with the Moon". In: *Journal of Geophysical Research: Planets* 111.E6 (2006).
- [89] A Menicucci et al. "The Radiation Environment and effects analysis of the LUMIO Mission". In: *72nd International Astronautical Congress (IAC 2021)*. 2021, pp. 1–7.
- [90] William de Meyer. "Characterisation of a Floating Gate Dosimeter for Space Applications". MA thesis. Delft, NL: Delft University of Technology, Mar. 2022.
- [91] HA Moser et al. "Manfred Memorial Moon Mission (4M): development, operations and results of a privately funded low cost lunar flyby". In: (2015).
- [92] Elon Musk. "Making humans a multi-planetary species". In: *New Space* 5.2 (2017), pp. 46–61.
- [93] Masayuki Naito et al. "Radiation dose and its protection in the Moon from galactic cosmic rays and solar energetic particles: At the lunar surface and in a lava tube". In: *Journal of Radiological Protection* 40 (4 Dec. 2020), pp. 947–961. ISSN: 13616498. DOI: 10.1088/1361-6498/ABB120.
- [94] Livio Narici et al. "Radiation measurements performed with active detectors relevant for human space exploration". In: *Frontiers in Oncology* 5 (DEC 2015). Complete overview of Dosimeters in Space<br/>Useful SUMMARY TABLES, p. 273. ISSN: 2234943X. DOI: 10.3389/FONC.2015.00273/BIBTEX.
- [95] NIST. *Stopping-Power Range Tables for Electrons, Protons, and Helium Ions*. <https://www.nist.gov/pml/stopping-power-range-tables-electrons-protons-and-helium-ions>. Accessed: 2022-01-21. 2022.
- [96] John W Norbury et al. "Comparing HZETRN, SHIELD, FLUKA and GEANT transport codes". In: *Life sciences in space research* 14 (2017), pp. 64–73.
- [97] RA Nymmik. "Improved environment radiation models". In: *Advances in Space Research* 40.3 (2007), pp. 313–320.
- [98] RA Nymmik et al. "A model of galactic cosmic ray fluxes". In: *International Journal of Radiation Applications and Instrumentation. Part D. Nuclear Tracks and Radiation Measurements* 20.3 (1992), pp. 427–429.
- [99] Paul O'Brien et al. "The AE9/AP9 Next Generation Radiation Specification Models". In: *38th COSPAR Scientific Assembly* 38 (2010), p. 5.
- [100] JJ Papike, SB Simon, and JC Laul. "The lunar regolith: Chemistry, mineralogy, and petrology". In: *Reviews of Geophysics* 20.4 (1982), pp. 761–826.
- [101] Jennifer L Parsons and Lawrence W Townsend. "Interplanetary crew dose rates for the August 1972 solar particle event". In: *Radiation research* 153.6 (2000), pp. 729–733.
- [102] Walter Peeters. "From suborbital space tourism to commercial personal spaceflight". In: *Acta Astronautica* 66.11 (2010). Private Human Access To Space, pp. 1625–1632. ISSN: 0094-5765. DOI: <https://doi.org/10.1016/j.actaastro.2009.10.026>. URL: <https://www.sciencedirect.com/science/article/pii/S0094576509005165>.

- [103] PF Peyrard et al. "OMERE 2.0 a toolkit for space environment". In: *IEEE Proceedings of the 7th European Conference on Radiation and its Effects on Components and Systems RADECS*. 2003, pp. 639–641.
- [104] Vincent L Pisacane. *The space environment and its effects on space systems*. American Institute of aeronautics and Astronautics, 2008.
- [105] Guenther Reitz. "Characteristic of the radiation field in low earth orbit and in deep space". In: *Zeitschrift fur Medizinische Physik* 18 (4 Dec. 2008), pp. 233–243. ISSN: 09393889. DOI: 10.1016/j.zemedi.2008.06.015.
- [106] Marta Rizzo et al. "An Enhanced Sensitivity Operation Mode for Floating Gate Dosimeters". In: *IEEE Transactions on Nuclear Science* (2022).
- [107] James Rosenthal, Bryan Hayes, and Christopher Mertens. "A silicon micro dosimeter for high-altitude measurements of cosmic radiation". In: *2018 IEEE Aerospace Conference*. IEEE. 2018, pp. 1–7.
- [108] Eddie Ross and William J Chaplin. "The behaviour of galactic cosmic-ray intensity during solar activity cycle 24". In: *Solar physics* 294.1 (2019), p. 8.
- [109] S. Danzeca. *Overview of RDMD activities in CERN Engineering Department*. 2022.
- [110] Chris A Sandridge et al. "On-Line Tool for the Assessment of Radiation in Space—Deep space mission enhancements". In: *2011 Aerospace Conference*. IEEE. 2011, pp. 1–7.
- [111] G Santin et al. "Geant4 for space: Mission simulations and engineering tools". In: *ESA Special Publication*. Vol. 536. 2004, p. 185.
- [112] Kevin Sato. "Science Opportunities on the Lunar Surface and Gateway". In: *International Microgravity Strategic Planning Group*.
- [113] Rana Sayyah, Todd C Macleod, and Fat D Ho. "Radiation-hardened electronics and ferroelectric memory for space flight systems". In: *Ferroelectrics* 413.1 (2011), pp. 170–175.
- [114] Ethan W Schaler et al. "SWIM-Sensing With Independent Micro-Swimmers". In: (2021).
- [115] LZ Scheick, PJ McNulty, and DR Roth. "Dosimetry based on the erasure of floating gates in the natural radiation environments in space". In: *IEEE Transactions on Nuclear Science* 45.6 (1998), pp. 2681–2688.
- [116] N. A. Schwadron et al. "Lunar radiation environment and space weathering from the Cosmic Ray Telescope for the Effects of Radiation (CRaTER)". In: *undefined* 117 (3 2012). ISSN: 01480227. DOI: 10.1029/2011JE003978.
- [117] sealicon. *FGD-03F Floating Gate Dosimeter (FGDOS®) Target Specification*. [https://www.sealiconmicro.com/ficha\\_productos.php?prod=3](https://www.sealiconmicro.com/ficha_productos.php?prod=3). Rev: A0.11. 2022.
- [118] Edward J Semones and Catherine D McLeod. "Current and Future Developments of the Medipix Technology for Space Radiation Monitoring and their Radiation Missions/Platforms". In: *AIAA SPACE and Astronautics Forum and Exposition*. 2017, p. 5155.
- [119] Abhimanyu Shanbhag. *FGDOS Combined Irradiation & Temperature Characterization Test Procedure*. Tech. rep. TU Delft: Lunar Zebro, Aug. 2022.
- [120] Abhimanyu Shanbhag. *FGDOS Radiation Characterization Test Procedure*. Tech. rep. TU Delft: Lunar Zebro, Mar. 2022.
- [121] Abhimanyu Shanbhag. *FGDOS Temperature Characterization Test Procedure*. Tech. rep. TU Delft: Lunar Zebro, Apr. 2022.
- [122] Abhimanyu Shanbhag. *Literature Study: Radiation Measurement on a Lunar Nano-Rover Platform*. 2021.
- [123] Abhimanyu Shanbhag. *Radiation Payload Performance Test Procedure*. Tech. rep. TU Delft: Lunar Zebro, Aug. 2022.
- [124] Kiran Sharma. "Adaptation Study of Zebro as Nano Rover for Lunar Exploration and Demonstration of Locomotion on Simulated Lunar Surface". MA thesis. Delft, NL: Delft University of Technology, Feb. 2018.

- [125] J-H Shue and P Song. "The location and shape of the magnetopause". In: *Planetary and Space Science* 50.5-6 (2002), pp. 549–558.
- [126] Robert C Singleterry Jr et al. "OLTARIS: On-line tool for the assessment of radiation in space". In: *Acta Astronautica* 68.7-8 (2011), pp. 1086–1097.
- [127] Tony C Slaba and Kathryn Whitman. "The Badhwar-O'Neill 2020 GCR Model". In: *Space Weather* 18.6 (2020), e2020SW002456.
- [128] Marshall Smith et al. "The artemis program: An overview of nasa's activities to return humans to the moon". In: *2020 IEEE Aerospace Conference*. IEEE. 2020, pp. 1–10.
- [129] Leonardo Navarenho de Souza Fino et al. "Design of a radiation tolerant system for total ionizing dose monitoring using floating gate and RadFET dosimeters". In: *Journal of Instrumentation* 12 (04 Apr. 2017), p. C04007. ISSN: 1748-0221. DOI: 10.1088/1748-0221/12/04/C04007. URL: <https://iopscience.iop.org/article/10.1088/1748-0221/12/04/C04007>; <https://iopscience.iop.org/article/10.1088/1748-0221/12/04/C04007/meta>.
- [130] Harlan E. Spence et al. "Relative contributions of galactic cosmic rays and lunar proton "albedo" to dose and dose rates near the Moon". In: *Space Weather* 11 (11 Nov. 2013), pp. 643–650. ISSN: 15427390. DOI: 10.1002/2013SW000995.
- [131] Stefano Speretta et al. "Cubesats to pocketqubes: Opportunities and challenges". In: *Proceedings of the 67th International Astronautical Congress (IAC)*. IAF. 2016.
- [132] Neal Stephenson. *Seveneves*. B DE BOOKS, 2016.
- [133] Nicholas Stoffle et al. "Timepix-based radiation environment monitor measurements aboard the International Space Station". In: *Nuclear Instruments and Methods in Physics Research Section A: Accelerators, Spectrometers, Detectors and Associated Equipment* 782 (2015), pp. 143–148.
- [134] Dennis Stone. "A New Era in Space Flight: The COTS Model of Commercial Partnerships at NASA". In: *Proceedings of the 13th Reinventing Space Conference*. Springer. 2018, pp. 117–123.
- [135] Neil Storey. *Electronics: a systems approach*. Pearson Education, 2006.
- [136] Lunar Zebro Assembly Team. *Belka 2 Assembly Plan*. Tech. rep. TU Delft: Lunar Zebro, May 2022.
- [137] JM Muñoz Tejada et al. "Environmental analysis of nanorovers in a swarm for lunar scientific missions". In: *70th International Astronautical Congress, IAC 2019*. 2019.
- [138] Texas Instruments. *LP2981 100-mA Ultra-Low Dropout Regulators With Shutdown*. <http://www.ti.com/>. LP2981-30DBVR. 2016.
- [139] Texas Instruments. *MSP430FR58xx, MSP430FR59xx, and MSP430FR6xx Family User's Guide*. <https://www.ti.com/lit/ug/slau367p/slau367p.pdf>. SLAU367P. 2020.
- [140] Texas Instruments. *MSP430FR5969 LaunchPad™ Development Kit (MSP-EXP430FR5969)*. <https://www.ti.com/lit/ug/slau535b/slau535b.pdf>. SLAU535B. 2015.
- [141] Texas Instruments. *MSP430FR596x, MSP430FR594x Mixed-Signal Microcontrollers*. <https://www.ti.com/lit/ds/symlink/msp430fr5969.pdf>. SLAS704G. 2018.
- [142] Texas Instruments. *TMP100EP DIGITAL TEMPERATURE SENSOR WITH I2C INTERFACE*. <http://www.ti.com/>. TMP100MDBVREP. 2013.
- [143] Craig R Tooley et al. "Lunar Reconnaissance Orbiter mission and spacecraft design". In: *Space Science Reviews* 150.1 (2010), pp. 23–62.
- [144] Allan J Tylka et al. "CREME96: A revision of the cosmic ray effects on micro-electronics code". In: *IEEE Transactions on Nuclear Science* 44.6 (1997), pp. 2150–2160.
- [145] WJ Ubbels et al. "Delfi-C3: a student nanosatellite as a test-bed for thin film solar cells and wireless onboard communication". In: *Proceedings of 2nd International Conference on Recent Advances in Space Technologies, 2005. RAST 2005*. IEEE. 2005, pp. 167–172.
- [146] University of New Hampshire. *CRaTER Data Products*. [https://crater-web.sr.unh.edu/products.php?numplots=1&durationtype=span&ProductG111=doserates&SepGcrAllType111=all&InvCombG111=doserates\\_micro](https://crater-web.sr.unh.edu/products.php?numplots=1&durationtype=span&ProductG111=doserates&SepGcrAllType111=all&InvCombG111=doserates_micro). Accessed: 2022-09-10. 2022.

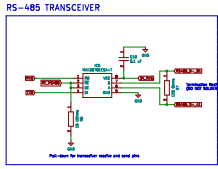
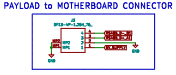
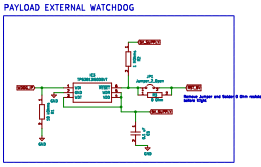
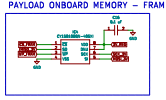
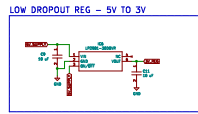
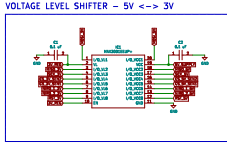
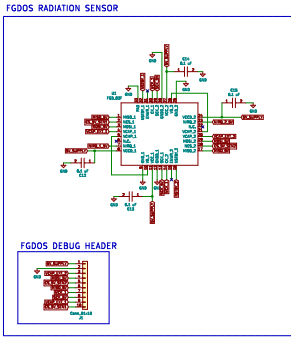
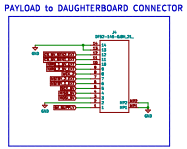
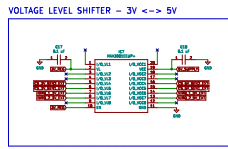
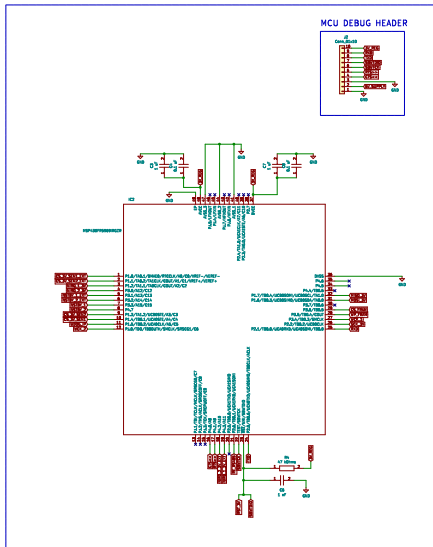
- [147] Miguel Vazquez et al. “Solar Panels for Scientific Missions Using CubeSat Platforms for LEO, MEO and GTO”. In: (2020).
- [148] Sandra Wagner. *The Apollo experience lessons learned for constellation lunar dust management*. Tech. rep. 2006.
- [149] Weller. *WHP 200 infrared preheating plate*. <https://www.weller-tools.com/professional/EUR/en/Professional/Soldering+technology/Accessories/Pre-heating+plates/WHP+200>. Accessed: 2022-08-03. 2022.
- [150] James R Wertz, David F Everett, and Jeffery J Puschell. *Space mission engineering: the new SMAD*. Microcosm Press, 2011.
- [151] Teyen Widdicombe and RA Borrelli. “MCNP modelling of radiation effects of the Dragonfly mission’s RTG on Titan”. In: *Acta Astronautica* 183 (2021), pp. 363–373.
- [152] J-P Williams et al. “The global surface temperatures of the Moon as measured by the Diviner Lunar Radiometer Experiment”. In: *Icarus* 283 (2017), pp. 300–325.
- [153] Jody K Wilson et al. “The first cosmic ray albedo proton map of the Moon”. In: *Journal of Geophysical Research: Planets* 117.E12 (2012).
- [154] Robert F Wimmer-Schweingruber et al. “The Lunar Lander Neutron and Dosimetry (LND) Experiment on Chang’E 4”. In: *Space Science Reviews* 216 (6 Sept. 2020). ISSN: 15729672. DOI: 10.1007/S11214-020-00725-3.
- [155] Kenneth Wood et al. “Introduction to Monte Carlo radiation transfer”. In: *The Astronomy Group of University of St Andrews* (2013).
- [156] Michael A Xapsos, Patrick M O’Neill, and T Paul O’Brien. “Near-Earth space radiation models”. In: *IEEE transactions on nuclear science* 60.3 (2012), pp. 1691–1705.
- [157] A Zanella et al. “Sonification and Sound Design for Astronomy Research, Education and Public Engagement”. In: *arXiv preprint arXiv:2206.13536* (2022).
- [158] C. Zeitlin et al. “Measurements of energetic particle radiation in transit to mars on the mars science laboratory”. In: *Science* 340 (6136 May 2013), pp. 1080–1084. ISSN: 10959203. DOI: 10.1126/SCIENCE.1235989/SUPPL\_FILE/ZEITLIN.SM.PDF. URL: <https://www-science-org.tudelft.idm.oclc.org/doi/abs/10.1126/science.1235989>.
- [159] Shenyi Zhang et al. “First measurements of the radiation dose on the lunar surface”. In: *Science Advances* 6 (39 Sept. 2020). ISSN: 23752548. DOI: 10.1126/SCIADV.AAZ1334/ASSET/C00572EA-6738-4D50-98AB-BB2E3011AEF7/ASSETS/GRAPHIC/AAZ1334-F4.JPEG. URL: <https://www-science-org.tudelft.idm.oclc.org/doi/abs/10.1126/sciadv.aaz1334>.
- [160] Alessandro Zimmaro. “FPGA-MCU design for the performance improvement of a space payload for radiation monitoring”. MA thesis. INFN, Naples, 2020.
- [161] Alessandro Zimmaro et al. “Testing and Validation Methodology for a Radiation Monitoring Systems for Electronics in Particle Accelerators”. In: *IEEE Transactions on Nuclear Science* (2022).

# A Design Documentation

## **A.1. Electrical Schematics**

### **A.1.1. Radiation Payload MAIN V1**

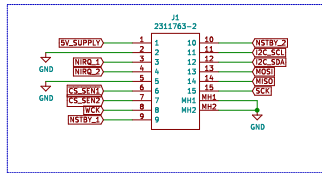
PAYLOAD MCU - MSP430



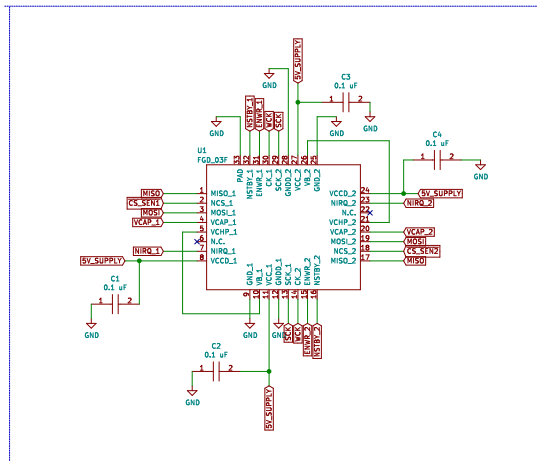
Author	
Design Date	
Proj Name	
Proj Path	
Proj Name	
Proj Path	
Proj Name	
Proj Path	

**A.1.2. Radiation Payload Daughterboard V1**

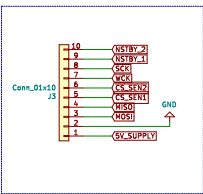
DAUGHTERBOARD - D Sub CONN



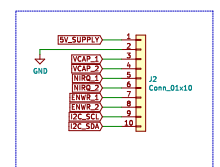
FGDOS SENSOR



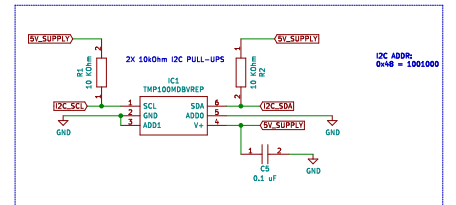
DEBUG HEADER - PRIMARY



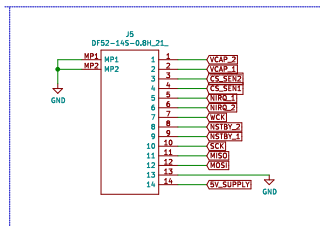
DEBUG HEADER - SECONDARY



EXTERNAL TEMP SENSOR - FOR TESTING



DAUGHTERBOARD CONN - TO PAYLOAD MAIN BOARD

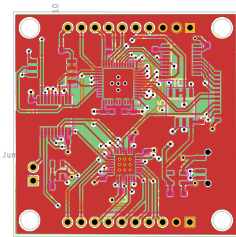


A. Shanbhag  
 Testing Hardware  
 Radiation Payload  
 Lunar Zebra  
 Sheet: /  
 File: Payload\_Daughterboard-V0.1.sch  
**Title: Payload\_Daughterboard\_V1**  
 Size: A3 | Date: 2022-09-30 | Rev:  
 RxCad E.D.A. kicad (6.1.10)-1 | Id: 1/1

**A.1.3. FGD-03F Breakout Board**

The schematics and PCB layout for the FGDOS breakout designed by William de Meyere [90] can be found at - [https://oshwlab.com/Willzyax/fgdos\\_simple](https://oshwlab.com/Willzyax/fgdos_simple)

**A.2. PCB Layouts****A.2.1. Payload MAIN V1**



Author: A. Shanbhag

**Lunar Zebro**

Sheet:

File: Payload\_Main-V0.1.kicad\_pcb

**Title: Payload\_Main**

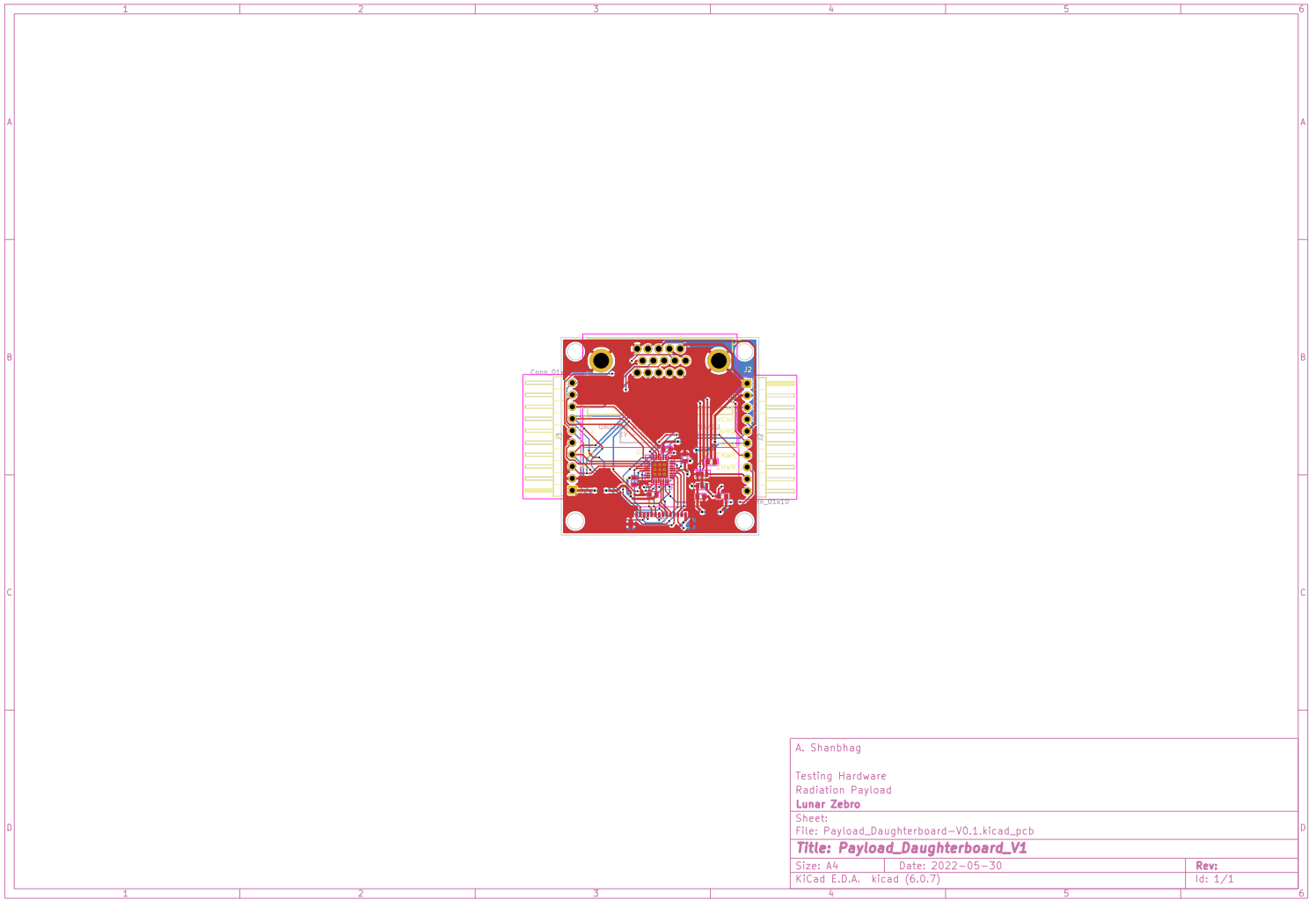
Size: A4 Date: 2022-02-27

KiCad E.D.A. kicad (6.0.7)

**Rev: V0.2**

Id: 1/1

**A.2.2. Payload Daughterboard V1**



A. Shanbhag		
Testing Hardware Radiation Payload <b>Lunar Zebro</b>		
Sheet: File: Payload_Daughterboard-V0.1.kicad_pcb		
<b>Title: Payload_Daughterboard_V1</b>		
Size: A4	Date: 2022-05-30	Rev:
KiCad E.D.A. kicad (6.0.7)		Id: 1/1

# B Software

All software scripts relevant to the Radiation Payload can be found on the Github repository - <https://github.com/Abhi-2049/REDMOON>.

## **B.1. Radiation Payload Telemetry and Commands**

**Table B.1:** Radiation Payload Telecommands and Telemetry List

Command ID	Command	Description	Return	Data Type	Notes
1	GET_RUNTIME	Returns the Radiation Payload ON Time (time since the last power cycle has happened in milliseconds)	Time since last power cycle (ms)	uint32_t	
2	GET_MOSFET_FREQ_1	Returns the Sensor MOSFET frequency of FGDOS Sensor 1	Sensor Frequency 1 (Hz)	uint32_t	Each FGDOS (Floating gate dosimeter) chip which consists of two radiation sensors
3	GET_MOSFET_FREQ_2	Returns the Reference MOSFET frequency of FGDOS Sensor 1	Reference Frequency 1 (Hz)	uint32_t	
4	GET_MOSFET_REF_FREQ_1	Returns the Sensor MOSFET frequency of FGDOS Sensor 2	Sensor Frequency 2 (Hz)	uint32_t	
5	GET_MOSFET_REF_FREQ_2	Returns the Reference MOSFET frequency of FGDOS Sensor 2	Reference Frequency 2 (Hz)	uint32_t	
6	GET_TEMP_1	Returns the Internal Temperature Monitor reading from Sensor 1	Sensor 1 Temperature (digits)	uint8_t	Conversion from digits to deg C done in data post processing
7	GET_TEMP_2	Returns the Internal Temperature Monitor reading from Sensor 2	Sensor 2 Temperature (digits)	uint8_t	
8	GET_RECHARGES_1	Returns the number of times sensor 1 has been recharged	Recharge count 1	uint8_t	
9	GET_RECHARGES_2	Returns the number of times sensor 2 has been recharged	Recharge count 2	uint8_t	
10	GET_RECHARGE_TARGET_FREQ_1	Returns the target recharge frequency of sensor 1	Sensor 1 recharge target (Hz)	uint32_t	
11	GET_RECHARGE_TARGET_FREQ_2	Returns the target recharge frequency of sensor 2	Sensor 2 recharge target (Hz)	uint32_t	
12	GET_RECHARGE_THRESHOLD_FREQ_1	Returns the threshold recharge frequency of sensor 1	Sensor 1 recharge threshold (Hz)	uint32_t	

Table B.1 continued from previous page

Command ID	Command	Description	Return	Data Type	Notes
13	GET_RECHARGE_THRESHOLD_FREQ_2	Returns the threshold recharge frequency of sensor 2	Sensor 2 recharge threshold (Hz)	uint32_t	
14	GET_MOSFET_FREQ_3	Returns the Sensor MOSFET frequency of FGDOS Sensor 3	Sensor Frequency 3 (Hz)	uint32_t	"Sensor 3" refers to the first sensor of the FG-DOS chip that will be on the Radiation Payload Daughterboard i.e. the external Payload board
15	GET_MOSFET_FREQ_4	Returns the Reference MOSFET frequency of FGDOS Sensor 4	Reference Frequency 4 (Hz)	uint32_t	"Sensor 4" refers to the second sensor of the FG-DOS chip that will be on the Radiation Payload Daughterboard i.e. the external Payload board
16	GET_MOSFET_REF_FREQ_3	Returns the Sensor MOSFET frequency of FGDOS Sensor 3	Sensor Frequency 3 (Hz)	uint32_t	
17	GET_MOSFET_REF_FREQ_4	Returns the Reference MOSFET frequency of FGDOS Sensor 4	Reference Frequency 4 (Hz)	uint32_t	
18	GET_TEMP_3	Returns the Internal Temperature Monitor reading from Sensor 3	Sensor 3 Temperature (digits)	uint8_t	
19	GET_TEMP_4	Returns the Internal Temperature Monitor reading from Sensor 4	Sensor 4 Temperature (digits)	uint8_t	
20	GET_RECHARGES_3	Returns the number of times sensor 3 has been recharged	Recharge count 3	uint8_t	
21	GET_RECHARGES_4	Returns the number of times sensor 4 has been recharged	Recharge count 4	uint8_t	
22	GET_RECHARGE_TARGET_FREQ_3	Returns the target recharge frequency of sensor 3	Sensor 3 recharge target (Hz)	uint32_t	
23	GET_RECHARGE_TARGET_FREQ_4	Returns the target recharge frequency of sensor 4	Sensor 4 recharge target (Hz)	uint32_t	

Table B.1 continued from previous page

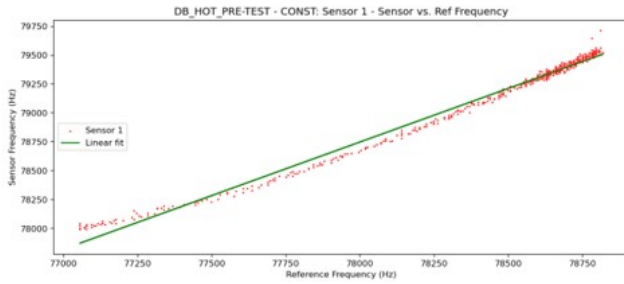
Command ID	Command	Description	Return	Data Type	Notes
24	GET_RECHARGE_THRESHOLD_FREQ <sub>3</sub>	Returns the threshold recharge frequency of sensor 3	Sensor 3 recharge threshold (Hz)	uint32_t	
25	GET_RECHARGE_THRESHOLD_FREQ <sub>4</sub>	Returns the threshold recharge frequency of sensor 4	Sensor 4 recharge threshold (Hz)	uint32_t	
26	GET_MICROCONTROLLER_TEMP	Returns the temperature measured from the internal temperature sensor in the microcontroller that controls the Payload Subsystem	MCU temperature	uint8_t	
27	GET_OPERATIONAL_MODE	Returns the current operational mode of the Payload Subsystem	Payload Mode	uint8_t	
28	GET_ERROR_CODE	Returns a sequence of bits which indicate whether or not the Payload had any error or anomaly	Error Code	uint8_t	Return 0 indicates no errors detected
29	RESET_MICROCONTROLLER	Resets the microcontroller that controls the Payload Subsystem	NA	NA	
30	SEND_PAYLOAD_OB_DATA	Sends the data that is stored in the Radiation Payload's on-board FRAM storage chip	Radiation Payload On-board Data	TBD	The FRAM chip on board the Radiation Payload will store all payload data that is produced until this command is received or the FRAM's storage capacity is reached. Once this command is received, the FRAM will be cleared for new data.

# C Test Results

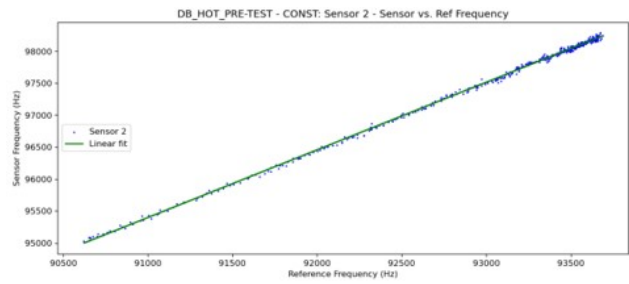
A comprehensive collection of the plots and results from the tests can be found in the Jupyter Notebooks in the repository at - <https://github.com/Abhi-2049/REDMOON/tree/main/Jupyter%20Notebooks>.

## C.1. FGDOS Sensor Characterization

### C.1.1. Simultaneous Irradiation & Temperature Characterization



(a) Sensor 1



(b) Sensor 2

**Figure C.1:** Sensor vs. reference frequency characteristic for temperature compensation with constant heater power

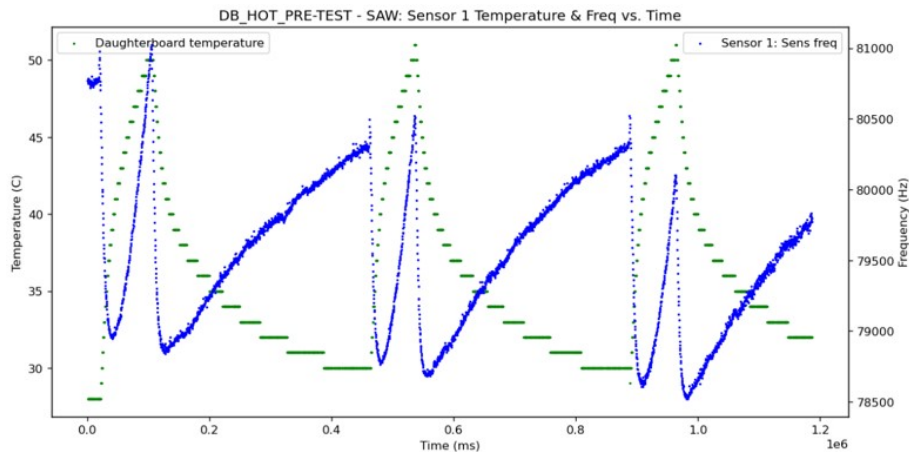


**Figure C.2:** Anomalous behavior of s1 frequency with change in temperature

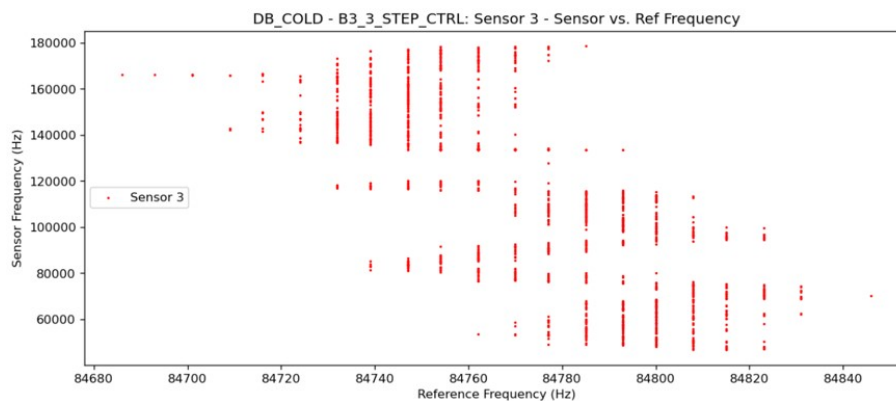


**Figure C.3:** Sensor vs reference frequency relationship under irradiation at constant temperature

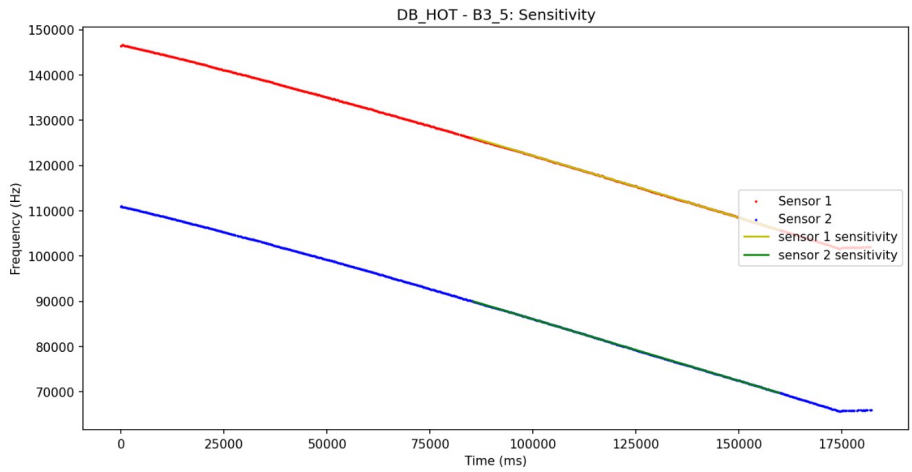


Figure C.4: Post test thermal degradation run

## C.2. Radiation Payload Functional Testing

### C.2.1. Noise, power, temperature

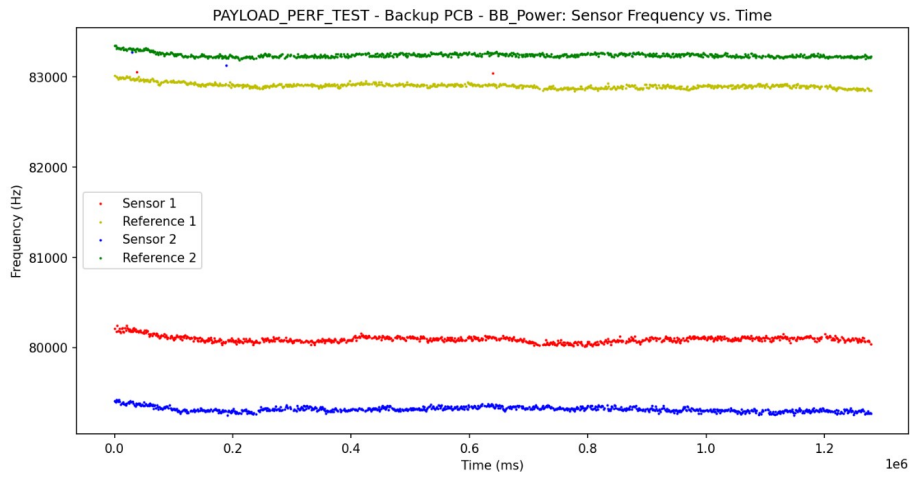


Figure C.5: Time history plot of FGDOS frequencies using LDO supply

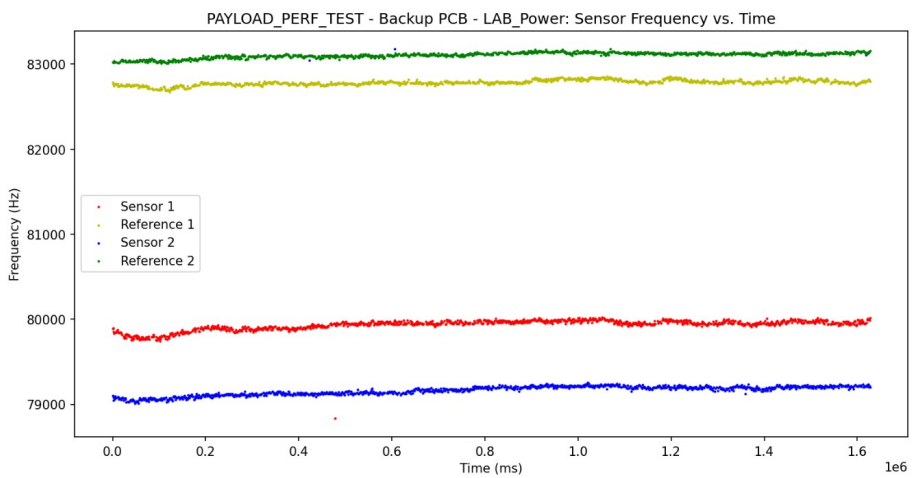


Figure C.6: Time history plot of FGDOS frequencies using lab supply

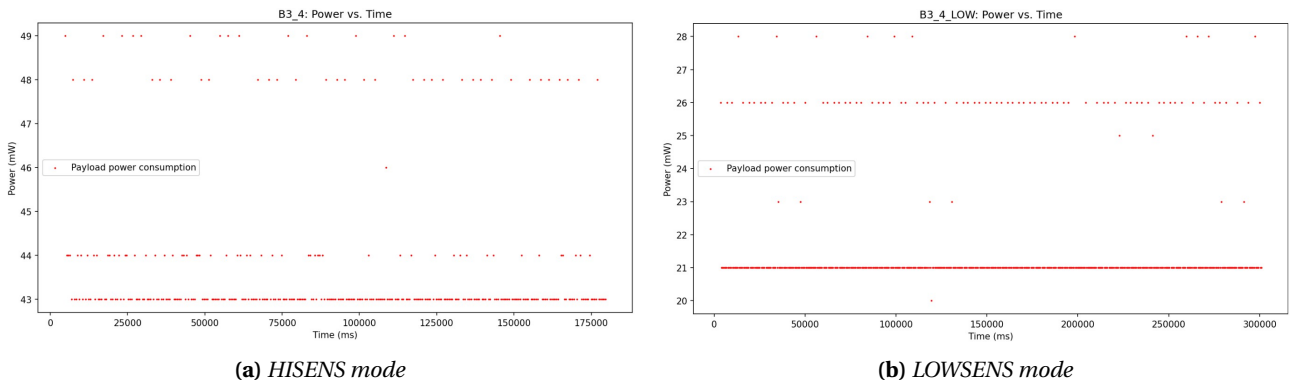


Figure C.7: Payload Performance: Nominal power consumption

### C.3. Radiation Payload Performance Testing: Proton beam Irradiation

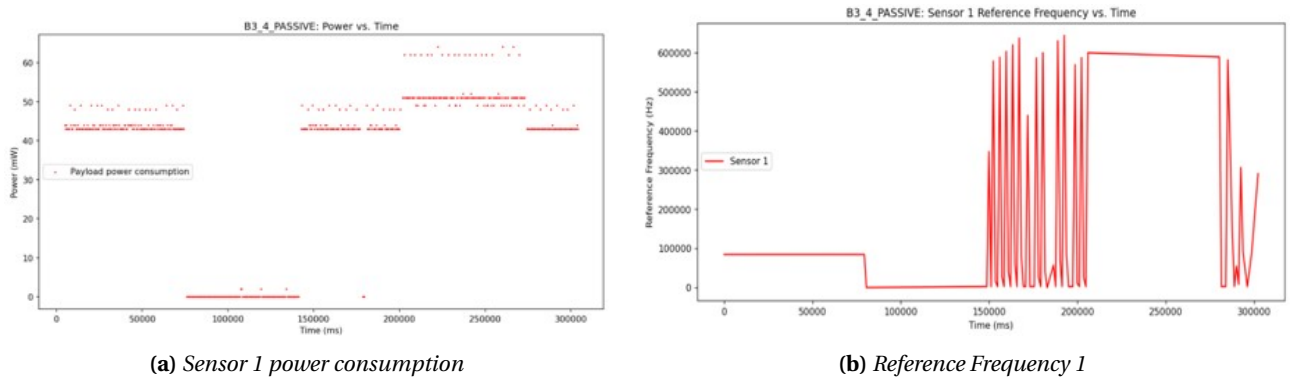


Figure C.8: Payload Performance: Reference frequency and power variation in passive mode

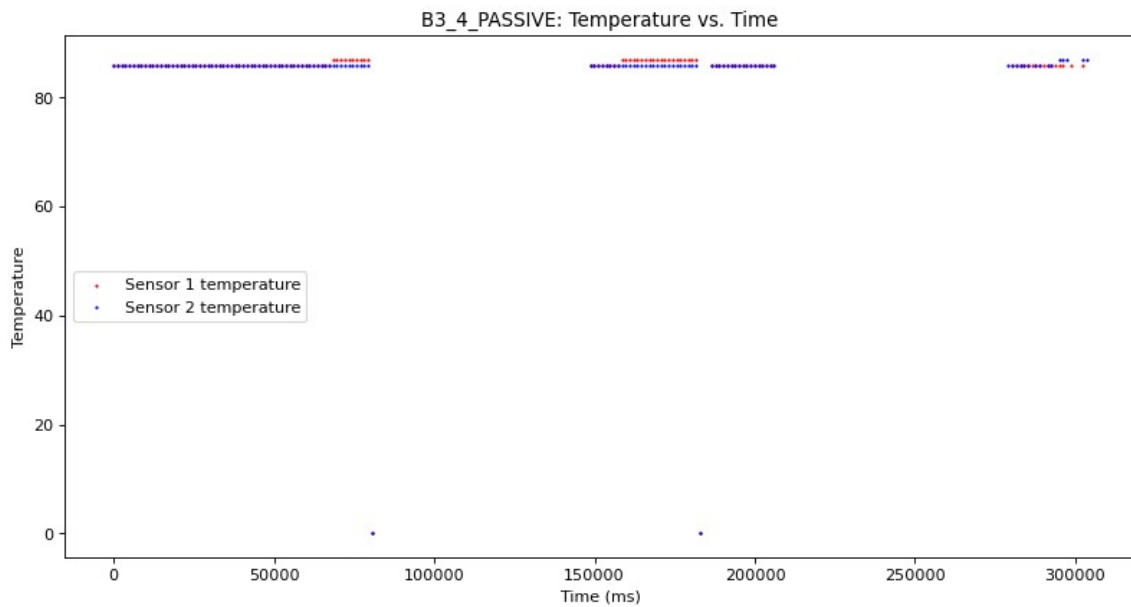
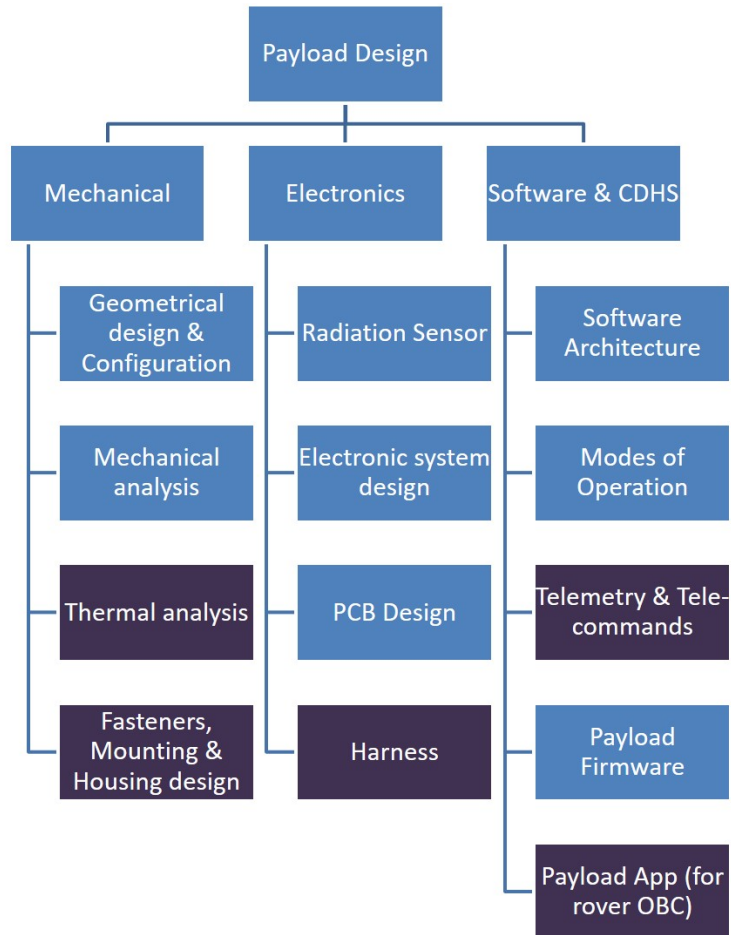


Figure C.9: Payload Performance: Passive mode

# D Systems Engineering Supplement

## D.1. Work Breakdown Structure



**Figure D.1:** *Radiation Payload Work Breakdown Structure*

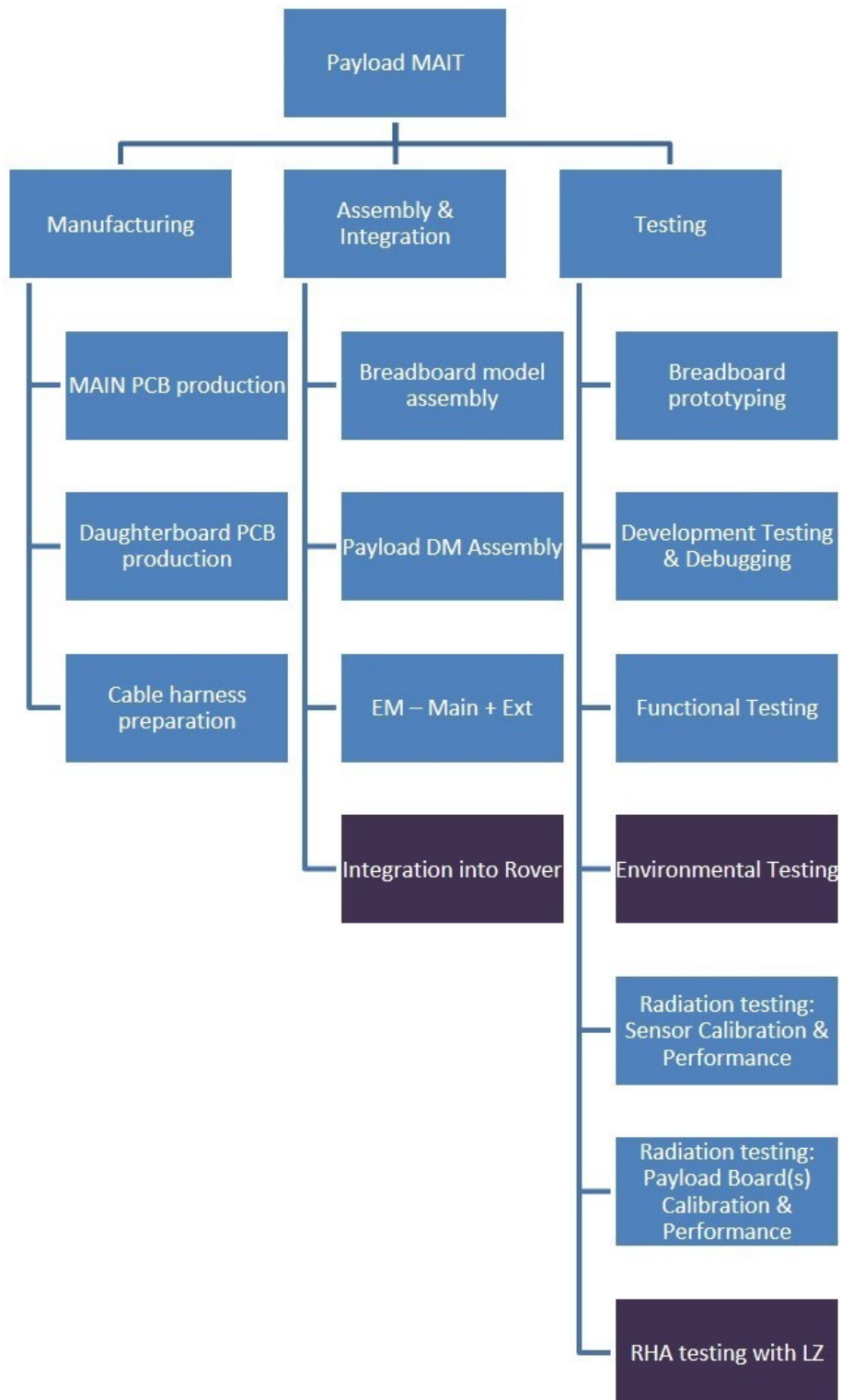


Figure D.2: Radiation Payload Work Breakdown Structure

## D.2. Risk Management

Table D.1: Radiation Payload Risk Register

#	Risk	Relevant part / aspect	Potential Consequence	Severity (1-5)	Potential Cause(s)	Prob. of Occ. (1-5)	Risk Magnitude	Mitigation Strategy (Rem / Red / Acc/ Tran)	Mitigation Measure	Comments
<b>A</b>	<b>Technical</b>									
1	The payload MCU enters a deadlock	MCU S/W	Payload S/W gets stuck	4	Undefined software state; SEE	3	12	Reduce	Watchdog timer resets the MCU	
2	Rover OBC enters a deadlock	OBC S/W	Payload Driver App gets stuck	3	Undefined software state; SEE	3	9	Reduce	Payload MCU S/W runs independently of driver App and OBC. Communication between the two is re-established when the OBC is reset or the issue is resolved	

Table D.1: Radiation Payload Risk Register

#	Risk	Relevant part / aspect	Potential Consequence	Severity (1-5)	Potential Cause(s)	Prob. of Occ. (1-5)	Risk Magnitude	Mitigation Strategy (Rem /Red / Acc/ Tran)	Mitigation Measure	Comments
3	An Electrical discharge causes the FG charge to be altered	FGDOS sensor	Sensor data gets altered	3	Floating / ungrounded metallic parts on Payload PCB, exposure to lunar dust	2	6	Remove	Proper grounding scheme incorporated into Payload Design ESD precautions followed during testing and assembly; Reinitialize the sensor; based on monitoring from GND segment or onboard FDIR	FDIR function to sense abrupt jumps in sensor frequency data can be implemented
4	Single event upsets occur in the sensor module	FGDOS sensor	Sensor data gets corrupted	3	SEE	4	12	Reduce	SEU in sensor data can be detected in GND based post processing of Payload Data	
5	Single event upsets occur in the MCU	MCU	Payload data gets corrupted; Payload S/W enters undefined state	3	SEE	4	12	Reduce	Onboard FDIR functions in Payload S/W; Post processing of Payload data on ground	

Table D.1: Radiation Payload Risk Register

#	Risk	Relevant part / aspect	Potential Consequence	Severity (1-5)	Potential Cause(s)	Prob. of Occ. (1-5)	Risk Magnitude	Mitigation Strategy (Rem /Red / Acc/ Tran)	Mitigation Measure	Comments
6	Single event upsets occur in the onboard Memory (FRAM)	Onboard Memory (FRAM)	Payload data gets corrupted	3	SEE	4	12	Reduce	Onboard FDIR functions in Payload S/W; Post processing of Payload data on ground	
7	Latchup on the MCU	MCU	Electrical damage and possible burnout or Payload components	5	SEL due to incident radiation	2	10	Reduce	Latchup protection provided upstream (on Motherboard)	
8	Total Ionizing Dose effects (TID)	Payload electronics	Sensor degradation; TID effects in other electronic components	3	Prolonged exposure to ionizing radiation; SPEs during mission	3	9	Reduce	Prior assessment and analysis of expected Radiation environments, RHA testing	
9	Ground offset and noise	Electrical ground	Increased electrical noise in Payload signals	2	Improper grounding of Payload	2	4	Remove	Proper grounding scheme to be followed in PCB design	

Table D.1: Radiation Payload Risk Register

#	Risk	Relevant part / aspect	Potential Consequence	Severity (1-5)	Potential Cause(s)	Prob. of Occ. (1-5)	Risk Magnitude	Mitigation Strategy (Rem /Red / Acc/ Tran)	Mitigation Measure	Comments
10	Onboard storage becomes overloaded	Payload Data Storage	A portion of the Payload data is lost	4	Too high sampling rates; error in data budget calculations; Insufficient on-board storage capacity	3	12	Reduce	Preparation of Payload Data Budget; Scheduled downlink of Payload Data; Onboard memory from Motherboard can be used for storing some data	
11	RS485 line polluted with Payload data	RS-485 bus	Rover subsystems cannot communicate on the RS-485 bus connected to the Payload	3	GPIO malfunction or S/W error in MCU	2	6	Remove	Drive enable pin pulled down in transceiver, payload is on listening mode by default	
12	Undesirable switching by PPU	PPU & Motherboard	Payload loses power	3	Malfunction in MOSFET switch and/or PPU	2	6	Transfer	PPU to be functionally tested by LZ Team	
13	The external PCB goes out of operating temperature range of the sensor and electronics	Thermal Environment	External FGDS sensor stops functioning	4	Improper thermal analysis and/or thermal environment specification	5	20	Reduce	Thermal analysis and thermo-vac testing	

Table D.1: Radiation Payload Risk Register

#	Risk	Relevant part / aspect	Potential Consequence	Severity (1-5)	Potential Cause(s)	Prob. of Occ. (1-5)	Risk Magnitude	Mitigation Strategy (Rem /Red / Acc/ Tran)	Mitigation Measure	Comments
14	Outgassing from Payload PCBs	Payload PCBs	Volatile matter deposited on Payload and Rover parts	2	Volatiles or contaminants present on Payload PCBs; PCB material or components outgas	2	4	Reduce	Vacuum bake-out	
15	PCB gets structurally damaged	Mechanical Environment	PCB delamination; Cracked traces leading to broken electrical signals	4	Launch loads and vibrations	3	12	Reduce	Mechanical analysis (FEM) and vibration testing	
16	Sensor gets damaged while recharging	FGDOS sensor	Sensor cannot perform radiation measurements	4	Malfunction of FGDOS internal recharge pump	2	8	Accept	In-built sensor redundancy in FGDOS chip	
17	Poor connections on PCB	PCB design and production	Electrical shorts	5	Poor PCB production quality; workmanship defects; Poor soldering	3	15	Reduce	Reliable supplier chosen for PCB production; PCB testing before and after soldering	

Table D.1: Radiation Payload Risk Register

#	Risk	Relevant part / aspect	Potential Consequence	Severity (1-5)	Potential Cause(s)	Prob. of Occ. (1-5)	Risk Magnitude	Mitigation Strategy (Rem /Red / Acc/ Tran)	Mitigation Measure	Comments
18	Payload connector gets detached from the PCB	Connectors and Harness	Payload stops functioning	5	Poor soldering; vibrations	3	15	Reduce	Vibration testing; Connector joint secured using space grade epoxy adhesive	
19	Incorrect harness preparation and assembly	Harness specification & preparation	Payload / Rover electronics get damaged	5	Human error; Incorrect pinout	2	10	Reduce	Electronic protection included in Payload design	
20	Wrong electrical signals received from Motherboard	Electrical interface with Motherboard	Payload electronics get damaged	4	Incorrect harness preparation and assembly; RS-485 bus malfunction	2	8	Reduce	Integrated functional testing of Payload with the rover;	
<b>B</b>	<b>Schedule</b>									
1	Electronic components are unavailable	Procurement	Redesign of Payload electronics; re-selection of components	4	global chip shortage triggered by the Covid-19 pandemic	4	16	Reduce	Use alternate COTS components	
2	Payload bare PCB not produced in time	Payload Development Schedule	Payload PCBs cannot be assembled	4	PCB design takes too long; issues with PCB production facility	2	8	Reduce	Simplify design and use COTS components	

Table D.1: Radiation Payload Risk Register

#	Risk	Relevant part / aspect	Potential Consequence	Severity (1-5)	Potential Cause(s)	Prob. of Occ. (1-5)	Risk Magnitude	Mitigation Strategy (Rem /Red / Acc/ Tran)	Mitigation Measure	Comments
3	FGDOS sensor delivery takes too long	Procurement	Payload PCBs cannot be assembled	4	Chip shortage, issues on supplier side	2	8	Accept	Order sensors in advance	
4	Radiation testing facilities are unavailable	Payload Testing	Payload and FGDOS sensor characterization and performance testing is not possible	5	High demand for facilities	2	10	Reduce	Plan testing and contact facilities well in advance	
5	Radiation beam time available is less than desired	Payload Testing	Comprehensive Payload and FGDOS sensor characterization and performance testing is not possible	3	High demand for facilities	4	12	Accept	Adapt test plans and procedures	
6	The Payload DM is not produced in time to be assembled into Belka 2	Payload Development Schedule	Overall payload development schedule gets delayed, Payload environmental testing has to be done with the next rover model or standalone	5	Schedule overruns in design and testing of PCBs	3	15	Accept	Monitor Payload development frequently	
<b>C</b>	<b>Cost</b>									

Table D.1: Radiation Payload Risk Register

#	Risk	Relevant part / aspect	Potential Consequence	Severity (1-5)	Potential Cause(s)	Prob. of Occ. (1-5)	Risk Magnitude	Mitigation Strategy (Rem /Red / Acc/ Tran)	Mitigation Measure	Comments
1	The Payload PCB production cost lies outside MSc student budget	Payload Budget	Purchasing of some components is delayed or rendered unfeasible	3	Estimated cost of development and production exceeds MSc budget	5	15	Transfer	Request additional funds from SSE	
2	FGDOS sensor flight model characterization costs too much	Payload Budget	Budget exceeded	5	Sensor behavior is unpredictable w.r.t incident radiation	3	15	Accept	Request additional funds from TU Delft	
3	Test facility costs are too high	Payload Budget	Alternate test facilities have to be selected	4	High demand for facilities	2	8	Accept	Reduce test requirements	
<b>D</b>	<b>Safety</b>									
1	Electrical short occurs on the Payload during integration into rover	Payload Assembly	Injury to assembly or test personnel	2	Flaw in Cable harness preparation; Mistake during rover assembly	2	4	Reduce	Sufficient safety training of assembly and test personnel; Functional checks to be performed during integration	

Table D.1: Radiation Payload Risk Register

#	Risk	Relevant part / aspect	Potential Consequence	Severity (1-5)	Potential Cause(s)	Prob. of Occ. (1-5)	Risk Magnitude	Mitigation Strategy (Rem /Red / Acc/ Tran)	Mitigation Measure	Comments
2	Injury caused while crimping payload connection cables	Payload Cable Harness Assembly	Injury to harness prep personnel	2	Improper usage of crimping tool; Improper assembly of connectors	2	4	Transfer	Payload harness to be prepared professionally by external company	

	NEGLIGIBLE	MINOR	MODERATE	SIGNIFICANT	SEVERE
VERY LIKELY			C-1	A-13, B-1	
LIKELY			A-4, A-5, A-6, B-5		
POSSIBLE			A-2, A-8	A-1, A-10, A-15	A-17, A-18, B-6, C-2
UNLIKELY		A-9, A-14, D-1, D-2	A-3, A-11, A-12	A-16, A-20, B-2, B-3, C-3	A-7, A-19, B-4
VERY UNLIKELY					

Figure D.3: Risk Matrix

### D.3. Radiation Detector Comparison

	<b>RADFETs</b>	<b>FGDOS</b>	<b>Teledyne Microdosimeter</b>	<b>TimePix based Instruments</b>
Type of technology	Detector chip	Detector chip	Radiation measuring instrument	Instruments based on TimePix detector
Principle of Operation	Threshold voltage shift in p-channel MOSFET	Erasure of charge on floating gate in Floating Gate MOSFET	Si detector with ASIC	Pixelated Si detector with ASIC
Detection capabilities	Ionizing radiation	Ionizing radiation from Protons, gamma rays etc	Electrons, protons, gamma rays	Particle identification
Measured Quantity	Absorbed Dose	Absorbed Dose	Absorbed dose	Absorbed Dose, LET
Measurement Characteristics	Resolution: ~200 mGy Range: 200 mGy to 20 kGy	Resolution: 2 mGy Range: 200 uGy to 500 Gy	Resolution: 14 uRad Range: 14 uRads to 40 kRads	Resolution: 2-5 keV <sup>1</sup> Dose range: up to 10 mGy/min LET Range: 0.1 - 500 keV/um
Size & Mass	3 X 3 X 1 mm <sup>2</sup> ~1g	5 X 5 X 0.9 mm 2 g (without interface board)	35 X 25 X 4.5 mm 20 g (without interface board)	160 X 100 X 50 mm [45] 750 g with housing 20 g (detector only) [133]
Power	Very low or zero power	Very low; 20-30 mW @ 5V supply or zero power mode	Medium ; 280 mW @ 28V supply	High power consumption ~2 W; high bias voltage
Cost	Very low cost	Low cost	High cost	High cost
Drawbacks	Low resolution and accuracy	Sensitivity dependence on temperature	Low operating temperature range	High power consumption and size, low temperature range
Integration & Read-out	Output voltage read via electronics	SPI Interface, can be read out with MCU acting as 'master'	Analog & Digital O/P pins; Interface board with ADC needed for integration into spacecraft	Interface board with readout and processing electronics
Special features	0 bias operation	Passive detection	Very high resolution	Particle identification and track capture
Uses in Space	Various spacecrafts in LEO [63], [73]	Lunar 4M [27] TriSat-R [147]	CRaTER [87] Rad-X [107] Rad-PC [83]	ISS REM [133] Proba V [57] NASA LETs [45] HERA Orion [54] BIRD – Orion [54]

**Table D.2:** Summary of some miniaturized radiation detectors

## **D.4. Payload Financial Budget**

The assumptions and considerations which were taken into account while drafting the budget are mentioned hereafter:

1. All estimated costs for the Radiation Payload are included, assuming flight onboard the first Lunar Zebro Mission in late 2023/early 2024
2. Conservative estimates were made regarding design iterations that would be required to reach the final flight ready Radiation Payload
3. Costs for activities that would be performed within the TU Delft or TU Delft associated facilities are marked 'NA' since these might be covered under collaborations and may not require extra expenditure on behalf of the Radiation Payload Developers
4. Some costs that are incurred by the Lunar Zebro team, such as conduction of environmental tests, cable preparation etc. are marked as TBD
5. Some other costs which were not known at the time have been marked as TBC/TBD for re-evaluation in the future

Category	Type	Expense Description	Estimated Cost (in EUR)	Comments
Parts	Electronic Components	FGDOS rad sensor	TBC	check actual cost with AM
		Microcontrollers	140	Qty=20 @ 7 EUR
		Peripheral components	1000	LDO, transceiver, FRAMs, Watchdogs, level shifters; Qty =
	Breadboarding components	Connectors	100	Connectors, cables, header pins, crimp contacts etc; Qty =
		MSP430 Launchpads	100	Qty = 4
		Arduinos	100	Qty = 3
		Others	400	Component breakouts, jumpers, breadboards etc
	PCB Mfg	DM 1	220	Payload Main V1
		DM 2	220	Iteration
		EM 1	250	Payload Main + Daughterboard
		EM 2	250	Iteration
		PFM 1	250	Proto Flight Model
		PFM 2	250	Iteration
		GM	400	Ground Model / Payload Development Board
		Extra design iterations	500	In case of failures or unexpected events
Assembly	Soldering	Payload PCB Soldering	TBD	Done in-house so far, may be outsourced for space grade
	Cable harness	Payload to rover connection	TBC	Prepared by external company for DM, costs handled by LZ
Testing	Sensor Characterization testing	Proton Beam testing @ HPTC	NA	Collaboration with HPTC
	Sensor Characterization testing	Co-60 testing	NA	Collaboration with Reactor institute
	Payload Performance	Proton Beam / other rad source testing	NA	Collaboration with HPTC
	Payload Performance	other rad source	TBD	Other facilities
	Payload Performance	Functional testing	NA	To be carried out at AE and EWI
Payload Environmental testing	TVAC, Vibration etc	TBD	To be carried out with LZ at NLR and other sites	
	Rad hardness assurance	TBD	To be carried out with LZ; payload integrated into rover	
	Delivery to events /launch / test sites	TBD	Not sure about this	
Logistics	Travel to test location	HPTC	NA	
	Travel to test location	Reactor institute Delft	NA	
	Travel to test location	CERN	TBC	
<b>TOTAL</b>			<b>4180</b>	
<b>Total with Margin</b>			<b>5016</b>	
		Margin - 20%		

# E Simulation Results

## E.1. Radiation Environment Modelling

### E.1.1. SPENVIS Methodology

SPENVIS Project: TEST 1	
Model packages	
Planet: Earth	
<b>Coordinate generators</b>	
<b>Radiation sources and effects</b>	
<b>Radiation sources</b>	
<a href="#">Trapped proton and electron fluxes</a>	Standard models ▾
<a href="#">Trapped proton flux anisotropy</a>	
<a href="#">Solar particle peak fluxes</a> (only for SEU)	
<a href="#">Solar particle mission fluxes</a>	
<a href="#">Galactic cosmic ray fluxes</a>	
<a href="#">Shielded flux</a>	
<b>Solar cell radiation damage</b>	
<a href="#">Damage equivalent fluences for solar cells (EQFLUX)</a>	
<a href="#">NIEL based damage equivalent fluences for solar cells (MC-SCREAM)</a>	
<b>Long-term radiation doses</b>	
<a href="#">Ionizing dose for simple geometries</a>	
<a href="#">Non-ionizing energy loss for simple geometries</a>	
<a href="#">Effective dose and ambient dose equivalent</a>	
<b>Single event effects</b>	
<a href="#">Short-term SEU rates and LET spectra</a>	
<a href="#">Long-term SEUs and LET spectra</a>	
<b>Spacecraft charging</b>	
<b>Atmosphere and ionosphere</b>	
<b>Magnetic field</b>	
<b>Meteoroids and debris</b>	
<b>Miscellaneous</b>	
<b>Geant4 Tools</b>	
<b>ECSS Space Environment Standard</b>	

Figure E.1: Project setup in SPENVIS

<b>Trajectory generation:</b>	use orbit generator ▾
<b>Number of mission segments:</b>	3 ▾
<b>Mission end:</b>	total mission duration ▾
<b>Mission duration:</b>	125 days ▾
<b>Satellite orientation:</b>	one axis parallel to the velocity vector ▾
<b>Account for solar radiation pressure:</b>	no ▾
<b>Account for atmospheric drag:</b>	no ▾

Figure E.2: Set up of mission segments

**Segment title:**

Earth Orbit

---

**Orbit type:** general

**Orbit start:** calendar date

01 Jan 2024 00 : 00 : 00

**Representative trajectory duration [days]:** 4

**Altitude specification:** altitude for a circular orbit

**Altitude [km]:** 300

**Inclination [deg]:** 30.0

R. asc. of asc. node [deg w.r.t. gamma50]: 0

**Argument of perigee [deg]:** 0

**True anomaly [deg]:** 0

---

**Output resolution**

1.	60.0	s below	20000.0	km
2.	240.0	s below	80000.0	km
3.	3600.0	s elsewhere		

Figure E.3: Set up of mission segment 1

**Segment title:**

VAB passage

---

**Orbit type:** general

**Orbit start:** end of previous segment

**Representative trajectory duration [days]:** 2

**Altitude specification:** perigee and apogee altitudes

**Perigee altitude [km]:** 300

**Apogee altitude [km]:** 378029

**Inclination [deg]:** 30.0

R. asc. of asc. node [deg w.r.t. gamma50]: 0

**Argument of perigee [deg]:** 0

**True anomaly [deg]:** 0

---

**Output resolution**

1.	60.0	s below	20000.0	km
2.	240.0	s below	80000.0	km
3.	3600.0	s elsewhere		

Figure E.4: Set up of mission segment 2

Segment title:	
Trans-lunar and Lunar Orbit	
<b>Orbit type:</b>	near Earth interplanetary ▾
<b>Orbit start:</b>	end of previous segment ▾
<b>Distance from Sun [AU]:</b>	1.0

Figure E.5: Set up of mission segment 3

Number of mission segments: 3	
<b>Segment 1: Earth Orbit</b>	
Orbit type: general	
Orbit start: 1/1/2024 0:0:0	
Trajectory duration: 4 day(s)	
<b>Segment 2: VAB passage</b>	
Orbit type: general	
Orbit start: end of previous segment	
Trajectory duration: 2 day(s)	
<b>Segment 3: Trans-lunar and Lunar Orbit</b>	
Orbit type: near Earth interplanetary	
Orbit start: end of previous segment	

Figure E.6: Summary of mission segments

Trapped radiation models	
<b>Proton model:</b> AP-8 ▾	<b>Electron model:</b> AE-8 ▾
<b>Model version:</b> solar minimum ▾	<b>Model version:</b> solar maximum ▾
<b>Threshold flux for exposure(/cm2/s):</b> 0.1	<b>do not include</b> ▾ <b>local time variation</b>
	<b>Confidence level:</b> 97.725% ▾
	<b>Threshold flux for exposure(/cm2/s):</b> 0.1
<b>Model developed by:</b>	<b>Model developed by:</b>
	

Figure E.7: Trapped radiation model setup

Solar particle fluxes: Parameters	
<b>Solar particle flux model:</b> CREME-96 ▾	
<b>Ion range:</b> H ▾ to U ▾	
<input type="radio"/> Worst Week <input type="radio"/> Worst Day <input checked="" type="radio"/> Peak 5-minute-averaged fluxes	
<b>Magnetic shielding:</b> on (quiet magnetosphere) <a href="#">edit</a>	

Figure E.8: Solar particle fluxes

### Solar particle fluences: Parameters

<b>Solar particle model:</b> ESP-PSYCHIC (total fluence) <span style="float: right;">▼</span>
<b>Ion range:</b> H <span style="float: right;">▼</span> to U <span style="float: right;">▼</span>
<b>Prediction period:</b> automatic <span style="float: right;">▼</span>
<b>Offset in solar cycle:</b> automatic <span style="float: right;">▼</span>
<b>Confidence level [%]:</b> 97.725
<b>Magnetic shielding:</b> on (quiet magnetosphere) <span style="float: right;">edit</span>

Figure E.9: Solar particle fluences

### GCR spectra: Input parameters

<b>Ion range:</b> H <span style="float: right;">▼</span> to U <span style="float: right;">▼</span>
<b>GCR model at 1 AU:</b> ISO 15390 <span style="float: right;">▼</span>
ISO-15390 standard model + 2 sigma <span style="float: right;">▼</span>
<b>solar activity data:</b> mission epoch <span style="float: right;">▼</span>
<b>Magnetic shielding:</b> on (quiet magn.) <span style="float: right;">edit</span>

Figure E.10: GCR spectra setup

### MFLUX: Parameters

Source		
<input checked="" type="checkbox"/>	Trapped protons	<input checked="" type="checkbox"/>
<input checked="" type="checkbox"/>	Trapped electrons	<input checked="" type="checkbox"/>
<input checked="" type="checkbox"/>	Solar protons	
Shielding		
Total thickness:	1.0 <span style="float: right;">▼</span>	[g/cm <sup>2</sup> ]
Ta to Al mass ratio:	0 <span style="float: right;">▼</span>	[%]
Shielding: 3.705 [mm] Al + 0.000 [mm] Ta		

Figure E.11: Set up of shielded flux from MFLUX

### Ionizing dose models: Parameters

<b>Shielding depths:</b> default values <span style="float: right;">▼</span>
<b>Dose model:</b> SHIELDOSE-2Q <span style="float: right;">▼</span>
<b>Shielding configuration:</b> centre of Al spheres <span style="float: right;">▼</span>
<b>Shield composition:</b> Aluminium <span style="float: right;">▼</span>
<b>Target material:</b> Silicon <span style="float: right;">▼</span>

Figure E.12: Set up of dose depth curve using SHIELDOSE

### E.1.2. SPENVIS: Supplementary Analysis Results

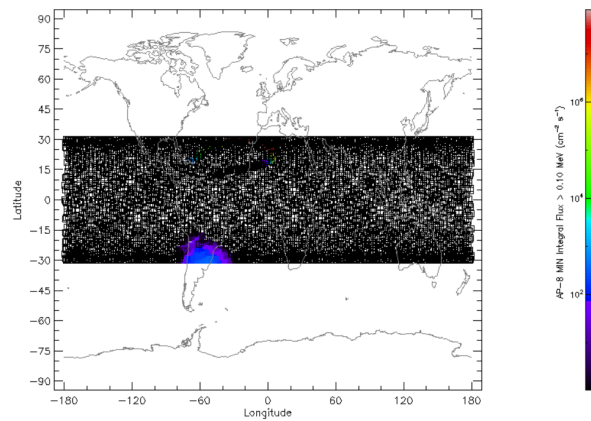


Figure E.13: AP8 MIN: World Map

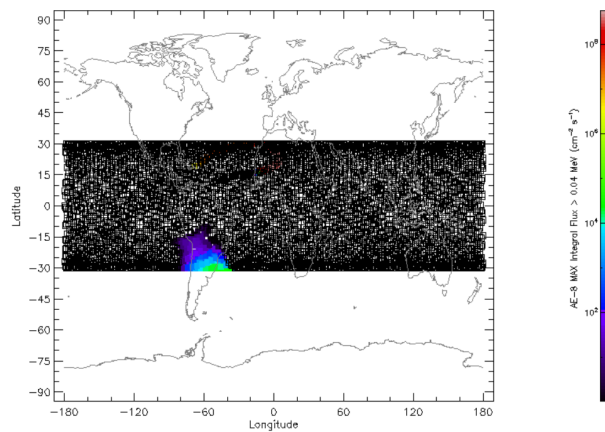


Figure E.14: AE8 MIN: World Map

### E.1.3. OLTARIS Methodology

**New Project** Help

Test\_1

Test of GCR Radiation Environment on the Lunar Surface for assumed LZ Mission Baseline

**Environment Selection** Help | Reference

GCR, Lunar Surface

**Environment Definition: GCR, Lunar Surface** Help | Reference

For GCR environments, the freespace GCR is applied to the upward facing rays and the albedo is computed with a 3D transport through regolith, then applied to the downward facing rays. The albedo calculation can take a couple hours to run, but will be reused in future jobs as long as the GCR parameters haven't changed. Lunar surface environments are run with thickness distributions only. The orientation of the thickness distribution with respect to the lunar surface is defined by specifying a material thickness with a type\_id="-1" for rays in the thickness distribution pointing from the target point toward the surface, or by defining a surface normal (recommended) next to the thickness distribution selection below.

**GCR model** Badhwar-O'Neill 2020  Select Specific Ion

**Mission definition**  Select Historical Solar Min/Max  Enter Date  Enter Fitting Parameter

**Historical min/max** 2010 Solar Min

**Mission duration in days** 14.0

**Save external differential flux for space environment?**  Yes  No

**Geometry** Help

Al Sphere (0.4 g/cm2) X 0 Y 0 Z -1

The boxes indicate the x-, y-, and z- components of a vector used to define the direction perpendicular to the surface in the vehicle coordinate system.

Figure E.15: OLTARIS GCR analysis set up 1

**Response Functions**
[Help](#) | [Reference](#)

Differential Flux/Fluence Differential Flux/Fluence after Transport (Function of Depth, Energy and Isotope)

Dose Silicon

Dose Equivalent Select Quality Factor

Effective Dose Equivalent Whole body quantity, uses anatomical model, also computes Avg. Dose and Dose Equiv. to organs. Background population for NASA Eff. Dose Equiv. and REID.

Gray Equivalent Select Anatomical Model Select Tissue Weights

Risk of Exposure Induced Death (REID) Enter age of exposure for REID (range 20-70):

Linear Energy Transfer (LET) Silicon

CREATE PROJECT
CANCEL

**Figure E.16: OLтарis GCR analysis set up 2**

Project Test\_1 was successfully created.
×

RETURN TO PROJECTS LIST
SUBMIT PROJECT AS JOB
EDIT THIS PROJECT'S ATTRIBUTES

**Project name:** Test\_1 Hint: Click on project name or description to edit in-place.

**Description:** Test of GCR Radiation Environment on the Lunar Surface for assumed LZ Mission Baseline

**Environment:** Galactic Cosmic Ray (GCR), Lunar Surface

GCR Model: BO-20

Event: 2010 Solar Min

Mission Duration: 14.0 days

**Geometry:** Al Sphere (0.4 g/cm2) (1002 rays in thickness distribution)

Thickness values in the thickness distribution are density-based.

**Surface normal:** [0.0, 0.0, -1.0]

**Responses:** Differential Flux / Fluence Dose in Silicon LET in Silicon

**Figure E.17: OLтарis GCR analysis set up 3**

**New Project**
[Help](#)

**Environment Selection**
[Help](#) | [Reference](#)

**Environment Definition: SPE, Lunar Surface**
[Help](#) | [Reference](#)

For SPE environments, the freespace SPE is applied to the upward facing rays and since the albedo contribution is considered negligible, no boundary condition is applied to the downward facing rays. Lunar surface environments are run with thickness distributions only. The orientation of the thickness distribution with respect to the lunar surface is defined by specifying a material thickness with a type\_id="-1" for rays in the thickness distribution pointing from the target point toward the surface, or by defining a surface normal (recommended) next to the thickness distribution selection below.

**SPE type**  Historical SPE  User Defined SPE

Use the check boxes to select one or more events, and numeric input fields to enter a multiplication factor. The multiplication factor multiplies the external flare fluence by the factor specified. If more than one event is selected, they are combined.

<p>1.0 <input type="checkbox"/> Sept 1859 (Carrington - Sept 1989 hard fit)</p> <p>1.0 <input type="checkbox"/> Sept 1859 (Carrington - March 1991 soft fit)</p> <p>1.0 <input type="checkbox"/> Feb 1956 (Webber)</p> <p>1.0 <input type="checkbox"/> Feb 1956 (LaRC)</p> <p>1.0 <input type="checkbox"/> Nov 1960</p> <p>1.0 <input type="checkbox"/> Sum of October 1989 Tylka Band fits</p>	<p>1.0 <input type="checkbox"/> Aug 1972 (LaRC)</p> <p>1.0 <input checked="" type="checkbox"/> Aug 1972 (King)</p> <p>1.0 <input type="checkbox"/> Aug 1989</p> <p>1.0 <input type="checkbox"/> Sept 1989</p> <p>1.0 <input type="checkbox"/> Oct 1989</p>
---	--

**Save external differential flux for space environment?**  Yes  No

**Figure E.18: OLтарis SPE analysis set up 1**

**Geometry** Help

Al Sphere (0.4 g/cm2) X 0 Y 0 Z -1

The boxes indicate the x-, y-, and z- components of a vector used to define the direction perpendicular to the surface in the vehicle coordinate system. It can be indicated either in the Thickness Distribution or defined/changed here. [Link to more info about direction vectors](#)

**Response Functions** Help | Reference

Differential Flux/Fluence Differential Flux/Fluence after Transport (Function of Depth, Energy and Isotope)

Dose Silicon

Dose Equivalent Select Quality Factor

Effective Dose Equivalent Whole body quantity, uses anatomical model, also computes Avg. Dose and Dose Equiv. to organs. Background population for NASA Eff. Dose Equiv. and REID.

Gray Equivalent Select Anatomical Model Select Tissue Weights

Risk of Exposure Induced Death (REID) Enter age of exposure for REID (range 20-70): Age

Linear Energy Transfer (LET) Silicon

CREATE PROJECT
CANCEL

Figure E.19: *OLTARIS SPE analysis set up 2*

### E.1.4. OLTARIS: Supplementary Analysis Results

**Project Summary**

Project: Test\_1

Environment: Galactic Cosmic Ray (GCR), Lunar Surface  
 GCR Model: BO-20  
 Event: 2010 Solar Min  
 Mission Duration: 14.0 days

Geometry: Al Sphere (0.4 g/cm2) (1002 rays in thickness distribution)

Grid engine id: 8443523

TARIS version: 5.0

NOTE: The Lunar albedo is computed without the vehicle in place. x

Figure E.20: *OLTARIS GCR analysis results 1*

**Mission Totals**

Mission Duration = 14.0 Days

Totals	Value	Unit
Dose at point 1	2.881E+00	mGy

Freospace GCR Effects only	Value	Unit
Dose at point 1	2.170E+00	mGy

Lunar Albedo Effects only	Value	Unit
Dose at point 1	7.113E-01	mGy

**Mission Rates**

Rates	Per day	Per year	Unit
Dose at point 1	2.058E-01	7.512E+01	mGy

Freospace GCR Effects only	Per day	Per year	Unit	Link
Dose at point 1	1.550E-01	5.658E+01	mGy	<a href="#">Sphere Viewer</a>

Lunar Albedo Effects only	Per day	Per year	Unit	Link
Dose at point 1	5.080E-02	1.854E+01	mGy	<a href="#">Sphere Viewer</a>

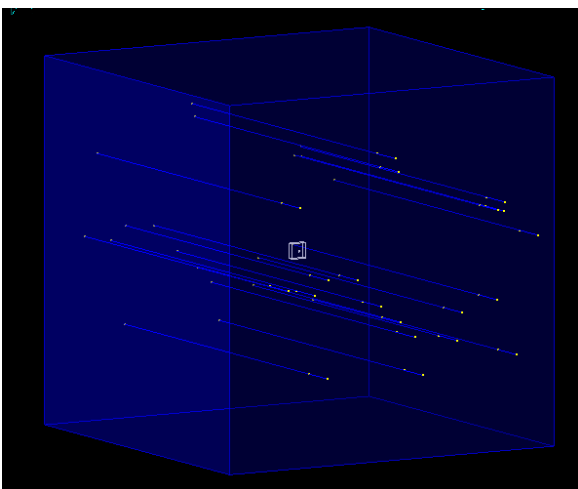
Figure E.21: *OLTARIS GCR analysis results 2*



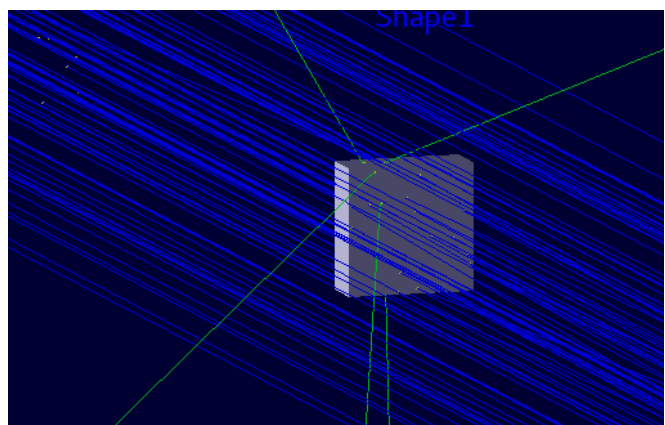
Figure E.22: OLARIS SPE analysis results

## E.2. Radiation Transport Simulations: Supplementary Results

### E.2.1. Basic model setup in Geant4



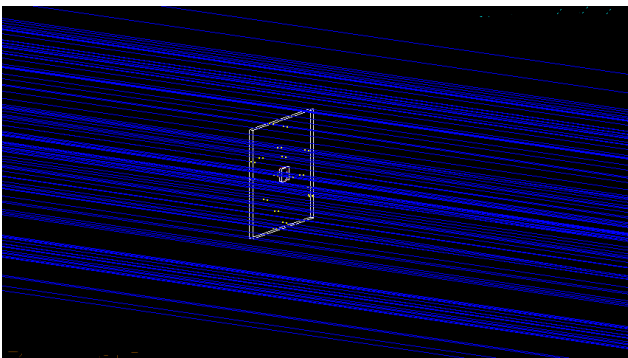
(a) Box shaped envelope with Si box at the centre



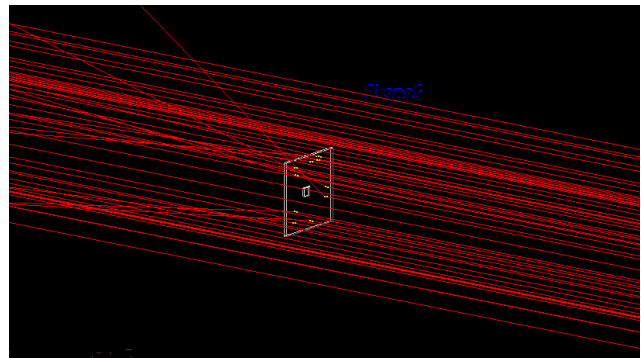
(b) Protons hitting Si box and generation of secondary photons (shown in green)

Figure E.23: Mock simulation setup visualized in Geant4

### E.2.2. Radiation Payload MAIN Board Model



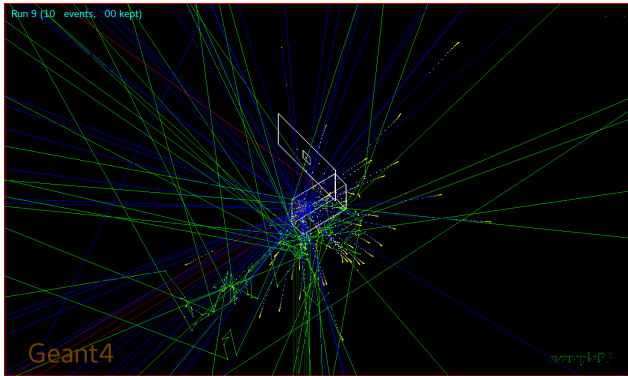
(a) Proton incidence



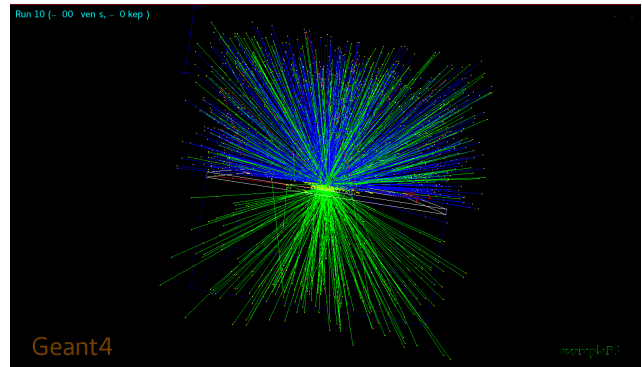
(b) Electron incidence

Figure E.24: Electron and proton incidence on simplified Radiation Payload MAIN

### E.2.3. Rover on a lunar regolith slab



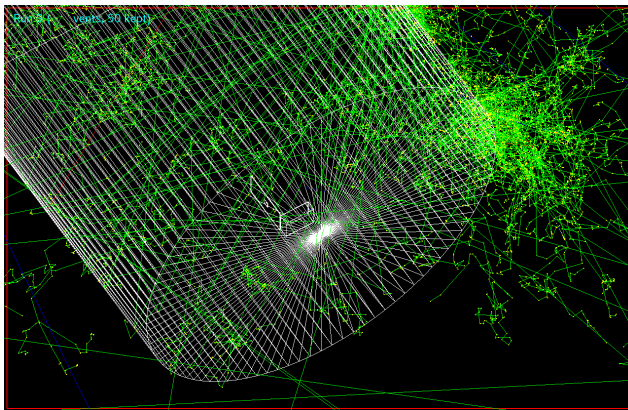
(a) Close-up view of rover



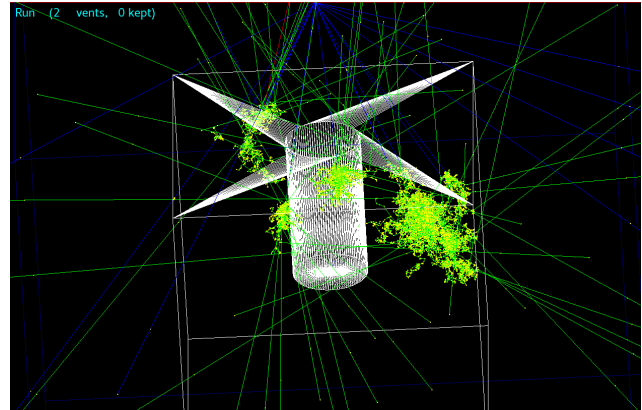
(b) Wide angle view of world volume

Figure E.25: Monte Carlo simulation of the rover on a lunar regolith slab

### E.2.4. Rover in a lunar lava tube



(a) Close-up view of rover



(b) Wide angle view of world volume

Figure E.26: Monte Carlo simulation of the rover inside a lunar lava tube

### E.2.5. Source macro generated in SPENVIS

```

1
2 #
3 #Source definition
4 #
5 # =====
6 # SPENVIS particle source
7 # Project: TEST
8 # title:
9 # Particle: GCR ion
10 # Mission Avg Spectrum: duration= 60.0 Days
11 # =====
12 /gps/particle proton
13 /gps/ene/type Arb
14 /gps/hist/type arb
15 /gps/hist/point 1.000000E+00 5.066761E-08
16 /gps/hist/point 1.100000E+00 6.217840E-08
17 /gps/hist/point 1.200000E+00 7.491190E-08
18 /gps/hist/point 1.400000E+00 1.040470E-07
19 /gps/hist/point 1.600000E+00 1.380793E-07
20 /gps/hist/point 1.800000E+00 1.769848E-07
21 /gps/hist/point 2.000000E+00 2.207409E-07
22 /gps/hist/point 2.200000E+00 2.693224E-07
23 /gps/hist/point 2.500000E+00 3.511421E-07
24 /gps/hist/point 2.800000E+00 4.435677E-07
25 /gps/hist/point 3.200000E+00 2.212812E-07

```

26	/gps/hist/point	3.500000E+00	2.665578E-07
27	/gps/hist/point	4.000000E+00	3.511798E-07
28	/gps/hist/point	4.500000E+00	4.470863E-07
29	/gps/hist/point	5.000000E+00	5.540890E-07
30	/gps/hist/point	5.500000E+00	6.719490E-07
31	/gps/hist/point	6.300000E+00	8.826116E-07
32	/gps/hist/point	7.100000E+00	1.119664E-06
33	/gps/hist/point	8.000000E+00	1.416858E-06
34	/gps/hist/point	9.000000E+00	1.783294E-06
35	/gps/hist/point	1.000000E+01	2.186674E-06
36	/gps/hist/point	1.100000E+01	2.625240E-06
37	/gps/hist/point	1.200000E+01	3.097610E-06
38	/gps/hist/point	1.400000E+01	4.138231E-06
39	/gps/hist/point	1.600000E+01	5.297982E-06
40	/gps/hist/point	1.800000E+01	6.567813E-06
41	/gps/hist/point	2.000000E+01	7.938930E-06
42	/gps/hist/point	2.200000E+01	9.403792E-06
43	/gps/hist/point	2.500000E+01	1.176124E-05
44	/gps/hist/point	2.800000E+01	1.429173E-05
45	/gps/hist/point	3.200000E+01	1.790331E-05
46	/gps/hist/point	3.500000E+01	2.076844E-05
47	/gps/hist/point	4.000000E+01	2.580001E-05
48	/gps/hist/point	4.500000E+01	3.110177E-05
49	/gps/hist/point	5.000000E+01	3.662469E-05
50	/gps/hist/point	5.500000E+01	4.232856E-05
51	/gps/hist/point	6.300000E+01	5.539507E-05
52	/gps/hist/point	7.100000E+01	6.567059E-05
53	/gps/hist/point	8.000000E+01	7.741135E-05
54	/gps/hist/point	9.000000E+01	9.055452E-05
55	/gps/hist/point	1.000000E+02	1.036901E-04
56	/gps/hist/point	1.100000E+02	1.167265E-04
57	/gps/hist/point	1.200000E+02	1.295970E-04
58	/gps/hist/point	1.400000E+02	1.546543E-04
59	/gps/hist/point	1.600000E+02	1.785681E-04
60	/gps/hist/point	1.800000E+02	2.012002E-04
61	/gps/hist/point	2.000000E+02	2.224625E-04
62	/gps/hist/point	2.200000E+02	2.423550E-04
63	/gps/hist/point	2.500000E+02	2.696240E-04
64	/gps/hist/point	2.800000E+02	2.939525E-04
65	/gps/hist/point	3.200000E+02	3.221138E-04
66	/gps/hist/point	3.500000E+02	3.402973E-04
67	/gps/hist/point	4.000000E+02	3.655808E-04
68	/gps/hist/point	4.500000E+02	3.853980E-04
69	/gps/hist/point	5.000000E+02	4.005656E-04
70	/gps/hist/point	5.500000E+02	4.118000E-04
71	/gps/hist/point	6.300000E+02	4.230846E-04
72	/gps/hist/point	7.100000E+02	4.279226E-04
73	/gps/hist/point	8.000000E+02	4.276461E-04
74	/gps/hist/point	9.000000E+02	4.222175E-04
75	/gps/hist/point	1.000000E+03	4.130692E-04
76	/gps/hist/point	1.100000E+03	4.014578E-04
77	/gps/hist/point	1.200000E+03	3.882883E-04
78	/gps/hist/point	1.400000E+03	3.596747E-04
79	/gps/hist/point	1.600000E+03	3.305207E-04
80	/gps/hist/point	1.800000E+03	3.024725E-04
81	/gps/hist/point	2.000000E+03	2.762842E-04
82	/gps/hist/point	2.200000E+03	2.522448E-04
83	/gps/hist/point	2.500000E+03	2.202885E-04
84	/gps/hist/point	2.800000E+03	1.929189E-04
85	/gps/hist/point	3.200000E+03	1.625586E-04
86	/gps/hist/point	3.500000E+03	1.436587E-04
87	/gps/hist/point	4.000000E+03	1.179919E-04
88	/gps/hist/point	4.500000E+03	9.800638E-05
89	/gps/hist/point	5.000000E+03	8.226323E-05
90	/gps/hist/point	5.500000E+03	6.971822E-05
91	/gps/hist/point	6.300000E+03	5.447396E-05
92	/gps/hist/point	7.100000E+03	4.340047E-05
93	/gps/hist/point	8.000000E+03	3.428734E-05
94	/gps/hist/point	9.000000E+03	2.695361E-05

```
95 /gps/hist/point      1.000000E+04    2.159656E-05
96 /gps/hist/point      1.100000E+04    1.758915E-05
97 /gps/hist/point      1.200000E+04    1.452924E-05
98 /gps/hist/point      1.400000E+04    1.027238E-05
99 /gps/hist/point      1.600000E+04    7.549373E-06
100 /gps/hist/point     1.800000E+04    5.722725E-06
101 /gps/hist/point     2.000000E+04    4.449375E-06
102 /gps/hist/point     3.000000E+04    1.641042E-06
103 /gps/hist/point     4.000000E+04    7.908394E-07
104 /gps/hist/point     5.000000E+04    4.445856E-07
105 /gps/hist/point     6.000000E+04    2.762717E-07
106 /gps/hist/point     7.000000E+04    1.842230E-07
107 /gps/hist/point     8.000000E+04    1.294336E-07
108 /gps/hist/point     9.000000E+04    9.468383E-08
109 /gps/hist/point     1.000000E+05    7.151647E-08
110 /gps/hist/inter      Lin
111 /gps/ang/type        cos
112 /gps/ang/mintheta    0.000E+00 deg
113 /gps/ang/maxtheta    9.000E+01 deg
114 /gps/source/list
115
116 #
117 #Normalisation
118 #
119 /control/alias       NORM_FACTOR_SPECTRUM " 7.876719E+06 "
120 /control/alias       NORM_FACTOR_ANGULAR  " 2.500000E-01 "
```

**Listing E.1:** Particle source definition macro

# F Miscellaneous

## F.1. Radiation Measurement & Relevant Quantities

Radiation can be measured and quantified by the use of radiation detectors, and instruments which incorporate these detectors. Most detectors are made up of two main parts - a material or substance that is responsive to incident ionizing radiation and an external device that can take this response and convert it into physical signals that can be measured and recorded <sup>1</sup>. Detectors of ionizing radiation can be categorized based on the type of radiation being detected or the purpose of the detector. Based on the purpose of the detector, the classification can be made as:

- Dosimeters: These detectors measure ionizing radiation exposure in terms of the dose i.e energy absorbed in the detector volume
- Spectrometers: These detectors measure the spectrum of incident ionizing radiation which can later be used to derive the energy of particles
- Counters: Counters detect the number of hits or interactions of ionizing radiation particles with the detector. They are used to measure radioactivity in counts per unit time. An example of these is the famous Geiger Counter

Hereon, some quantities which are relevant to radiation measurement and this study are discussed in short:

### Flux

Radiation flux is defined as the amount of particles passing through a unit cross-sectional area in a given time. Flux has the units of *particles/cm<sup>2</sup>/sec*. Fluence is the flux integrated over a period of time. The number of particles detected per unit time are expressed in terms of counts per second (cps).

### Cross-section

Cross-section is a quantity which signifies the probability of an interaction occurring between an incident radiation particle and a target particle or object <sup>2</sup>. Cross-section is usually expressed in units of *cm<sup>2</sup>* or *m<sup>2</sup>* and a larger cross-section implies a higher likelihood of interaction. In relation to incidence of ionizing radiation on electronic devices and its effects such as SEEs, cross-section is expressed as the number of events divided by the total fluence of the particles.

### Radioactivity & Exposure

Radiation activity is the amount of radiation emitted by a certain source whereas radiation exposure is applicable to the effect that radiation has on the objects or materials that absorb said radiation. Radioactivity is measured in terms of the number of particles or photons that a source emits per unit time. The SI Unit of radioactivity is becquerel (Bq). The unit curie (Ci) is also used sometimes and the conversion factor is given by  $1 Ci = 37 GBq$ .

Radiation exposure can be expressed in the following ways, based on the method of calculation and the application for which the exposure is being calculated.

- The absorbed dose, D in a body of mass m which is exposed to radiation that deposits energy E in the mass, can be calculated as:

$$D = \frac{E}{m} \quad (F.1)$$

the absorbed dose is expressed in the S.I. unit Gray (Gy). 1 Gy represents 1 J of energy deposited in a substance of mass 1 kg. Absorbed dose can also be expressed in rads, where  $1 Gy = 100 rad$ . Absorbed dose is proportional to the square of the charge deposited by incident radiation [104]. The absorbed

<sup>1</sup><https://www.nuclear-power.com/nuclear-engineering/radiation-detection/>

<sup>2</sup><https://www.nuclear-power.com/nuclear-power/reactor-physics/nuclear-engineering-fundamentals/neutron-nuclear-reactions/definition-of-cross-section/>

dose is a purely physical quantity and hence it can be measured directly using detectors. In contrast, effective and equivalent dose are derived quantities which are calculated from the absorbed dose and cannot be measured directly.

- The equivalent dose is calculated for individual tissues or organs, based on the effectiveness of the type of absorbed radiation on a specific tissue/organ. Hence, it depends on both particle type and energies. This is achieved using radiation weighting factors,  $w_R$  which are numerically assigned based on reviews of biological information and studies of living tissue subjected to radiation [39]. Based on the absorbed dose, the equivalent dose for a given organ/tissue (T) can be calculated as:

$$H_T = \sum w_R \cdot D \quad (\text{F.2})$$

Equivalent dose is measured in the unit Sieverts (Sv) or the CGS unit, roentgen equivalent man (rem), where  $1 \text{ Sv} = 100 \text{ rem}$ . Radiation detectors usually measure the absorbed dose in Silicon i.e. the dose (Si). The equivalent dose in water is more relevant for radiation protection applications since water can be approximated to living tissue. The conversion from dose in Si to that in water can be calculated by using a scaling factor of 1.33 [116].

- The effective dose or 'whole body dose' is calculated as the sum of equivalent doses to all organs or tissues in an organism, weighted using applicable tissue weighting factors,  $w_T$ . These factors are based on the sensitivity of various organs or tissues to the incoming radiation. Based on the equivalent dose calculated for various parts of a body, the effective dose can be calculated as:

$$E_d = \sum w_T \cdot H_T \quad (\text{F.3})$$

The effective dose is also expressed in Sv or rem.

The dose rate is defined as the amount of dose that is delivered per unit time and can be calculated using time resolved measurements of the dose quantities mentioned above. Figure F.1 depicts a summary of the dose quantities described above and what they mean. Since the absorbed dose is a directly measured quantity, it is more appropriate for the description and characterization of radiation fields in space. The effective and equivalent dose serve as better tools for radiobiology applications such as calculating amount of harm to living tissue, predicting radiation induced diseases, making occupational risk assessments and mitigation plans for astronauts etc.

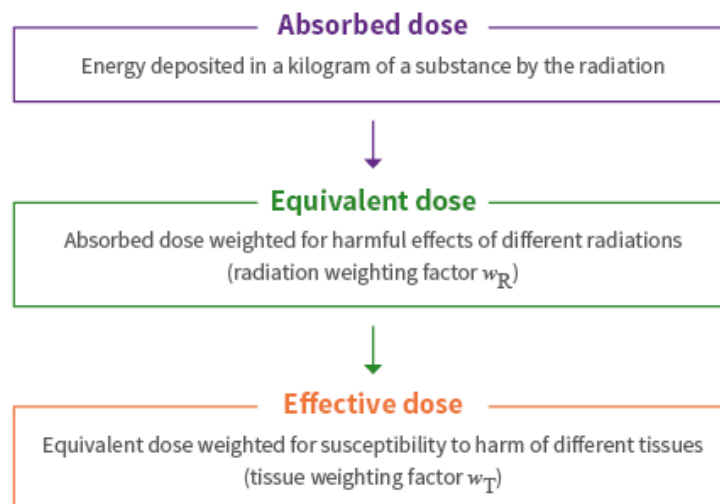


**Figure F.1:** Summary of radiation exposure quantities [5]

## LET

Linear energy transfer (LET) is defined as the "rate of energy deposited through ionisation from a slowing energetic particle with distance travelled in matter, the energy being imparted to the material" [ECSS\_std\_rad]. LET depends on the material and also on the energy and charge of the incident radiation. LET is a quantity of importance since it can be used to gauge the effects of radiation on matter, both living and non-living.

LET can be approximated to the stopping power, which is the energy loss due to ionization and excitation per unit path length in matter. The stopping power represents the energy loss per unit length of a particle in a material, so it also includes the effect of secondary radiation such as bremsstrahlung. Sometimes, quantities such as 'lineal energy transfer' or 'normalized energy deposit' are used instead of the conventional LET, for denoting the amount of energy deposited in total in radiation detectors [80]. Data such as tables for stopping power and range for various particles and ions can be obtained from the NIST database [95] or SRIM<sup>3</sup>.

---

<sup>3</sup><http://www.srim.org/>